Dissertation zur Erlangung des Doktorgrades
der Fakultät für Chemie und Pharmazie
der Ludwig-Maximilians-Universität München

# Synthesis and Characterization of Nanoporous Covalent Organic Frameworks for Optoelectronic Applications

Torben Sick

aus

Hamburg, Deutschland

2018

Erklärung:

Diese Dissertation wurde im Sinne von § 7 der Promotionsordnung vom 28. November 2011 von Herr Prof. Dr. Thomas Bein betreut.

Eidesstattliche Versicherung

Diese Dissertation wurde eigenständig und ohne unerlaubte Hilfe bearbeitet.

München, den 05.08.2018 Torben Sick

Dissertation eingereicht am 25.06.2018

1. Gutachter: Prof. Dr. Thomas Bein

2. Gutachterin: Prof. Dr. Dina Fattakhova

Mündliche Prüfung am 23.07.2018

# ACKNOWLEDGEMENTS

First, I would like to express my gratitude to my doctorate adviser Prof. Dr. Thomas Bein for his support during my PhD in his working group.

I'm as well very grateful to Prof. Dr. Fattakhova for being my second supervisor, for the guidance and advice through the last stage of my PhD.

The possibility to work in an international group on the comparably young and very challenging topic of Covalent Organic Frameworks extended my skills in many different fields. Focusing a lot on organic chemistry synthesis allows for the use of powerful techniques like NMR, MS, column purification and others. The combination with physical measurements like ssPL, TCSPC, UV-Vis, physisorption, SEM, TEM, and XRD led to much personal progress over the last 3.5 years. Providing all these high-end analytical laboratory techniques was the basis for optimum working conditions. I also want to thank Thomas for the possibility to travel to many very interesting conferences all over the world, presenting my results and representing the LMU. In this context I also want to thank the GDCh and the CeNS cluster for funding. Furthermore, I want to thank the GDCh for their very interesting mentoring program CheMento and the highly motivated people of the Jungchemikerforum in Munich for many fruitful discussions how to improve chemsistry students' life and accelerate careers in Munich, namely the Alpenforum.

I want to thank the DAAD Rise program, where I had the chance to get in contact with Austin Evans, formerly being my supervised student and today for making our friendship possible. I also want to thank Max Hofmayer, Nadja Klipfel, Nikolai Bach, Andreas Koszalkowski and Konstantin Mallon for being diligent and hardworking throughout their internships. I had a great time with you.

I want to thank my collaboration partners, who as well became friends to me. First, I want to thank Dana and Dina for the supervision of my projects. The progress was not always as fast as both sides would have hoped it to be, but I thank you for your time, comments and advice. Without these it would have been a never ending story. I want to thank Mona for helping me a lot with integration and arriving in the working group Bein. You have been my mentor for the first two years and I'm very grateful. I also want to thank Julian, Patrick, Derya, Stephan and Niklas for many hours chatting at the glove boxes, in the laboratories or for the definitely necessary distraction during coffee and beer breaks. I want furthermore to thank Alexander and

Jonathan for being great collaborators during the COF-water splitting project. My office colleagues made life a lot easier and I remember a lot of laughing in all of my offices. Therefore, I want to thank Enrico, Sabrina, Mona, Julian, Derya, Fabian, Jonathan, Ilina, Alexander, Lisa, Michiel (unfortunately only for 3.5 weeks), Stefan and Noggi for being such nice people. I want to thank Markus Döblinger for all the excellent TEM images. Special thanks go to Regina, our former secretary, as well as to Hans and Norma for every kind of organization and integration within the group and in Bavaria. I also want to thank Corinna for her organization skills and help throughout the last steps of my PhD.

I also want to thank my collaboration partners in Germany and all over the world, ranging from Munich to Nuremberg-Erlangen, Würzburg, and Prague to Cambridge and Argonne. Projects often turned out to be dead ends, but I'm very grateful for all the patience, time and measurements.

I would like to thank the PhD candidates and students from the other chemistry divisions for the soccer time on Thursdays, allowing for venting frustration during the week.

I have to say thank you to my dear friends. First, I have to mention Svea as my best friend. I love you for your completely honest and open mind. You definitely tell me whenever I'm a fool. I can tell you everything that is on my mind. Thanks to Roy, Valerie, and Paul for making Munich a nice place for me. I also want to thank my friends all over Germany, Jos and Julia, Basti, Tina, Tobi and Sandra, Michi, and Martin for making life more adorable and worth living.

All in all, I have to admit that I am a very lucky fellow. But I also want to say thank you to Kristina. I'm infinitely lucky to know that you are by my side. Meeting you was definitely the best part of moving to Munich. I'm happy spending time with you, your friends and your family.

Zum Schluss möchte ich natürlich noch ganz herzlich den wichtigsten Menschen in meinem Leben danken, meiner Familie. Susanne und Uwe, euch möchte ich für die Hingabe, die Werte und die Zeit danken, die ihr meiner Schwester Anika und mir habt zukommen lassen. Davon profitiert nun auch Christian. Außerdem möchte ich euch dreien für die offenen Ohren in guten und in schweren Zeiten danken. Ich bin sehr froh, dass es euch gibt. Außerdem möchte ich meinen Großeltern Waldtraut, Gisela und Horst danken. Waldtraut, du warst immer für mich da. Dafür werde ich dir immer unendlich dankbar sein. Ich bin sehr froh, dass es euch alle gibt.

# ABSTRACT

Nanostructured materials represent an intriguing and growing field of research aimed at developing new, application-targeted materials. Different techniques have been established for the synthesis of porous materials, particularly for those with defined pore size, volume and surface area. Covalent organic frameworks (COFs) are a class of lightweight and highly crystalline open porous networks, where different organic building blocks are connected *via* covalent bonds to form polymers. By the choice of the building blocks' geometry, dimensionality and incorporated functionality, the pore shape and size can be tailored. COFs exhibit high thermal and reasonable chemical stability in combination with high specific surface area and a long-range order. With these features in hand, COFs allow for a precise spatial arrangement of variable building blocks. This allows for the examination of potential correlations between the degree of crystallinity and porosity, aiming at other desired properties and behavior like host-guest interactions, light absorption, diffusion, and conductivity. While 3D COFs are interconnected in all three dimensions, in 2D COFs polymeric sheets stack in the third dimension *via* comparably weak dispersive forces (π-stacking). Thereby, the distance of building blocks within adjacent layers can be much smaller compared to the 3D structures, which allows for enhanced interactions in the stacking direction. The respective stacking distance mainly depends on the spatial requirements, steric hindrances and stacking affinities of the incorporated building blocks.

As COF growth is a highly dynamic process simultaneously occurring at different reactive sites, and at a high reaction rate by reversible bond formation, crystallites with small domain sizes and orientations are most likely to form. As the reversible bond formation enables the self-healing mechanism of COF crystallites and defines the degree of overall order, influencing the reversibility and the reaction rate is an important goal in COF syntheses. In chapter three, we introduce a strategy to slow down the overall reaction rate by the addition of competitive molecular agents named modulators. The modulator agents act on the covalent bond formation and on the formation of the 2D sheets. The modulator molecule usually lacks symmetric reactive linking groups and thereby, under reversible reaction conditions, can attach and leave the growing fragment. It temporarily truncates the active linking sites of the respective counterpart. Furthermore, this approach allows for the incorporation of accessible functional groups or stabilizing polymer chains, as the modulators finally most probably partially decorate the COF crystallite outer surface. By employing the modulator approach, enlarged domain sizes

are obtained. Furthermore, the overall porosity and accessible surface area are positively affected.

As the first COFs were constructed by connecting building blocks through the formation of sigma bonds, charge migration within the polymeric sheets was effectively inhibited. To enable charge carrier mobility within the sheets, conjugated COFs like imines or imides were developed. Importantly, in COFs consisting of completely planar and rigid building blocks, the incorporation of heteroatoms can result in lateral offsets between adjacent layers due to the electrostatic repulsion and bond polarization. Thereby, adjacent COF layers start to stack – energetically driven – in a staggered mode without any preferential displacement direction and slight lateral offsets are the result. This inconsistent displacement can result in comparably small domain sizes in all three dimensions of the individual crystallites. In chapter four we addressed this issue by the incorporation of propeller-like building blocks (4,4′,4″,4‴-(ethylene-1,1,2,2-tetrayl)tetraaniline (ETTA), 1,3,5-tris(4-aminophenyl)benzene (TAPB) and tris(4-aminophenyl)amine (TAPA)). These sterically demanding building blocks serve as anchors by predefining a thermodynamically favored docking site of attachment.

In chapter five we describe the incorporation of an electroactive counterpart, namely 2,6-imine connected benzo[1,2-*b*:4,5-*b*']dithiophene (BDT) to the ETTA building block, which provides a highly crystalline and open porous, kagome-structured COF. Oriented thin films of the BDT-ETTA-COF were fabricated using the well-established in-situ film growth. By variation of the precursor concentration, thin COF films with a high degree of orientation and different thicknesses could be synthesized on different substrates like quartz or conducting oxides (indium tin oxide (ITO) and fluorine-doped tin oxide (FTO)). Finally, the very first COF-photocathodes were fabricated and utilized in noble metal-free photoelectrochemical water splitting to hydrogen and oxygen. The deposition of platinum nanoparticle co-catalysts on top of the photoabsorbing COF allowed for a significant increase in photocurrent.

In chapter six, the realization of an isoreticular series of the propeller-like TAPB building block featuring hexagonal COF pores is shown. The TAPB-COFs with comparably short linear linkers such as 1,4-imine connected phenylene (TA), 2,5-imine connected thieno[3,2-*b*]thiophene (TT) or BDT revealed structural instability towards post-synthetic treatments. Neither the desired property of crystallinity nor of porosity could be preserved upon usual powder isolation treatments like filtering, washing, or solvent exchange. The development of a very successful and fast work up procedure with supercritical carbon dioxide ($scCO_2$) resulted in the desired highly crystalline and open porous frameworks, which were stable under ambient

conditions for months. However, treatments with solvents or even solvent vapors drove these COFs back to poorly crystalline non-porous materials. To overcome this stability issue, an extension of the π-system such as 2,7-imine connected pyrene (Pyrene-2,7) or alkoxy functionalization of the BDT cores (4,8-dialkoxy-functionalized BDT: BDT-OMe, BDT-OEt, and BDT-OPr) dramatically increased the COFs' stabilities. Even a continuous Soxhlet-extraction became a possible work-up procedure for these robust COFs. The incorporation of the pyrene building block results in a comparably closer stacking distance between the adjacent Pyrene-2,7 TAPB layers. This emphasizes the role of the linear counterpart in the overall TAPB-COF structural stability. Furthermore, it illustrates that the TAPB core features a somewhat flexible propeller configuration rather than providing a rigid docking site dictating the COF stacking distance. Depending on the employed linear counterpart that was previously viewed to serve only as a bridge between the two rigid propeller nodes, this approach has the potential to modulate and dictate the stacking profile of the final TAPB-COF. Surprisingly, all TAPB-COFs, whether fragile or robust, exhibit a high degree of sensitivity towards the main component of the reaction mixtures, namely 1,4-dioxane. Upon exposure to 1,4-dioxane vapor, time-dependent PXRD measurements revealed a significant impact on the π-stacking distance of adjacent layers, which was enlarged in all COFs. We propose a molecular layer intercalation mechanism, which in the case of 1,4-dioxane results in an amorphization of the COF structures. In 1,4-dioxane atmosphere, the π–attractive forces between adjacent COF layers are weakened, resulting in a complete layer displacement in all three dimensions. Strikingly, we were able to reestablish all 1,4-dioxane treated, amorphous COF powders using the $scCO_2$ treatment, thus converting the amorphous powder back into crystalline and highly porous COF structures. This process can be cycled as often as desired and shows that $scCO_2$ treatment is an excellent, fast, and efficient work-up procedure for all investigated TAPB-COFs, whether robust or fragile.

In chapter seven we introduce chrysene as the core of a four-arm ETTA-like building block, i.e. dibenzo[*g*,*p*]chrysene-2,7,10,15-tetraamine (DBCA). In condensation reactions with linear bifunctional aldehyde counterparts dual pore kagome DBC-COF structures with imine linkages are obtained. With propeller-like molecular building blocks such as ETTA featuring docking sites for COF construction, the stacking distance of adjacent layers still is comparably large with about 4.7 Å. Close stacking distances of the adjacent COF layers with preservation of the structural guidance provided by a rigid docking site are beneficial for an improved π-orbital overlap of the building blocks and thereby electronic interactions of the adjacent layers. This feature should allow for enhanced charge migration within the COF. In this context, the central

naphthyl unit of DBC instead of the central ethylene unit of ETTA offers two advantages. Firstly, a fully conjugated π-system in the DBC core. In DBC all phenyl groups contribute to one π-system. Secondly, while the rotation of the phenyl groups in ETTA provides for the desired molecular docking sites, it simultaneously results in a weaker π-overlap. In DBC the tilting is minimized upon incorporation of two new chemical bonds, resulting in a large π-overlap as well as a closer stacking distance of adjacent layers.

# TABLE OF CONTENTS

# 1. INTRODUCTION

## 1.1 COVALENT ORGANIC FRAMEWORKS

Covalent Organic Frameworks (COFs) represent a class of crystalline and porous polymers. In particular, the precise spatial assembly of the incorporated, rigid molecular organic building units has attracted much research interest. Combining properties of organic and crystalline matter, COFs' pore diameters range from micropores to mesopores (presently from about 1 to 5 nm).[1-3] It is even possible to construct dual-pore and hierarchically porous frameworks, which allows for the synthesis of a plethora of different COF structures with different pore sizes.[4-6]

Porous systems in the range of micropores (≤ 2 nm) are commonly obtained by synthesizing zeolites[7], metal organic frameworks (MOFs)[8-10] or zeolitic imidazolate frameworks (ZIFs)[11]. Approaching mesoporous systems (2-50 nm) is often based on soft- or hard-templated synthesis.[12] Under soft-templating synthesis conditions, micelles are formed *via* concentration-controlled approaches with charged or neutral surfactants. Charged surfactants like quaternary ammonium cations or neutral surfactants like triblock copolymers (F127, P123) form these micelles in solvents depending on their critical micelle concentration (CMC). The structure of the micelles is dependent on temperature, concentration, and the surfactants' molecular structure and characteristics. A reactive precursor is added to the solvent/surfactant mixture, which infiltrates the voids between the surfactant micelles and finally, the precursor reacts to form the desired product. Soft templates finally can be removed from the resulting composite material by extraction or thermal treatment (calcination, combustion).

By contrast, in hard-templated syntheses, the template is solid and does not form during synthesis. After reaction towards the composite material, hard templates can be removed, depending on their chemical composition, by extraction, combustion or dissolving agents (like hydrofluoric acid for silica hard templates). A schematic overview of soft- and hard-templating syntheses is shown in Figure 1.1.

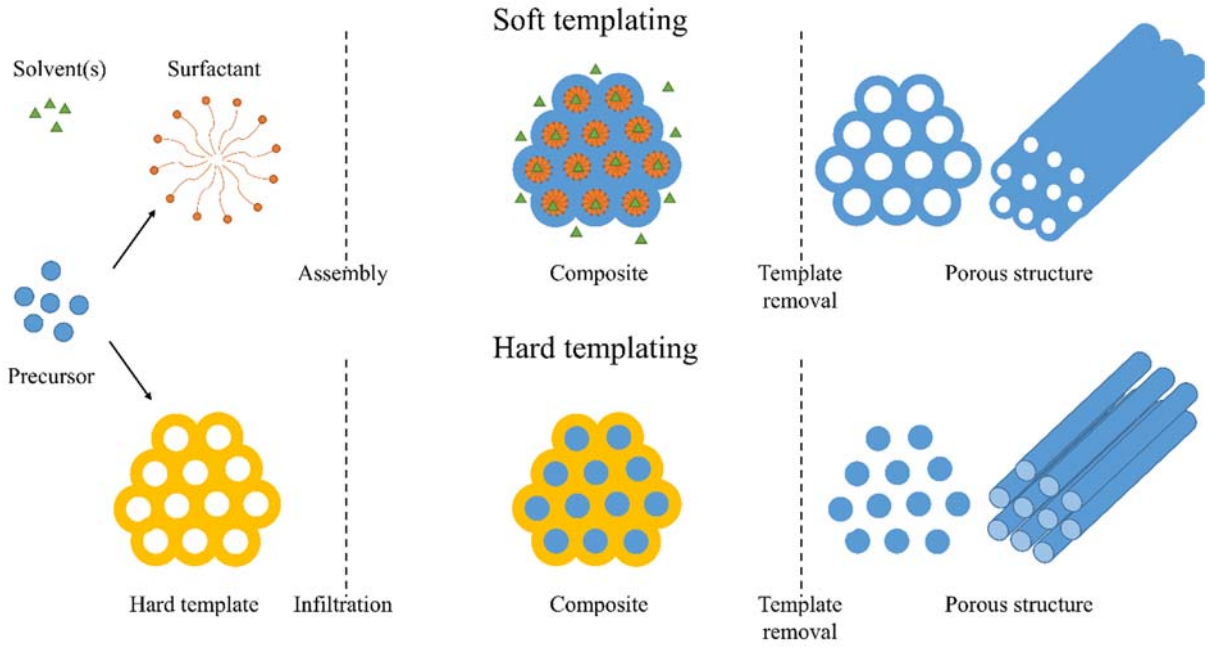


Figure 1.1: Schematic illustration of soft- and hard-templating approaches. While in soft-templating (top) surfactant molecules self-assemble in superstructures, where the created voids can be accessed *via* infiltration by the precursor, in hard-templating (bottom), the voids are an inherent feature. After successive reaction of the precursor towards the final structure, the templates can be removed from the composite material to obtain the final porous material.

In COF syntheses, neither hard- nor soft-templates have to be used, which can represent a significant benefit in the realization of porous systems. The pores in COFs are already predefined by the structure of the building blocks and their inherent geometry. Furthermore, 2D and 3D COFs can be distinguished by their structural design of building units. While 3D COFs consist of a framework of covalent bonds extending in all dimensions, 2D COFs are made up of two-dimensional polymer sheets stacking in the third dimension. The respective choice of linker affects the pore size, the symmetry of the framework and the connectivity. Most COFs are prepared under solvothermal conditions by a reversible bond formation process from different building blocks. These building blocks are alternatingly incorporated into the growing framework. As the different building units exhibit specific complementary geometries, predefined skeletons with the respective characteristics are created. By tailoring the building blocks' design concerning structure, decoration with side groups or incorporation of functional groups, the pore shape, topology, and size can further be fine-tuned. Ranging from hexagonal and square-like structures, dual-pore triangular and hexagonal pore shapes (kagome) to triangular and rhombic structures, COFs exhibit the potential to fine-tune the properties of

crystalline and porous matter. An overview of selected topologies resulting in different frameworks is shown in Figure 1.2.

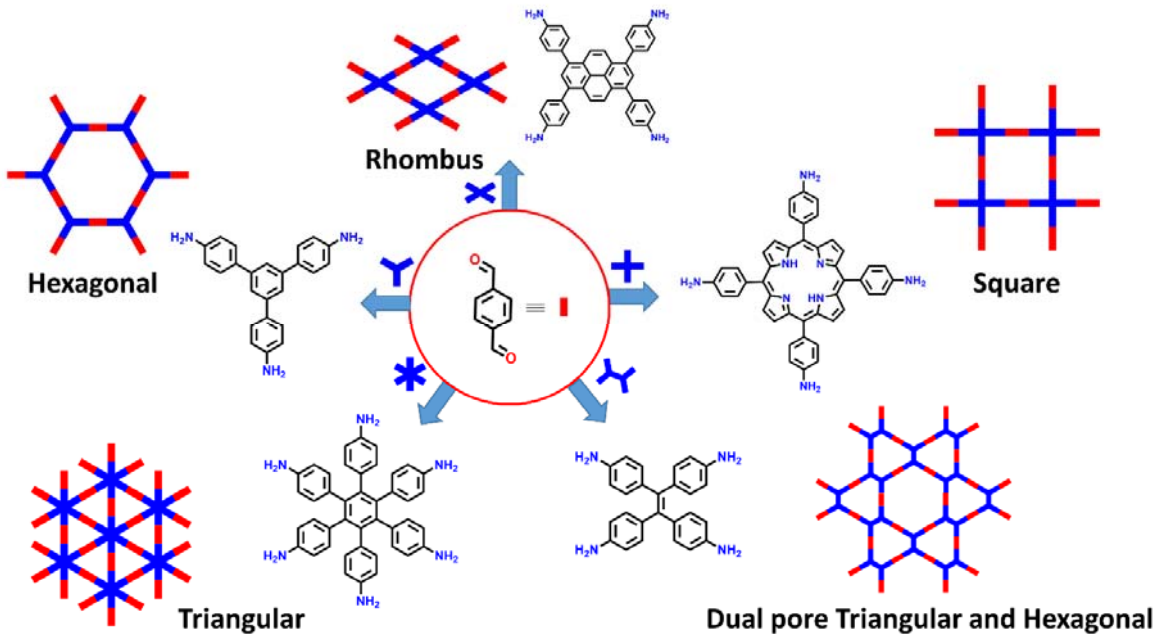


Figure 1.2: Potential topologies of a linear, bifunctional linker (red) in combination with complementary amine-functionalized linkers (blue) exhibiting different symmetries. The linker selection results in COFs with different pore shapes and pore sizes.[13]

Besides this, attempts have been realized to incorporate desymmetrized linkers[14-16] or to combine linkers of different lengths[17] resulting in heterogeneously porous COF structures.

As it is dependent on the bond type, the equilibrium of the bond formation process can be influenced by reversible condensation reactions. Catalyzing agents can be used to vary the rate of reaction. Various COF structures with different geometries and pore topologies have been synthesized and investigated since Yaghi and co-workers reported the very first COF structures in 2005.[18] The most widely investigated COFs are boronic esters, synthesized through reaction of boronic acids and polyols, and on the other hand imine COFs, realized from amines and aldehydes. Further functional groups have been successfully integrated within new frameworks, as shown in Figure 1.3.

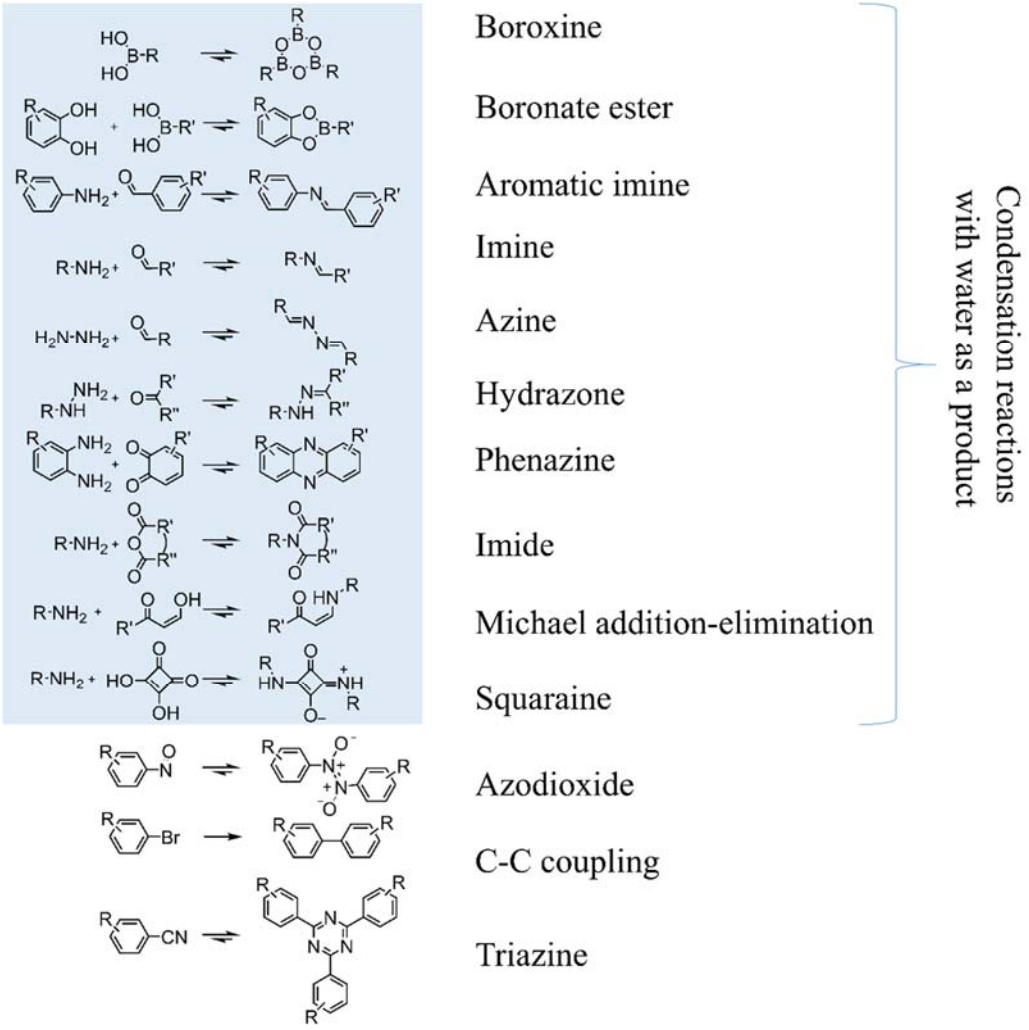


Figure 1.3: Different linkage motifs being realized in crystalline COFs. The majority is based on condensation reactions with water as a byproduct (blue background).[13]

The majority of COFs is prepared by reversible condensation reactions with water as a byproduct. Starting from boroxines and boronic esters in 2005[18], borosilicates[19] and borazine[20] COFs were established. The conjugated imine-based COFs have attracted much research attention since 2009.[21-28] Followed by the first COFs based on hydrazones[29], azines[30], phenazines[31] and squaraines[32], the first synthesis of imide COFs[33] was demonstrated in 2014. Michael addition-elimination reactions have shown potential in COF syntheses[34] as well as Knoevenagel condensation reactions[35-36], which further expanded the possibilities in COF design.

COFs constructed *via* reversible reactions that are not based on producing water, are the widespread covalent triazine frameworks (CTFs)[37] and azodioxide frameworks[38]. The use of fully non-reversible reactions to realize COFs still is rare. One approach uses bromine-functionalized linkers being reacted at very high synthesis temperatures.[39]

Under optimum reaction conditions concerning concentration, solvents, temperature and time, reticular building units allow for high regularity of the resulting geometry. The great variety in accessible geometries as well as in linkage motifs allows for the incorporation of a plethora of different building blocks, functional motifs and heteroatoms within the linkers. Porphyrins[40] and phthalocyanines[41] have been incorporated into COF structures as well as pyrene[22] or coronene[2, 42] molecules. The conditions for successful syntheses are the necessary solubility and the reactivity of the mono- and oligomers. A high degree of order can only be realized if the reactions within the growing framework are slightly reversible. An equilibrium in covalent bond formation allows for a dynamic 'self-healing mechanism' within the growing framework, making a rearrangement of misplaced bonds or molecules possible. This enables the synthesis of 'error-checked' highly ordered polymeric sheets and frameworks. Resulting voids within these polymeric sheets make up the accessible surface area when these sheets stack upon each other due to π-attractive interactions in an approximately eclipsed manner. Without spatial control, the beneficial and desired properties of order and porosity would not occur. These mechanisms of ordering and arrangement result from comparably small dispersive forces, like van der Waals forces, dipole-dipole interactions and (partial) charge attractions.

Boronic ester COFs already exhibit a high degree of crystallinity, open porosity and thermal stability. Nevertheless, upon treatment with protic solutions, boronic esters decompose. Furthermore, the interconnections of the frameworks *via* sigma bonds result in non-conjugated crystalline and porous polymers. These features have a great impact on the conductivity through the polymeric sheets. The differences in completely sigma-bond-conjugated boronic esters in comparison to conjugated imine-, nitrile-, or imide-based frameworks result in different charge-carrier propagation pathways within the planes as well as perpendicular to the layers. The realization of conjugated frameworks is expected to result in high charge carrier mobility through the whole interconnected COF crystallite or sheet.

COFs as lightweight, porous and ordered polymers have attracted attention in many fields of application, like gas storage[22, 43-44], proton conduction[45-46], catalysis[23, 47-50], separation[51-52], energy storage[53-54] and optoelectronics[26, 55-57]. As they exhibit predefined pore geometries, a direct correlation between pore size and material properties can be established. First interdisciplinary approaches have shown potential advantageous features of COFs being integrated in HPLC[58-60], magnetic[61-62] and electroactive materials[13]. As micro- and mesopores are accessible, even hierarchically porous composites can be achieved by combining COFs and other materials[63-68] or by growing COFs on or within other porous structures[52]. As even

postsynthetic modifications[23, 69-70] and the incorporation of linkers with different substitutents[71] are relatively easy to accomplish, the frameworks can be tailored with respect to opto-electronic and photophysical properties as well as geometric structure.

## 1.2 SYNTHETIC STRATEGIES

The crystallinity and porosity of the synthesized covalent organic frameworks is mainly dependent on the reaction conditions, namely the purity of the used monomers, the strength and the concentration of catalyzing agents, the used solvent or solvent mixture, as well as preparation technique, temperature, reaction time and the final work-up procedures. As the products' properties and potential applicability are highly affected by the samples' design and quality, different strategies to result in bulk powders or oriented as well as non-oriented films have been introduced. Usually, a new COF structure is initially synthesized as a bulk material. For this purpose, different variations of solvent mixtures and temperatures are tested to compare their impact on the desired properties of the frameworks concerning crystallinity (powder X-ray diffraction, PXRD) and porosity (physisorption). For bulk syntheses, a homogeneous distribution of precursors is preferred, as incipient reaction and nucleation of monomers to oligo- and polymers should result in the growth of layers, which finally stack in the third dimension. Dispersions of starting materials might result in heterogeneous growth conditions, such as concentration gradients or deficiencies. On the other hand, to grow films on a substrate surface, the growth surface is placed facing downwards, allowing for the growth of an oriented or non-oriented film by layer stacking. The reaction conditions from bulk synthesis often cannot be directly transferred to film synthesis of the same material and have to be optimized separately. The synthesis of COF films in an autoclave is illustrated in Figure 1.4. It is possible to introduce several slides to one autoclave to obtain multiple films from one batch. Furthermore, the bulk material precipitated at the bottom of the vessel can be collected, purified and investigated.

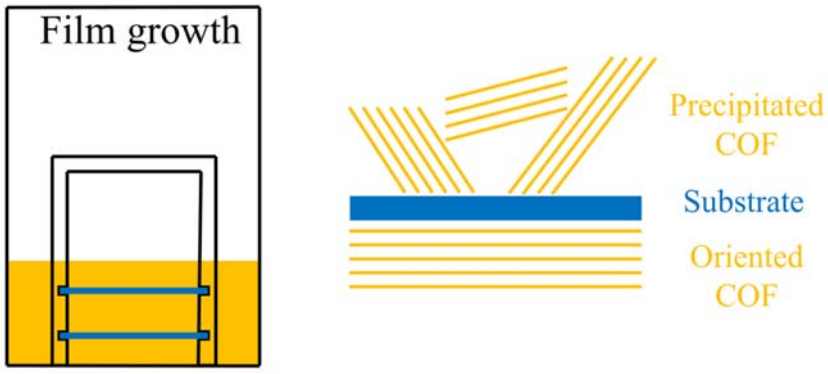


Figure 1.4: The growth of COF films growth within an autoclave is shown on the left side. The respective substrates are plasma-cleaned to avoid contamination with dust and other surface contaminations. After insertion of the substrate to a Teflon holder, the films are placed in the reaction mixture and transferred to the oven. The COF starts to form at different nucleation centers within the reaction mixture. On top of the substrate, non-oriented precipitate forms a polycrystalline film, as illustrated on the right side. From beneath, under the right synthesis conditions, the successive layer growth results in an oriented COF film.

Another film approach is based on a vapor-assisted conversion of precursors deposited on the substrate.[72] In a sealed vapor chamber, the respective solvents are able to access the precursors only by vaporization. This approach is very promising, especially for boronic ester COFs, as no catalyst is needed for the subsequent conversion to the final crystalline product. Furthermore, we note that to date only the film thickness can be controlled, but the films grow as non-oriented, polycrystalline matter.

Depending on the stability of the final products, different potential work-up procedures can be utilized to purify the resulting COF. Usually COFs are rinsed with the main solvent of the reaction mixture to remove non-reacted monomers, poorly connected oligomers, catalyzing agents and excess solvent from the porous system. High-boiling solvents can be slowly exchanged with low-boiling solvents prior to vacuum drying. Highly stable frameworks can be Soxhlet-extracted over hours or days to allow for complete removal of all potential guest molecules. In the case of highly sensitive or fragile COFs, slow drying under argon[26] or supercritical fluids can be used to finally obtain the desired product in the desired quality.

# 1.3 IMPROVING THE CRYSTALLINITY AND POROSITY OF COVALENT ORGANIC FRAMEWORKS

## 1.3.1 MODULATING AGENTS

In the synthesis of highly crystalline and open porous networks under solvothermal conditions, the ratio of linkers is usually exactly adapted for the relative number of reactive sites. But due to the different solubility and reactivity of the starting compounds, the concentration and the activity of the available reactive sites may change over time, which implies that crystallinity and porosity will be influenced by the reaction rate, an excess of any compound or a potential saturation. One strategy to address this issue is the addition of competitor molecules to slow down reaction rate. Another possibility is the partial substitution of one reaction partner by competitor molecules to partially block reactive sites within the growing system. Although widely used in the synthesis of porous coordination polymers, zeolitic imidazolate frameworks (ZIFs) or metal-organic frameworks (MOFs)[73-80], the use of modulating agents in COF synthesis has been investigated only in a few studies[43, 81]. In MOF syntheses, different modulator agents allow for anisotropic crystallite growth.[82] A schematic overview on the MOF crystallite growth is shown in Figure 1.5. This makes modulators very interesting for COF syntheses as well.

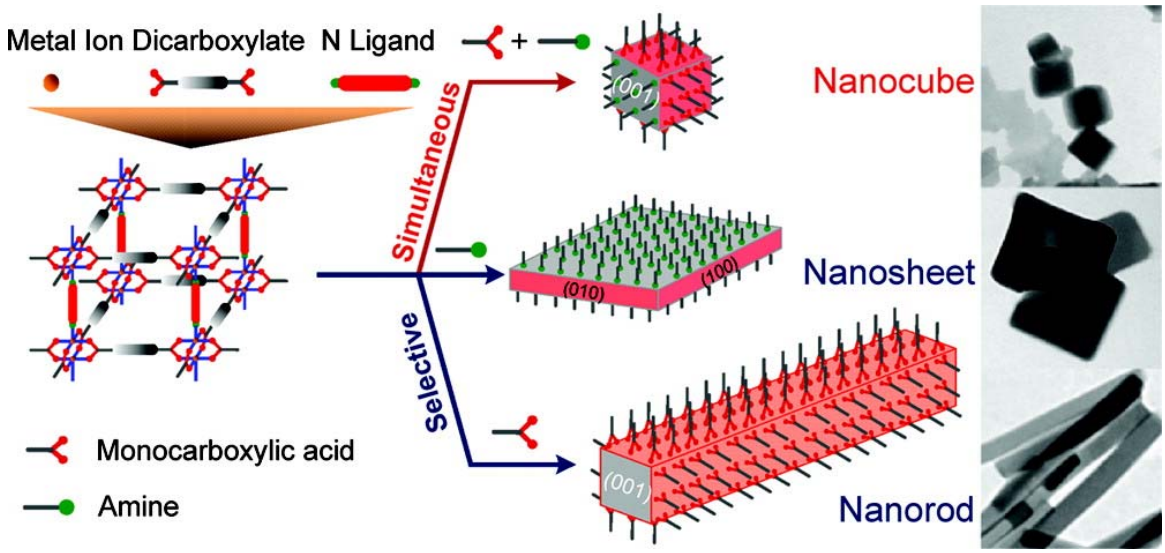


Figure 1.5: Schematic illustration of modulating agents on the growth of MOF crystallites. The synthesis can be adjusted to result in nanocubes, nanosheets or nanorods, only dependent on the respective synthesis condition.[82]

### 1.3.2 INFLUENCING STACKING DISTANCES AND STABILITIES BY USING APPROPRIATE BUILDING BLOCKS

The choice of building blocks has a tremendous effect on the quality of the resulting framework. Apart from solvents, solvents' ratio, temperature, reaction time, type as well as quantity of the catalyzing agent, the reactivity and the geometry of the used building blocks are the main factors influencing the COF's structure and properties. By the choice of linkers, the geometry of the 2D sheets can be easily predesigned in a reticular synthesis strategy. Different framework patterns can be obtained by combining C2 with C3, C4 or C6 linkers (Figure 1.2). As the linear C2 part can be tuned in length as well as by chemical pre- or post-modification, in principle a broad range of frameworks can be realized. Within the linkage motifs often heteroatoms are incorporated, resulting in a polarization of the covalent bonds. This bond polarization affects the stacking affinity of adjacent layers. In 2D COFs, especially in B-, Si-, S-, O- or N-containing frameworks, the resulting electrostatic repulsion has to be considered during stacking, where adjacent layers tend to arrange not perfectly eclipsed, but slightly staggered.[83-84] As this shifting from a perfect AA-stacking to an AB-stacking also directly affects the respective stacking distance, a peak broadening of the X-ray reflection that indicates various stacking distances (as well as defects and small domain sizes) may occur.[85]

Different strategies have been developed to stabilize the COFs by enhancing the comparably weak stacking forces. One approach creates enhanced attraction between individual layers by improving the complementary π–π interactions of adjacent layers or by adjustments of the dipole moment. Jiang and co-workers used mixtures of arene and perfluoroarene dialdehydes[86], while Salonen *et al.* incorporated pyrene-diones with a strong dipole moment[87]. Another strategy addresses the chemical stability of imine COF systems by using a beneficial *β*-ketoenamine-linked route. Intramolecular hydrogen bonding stabilizes the resulting imine-based COFs by an induced planarization and non-reversible tautomerization.[88] Many studies on these ketoenamine COFs show their impressive stability towards organic solvents as well as aqueous solutions.[45, 89-94]

Another approach by Jiang and co-workers achieves a reinforcement of imine bonds by the incorporation of alkoxy-groups.[23] Through a resonance effect, the polarization of the imine bond is weakened, and electrons become delocalized over the more positively polarized phenyl groups. The usage of propeller and screw-like structures has attracted attention over the past years. In totally flat 2D COF systems lateral offsets are likely to occur due to interlayer orbital

repulsion and shear forces.[25, 83, 95] On the other hand, propeller and screw-like structures were expected to result in more stable COFs without lateral offsets.[96] Due to the locking of adjacent layers in structurally predefined nodes through synchronized twisting and stacking, highly crystalline, and long-range ordered structures based on 4,4′,4″,4‴-(ethylene-1,1,2,2-tetrayl)tetraaniline (ETTA), 1,3,5-tris(4-aminophenyl)benzene (TAPB) and tris(4-aminophenyl)amine (TAPA) have been successfully implemented and synthesized.[5, 96] Nevertheless, as the spatially controlled stacking of adjacent COF layers not only results in improved porosity and crystallinity, but also is the key to control the π-overlap and conductivity perpendicular to the layers, one goal of current research aims at the incorporation of predefined propellers or screws, which still allow for close stacking.

### 1.3.3 SUPERCRITICAL CARBON DIOXIDE ACTIVATION

Supercritical carbon dioxide ($scCO_2$) activation/extraction has been in use for a long time. Carbon dioxide becomes supercritical when the pressure $p$ and the temperature $T$ exceed the critical point $P_C$ in the phase diagram (Figure 1.6). At a temperature of 31.1 °C (304.25 K) and a pressure of 73.8 bar, carbon dioxide exhibits unusual properties, such as a density of liquid carbon dioxide, but viscosity of gaseous carbon dioxide. $ScCO_2$ is important as a solvent in extraction. Firstly, because a working temperature between 31.1 and 40 °C is favorable for preventing damage or denaturation of heat-sensitive compounds. Secondly, the solubility of different compounds varies with pressure, allowing for selective extraction, for example in the decaffeination process of coffee[97] or for volatile oils and lipids[98]. Another advantage of $scCO_2$ extraction is the high speed of the activation process. As slow diffusion mainly limits fast extraction, the low viscosity and the lack of surface tension in $scCO_2$ allow for fast and efficient diffusion through the whole treated material to be extracted.

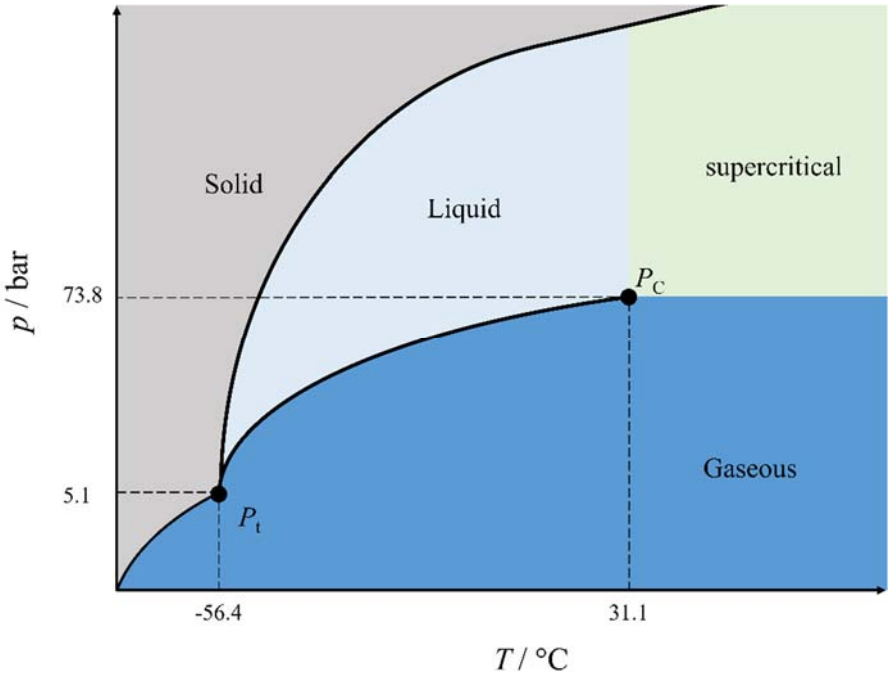


Figure 1.6: Pressure-temperature phase diagram of carbon dioxide.

$ScCO_2$ extraction of porous materials is widely used for their activation (implying opening their porosity by extracting undesired materials). Micro- and mesoporous materials can trap high-boiling solvents or other guest molecules (e.g. reaction compounds) within their porous channels or networks. Time-consuming solvent exchange with low-boiling solvents allows for a reduction of the amount of these guest molecules, but due to solubility issues or diffusion limits, $scCO_2$ is favorable for fast, efficient and complete activation.

Supercritical fluids were found to be beneficial for the synthesis or activation of ZIFs[99], MOFs[100-106] and porous polymers[107-109]. Furthermore, $scCO_2$ was successfully introduced for the generation of porous materials like foams, gels as well as for modification of porous matter by film deposition or metallization *via* supercritical fluids.[108] For COFs, $scCO_2$ also has been found to be efficient in activation and purification. [100, 110-112] Nevertheless, one aim is to make $scCO_2$ activation more generally applicable. As it has already shown high potential in stabilization and activation, its usage in reactivation and the influence on the overall crystalline order still has to be investigated.

# 1.4 OPTOELECTRONIC PROPERTIES OF COFS

Besides optical properties like absorbance and photoluminescence, COFs have been investigated in the context of optoelectronic applications such as organic photovoltaics or photoelectrochemical water-splitting with photoabsorbing COFs. First examples of capacitors and solar cells based on COF materials have paved the way towards many potential electronic and optoelectronic applications.[53, 57, 89, 113] Host-guest chemistry allows for selective adsorption of dyes or pollutants as well as for the incorporation of conductive electron acceptors like $PC_{60}BM$ or $PC_{70}BM$. Especially for optoelectronic applications the realization of covalent organic frameworks as oriented, thin and open porous films is essential.

The next parts (1.4.1 to 1.4.3) are based on the following publication:

**Photoactive and Conducting Covalent Organic Frameworks**

D. D. Medina, T. Sick and T. Bein

*Adv. Energy Mater.* **2017**, *7*, 1700387.

## 1.4.1 ELECTROACTIVE AND PHOTOACTIVE COF BULK MATERIALS

The self-organization of molecular COF layers into defined stacked columns has attracted attention as a platform for assembling semiconducting polymers. With the required structural modification, addressing the symmetry constraints for the formation of a COF, a variety of chromophores and subunits for semiconducting materials were included into the COF backbones. To date, these types of COFs were synthesized as bulk materials mainly by using the well-established boronic ester and imine bond linkages (Figure 1.3). The boronic ester COFs exhibit limited electronic coupling within the layer and therefore allow for the formation of a continuous pattern of chemically segregated 1D stacks. Thereby, in principle, a precise spatial positioning of independent electron donor and electron acceptor stacks is possible. By contrast, the imine linkage motif offers a path toward extended conjugation within the COF layers. Considering charge transport in these two types of structures, in boronic ester COFs charge carriers are expected to travel mainly in transverse direction (along the stacking direction) whereas imine-based COFs offer, in principle, additional transport paths in the lateral direction. Therefore, boronic ester COFs are more likely to be inspired by the design of small molecule based electronics while imine-based COFs are conceptually related to conjugated conducting polymers.

A reticular series of boronic ester COFs comprising diimide linear chromophores featuring interdigitated 1D electron donor–acceptor architectures were introduced by Jiang and co-workers.[3] The $D_{TP}$-$A_{NDI}$ COF formed by the condensation of triphenylene and naphthalene diimide subunits exhibits very large hexagonal open pores of 5.3 nm in diameter (Figure 1.7a). For this COF, time-resolved electron spin resonance spectroscopy (TR-ESR) measurements revealed a charge transfer state lifetime of 2.5 μs, indicating the presence of long-lived radical species originating from an efficient charge transfer from the triphenylene donor phase to the naphthalene diimide acceptor phase. A $D_{MPc}$-$A_{DI}$ COF series based on metallophthalocyanine electron donor and diimide chromophore electron acceptor subunits featured a so-called super heterojunction where two types of ordered donor–acceptor heterojunctions are present within the COF structure.[114] The well-defined organization of the electron donor and acceptor stacks provides a distinct chemical and physical environment that can facilitate electron transfer, charge separation, and allow for extended charge transfer lifetimes. For example, a long charge separated state lifetime of 33 μs for $D_{CuPc}$-$A_{DI}$ COF in this series was detected by the TR-ESR measurements. In combination with the possible discrete 1D charge carrier paths in opposite directions (for electrons and holes), this COF platform shows great promise for light-induced charge-carrier separation and collection, respectively.

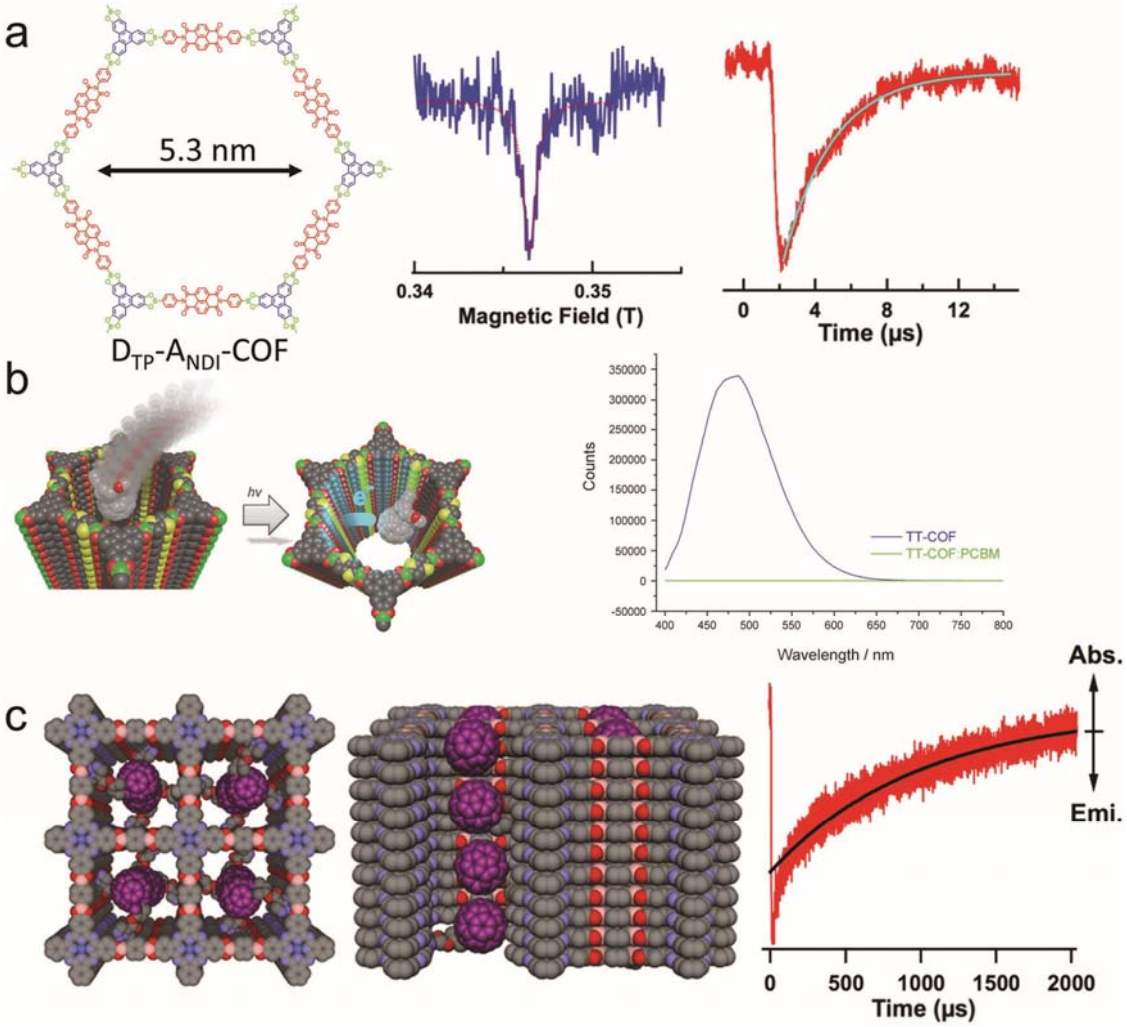


Figure 1.7: a) Intrinsic donor–acceptor heterojunction in DTP-ANDI-COF resulting in the presence of long-lived light-induced radical species. Reproduced with permission.[3] Copyright 2013, Royal Society of Chemistry. b) TT-COF with PCBM acceptor molecules penetrating into the porous COF network. This construction led to fluorescence quenching in the device architecture. Reproduced with permission.[113] Copyright 2013, John Wiley and Sons. c) Construction of ZnPc-COF with covalent attachment of fullerene acceptor molecules resulting in long-lived charge-separation. Reproduced with permission.[115] Copyright 2014, American Chemical Society.

The second approach for the construction of defined electron donor and acceptor phases within a COF is by forming interpenetrated systems. In contrast to the previous approach, here, the COF pores are occupied with guest molecules allowing for the formation of a second continuous phase in the COF. In principle, photoinduced charge transfer from a semiconducting electron donating COF to a complementary guest phase accommodated in the COF pores is expected. For example, a highly porous thienothiophene (TT)-containing mesoporous boronic ester COF was designed and synthesized for this purpose. Photoinduced charge transfer from the TT-COF toward [6,6]-phenyl-$C_{61}$-butyric acid methyl ester (PCBM) acting as electron acceptor guest

molecules was demonstrated by an efficient COF fluorescence emission quenching (Figure 1.7b).[113] Moreover, the TT-COF was integrated into a photo voltaic device, illustrating that extraction of charge carriers in interpenetrated COF systems is possible. Following a different approach, the covalent attachment of fullerene acceptor molecules to the COF pore walls by postsynthetic modification was pursued in a boronic ester zinc phthalocyanine COF, ZnPc-COF (Figure 1.7c). Separated by saturated covalent bonds, the PCBM acceptor phase and the COF backbone do not exhibit electronic coupling but allow for light-induced charge transfer. In this case, a long charge-separation lifetime of 2.66 ms in $[C_{60}]_{30\%}$-ZnPc-COF was detected by TR-ESR measurements.[115] Charge carrier transport studies were performed with bulk COFs to reveal the COF intrinsic semiconducting properties and thereby identify COF candidates suitable for optoelectronic applications. For example, the charge carrier mobility for boronic ester and imine-linked porphyrin COFs, COF-66 and COF-366, in the form of a thick blended COF/PMMA (poly(methyl methacrylate)) film sandwiched between two electrodes was determined by laser flash-photolysis time-resolved microwave conductivity measurements (FP-TRMC) in combination with time-of-flight (TOF) transients at different bias voltages. The measurements revealed high charge carrier mobility of 3.0 $cm^2\ V^{-1}\ s^{-1}$ for COF-66 and 8.1 $cm^2\ V^{-1}\ s^{-1}$ for COF366.[116] Later, a rotational symmetry hexabenzocoronene (HBC) subunit was integrated into an imine-based COF.[2] Here, the extended conjugation of the coronene core promotes a tight COF layer stacking and in combination with a small triangular pore geometry yielded a π-electron columnar density of 25 $nm^{-2}$. The charge carrier mobility for an HBC-COF dropcast film was determined to be as high as 0.7 $cm^2\ V^{-1}\ s^{-1}$ by FP-TRMC measurements and TOF transients at different bias voltages. In a related study, the charge carrier mobilities of cast films of an imine-linked TTF-Ph-COF containing tetrathiafulvalene and arene subunits and TTF-Py-COF consisting of tetrathiafulvalene and tetraaminophenyl pyrene subunits were studied by FP-TRMC.[117] The charge carrier mobilities for TTF-Ph-COF and TTF-Py-COF were evaluated to be 0.2 and 0.08 $cm^2\ V^{-1}\ s^{-1}$, respectively. The higher charge carrier mobility obtained for the TTF-Ph-COF was attributed to the structural difference between the two COFs. First, a slightly shorter stacking distance was obtained for TTF-Ph-COF in the structure simulations. Second, TTF-Ph-COF exhibited a more planar layer conformation and thereby was proposed to feature improved π-electron overlap between successive COF layers. Additionally, transport properties such as electrical conductivity were investigated for these COFs in bulk form. Prior to the electrical conductivity measurement, the COF powders were chemically oxidized by exposure to iodine vapor. For electrical conductivity measurements the iodine-oxidized COF powders were pressed on a substrate with a gold electrode pattern. TTF-Ph-COF

and TTF-Py-COF exhibited electrical conductivity values of $10^{-5}$ and $10^{-6}$ S $cm^{-1}$, respectively.

Benzodithiophene (BDT), a prominent building unit in conducting polymers was integrated into boronic ester COFs by Medina, Bein and co-workers.[71, 118] Later, a reticular series consisting of the BDT-COF and its heavier chalcogen analogs was reported by Dinca and co-workers.[119] However, COFs of moderate crystallinity were obtained with the incorporation of heavier elements in the backbone. A direct comparison of the charge transport properties within this series was therefore difficult, as disordered COF domains and a large number of grain boundaries can significantly reduce charge migration. Nevertheless, two-point probe electrical conductivity data of this series, obtained with compressed COF pellets, revealed a several orders of magnitude higher conductivity for the heavier chalcogen COF analogues.

## 1.4.2 COF-BASED OPTOELECTRONIC DEVICES

### 1.4.2.1 Thin COF Films

The deposition of COFs onto a surface and the formation of thin films open up a large scope of possible functionalities. Exploring the physical properties of COFs in the form of a device can give insights into the performance of these materials on a macroscopic scale and eventually will assist in formulating general design principles leading to COFs for specific applications. In the context of charge carrier transport and charge collection in 2D COFs, the orientation of the COF layers is of great importance for efficient charge migration toward the respective electrodes.

Under solvothermal conditions, COFs typically form as intergrown nanocrystalline bulk materials. Therefore, their processability is challenging, which has direct implications regarding the synthesis of high quality COF thin films. To date, the deposition of thin COF films for device fabrication has been mostly carried out through an in situ process where the desired surface is immersed into the reaction mixture. Subsequently, the COF film is deposited on the substrate throughout the condensation reaction, while COF powder is formed simultaneously. With this approach, oriented thin films are accessible where the COF layers are deposited parallel to the substrate, and therefore the columnar stacks are positioned in a perpendicular manner. This offers favorable direct pathways for charge carrier percolation to the electrodes. Dichtel and co-workers reported the growth of four boronic ester-based oriented thin COF films, i.e., COF-5 and TP-COF with hexagonal symmetry, and NiPc- and ZnPc-PBBA COFs with tetragonal symmetry.[120-121] Uniform films of about 100 nm thickness on surface-supported

single layer graphene were synthesized, and when grown on quartz slides their absorption spectrum could be recorded.[56]

Expanding the scope of the in situ method, we demonstrated the direct deposition of oriented BDT-COF onto a variety of inorganic, crystalline, and semiconducting electrodes.[118] The 150 nm BDT-COF films produced by this approach were found to be porous by krypton sorption analysis, and thereby an acceptor phase could be infiltrated into the film pores forming an interpenetrated system BDT-COF:[60]PCBM. Upon illumination, the photoinduced charge carrier dynamics were recorded by ultra-fast pump–probe transient absorption measurements. The BDT-COF:[60]PCBM exhibited biexponential signal decay time characteristics with $\tau_1$ = 6 ps and $\tau_2$ = 178 ps, which is significantly slower in comparison to the signal decay time characteristics of the pristine BDT-COF film, indicating charge transfer and the presence of stabilized hole-polarons.

#### 1.4.2.2 Charge Migration and Collection in COF Thin Film Based Devices

Recently, we reported the first COF-based solar device for the photoconductive TT-COF, based on an ordered bulk heterojunction of the interpenetrated COF network with PCBM as the acceptor phase (Figure 1.7b). In an ITO/TT-COF:PCBM/Al device architecture, a moderate power conversion efficiency (PCE) of 0.053% (under 1.5 AM) was obtained for a 200 nm thick TTCOF:PCBM film, illustrating that charge collection in interpenetrated COF systems is feasible.[113]

Later, Jiang and co-workers introduced the phenazine-based CS-COF by the co-condensation of triphenylene hexamine and tert-butylpyrene tetraone, resulting in a planar fully conjugated and highly stable microporous (1.6 nm) COF (Figure 1.8a–c). A CS-COF⊃PCBM interpenetrated system was prepared *via* sublimation under vacuum. To build a corresponding device architecture, about 100 nm spin-coated film of the interpenetrated CS-COF⊃PCBM was integrated into a solar device. The solar device exhibited a PCE of 0.9%, a high $V_{OC}$ of 0.98 V attributed to a deep highest occupied molecular orbital (HOMO) level, a $J_{SC}$ of 1.7 mA cm$^{-2}$, and a fill factor of 54% (under 1.5 AM), respectively.[31]

Charge collection from an integrated A–D COF in the form of a solar device was demonstrated by Bein and co-workers.[122]

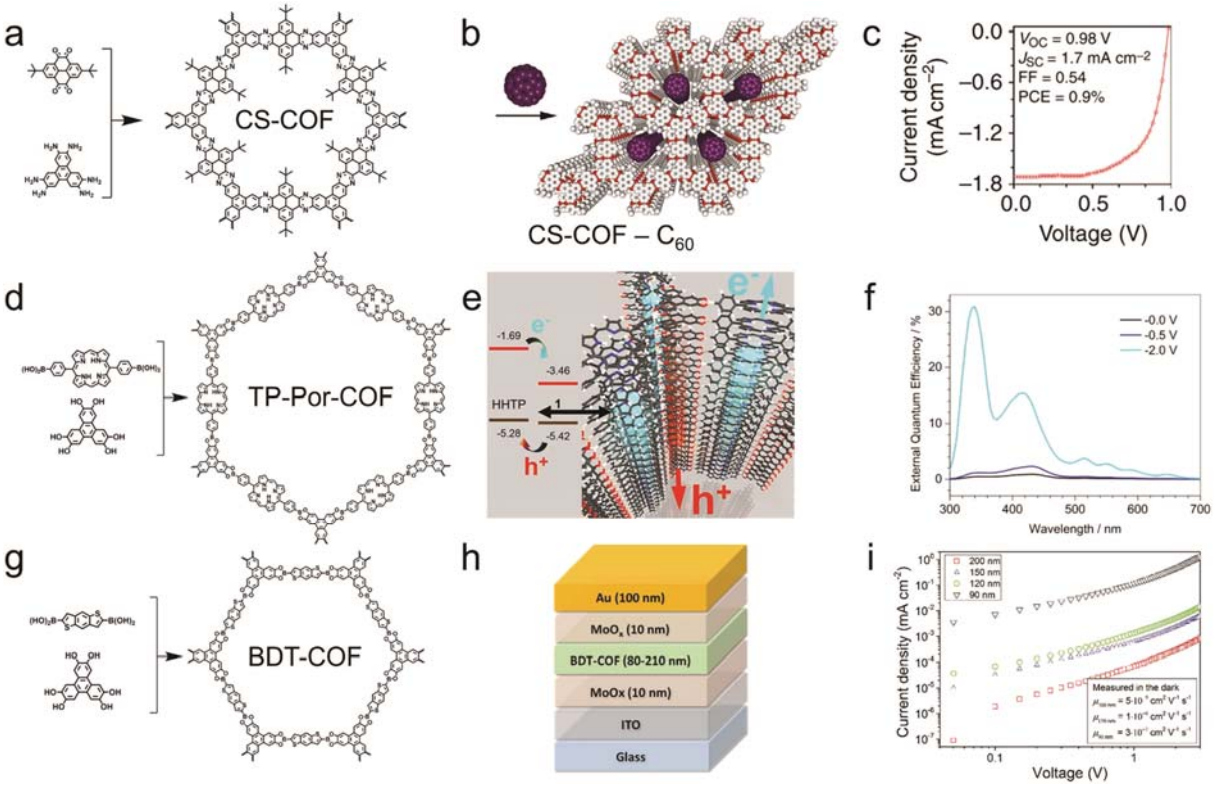


Figure 1.8: a–c) Topology, incorporation of an acceptor phase, and current–voltage curve of CS-COF. Reproduced with permission.[31] Copyright 2013, Macmillan Publishers Ltd. d–f) TP-Por-COF with energy alignment and EQE spectra. Reproduced with permission.[122] Copyright 2014, American Chemical Society. g–i) BDT-COF with topology, device architecture, and current density measurements. Reproduced with permission.[55] Copyright 2017, American Chemical Society.

Separating the triphenylene electron donor and porphyrin electron acceptor stacks by boronic ester groups led to the formation of TP-Por COF with an inherent type II heterojunction (Figure 1.8d–f). For the device fabrication, the TP-Por COF was grown as about 50 nm thick oriented thin film and sandwiched between ITO/MoOx and ZnO/Al electrodes. The external quantum efficiency (EQE) measured at short circuit conditions followed closely the absorbance spectrum of the TP-Por COF, indicating that the observed photoresponse originated from both components present in the TP-Por COF film. However, the EQE measurement indicated collection efficiencies below 1%, which points to effective loss mechanisms. By applying a strong reverse bias of -2 V, a dramatic rise in the photocurrent was observed and apparent EQE values of up to 30% were obtained. Electrical conductivity measurements were carried out for oriented thin TTF-COF films grown on interdigitated gold electrode surfaces.[123] The oriented thin film architecture allowed for dopant diffusion through the COF pores. Conductivity as high

as $0.28 \times 10^{-3}$ S $m^{-1}$ was observed for the iodine-doped COF thin films, which is three orders of magnitude higher than that of the pristine film.

Field-effect transistors (FETs) with imine-based PolyTB-COF (consisting of a BDT core bearing extended alkoxy chains and triphenylamine) acting as active semiconductor layer were introduced by Bao and co-workers.[124] The extended alkoxy chains protruding into the COF pores promoted a large-area, few-layer PolyTB-COF formation at the solution/air interface. These COF layers were lifted off and transferred onto the desired substrate. The FETs were built by transferring the thin COF films to a Si wafer with a 300 nm oxide layer. Afterward, source and drain gold electrodes were deposited to form the top-contact transistor. A relatively low charge carrier mobility of $3.0 \times 10^{-6}$ $cm^2$ $V^{-1}$ $s^{-1}$ was measured for the ultrathin PolyTB-COF layers, with an average on/off ratio of 850. COF-366 was grown as thin film in situ on boron nitride surfaces which were later used to construct an FET device.[125] Wang and co-workers reported an OFET device based on COF-366 ultrathin films featuring a p-type current modulation with an on/off ratio of $10^5$ and mobility value of 0.015 $cm^2$ $V^{-1}$ $s^{-1}$.

Very recently, we reported on a directional charge carrier transport study of oriented BDT-COF thin films where the in-plane electrical conductivity and charge carrier mobility in the stack were measured.[55] To study the columnar charge transport properties of the BDT-COF, hole-only devices with the following architecture were prepared: Glass/ITO/$MoO_x$/BDT-COF (80-210 nm)/$MoO_x$/Au (Figure 1.8g–i). Measurements preformed in the dark revealed a thickness dependency of the charge transport, where thinner films exhibited hole-mobilities of $3 \times 10^{-7}$ $cm^2$ $V^{-1}$ $s^{-1}$, two orders of magnitude higher than thicker films. This was attributed to intrinsic electronic defects within the stacks of the BDT-COF layers. A threefold increase in the average hole-mobility was observed for 200 nm films under illumination, rendering the BDT-COF as photoactive material. In-plane electrical conductivity was found to be in the range of $(1–5) \times 10^{-7}$ S $cm^{-1}$, and no substantial light-dependence was observed. In comparison, the electrical conductivity reported for the oriented BDT-COF films is up to three orders of magnitudes higher than the two-point probe electrical conductivity values previously reported for the bulk powders.

### 1.4.3 CONCLUSIONS AND OUTLOOK

Alternating 2D copolymers consisting of covalently linked subunits of defined geometry that self-assemble through dispersive forces allow for the formation of highly ordered, porous structures known as 2D COFs. The interplay between the subunit geometry and linkage motifs, and the interactions between adjacent layers are important for the synthesis of COFs featuring long-range order. Thus, new design concepts and advanced synthesis protocols are expected to provide an increasing number of highly crystalline COF structures.

Once a desirable COF structure has been successfully synthesized, its deposition on relevant substrates is often critical when contemplating potential applications. Specifically, formation of COF thin films with a preferential orientation can be of great importance for optoelectronic applications. Although initial progress has been made toward the deposition of selected oriented COF films, control over the COF structural properties in the films and generalization to a wide range of COF structures are still important challenges. For example, crystallite domain sizes, the nature of the grain boundaries and the precise type of layer assembly within the COF films are key factors influencing charge migration. Exploring the deposition mechanisms is therefore believed to assist in the development of high quality COF films suitable for device fabrication. Moreover, a control over deposition rate, film thickness, and the nature of the COF-electrode interfaces plays an important role in constructing devices. COF structures integrated into appropriate device architectures will also provide an intriguing platform for studying key factors such as charge carrier dynamics, and how the latter are controlled by the building units, the unique topologies, and the geometries of the organic frameworks. The resulting insights will provide a valuable basis for identifying promising candidates for optoelectronic applications.

# 1.5 PHOTOELECTROCHEMICAL (PEC) WATER-SPLITTING

In PEC water-splitting solar energy is used for the production of hydrogen from water, the supply of which is effectively endless. Hydrogen as a chemical energy carrier can be stored, transported and later be converted to heat or electrical energy. Besides hydrogen, oxygen is evolved in a full water-splitting process. The energy required for the endergonic reaction ($\Delta G = 237.2$ kJ $mol^{-1}$) can ideally be supplied by renewable energy sources, like solar energy. The oxidation to oxygen and the reduction to hydrogen can be considered as two half reactions, namely the hydrogen evolution reaction (HER) and the oxygen evolution reaction (OER) with the corresponding standard potentials $E^0$ at pH 0 referenced to the normal hydrogen electrode (NHE).[126]

HER: $2H^+ + 2e^- \rightarrow H_2$ (g) $E^0 = 0$ V

OER: $2H_2O$ (l) $\rightarrow O_2$ (g) $+ 4H^+ + 4e^-$ $E^0 = 1.23$ V

For full water-splitting, a standard potential difference of $\Delta E^0 = 1.23$ V is required. A photoactive material, for example a semiconductor, can be utilized to absorb photons under illumination. If the energy of the interacting photons is larger than the band gap of the photoabsorber, electrons ($e^-$) and holes ($h^+$) are generated as charge carriers. The electrons are excited from the valence to the conduction band, generating holes in the valence band. One can differentiate between photocatalytic and photoelectrochemical water-splitting. While in photocatalysis, both half reactions occur at the same surface, e.g. that of suspended particles, in photoelectrochemical water-splitting the evolution of oxygen and hydrogen takes places at two separate electrodes. The spatial separation of the gas evolution processes allows for access to pure gas as well as preventing the formation of highly explosive gas mixtures. To create viable HER and OER photoelectrodes, suitable photoactive materials have to be synthesized on conducting substrates. Often, organic, inorganic or hybrid semiconductors are grown as films on conducting, transparent oxides like fluorine-doped tin oxide (FTO) or indium tin oxide (ITO). In general, two types of semiconducting materials can be distinguished. In an n-type semiconductor, a so-called photoanode, the holes take part in the OER at the semiconductor's surface. The electrons on the other hand are transferred through an external circuit to the counter electrode where they participate in the HER (Figure 1.9a). In contrast, in a p-type semiconductor (photocathode) the generated electrons are transported to the semiconductor-electrolyte junction and are used for the HER, while electrons from the oxidation towards

oxygen (OER) at the counter electrode are transferred *via* the external circuit to the photocathode, where they recombine with the holes at the substrate of the photocathode (Figure 1.9b). The band alignment of the semiconductor is crucial for the functionality as a photoactive semiconductor in water-splitting. In the case of a photoanode, the position of the valence band has to be more positive compared to the OER potential. For a working photocathode, the position of the conduction band has to be more negative than the HER potential. Combining a photoanode and a photocathode in a tandem configuration allows for simultaneous HER and OER using photoactive p- and n-type semiconductors, respectively (Figure 1.9c).[127]

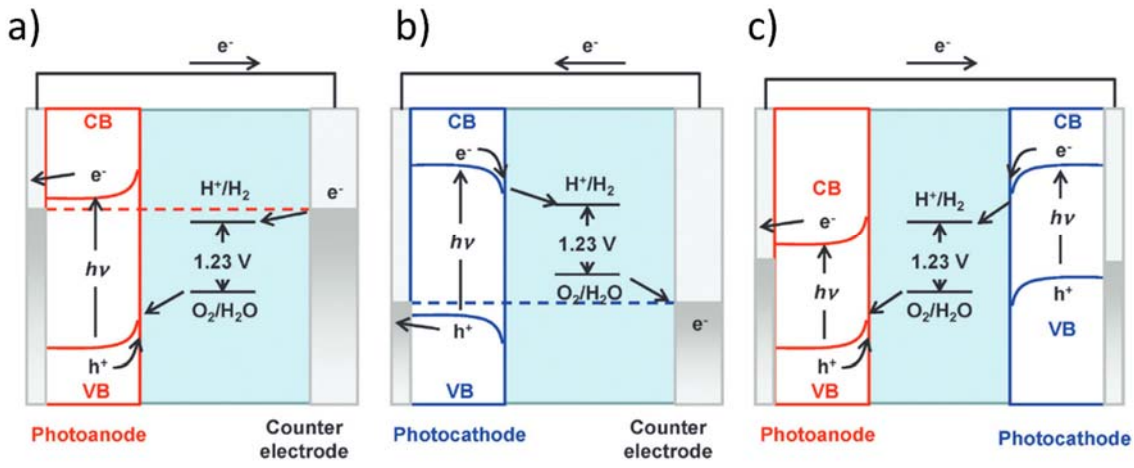


Figure 1.9: Schematic illustration of a photoanode (a), a photocathode (b), and a tandem configuration of a photoanode and a photocathode (c).[127]

In order to determine the efficiency of a photoabsorber, the solar-to-hydrogen conversion efficiency (STH) can be measured. Assuming, that the measured current is entirely used for the water-splitting, the output energy of hydrogen has to be divided by the energy of the incident solar irradiation as shown in Equation 1.1.

$$STH\ (\%) = \frac{output\ energy\ of\ H_2}{energy\ of\ the\ incident\ solar\ irridiation} \cdot 100\ \% \qquad (1.1)$$

To determine the efficiency as a function of the wavelength (λ), the incident photon-to-current efficiency (IPCE) is measured for the used spectrum, shown in Equation 1.2.

$$\text{IPCE}\ (\%) = \frac{number\ of\ generated\ electrons}{number\ of\ incident\ photons} \cdot 100\ \% \qquad (1.2)$$

### 1.5.1 PHOTOCATHODES FOR LIGHT-DRIVEN WATER-SPLITTING

In general, suitable materials for active photocathodes have to fulfil several requirements. Besides a high light harvesting efficiency and chemical stability during PEC reaction, the photoabsorber should provide suitable band positions, a small band gap, efficient charge transport and high mobilities. Furthermore, the used semiconductor should consist of abundant, non-toxic elements, ions or molecules and should be easily scalable and cheap to produce.[128]

The light harvesting efficiency of the used semiconductor preferably should be high over the whole solar irradiation spectrum. As sunlight (AM 1.5G, Figure 1.10) can be divided into three sections, ranging from the low energetic infrared (IR) range ($\lambda > 800$ nm) over the visible (Vis) range ($800\ \text{nm} > \lambda > 400\ \text{nm}$) to the highly energetic ultraviolet (UV) range ($\lambda < 400$ nm), absorbing the photons in these regions is required. The different regions contribute differently to the overall spectrum, ranging from about 49% (IR) and 46% (Vis) to only 5% (UV). As 1.23 eV is the required thermodynamic energy for the water-splitting reaction and considering additional losses that arise mainly from overpotentials due to slow reaction kinetics, the minimum bandgap for single-photon water-splitting is approximately 1.9 eV. This corresponds to an excitation wavelength of 650 nm or lower. In combination with the low share of UV light, the required band gap of the semiconductor lies between 1.9 and 3.1 eV and thus efficient absorption in the visible area is highly important.

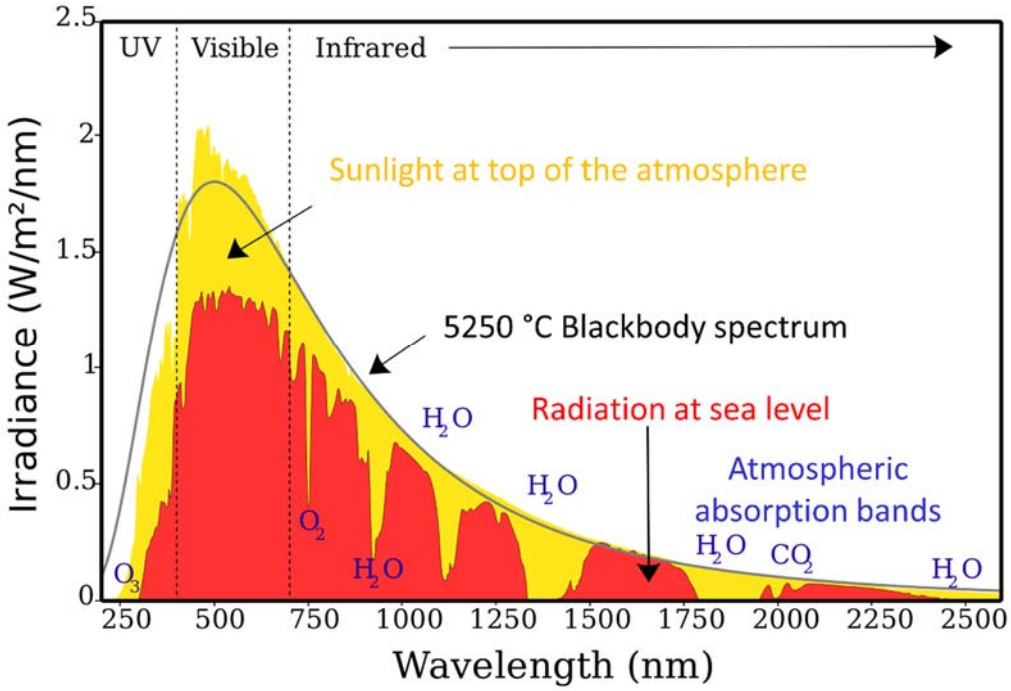


Figure 1.10: AM1.5 solar irradiance depending on the wavelength. The graph shows the radiation spectrum at the top of the atmosphere (yellow) and the spectrum at sea level (red), resulting from atmospheric absorption (blue). The black body spectrum at 5250 °C is expected to be comparable to the radiation emitted from the sun.[129] Online access on 19.03.2018

The band gap of each pure material, for example in metal oxides, is characteristic. Nevertheless, through doping or the creation of structural defects, the band gap of metal oxides and their electron-hole separation efficiency can be engineered.[130-132] This makes metal oxides suitable candidates for PEC. Nevertheless, metal oxides often lack chemical stability under working conditions due to photocorrosion or instability at the electrolyte's pH.[133] Furthermore, toxicity of some of the incorporated metals is a drawback. To improve charge collection efficiency and to enlarge the active surface, nanostructuring into periodically ordered and nanoporous materials is at the center of research. One approach is mimicking nature's opals by using the self-assembly of spherical hard templates and infiltrating the voids with a precursor of the desired material. After transformation to the metal oxide by calcination and the final removal of the hard template, macroporous inverse opals are accessible.[134-135] Another approach aims at the synthesis of mesoporous structures. For this, often an evaporation-induced self-assembly process (EISA) is used to fabricate films on top of solid substrates.[136] Upon evaporation of the solvent, ionic surfactants or amphiphilic block-copolymers as structure-directing agents (SDAs) start to self-assemble depending on their critical micelle concentration.[137] The precursor reacts to the final solid product within the voids of the self-assembled micelles. In

order to remove the SDA, the resulting composite material can be calcined or extracted to result in a nanostructured material.[138]

As organic semiconductors like polymers have already shown attractive properties regarding optical absorption, they have been used as photoanodes[139] or photocathodes[140], respectively, as well as in organic photovoltaics (OPV)[141-142]. Furthermore, hybrids of organic and inorganic materials were established as composite materials.[143-145] The advantages of organic semiconductors are low cost, scalable fabrication and especially the possibility to easily fine-tune the materials' properties.

Nevertheless, organic semiconductors still have to be improved significantly with regard to efficiency and stability to compete with inorganic or hybrid materials. One possibility is using porous materials. The construction of highly microporous hybrids of organic linkers and metal clusters results in highly crystalline metal organic frameworks (MOFs). MOFs have shown potential in many different fields of applications[146-148], but also photoactive MOFs[149-150] are under investigation. By the availability of reticular chemistry, the pore sizes and geometries can be adjusted as designed. But the toxicity of some of the incorporated metals is still a concern. Another possibility is to use non-porous or open porous polymers to avoid the incorporation of metals.[151-154] Open porosity increases the accessible surface area and thereby the potential interaction surfaces. For example, porous carbon nitrides represent an interesting class of active materials.[155-156] It would furthermore be desirable to study in detail the correlation between efficiency and well-defined pore size distributions as well as inter- and intramolecular distances within the polymer to reveal the role of the active polymer parts. In this context, COFs represent a unique and suitable class of materials, as they provide spatial control over the incorporated atoms and molecules in combination with high crystallinity and open porosity.

### 1.5.2 COFS FOR WATER-SPLITTING

Covalent organic frameworks as porous organic compounds with photoactive building units provide potential applications in photoelectrochemical water-splitting. As already shown for porous and non-porous polymers, excitation of photoactive COFs results in the generation of charge carriers, which can be used for the purpose of the hydrogen evolution reaction (HER) and/or the oxygen evolution reaction (OER). Depending on their properties and fabrication, the COF materials can either be used as photocatalysts or as photocathodes.

#### 1.5.2.1 COF photocatalysts

COF photocatalysts are mainly realized as crystalline and open porous powders in an aqueous solution. Under illumination and upon photoexcitation, charge carriers are generated and can be used, depending on the HOMO/LUMO band alignment, for the purpose of direct charge transfer to water in order to reduce protons to hydrogen. In most cases, a co-catalyst, for example platinum or palladium metal, is added to act as electron acceptor sites and to take over the charge transfer for water reduction.[95, 157-160] The Lotsch group was recently able to use the molecular co-catalyst cobaloxime to avoid using noble metals.[161] The ultimate goal is to achieve full water-splitting, by oxidizing hydroxide ions to oxygen and simultaneously use the photogenerated electrons for the reduction towards hydrogen. There are still several hurdles to be overcome on this pathway. On the one hand, the material must be suitable for oxidation and reduction processes and must be stable in the reaction medium. To address these challenges, often a sacrificial electron donor agent (scavenger), like triethanolamine (TEOA) or methanol, is added to be consumed in the oxidation process instead of the OER.[157, 162] This allows for detailed investigation of the reduction process towards hydrogen and prevents the evolution of an explosive gas mixture of hydrogen and oxygen. Nevertheless, as the sacrificial agent is consumed over time, it has to be recurrently added to the mixture. Ultimately, the goal will be to either avoid the sacrificial agent or to use the oxidation reaction for the generation of usable products.

#### 1.5.2.2 COF photocathodes

As mentioned earlier, using COFs as photocathodes would allow for the separation of the gas evolution centers, enabling the accumulation of pure gases. Therefore, the synthesis of COF photocathodes as (thin) films on transparent conductive oxides like FTO or ITO is desirable to access the possibility of charge transfer towards the counter electrode. To benefit from the crystalline and open porous characteristics of COFs, an oriented growth of the films is preferential. Varying the thickness of the COF films by adjusting the synthesis conditions results in tunable optical densities. So far, only one study has been reported by the group of Bein and co-workers[163], thus opening the pathway to fine-tune the COFs' properties by defined tailoring of the molecular design.

# 1.6 REFERENCES

(1) Xu, S.-Q.; Zhan, T.-G.; Wen, Q.; Pang, Z.-F.; Zhao, X., *ACS Macro Letters* **2015**, *5*, 99-102.

(2) Dalapati, S.; Addicoat, M.; Jin, S.; Sakurai, T.; Gao, J.; Xu, H.; Irle, S.; Seki, S.; Jiang, D., *Nat. Commun.* **2015**, *6*, 7786.

(3) Jin, S.; Furukawa, K.; Addicoat, M.; Chen, L.; Takahashi, S.; Irle, S.; Nakamura, T.; Jiang, D., *Chem. Sci.* **2013**, *4*, 4505.

(4) Tian, Y.; Xu, S. Q.; Qian, C.; Pang, Z. F.; Jiang, G. F.; Zhao, X., *Chem Commun (Camb)* **2016**, *52*, 11704-11707.

(5) Zhou, T. Y.; Xu, S. Q.; Wen, Q.; Pang, Z. F.; Zhao, X., *J. Am. Chem. Soc.* **2014**, *136*, 15885-15888.

(6) Qian, C.; Qi, Q. Y.; Jiang, G. F.; Cui, F. Z.; Tian, Y.; Zhao, X., *J. Am. Chem. Soc.* **2017**, *139*, 6736-6743.

(7) Weitkamp, J. Puppe, L., *Catalysis and Zeolites*. Springer-Verlag Berlin Heidelberg: Berlin Heidelberg, 1999; p 564.

(8) Kitagawa, S.; Kitaura, R.; Noro, S., *Angew. Chem. Int. Ed. Engl.* **2004**, *43*, 2334-2375.

(9) Férey, G., *Chem. Mater.* **2001**, *13*, 3084-3098.

(10) Rowsell, J. L. C.; Yaghi, O. M., *Microporous Mesoporous Mater.* **2004**, *73*, 3-14.

(11) Phan, A.; Doonan, C. J.; Uribe-Romo, F. J.; Knobler, C. B.; O'Keeffe, M.; Yaghi, O. M., *Acc. Chem. Res.* **2010**, *43*, 58-67.

(12) Xie, Y.; Kocaefe, D.; Chen, C.; Kocaefe, Y., *Journal of Nanomaterials* **2016**, *2016*, 1-10.

(13) Medina, D. D.; Sick, T.; Bein, T., *Advanced Energy Materials* **2017**, *7*, 1700387.

(14) Qian, C.; Liu, E.-C.; Qi, Q.-Y.; Xu, K.; Jiang, G.-F.; Zhao, X., *Polymer Chemistry* **2018**, *9*, 279-283.

(15) Liang, R. R.; Xu, S. Q.; Pang, Z. F.; Qi, Q. Y.; Zhao, X., *Chem Commun (Camb)* **2018**, *54*, 880-883.

(16) Zhu, M. W.; Xu, S. Q.; Wang, X. Z.; Chen, Y.; Dai, L.; Zhao, X., *Chem Commun (Camb)* **2018**, *54*, 2308-2311.

(17) Huang, N.; Zhai, L.; Coupry, D. E.; Addicoat, M. A.; Okushita, K.; Nishimura, K.; Heine, T.; Jiang, D., *Nat. Commun.* **2016**, *7*, 12325.

(18) Cote, A. P.; Benin, A. I.; Ockwig, N. W.; O'Keeffe, M.; Matzger, A. J.; Yaghi, O. M., *Science* **2005**, *310*, 1166-1170.

(19) Hunt, J. R.; Doonan, C. J.; LeVangie, J. D.; Cote, A. P.; Yaghi, O. M., *J. Am. Chem. Soc.* **2008**, *130*, 11872-11873.

(20) Jackson, K. T.; Reich, T. E.; El-Kaderi, H. M., *Chem Commun (Camb)* **2012**, *48*, 8823-8825.

(21) Uribe-Romo, F. J.; Hunt, J. R.; Furukawa, H.; Klock, C.; O'Keeffe, M.; Yaghi, O. M., *J. Am. Chem. Soc.* **2009**, *131*, 4570-4571.

(22) Rabbani, M. G.; Sekizkardes, A. K.; Kahveci, Z.; Reich, T. E.; Ding, R.; El-Kaderi, H. M., *Chemistry* **2013**, *19*, 3324-3328.

(23) Xu, H.; Gao, J.; Jiang, D., *Nat. Chem.* **2015**, *7*, 905-912.

(24) Smith, B. J.; Overholts, A. C.; Hwang, N.; Dichtel, W. R., *Chem Commun (Camb)* **2016**, *52*, 3690-3693.

(25) Auras, F.; Ascherl, L.; Hakimioun, A. H.; Margraf, J. T.; Hanusch, F. C.; Reuter, S.; Bessinger, D.; Doblinger, M.; Hettstedt, C.; Karaghiosoff, K.; Herbert, S.; Knochel, P.; Clark, T.; Bein, T., *J. Am. Chem. Soc.* **2016**, *138*, 16703-16710.

(26) Keller, N.; Bessinger, D.; Reuter, S.; Calik, M.; Ascherl, L.; Hanusch, F. C.; Auras, F.; Bein, T., *J. Am. Chem. Soc.* **2017**, *139*, 8194-8199.

(27) Matsumoto, M.; Dasari, R. R.; Ji, W.; Feriante, C. H.; Parker, T. C.; Marder, S. R.; Dichtel, W. R., *J. Am. Chem. Soc.* **2017**, *139*,4999-5002.

(28) Bessinger, D.; Ascherl, L.; Auras, F.; Bein, T., *J. Am. Chem. Soc.* **2017**, *139*, 12035-12042.

(29) Uribe-Romo, F. J.; Doonan, C. J.; Furukawa, H.; Oisaki, K.; Yaghi, O. M., *J. Am. Chem. Soc.* **2011**, *133*, 11478-11481.

(30) Dalapati, S.; Jin, S.; Gao, J.; Xu, Y.; Nagai, A.; Jiang, D., *J. Am. Chem. Soc.* **2013**, *135*, 17310-17313.

(31) Guo, J.; Xu, Y.; Jin, S.; Chen, L.; Kaji, T.; Honsho, Y.; Addicoat, M. A.; Kim, J.; Saeki, A.; Ihee, H.; Seki, S.; Irle, S.; Hiramoto, M.; Gao, J.; Jiang, D., *Nat. Commun.* **2013**, *4*, 2736.

(32) Nagai, A.; Chen, X.; Feng, X.; Ding, X.; Guo, Z.; Jiang, D., *Angew. Chem. Int. Ed.* **2013**, *52*, 3770-3774.

(33) Fang, Q.; Zhuang, Z.; Gu, S.; Kaspar, R. B.; Zheng, J.; Wang, J.; Qiu, S.; Yan, Y., *Nat. Commun.* **2014**, *5*, 4503.

(34) Rao, M. R.; Fang, Y.; De Feyter, S.; Perepichka, D. F., *J. Am. Chem. Soc.* **2017**, *139*, 2421-2427.

(35) Zhuang, X.; Zhao, W.; Zhang, F.; Cao, Y.; Liu, F.; Bi, S.; Feng, X., *Polymer Chemistry* **2016**, *7*, 4176-4181.

(36) Jin, E.; Asada, M.; Xu, Q.; Dalapati, S.; Addicoat, M. A.; Brady, M. A.; Xu, H.; Nakamura, T.; Heine, T.; Chen, Q.; Jiang, D., *Science* **2017**, *357*, 673-676.

(37) Kuhn, P.; Antonietti, M.; Thomas, A., *Angew. Chem. Int. Ed. Engl.* **2008**, *47*, 3450-3453.

(38) Beaudoin, D.; Maris, T.; Wuest, J. D., *Nat. Chem.* **2013**, *5*, 830-834.

(39) Liu, W.; Luo, X.; Bao, Y.; Liu, Y. P.; Ning, G. H.; Abdelwahab, I.; Li, L.; Nai, C. T.; Hu, Z. G.; Zhao, D.; Liu, B.; Quek, S. Y.; Loh, K. P., *Nat. Chem.* **2017**, *9*, 563-570.

(40) Feng, X.; Chen, L.; Dong, Y.; Jiang, D., *Chem Commun (Camb)* **2011**, *47*, 1979-1981.

(41) Spitler, E. L.; Dichtel, W. R., *Nat. Chem.* **2010**, *2*, 672-677.

(42) Alahakoon, S. B.; Thompson, C. M.; Nguyen, A. X.; Occhialini, G.; McCandless, G. T.; Smaldone, R. A., *Chem Commun (Camb)* **2016**, *52*, 2843-2845.

(43) Lee, G. Y.; Lee, J.; Vo, H. T.; Kim, S.; Lee, H.; Park, T., *Sci Rep* **2017**, *7*, 557.

(44) Rao, K. V.; Haldar, R.; Maji, T. K.; George, S. J., *Polymer* **2014**, *55*, 1452-1458.

(45) Chandra, S.; Kundu, T.; Kandambeth, S.; Babarao, R.; Marathe, Y.; Kunjir, S. M.; Banerjee, R., *J. Am. Chem. Soc.* **2014**, *136*, 6570-6573.

(46) Xu, H.; Tao, S.; Jiang, D., *Nat. Mater.* **2016**, *15*, 722-726.

(47) Ding, S. Y.; Gao, J.; Wang, Q.; Zhang, Y.; Song, W. G.; Su, C. Y.; Wang, W., *J. Am. Chem. Soc.* **2011**, *133*, 19816-19822.

(48) Fang, Q.; Gu, S.; Zheng, J.; Zhuang, Z.; Qiu, S.; Yan, Y., *Angew. Chem. Int. Ed. Engl.* **2014**, *53*, 2878-2882.

(49) Xu, H.; Chen, X.; Gao, J.; Lin, J.; Addicoat, M.; Irle, S.; Jiang, D., *Chem Commun (Camb)* **2014**, *50*, 1292-1294.

(50) Shinde, D. B.; Kandambeth, S.; Pachfule, P.; Kumar, R. R.; Banerjee, R., *Chem Commun (Camb)* **2015**, *51*, 310-313.

(51) Oh, H.; Kalidindi, S. B.; Um, Y.; Bureekaew, S.; Schmid, R.; Fischer, R. A.; Hirscher, M., *Angew. Chem. Int. Ed. Engl.* **2013**, *52*, 13219-13222.

(52) Lu, H.; Wang, C.; Chen, J.; Ge, R.; Leng, W.; Dong, B.; Huang, J.; Gao, Y., *Chem Commun (Camb)* **2015**, *51*, 15562-15565.

(53) DeBlase, C. R.; Hernandez-Burgos, K.; Silberstein, K. E.; Rodriguez-Calero, G. G.; Bisbey, R. P.; Abruna, H. D.; Dichtel, W. R., *ACS Nano* **2015**, *9*, 3178-3183.

(54) Ding, H.; Li, Y.; Hu, H.; Sun, Y.; Wang, J.; Wang, C.; Wang, C.; Zhang, G.; Wang, B.; Xu, W.; Zhang, D., *Chemistry* **2014**, *20*, 14614-14618.

(55) Medina, D. D.; Petrus, M. L.; Jumabekov, A. N.; Margraf, J. T.; Weinberger, S.; Rotter, J. M.; Clark, T.; Bein, T., *ACS Nano* **2017**, *11*, 2706-2713.

(56) Chen, Y.; Cui, H.; Zhang, J.; Zhao, K.; Ding, D.; Guo, J.; Li, L.; Tian, Z.; Tang, Z., *RSC Adv.* **2015**, *5*, 92573-92576.

(57) Dogru, M.; Bein, T., *Chem Commun (Camb)* **2014**, *50*, 5531-5546.

(58) Liu, L. H.; Yang, C. X.; Yan, X. P., *J. Chromatogr. A* **2017**, *1479*, 137-144.

(59) Wang, L.-L.; Yang, C.-X.; Yan, X.-P., *ChemPlusChem* **2017**, *82*, 933-938.

(60) Han, X.; Huang, J.; Yuan, C.; Liu, Y.; Cui, Y., *J. Am. Chem. Soc.* **2018**, *140*, 892-895.

(61) He, S.; Zeng, T.; Wang, S.; Niu, H.; Cai, Y., *ACS Appl Mater Interfaces* **2017**, *9*, 2959-2965.

(62) Tan, J.; Namuangruk, S.; Kong, W.; Kungwan, N.; Guo, J.; Wang, C., *Angew. Chem. Int. Ed. Engl.* **2016**, *55*, 13979-13984.

(63) Wang, P.; Wu, Q.; Han, L.; Wang, S.; Fang, S.; Zhang, Z.; Sun, S., *RSC Adv.* **2015**, *5*, 27290-27294.

(64) Kang, Z.; Peng, Y.; Qian, Y.; Yuan, D.; Addicoat, M. A.; Heine, T.; Hu, Z.; Tee, L.; Guo, Z.; Zhao, D., *Chem. Mater.* **2016**, *28*, 1277-1285.

(65) Zhang, W.; Liang, F.; Li, C.; Qiu, L. G.; Yuan, Y. P.; Peng, F. M.; Jiang, X.; Xie, A. J.; Shen, Y. H.; Zhu, J. F., *J. Hazard. Mater.* **2011**, *186*, 984-990.

(66) Kalidindi, S. B.; Oh, H.; Hirscher, M.; Esken, D.; Wiktor, C.; Turner, S.; Van Tendeloo, G.; Fischer, R. A., *Chemistry* **2012**, *18*, 10848-10856.

(67) Wang, H.; Li, Z.; Feng, W.; Jia, Q., *New J. Chem.* **2017**, *41*, 13043-13050.

(68) Shi, X.; Yao, Y.; Xu, Y.; Liu, K.; Zhu, G.; Chi, L.; Lu, G., *ACS Appl Mater Interfaces* **2017**, *9*, 7481-7488.

(69) Bunck, D. N.; Dichtel, W. R., *Chem Commun (Camb)* **2013**, *49*, 2457-2459.

(70) Singh, V.; Jang, S.; Vishwakarma, N. K.; Kim, D.-P., *NPG Asia Materials* **2018**, *10*, e456.

(71) Lohse, M. S.; Rotter, J. M.; Margraf, J. T.; Werner, V.; Becker, M.; Herbert, S.; Knochel, P.; Clark, T.; Bein, T.; Medina, D. D., *CrystEngComm* **2016**, *18*, 4295-4302.

(72) Medina, D. D.; Rotter, J. M.; Hu, Y.; Dogru, M.; Werner, V.; Auras, F.; Markiewicz, J. T.; Knochel, P.; Bein, T., *J. Am. Chem. Soc.* **2015**, *137*, 1016-1019.

(73) Tsuruoka, T.; Furukawa, S.; Takashima, Y.; Yoshida, K.; Isoda, S.; Kitagawa, S., *Angew. Chem. Int. Ed. Engl.* **2009**, *48*, 4739-4743.

(74) Umemura, A.; Diring, S.; Furukawa, S.; Uehara, H.; Tsuruoka, T.; Kitagawa, S., *J. Am. Chem. Soc.* **2011**, *133*, 15506-15513.

(75) Diring, S. p.; Furukawa, S.; Takashima, Y.; Tsuruoka, T.; Kitagawa, S., *Chem. Mater.* **2010**, *22*, 4531-4538.

(76) Sakata, Y.; Furukawa, S.; Kondo, M.; Hirai, K.; Horike, N.; Takashima, Y.; Uehara, H.; Louvain, N.; Meilikhov, M.; Tsuruoka, T.; Isoda, S.; Kosaka, W.; Sakata, O.; Kitagawa, S., *Science* **2013**, *339*, 193-196.

(77) Cravillon, J.; Nayuk, R.; Springer, S.; Feldhoff, A.; Huber, K.; Wiebcke, M., *Chem. Mater.* **2011**, *23*, 2130-2141.

(78) Cravillon, J.; Schröder, C. A.; Bux, H.; Rothkirch, A.; Caro, J.; Wiebcke, M., *CrystEngComm* **2012**, *14*, 492-498.

(79) Schaate, A.; Roy, P.; Godt, A.; Lippke, J.; Waltz, F.; Wiebcke, M.; Behrens, P., *Chemistry* **2011**, *17*, 6643-6651.

(80) Zahn, G.; Zerner, P.; Lippke, J.; Kempf, F. L.; Lilienthal, S.; Schröder, C. A.; Schneider, A. M.; Behrens, P., *CrystEngComm* **2014**, *16*, 9198-9207.

(81) Pan, L.; Chen, Z.; Deng, W.; Yan, G.; Liu, X., *Macromolecular Research* **2016**, *24*, 366-370.

(82) Pham, M.-H.; Vuong, G.-T.; Fontaine, F.-G.; Do, T.-O., *Crystal Growth & Design* **2012**, *12*, 3091-3095.

(83) Haase, F.; Gottschling, K.; Stegbauer, L.; Germann, L. S.; Gutzler, R.; Duppel, V.; Vyas, V. S.; Kern, K.; Dinnebier, R. E.; Lotsch, B. V., *Materials Chemistry Frontiers* **2017**, *1*, 1354-1361.

(84) Lukose, B.; Kuc, A.; Heine, T., *Chemistry* **2011**, *17*, 2388-2392.

(85) Lukose, B.; Kuc, A.; Frenzel, J.; Heine, T., *Beilstein J Nanotechnol* **2010**, *1*, 60-70.

(86) Chen, X.; Addicoat, M.; Irle, S.; Nagai, A.; Jiang, D., *J. Am. Chem. Soc.* **2013**, *135*, 546-549.

(87) Salonen, L. M.; Medina, D. D.; Carbo-Argibay, E.; Goesten, M. G.; Mafra, L.; Guldris, N.; Rotter, J. M.; Stroppa, D. G.; Rodriguez-Abreu, C., *Chem Commun (Camb)* **2016**, *52*, 7986-7989.

(88) Kandambeth, S.; Mallick, A.; Lukose, B.; Mane, M. V.; Heine, T.; Banerjee, R., *J. Am. Chem. Soc.* **2012**, *134*, 19524-19527.

(89) DeBlase, C. R.; Silberstein, K. E.; Truong, T. T.; Abruna, H. D.; Dichtel, W. R., *J. Am. Chem. Soc.* **2013**, *135*, 16821-16824.

(90) Chong, S. Y., *IUCrJ* **2016**, *3*, 391-392.

(91) Thote, J.; Barike Aiyappa, H.; Rahul Kumar, R.; Kandambeth, S.; Biswal, B. P.; Balaji Shinde, D.; Chaki Roy, N.; Banerjee, R., *IUCrJ* **2016**, *3*, 402-407.

(92) Biswal, B. P.; Chandra, S.; Kandambeth, S.; Lukose, B.; Heine, T.; Banerjee, R., *J. Am. Chem. Soc.* **2013**, *135*, 5328-5331.

(93) Chandra, S.; Kandambeth, S.; Biswal, B. P.; Lukose, B.; Kunjir, S. M.; Chaudhary, M.; Babarao, R.; Heine, T.; Banerjee, R., *J. Am. Chem. Soc.* **2013**, *135*, 17853-17861.

(94) Lohse, M. S.; Stassin, T.; Naudin, G.; Wuttke, S.; Ameloot, R.; De Vos, D.; Medina, D. D.; Bein, T., *Chem. Mater.* **2016**, *28*, 626-631.

(95) Vyas, V. S.; Haase, F.; Stegbauer, L.; Savasci, G.; Podjaski, F.; Ochsenfeld, C.; Lotsch, B. V., *Nat. Commun.* **2015**, *6*, 8508.

(96) Ascherl, L.; Sick, T.; Margraf, J. T.; Lapidus, S. H.; Calik, M.; Hettstedt, C.; Karaghiosoff, K.; Döblinger, M.; Clark, T.; Chapman, K. W.; Auras, F.; Bein, T., *Nat. Chem.* **2016**, *8*, 310-316.

(97) Machmudah, S.; Kitada, K.; Sasaki, M.; Goto, M.; Munemasa, J.; Yamagata, M., *Industrial & Engineering Chemistry Research* **2011**, *50*, 2227-2235.

(98) Aizpurua-Olaizola, O.; Ormazabal, M.; Vallejo, A.; Olivares, M.; Navarro, P.; Etxebarria, N.; Usobiaga, A., *J. Food Sci.* **2015**, *80*, E101-107.

(99) López-Domínguez, P.; López-Periago, A. M.; Fernández-Porras, F. J.; Fraile, J.; Tobias, G.; Domingo, C., *Journal of CO2 Utilization* **2017**, *18*, 147-155.

(100) Matsuyama, K., *J. of Supercritical Fluids*.

(101) Nelson, A. P.; Farha, O. K.; Mulfort, K. L.; Hupp, J. T., *J. Am. Chem. Soc.* **2009**, *131*, 458-460.

(102) Lohe, M. R.; Rose, M.; Kaskel, S., *Chem Commun (Camb)* **2009**, 6056-6058.

(103) Zhang, B.; Zhang, J.; Han, B., *Chem Asian J* **2016**, *11*, 2610-2619.

(104) Ma, J.; Kalenak, A. P.; Wong-Foy, A. G.; Matzger, A. J., *Angew. Chem. Int. Ed. Engl.* **2017**, *56*, 14618-14621.

(105) Matsuyama, K.; Hayashi, N.; Yokomizo, M.; Kato, T.; Ohara, K.; Okuyama, T., *J. Mater. Chem. B* **2014**, *2*, 7551-7558.

(106) Lopez-Periago, A.; Vallcorba, O.; Frontera, C.; Domingo, C.; Ayllon, J. A., *Dalton Trans* **2015**, *44*, 7548-7553.

(107) Cooper, A. I., *J. Mater. Chem.* **2000**, *10*, 207-234.

(108) Cooper, A. I., *Adv. Mater.* **2003**, *15*, 1049-1059.

(109) Lubguban, J. A.; Gangopadhyay, S.; Lahlouh, B.; Rajagopalan, T.; Biswas, N.; Sun, J.; Huang, D. H.; Simon, S. L.; Mallikarjunan, A.; Kim, H. C.; Hedstrom, J.; Volksen, W.; Miller, R. D.; Toney, M. F., *J. Mater. Res.* **2011**, *19*, 3224-3233.

(110) Lin, S.; Diercks, C. S.; Zhang, Y. B.; Kornienko, N.; Nichols, E. M.; Zhao, Y.; Paris, A. R.; Kim, D.; Yang, P.; Yaghi, O. M.; Chang, C. J., *Science* **2015**, *349*, 1208-1213.

(111) Zhang, Y. B.; Su, J.; Furukawa, H.; Yun, Y.; Gandara, F.; Duong, A.; Zou, X.; Yaghi, O. M., *J. Am. Chem. Soc.* **2013**, *135*, 16336-16339.

(112) Waller, P. J.; Lyle, S. J.; Osborn Popp, T. M.; Diercks, C. S.; Reimer, J. A.; Yaghi, O. M., *J. Am. Chem. Soc.* **2016**, *138*, 15519-15522.

(113) Dogru, M.; Handloser, M.; Auras, F.; Kunz, T.; Medina, D.; Hartschuh, A.; Knochel, P.; Bein, T., *Angew. Chem. Int. Ed. Engl.* **2013**, *52*, 2920-2924.

(114) Jin, S.; Supur, M.; Addicoat, M.; Furukawa, K.; Chen, L.; Nakamura, T.; Fukuzumi, S.; Irle, S.; Jiang, D., *J. Am. Chem. Soc.* **2015**, *137*, 7817-7827.

(115) Chen, L.; Furukawa, K.; Gao, J.; Nagai, A.; Nakamura, T.; Dong, Y.; Jiang, D., *J. Am. Chem. Soc.* **2014**, *136*, 9806-9809.

(116) Wan, S.; Gándara, F.; Asano, A.; Furukawa, H.; Saeki, A.; Dey, S. K.; Liao, L.; Ambrogio, M. W.; Botros, Y. Y.; Duan, X.; Seki, S.; Stoddart, J. F.; Yaghi, O. M., *Chem. Mater.* **2011**, *23*, 4094-4097.

(117) Jin, S.; Sakurai, T.; Kowalczyk, T.; Dalapati, S.; Xu, F.; Wei, H.; Chen, X.; Gao, J.; Seki, S.; Irle, S.; Jiang, D., *Chemistry* **2014**, *20*, 14608-14613.

(118) Medina, D. D.; Werner, V.; Auras, F.; Tautz, R.; Dogru, M.; Schuster, J.; Linke, S.; Doblinger, M.; Feldmann, J.; Knochel, P.; Bein, T., *ACS Nano* **2014**, *8*, 4042-4052.

(119) Duhović, S.; Dincă, M., *Chem. Mater.* **2015**, *27*, 5487-5490.

(120) Colson, J. W.; Woll, A. R.; Mukherjee, A.; Levendorf, M. P.; Spitler, E. L.; Shields, V. B.; Spencer, M. G.; Park, J.; Dichtel, W. R., *Science* **2011**, *332*, 228-231.

(121) Colson, J. W.; Mann, J. A.; DeBlase, C. R.; Dichtel, W. R., *J. Polym. Sci., Part A: Polym. Chem.* **2015**, *53*, 378-384.

(122) Calik, M.; Auras, F.; Salonen, L. M.; Bader, K.; Grill, I.; Handloser, M.; Medina, D. D.; Dogru, M.; Lobermann, F.; Trauner, D.; Hartschuh, A.; Bein, T., *J. Am. Chem. Soc.* **2014**, *136*, 17802-17807.

(123) Cai, S.-L.; Zhang, Y.-B.; Pun, A. B.; He, B.; Yang, J.; Toma, F. M.; Sharp, I. D.; Yaghi, O. M.; Fan, J.; Zheng, S.-R.; Zhang, W.-G.; Liu, Y., *Chem. Sci.* **2014**, *5*, 4693-4700.

(124) Feldblyum, J. I.; McCreery, C. H.; Andrews, S. C.; Kurosawa, T.; Santos, E. J.; Duong, V.; Fang, L.; Ayzner, A. L.; Bao, Z., *Chem Commun (Camb)* **2015**, *51*, 13894-13897.

(125) Sun, B.; Li, J.; Dong, W.-L.; Wu, M.-L.; Wang, D., *J. Phys. Chem. C* **2016**, *120*, 14706-14711.

(126) van de Krol, R. G., M., *Photoelectrochemical Hydrogen Production*. Springer US: 2012; Vol. 1, p 324.

(127) Hisatomi, T.; Kubota, J.; Domen, K., *Chem. Soc. Rev.* **2014**, *43*, 7520-7535.

(128) Castelli, I. E.; Olsen, T.; Datta, S.; Landis, D. D.; Dahl, S.; Thygesen, K. S.; Jacobsen, K. W., *Energy Environ. Sci.* **2012**, *5*, 5814-5819.

(129) http://www.eplasty.com/index.php?option=com_content&view=article&id=453&catid=171:volume-10-eplasty-2010.

(130) Bryan, J. D.; Gamelin, D. R., **2005**, 47-126.

(131) Queisser, H. J., *Science* **1998**, *281*, 945-950.

(132) Serpone, N.; Emeline, A. V., *J Phys Chem Lett* **2012**, *3*, 673-677.

(133) Kang, D.; Kim, T. W.; Kubota, S. R.; Cardiel, A. C.; Cha, H. G.; Choi, K. S., *Chem. Rev.* **2015**, *115*, 12839-12887.

(134) Velev, O. D.; Kaler, E. W., *Adv. Mater.* **2000**, *12*, 531-534.

(135) Stein, A.; Wilson, B. E.; Rudisill, S. G., *Chem. Soc. Rev.* **2013**, *42*, 2763-2803.

(136) Brinker, C. J.; Lu, Y.; Sellinger, A.; Fan, H., *Adv. Mater.* **1999**, *11*, 579-585.

(137) Förster, S.; Antonietti, M., *Adv. Mater.* **1998**, *10*, 195-217.

(138) Sanchez, C.; Boissière, C.; Grosso, D.; Laberty, C.; Nicole, L., *Chem. Mater.* **2008**, *20*, 682-737.

(139) Bornoz, P.; Prevot, M. S.; Yu, X.; Guijarro, N.; Sivula, K., *J. Am. Chem. Soc.* **2015**, *137*, 15338-15341.

(140) Haro, M.; Solis, C.; Molina, G.; Otero, L.; Bisquert, J.; Gimenez, S.; Guerrero, A., *J. Phys. Chem. C* **2015**, *119*, 6488-6494.

(141) Chen, S. N.; Heeger, A. J.; Kiss, Z.; MacDiarmid, A. G.; Gau, S. C.; Peebles, D. L., *Appl. Phys. Lett.* **1980**, *36*, 96-98.

(142) Glenis, S.; Tourillon, G.; Garnier, F., *Thin Solid Films* **1984**, *122*, 9-17.

(143) Bourgeteau, T.; Tondelier, D.; Geffroy, B.; Brisse, R.; Laberty-Robert, C.; Campidelli, S.; de Bettignies, R.; Artero, V.; Palacin, S.; Jousselme, B., *Energy Sustain Soc* **2013**, *6*.

(144) Fumagalli, F.; Bellani, S.; Schreier, M.; Leonardi, S.; Rojas, H. C.; Ghadirzadeh, A.; Tullii, G.; Savoini, A.; Marra, G.; Meda, L.; Grätzel, M.; Lanzani, G.; Mayer, M. T.; Antognazza, M. R.; Di Fonzo, F., *J. Mater. Chem. A* **2016**, *4*, 2178-2187.

(145) Rojas, H. C.; Bellani, S.; Fumagalli, F.; Tullii, G.; Leonardi, S.; Mayer, M. T.; Schreier, M.; Grätzel, M.; Lanzani, G.; Di Fonzo, F.; Antognazza, M. R., *Energy Environ. Sci.* **2016**, *9*, 3710-3723.

(146) Zhou, H. C.; Long, J. R.; Yaghi, O. M., *Chem. Rev.* **2012**, *112*, 673-674.

(147) Shekhah, O.; Liu, J.; Fischer, R. A.; Woll, C., *Chem. Soc. Rev.* **2011**, *40*, 1081-1106.

(148) Czaja, A. U.; Trukhan, N.; Muller, U., *Chem. Soc. Rev.* **2009**, *38*, 1284-1293.

(149) Altaf, M.; Sohail, M.; Mansha, M.; Iqbal, N.; Sher, M.; Fazal, A.; Ullah, N.; Isab, A. A., *ChemSusChem* **2018**, *11*, 542-546.

(150) Zhang, L.; Cui, P.; Yang, H.; Chen, J.; Xiao, F.; Guo, Y.; Liu, Y.; Zhang, W.; Huo, F.; Liu, B., *Adv Sci (Weinh)* **2016**, *3*, 1500243.

(151) Sprick, R. S.; Jiang, J. X.; Bonillo, B.; Ren, S.; Ratvijitvech, T.; Guiglion, P.; Zwijnenburg, M. A.; Adams, D. J.; Cooper, A. I., *J. Am. Chem. Soc.* **2015**, *137*, 3265-3270.

(152) Wang, X.; Maeda, K.; Thomas, A.; Takanabe, K.; Xin, G.; Carlsson, J. M.; Domen, K.; Antonietti, M., *Nat. Mater.* **2009**, *8*, 76-80.

(153) Vyas, V. S.; Lau, V. W.-h.; Lotsch, B. V., *Chem. Mater.* **2016**, *28*, 5191-5204.

(154) Schwab, M. G.; Hamburger, M.; Feng, X.; Shu, J.; Spiess, H. W.; Wang, X.; Antonietti, M.; Mullen, K., *Chem Commun (Camb)* **2010**, *46*, 8932-8934.

(155) Peng, G.; Xing, L.; Barrio, J.; Volokh, M.; Shalom, M., *Angew. Chem. Int. Ed. Engl.* **2018**, *57*, 1186-1192.

(156) Lau, V. W.; Moudrakovski, I.; Botari, T.; Weinberger, S.; Mesch, M. B.; Duppel, V.; Senker, J.; Blum, V.; Lotsch, B. V., *Nat. Commun.* **2016**, *7*, 12165.

(157) Pachfule, P.; Acharjya, A.; Roeser, J.; Langenhahn, T.; Schwarze, M.; Schomacker, R.; Thomas, A.; Schmidt, J., *J. Am. Chem. Soc.* **2018**, *140*, 1423-1427.

(158) Stegbauer, L.; Schwinghammer, K.; Lotsch, B. V., *Chem. Sci.* **2014**, *5*, 2789-2793.

(159) Haase, F.; Banerjee, T.; Savasci, G.; Ochsenfeld, C.; Lotsch, B. V., *Faraday Discuss.* **2017**, *201*, 247-264.

(160) Banerjee, T.; Gottschling, K.; Savasci, G.; Ochsenfeld, C.; Lotsch, B. V., *ACS Energy Lett* **2018**, *3*, 400-409.

(161) Banerjee, T.; Haase, F.; Savasci, G.; Gottschling, K.; Ochsenfeld, C.; Lotsch, B. V., *J. Am. Chem. Soc.* **2017**, *139*, 16228-16234.

(162) Jones, W.; Martin, D. J.; Caravaca, A.; Beale, A. M.; Bowker, M.; Maschmeyer, T.; Hartley, G.; Masters, A., *Applied Catalysis B: Environmental* **2017**.

(163) Sick, T.; Hufnagel, A. G.; Kampmann, J.; Kondofersky, I.; Calik, M.; Rotter, J. M.; Evans, A.; Doblinger, M.; Herbert, S.; Peters, K.; Bohm, D.; Knochel, P.; Medina, D. D.; Fattakhova-Rohlfing, D.; Bein, T., *J. Am. Chem. Soc.* **2018**, *140*, 2085-2092.

# 2. CHARACTERIZATION

This chapter comprises the different analytical techniques that were essential for the comprehensive characterization of the synthesized precursors as well as of the nanoporous COF powders and films. The precursors were characterized by nuclear magnetic resonance (NMR) measurements and by mass spectrometry. The crystallinity and the domain sizes of the powders were determined by X-ray diffraction (XRD) while the orientation of the COF films was investigated by grazing-incident wide-angle X-ray scattering (GIWAXS). Nitrogen physisorption was used to characterize the porosity, particularly the surface area, pore size distribution and pore volume of the corresponding samples. Scanning electron microscopy (SEM) and transmission electron microscopy (TEM) were applied to investigate the morphology, crystallite sizes and the pore structure of the materials. Photoluminescence (ssPL and TCSPC) and UV-Vis were used to investigate the induced light emission and absorption characteristics. Infrared (IR) spectroscopy was used to characterize the precursors and the COFs regarding their absorption properties based on vibrations of involved groups. Thermogravimetric analysis (TGA) was used to determine the thermal stability of the frameworks.

## 2.1 X-RAY DIFFRACTION (XRD)

### 2.1.1 WIDE ANGLE X-RAY SCATTERING (WAXS)

The structural investigation of crystalline materials with X-ray diffraction (XRD) is a standard method in material sciences. This non-destructive analytical technique allows for identification of ordered structures, the degree of crystallinity and phase compositions of powders. Only small amounts of sample are needed to be examined. Furthermore, the phases, geometry, lattice parameters and orientation of crystals can be determined. For angles of $5° < 2\theta < 80°$, wide angle X-ray scattering (WAXS) is used. In contrast, small angle X-ray scattering (SAXS) can resolve larger, ordered structures between $0° < 2\theta < 5°$ with high accuracy. The X-rays are generated in a high vacuum tube, consisting of a cathode where electrons are accelerated with high voltages towards an anode material (Al, Cu, Mo or Mg). By collision of these electrons with the anode material, characteristic X-ray scattering ($\lambda = 0.01$ to 10 nm, within the range of atomic distances) is generated. The emitted X-rays are focused on the sample where they interact with the electron shell of the matter, resulting in reflection, scattering and absorption. Scattering of crystalline samples leads to diffraction. Ordered, periodic matter consists of

crystallographic planes, which are determined by the specific symmetry, the lattice constants and the occupation of the unit cell with atoms. The superposition of the resulting scattering waves is dependent on their phases. In-phase superpositions lead to constructive interference, while out-of-phase superpositions result in a destructive interference.[1] The requirement for a constructive interference of the diffracted X-ray scattering is illustrated in Bragg's Law in Figure 2.1.[2]

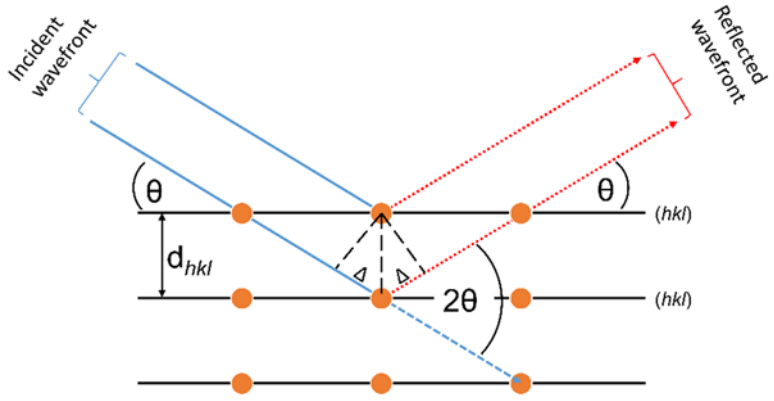


Figure 2.1: Bragg condition shown in a schematic illustration of a crystal's X-ray scattering.

For a constructive interference, Bragg's law as shown in Equation 2.1 must be fulfilled.

$$2\Delta = n\lambda = 2d\ sin\theta \tag{2.1}$$

$\Delta$ represents the path difference, $n$ the order of reflection, $\lambda$ the X-ray wavelength, $d$ the interplanar spacing and $\theta$ the incident angle.

Constructive interference results in the occurrence of reflections at system-specific °2θ. From the intensity, the order of crystallinity can be estimated. Furthermore, the amount of reflections, the relative intensities and the positions allow for calculation of the unit cell parameters. Furthermore, the peak broadening can be used to calculate crystallite domain sizes with the Scherrer equation (Equation 2.2). [3-4]

$$D = \frac{k\lambda}{\beta cos\theta} \tag{2.2}$$

The crystallite size D can be calculated by the Scherrer constant $k$, the wavelength of X-rays $\lambda$, the full width at half maximum (FWHM) $\beta$ and the diffraction angle $\theta$.

Small and wide angle X-ray Scattering was carried out in reflection mode on a Bruker D8 Discover with Ni-filtered Cu $K_\alpha$ radiation and a LynxEye position-sensitive detector.

Background correction was performed using spline-interpolated and intensity-adapted measurements of the empty sample holder.

### 2.1.2 GRAZING-INCIDENT WIDE ANGLE X-RAY SCATTERING (GIWAXS)

In contrast to WAXS, in GIWAXS measurements very thin layers of films can be investigated. These non-destructive measurements are very powerful in characterizing the crystallinity and orientation of thin (nano-)structured films. As a very small incident angle of the incoming X-ray beam is used, a broad area of the sample can be illuminated and investigated. Furthermore, in contrast to atomic force measurements (AFM) even buried or covered parts of the area are detectable with this technique, as depth-dependent measurements can be conducted by using different incident angles. As a result, GIWAXS is in fact a combination of three powerful measurement techniques. GID (grazing incidence diffraction) to investigate surface and near-surface scattering in reflection mode, secondly WAXS (wide angle X-ray scattering), which is able to resolve nanostructures in a size range from 3 to 50 nm and thirdly diffused scattering, giving insights in films' morphology and surfaces in reflection mode. This combination allows for investigation of a broad range of the sample's surface, spatial correlations and gives insights in the morphology, crystallinity and structure of the material.[5-6]

A typical investigation experiment is shown in Figure 2.2.

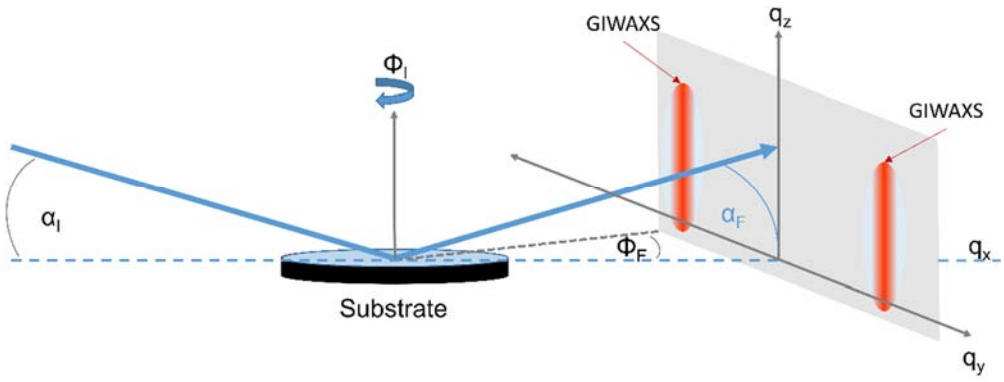


Figure 2.2: Scattering geometry in GIWAXS. The sample can be tilted ($\alpha_I$) with respect to the X-ray beam. The exit angle is termed with $\alpha_F$ and the in-plane angle is denoted with $\Phi_F$.

Under a very small angle, which is close to total reflection, the incident X-ray beam strikes the surface of the sample. This allows for long paths and penetration through even very thin films. The sample defines x and y with its own orientation, with *x* in line with the X-ray beam and *y* perpendicular to it. Perpendicular to the *xy* plane, *z* is aligned. The incident angle of the beam

is expressed with $\alpha_I$ and the exit angle with $\alpha_F$. A beam stop attenuates the intense beam, the scattering at the incident plane and the reflection to avoid damage to the detector. The diffuse scattering of the sample is recorded as a 2D image, from which the in-plane scattered intensity can be plotted to have insight into crystallinity and degree of orientation.

Experiments were conducted on an Anton Paar SAXSpace system. A Xenocs GeniX3D microfocus X-ray source was used with a Cu target to generate a monochromatic beam of 50 μm in diameter and a wavelength of 0.154 nm. A Dectris EIGER R 1M detector was used to collect the 2D scattering patterns. The GIWAXS experiments were carried out with an incident angle near 0.23°. A sample-to-detector distance of 200 mm was used.

## 2.2 ELECTRON MICROSCOPY

Revealing the structure and the morphology of nanostructured materials can be challenging and optical microscopy is limited in resolution. Electron microscopy (EM) enables imaging of the morphology of these samples. Different techniques have the potential to uncover specific and material characteristic nanostructures. Transmission electron microscopy (TEM) is used to get insight into the internal microstructure, while the external surface (morphology) is investigated by scanning electron microscopy (SEM). Furthermore, the chemical composition of the investigated sample can be determined by energy dispersive X-ray spectroscopy (EDX). During EM, the sample is bombarded with electrons. As a result of the interactions between the highly accelerated electrons and the solid matter, the electrons can be scattered, absorbed or emitted by the sample, as shown in Figure 2.3.

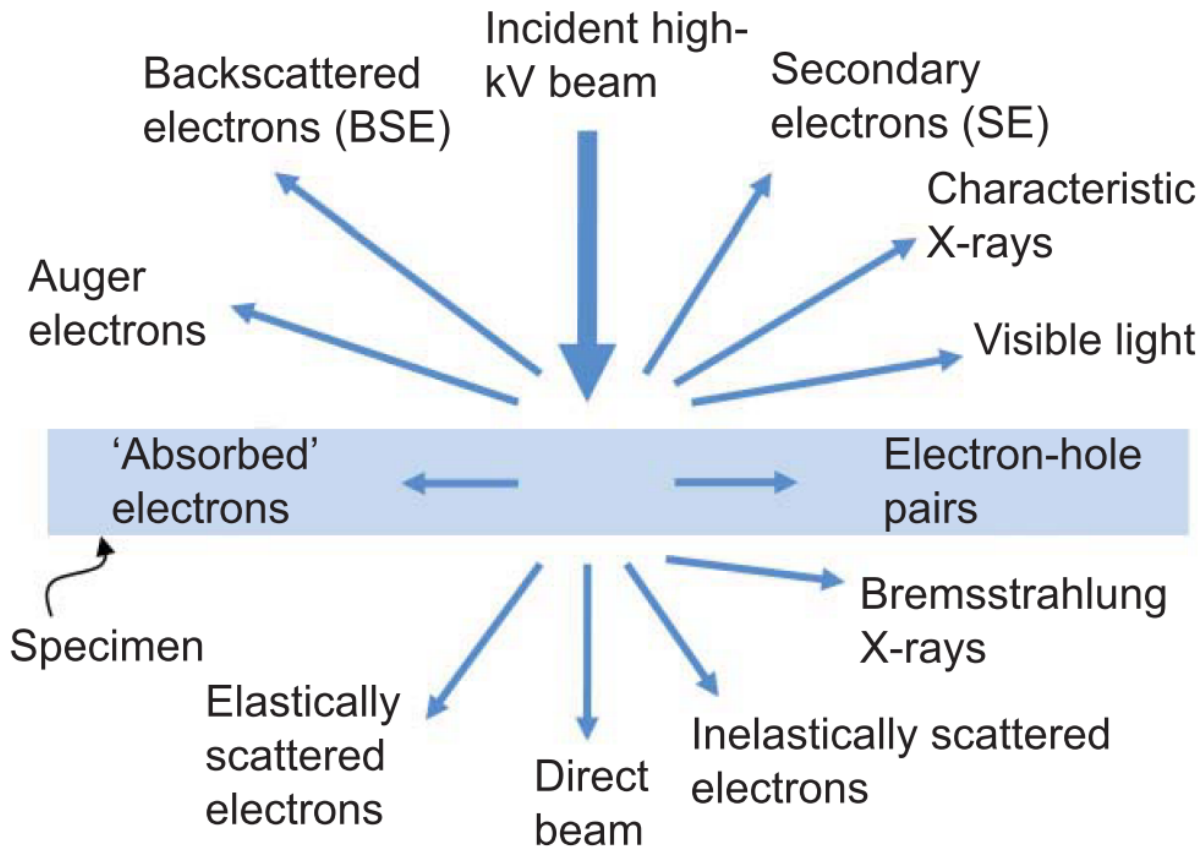


Figure 2.3: In electron microscopes, incident high kV accelerated electrons interact with matter and generate different signals.[7]

### 2.2.1 TRANSMISSION ELECTRON MICROSCOPY (TEM)

Compared to light microscopes, TEMs benefit from the very small effective wavelengths (λ) of electrons due to the de Broglie relationship compared to visible light. This allows for precise imaging down to 0.5 nm. In a TEM investigation, under ultrahigh vacuum, rather high voltages of 60 to 300 kV are used to accelerate the electrons coming from a pin-shaped tungsten filament of a field emission gun (FEG, cathode), which are subsequently focused onto a thin specimen by electromagnetic condenser lenses. With a so-called Schottky emitter, the advantages of FEGs and thermal emitters (tungsten or lanthanum hexaboride) can be combined concerning stability, long lifetimes, narrow energy widths, low work function, high total current and brightness.[8] The beam focus can either illuminate a large area of the sample by holding it parallel or it can be focused to a very small probe in the range of atomic diameters. Elastically scattered or transmitted electrons are used to generate the TEM image from a CCD camera with a fluorescent screen. The resulting contrast depends on the ratio of inelastic to elastic scattering from the electrons on the sample. At low resolution the image contrast, so-called amplitude contrast, is achieved by a reduction of the total amount of electrons reaching the detector. Electrons that were scattered to high angles or that lost energy by interacting with the sample will be removed by the objective aperture of the lenses or the energy filter. The amount of the removed electrons is mainly dependent on the density of the investigated material. Furthermore, bright and dark field images can be distinguished. While in bright field images high scattering angles are excluded by centering the objective aperture on the transmitted beam, in dark field images low angle scattered electrons and the transmitted beam are excluded from the image generation. Depending on the sample's stability, increasing the voltage results in a higher lateral spatial resolution which allows for revealing structures in the (sub-)nanometer region.[9] Furthermore, at higher acceleration voltages, the aberration is reduced. Nevertheless, the sample might be affected or destroyed by the electron bombardment, what represents a danger in particular for organic samples.

To gain crystallographic information on the sample, high resolution TEM (HRTEM) can be used. The images are generated only by elastically scattered electrons. The accelerated electrons are in phase prior to interaction with the sample. Due to Bragg diffraction at the sample, depending on the crystallites' orientation, phase transitions of the electrons are obtained after interaction. The phase transition is translated into contrast within the image generation. Under parallel illumination the operator is able to switch between diffraction and imaging mode by using a selected-area aperture. Crystalline samples can be investigated by selected-area electron

diffraction (SAED) that allows for the detection of diffraction patterns. From these patterns, single and polycrystalline materials can be measured, calculated and distinguished as different crystallite orientations result in different Bragg conditions.

TEM measurements were carried out using an FEI Tecnai G2 20 S-TWIN, a Titan Themis 300 or an FEI Titan 80-300 operated at 300 kV.

### 2.2.2 SCANNING ELECTRON MICROSCOPY (SEM)

To characterize a sample concerning the nanostructure or the general morphology, SEM is a powerful and widely used technique. An incident electron beam, accelerated by applied voltages of 0.1 to 30 kV, scans across the sample surface in lines (raster scanning) with a particular frequency. The scanned area can be divided into pixels corresponding to the respective electron beam probe position. The interactions of the highly focused electron beam (1 to 10 nm) with the sample results in several secondary signals, allowing for the detailed analysis on the chemical composition as well as on the morphology. The accelerated electrons penetrate the first layers of the sample generating the emission of further electrons and photons. Usually an Everhart-Thornley detector is used for this purpose. The detected signals of each pixel are finally combined to an image with a computer program. Depending on the acceleration voltage and the detection mode, three different types of SEM imaging can be distinguished, namely backscattered electron (BSE) images, secondary electron (SE) images and elemental X-ray maps, as shown in Figure 2.4. [10-11]

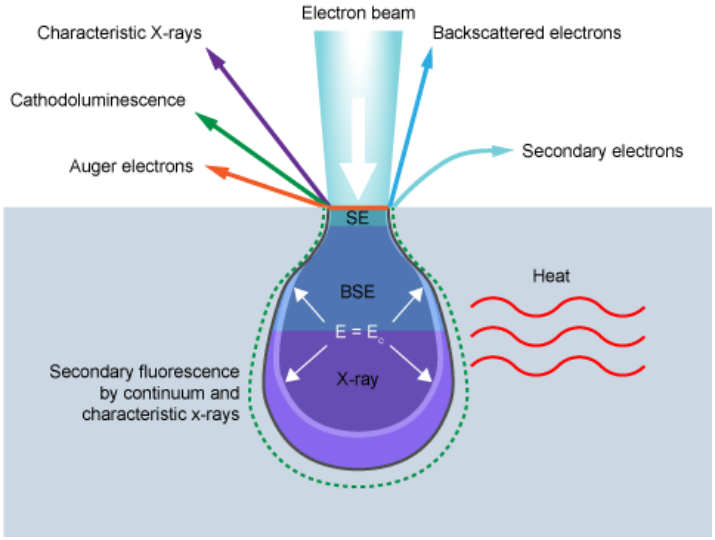


Figure 2.4: Scheme of the different electron and X-ray-specimen in SEM, their interaction volume and their penetration/signal depths.[12]

BSEs possess high-energy in the range of the incident, primary electrons and result from elastic scattering at the atomic nuclei. Secondary electrons (< 50 eV) result from inelastic scattering in less deep regions and thus are surface sensitive (outer surface morphology). The comparably high energetic BSEs result from the enlarged interaction volume. Furthermore, different atoms can be distinguished by the backscatter events, as this phenomenon is dependent on the atomic number Z. As a result, a contrast difference can be obtained for elements with different Z

numbers allowing for a spatial characterization of the chemical composition and assembly for a known system. To quantitatively characterize the sample's composition, elemental characteristic generated X-rays can be detected in an EDX mapping detector.[13] A general setup of a SEM is shown in Figure 2.5.

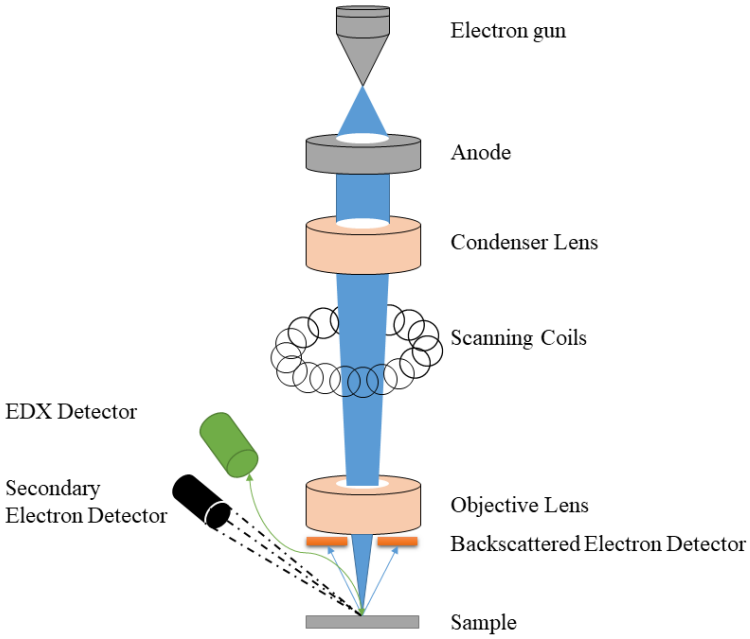


Figure 2.5: Schematic illustration of a scanning electron microscope (SEM) setup.

The limit in resolution ($R$) is dependent on the electron's wavelength of the electron beam ($\lambda$) and the numerical aperture ($NA$) of the instrument, as shown in Equation 2.3.

$$R = \frac{\lambda}{NA} \tag{2.3}$$

The numerical aperture $NA$ is dependent on the objective's electron gathering ability and the condenser's electron providing ability. [14]

SEM images were obtained using a JEOL JSM-6500F or an FEI Helios NanoLab G3 UC scanning electron microscope equipped with a field emission gun operated at 1–10 kV.

## 2.3 GAS SORPTION

Physisorption investigations allow for the characterization of porous materials regarding surface areas, pore size distributions and pore volumes. In contrast to chemisorption, where the surface of the sample is modified by the adsorptive by undergoing chemical reactions and bond-forming processes ($-\Delta_{Ad}.H$ 200 kJ mol$^{-1}$), physisorption uses (inert) gases as adsorptive, involving only less intense intermolecular interactions ranging from van der Waals and London dispersive forces to repulsion forces ($-\Delta_{Ad}.H \leq 100$ kJ mol$^{-1}$). The advantage of physisorption is the reversible, non-destructive investigation. The analysis itself is based on the adsorption and desorption of gas molecules, for example nitrogen, argon, krypton, carbon dioxide and hydrogen, on the surface of the sample under isothermal conditions. The equilibrium between adsorption and desorption can be changed by varying the pressure of the adsorptive. The amount of adsorbed adsorptive can be measured volumetrically or gravimetrically. To obtain a physisorption isotherm, the adsorbed volume $V_{ads}$ is plotted versus the relative pressure. Usually, the adsorbed volume is mass-related (specific) to allow for comparisons between different samples. The relative pressure represents the ratio between equilibrium pressure $p$ and saturated vapor pressure $p^0$ of pure adsorptive. The $p^0$ value is determined by using a glass rod with the same size as the sample's glass rod. To obtain the adsorption branch, the outgassed, weighed, and evacuated sample is exposed to increased gas pressures at predefined pressure points until a relative pressure close to $p^0$ is reached. By this, a condensation of adsorptive within the measuring rod can be prevented. Every measuring point is determined from equilibrium. Afterwards, the desorption branch, also called equilibrium branch, can be determined. Therefore, the relative pressure is decreased again to predefined pressure points. [15]

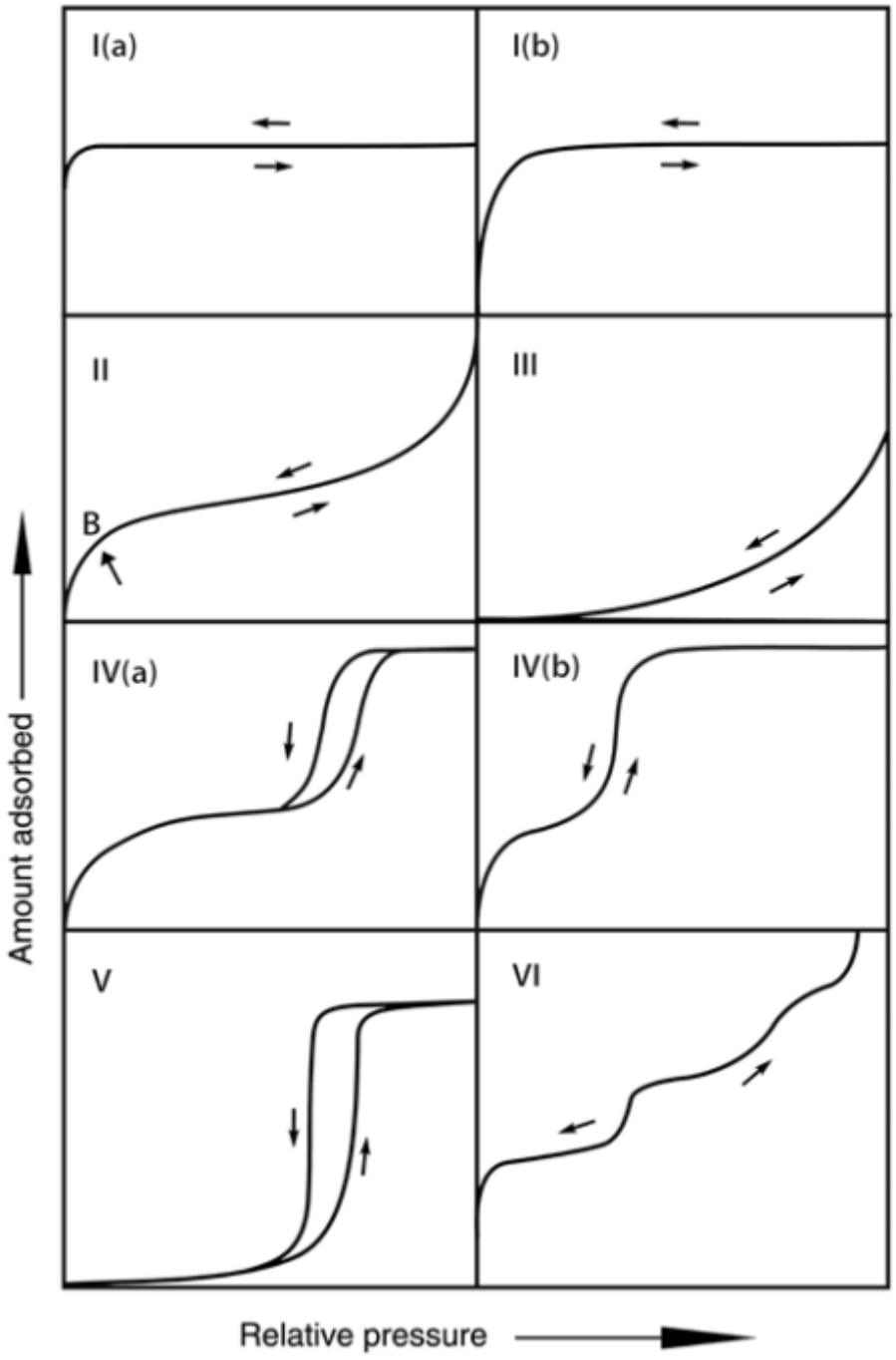


Figure 2.6: Types of isotherms classified by shape. [15]

The shape of the isotherm is only dependent on the material's properties and consequently distinctive. As different pore sizes and pore architectures result in different types of isotherms IUPAC classified eight prototypical isotherm shapes (Figure 2.6). As pores are divided into three different classes (micropores ≤ 2 nm, mesopores 2-50 nm and macropores ≥ 50 nm) these classes can be found in the isotherm shapes as well. In all cases, assumptions have to be made. First of all, a completely closed monolayer of adsorptive on the adsorbent is formed, before

multilayer adsorption can occur. Secondly, each adsorption site is equivalent on a uniform surface. And thirdly that there's no influence of adsorbate on the attractive force of adjacent adsorption sites.

In non-, macro- or big mesoporous materials type II, type III or type VI isotherms are obtained, as only monolayers and multilayers are formed. For mesoporous materials hysteresis loops can occur due to capillary condensation inside of the pores, as shown in type IVa. In type IVb, a mesoporous material with no hysteresis loop is shown. Whether a hysteresis loop appears or not is dependent on the pore size, the pore shape, the adsorption system as well as the temperature. Type III and type V isotherms are usually obtained for materials with weak adsorbent-adsorbate interactions. In the case of type V, pore filling occurs due to pore condensation, which often is observed for hydrophobic micro- and mesoporous materials in water adsorption. Type I isotherms are representative for microporous materials. The pore diameter is very small and the attractive potential result in a pore condensation, the so-called micropore filling.

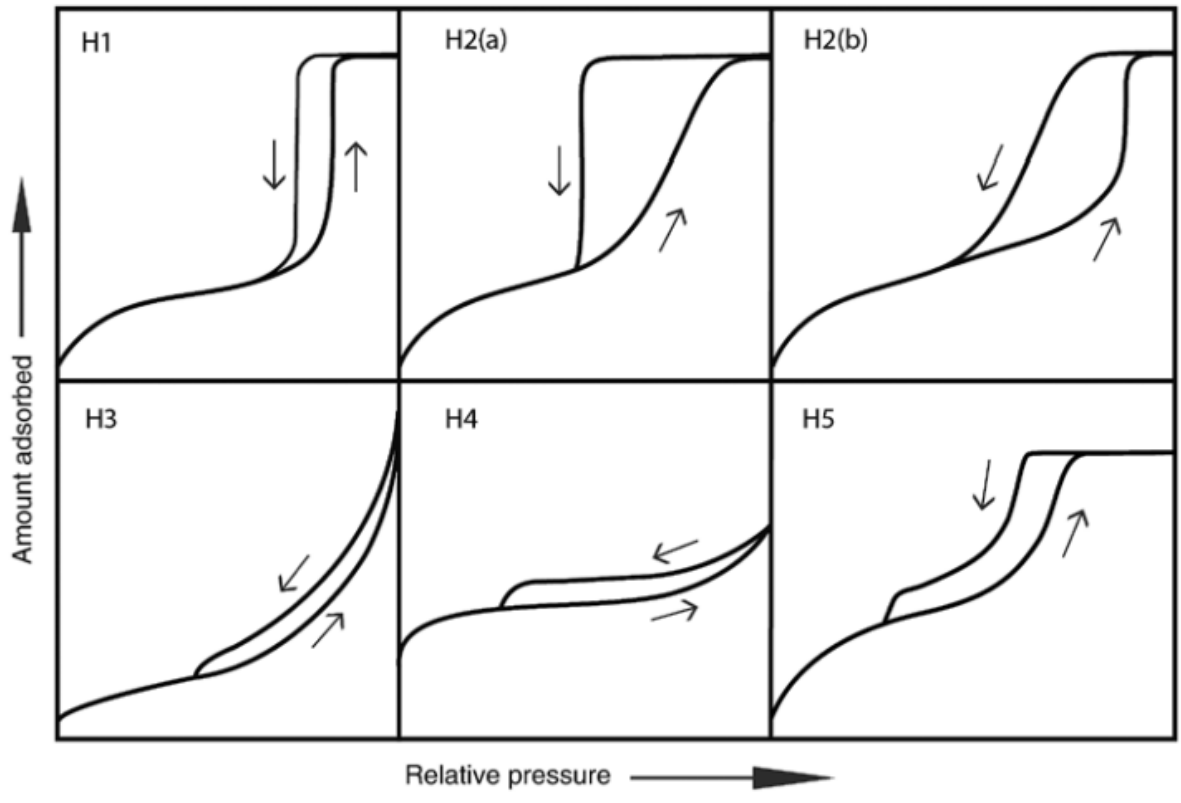


Figure 2.7: Different types of hysteresis loops. Dependent on the pore structure and network effects in mesopores, pore condensation, pore blocking, and cavitation can occur.[15]

The origin of the hysteresis loops is the result of a metastability of the adsorbed multilayer during the adsorption process in mesoporous materials. Processes like nucleation and network effects result in a delayed pore condensation. In contrast, the desorption process is a reversible liquid-vapor transition within a thermodynamically controlled equilibrium. The form of the hysteresis is dependent on network effects, pore shapes and the pore distribution. Pore blocking occurs, when ink-bottle pores are involved, as the narrow neck first has to be emptied. In this case, important information about the neck sizes can be obtained from the equilibrium branch. If the pore necks are very small, pore cavitation can occur. Within the big pores a growth of gas bubbles already occurs during desorption. The gas bubbles are released at an adsorptive-dependent pressure and no information about the pore necks can be determined. Type H1 loop represents uniform mesopores with a cylindrical shape. Type H2a is found in materials with pore blocking with a narrow distribution of pore necks, resulting in a sharp step during the desorption process. In contrast, the pore neck distribution for type H2b is broad. Type H3 is related to type II isotherms for "non-rigid aggregates or plate-like particles"[15], while usually cavitation occurs at lower $p/p^0$ region.[15] H4 is a composite of isotherm types I and II, in hierarchically micro- and mesoporous structures, for examples in zeolites or carbons. H5 is connected to both, partially blocked and open porous networks, for example plugged, hexagonal templated silicas (Figure 2.7).[15]

The surface areas are most widely calculated with the Brunauer-Emmett-Teller (BET) method. In a first step, a BET monolayer capacity is derived from a transformation of a physisorption isotherm into a so-called BET plot. Within two steps, from the BET plot a BET monolayer capacity can be derived and in the second step, from this capacity the BET surface area can be calculated based on the cross-sectional area of the adsorbed adsorptive.

The choice of adsorptive is dependent on different requirements. Nitrogen's advantage is its availability in big amounts, favorability and that it is an inert gas towards many porous materials. On the other hand, nitrogen is a diatomic molecule and does not fulfil the requirements of a good approximation for an ideal gas. Furthermore, it exhibits a quadrupole moment resulting in additional partial charge interactions with the surface of the sample. This influence on the molecules leads to an uncertainty of the orientation of the nitrogen molecules on the surface affecting the molecular cross-sectional area (up to 20% uncertainty). Better adsorptives represent noble gases like argon or krypton. Usually for price reasons, measurements with these gases are conducted at 77.3 K with a liquid nitrogen bath. But this temperature is below the bulk triple point temperature of the adsorptive, respectively.

Furthermore, the cross-sectional area is dependent on temperature and the sample's surface properties. To avoid these problems, either liquid argon (87 K) or a cryostat can be used. Krypton physisorption is highly preferred when measuring particularly small overall surface areas like in macroporous samples, non-porous materials or when measuring porous, but very thin films. The high sensitivity of krypton derives from the very low saturation pressure resulting in a reduction of the total amount of molecules in the measurement tube's free space. Nevertheless, as well as for argon, using krypton at 77 K has drawbacks, because the cross-sectional area varies with the sample's surface properties. For very small micropores, carbon dioxide is a valuable adsorptive, as the kinetic dimension is much smaller at 273 K in combination with a high saturation vapor pressure and a fast diffusion. It has to be kept in mind that carbon dioxide even has a higher quadrupole moment compared to nitrogen, so highly polar surface groups will strongly interact with the $CO_2$ molecules.[15]

The calculation of the sample's pore size distribution up to date is mainly based on density functional theory (DFT) or Monte Carlo simulation (MC). These methods are dependent on statistical mechanics of gases and fluids in confined spaces of porous systems. It is possible to precisely calculate the distribution of the physisorbed molecules or atoms under consideration of adsorptive-adsorbent interactions. Therefore, detailed models of adsorbents, adsorptives and pore geometry/shape have been developed (kernels). Based on these kernels for the specific adsorptive/adsorbent system, with the non-local-density functional theory (NLDFT) it is possible to calculate theoretical isotherms varying the system's pore widths at a given kernel. The program correlates the measured isotherm with the calculated isotherms and matches the best accordance to display the pore size distribution. As NLDFT neglects surface roughness and heterogeneity, quenched-solid-density functional theory (QSDFT) was developed.

Before these methods were developed, the pore size distribution was based on a modified and optimized Kelvin equations for example in the Barrett, Joyner and Halenda (BJH) approach. Nevertheless, the BJH underestimates the pore sizes systematically (< 10 nm up to 30 %).

The sample's pore volume can only be calculated, when the sample does not obtain macropores, as a, at least almost, horizontal progression of the isotherm in the upper range of $p/p^0$ is necessary. The total pore volume can be calculated from the totally adsorbed amount of nitrogen within the pores, the molecular mass and the density of the adsorptive.[15]

## 2.4 INFRARED SPECTROSCOPY

Infrared spectroscopy (IR spectroscopy) is based on the interaction of infrared radiation with matter. Molecules absorb infrared radiation with respect to their chemical structure. The respective resonant frequency of the absorption matches the rotational or vibrational excitation frequency. The frequencies are affected by the mass of the involved atoms as well as the types and strength of the chemical bonds (coupling) within the molecules. A vibrational mode can only be IR active, if the dipole moment changes during the vibration. The number of vibrational modes can be calculated by 3N-5 for linear molecules and with 3N-6 for non-linear molecules, where N represents the number of involved atoms. IR spectra range from near-IR (14000-4000 $cm^{-1}$, overtone or harmonic vibrations) over mid-IR (4000-400 $cm^{-1}$, fundamental vibrations) to far-IR (400-10 $cm^{-1}$, rotational spectroscopy), where the mid-IR range is mostly used for IR spectroscopy. The Fourier transformed infrared (FT-IR) spectroscopy technique can be used to access the IR spectra. Starting from the full spectrum of wavelengths, the beam of light passes a Michelson interferometer, a special arrangement of mirrors. By moving one of these mirrors, the resulting beam spectrum is modulated upon wave interference. After interacting with the sample, the respective beam spectrum is attenuated upon absorption and finally is detected. As each beam spectrum interacting with the sample contains a different combination of wavelengths, a computer can calculate the absorption of each wavelength and create the IR-spectrum. This technique allows for fast and accurate measurements in combination with a high signal-to-noise ratio (SNR).[16-17] IR spectra were recorded on a Perkin Elmer Spectrum BX II FT-IR system equipped with a diamond total reflection unit (ATR).

## 2.5 NUCLEAR MAGNETIC RESONANCE SPECTROSCOPY

Nuclear magnetic resonance spectroscopy (NMR) is used to determine magnetic fields in the environment of atomic nuclei of a sample allowing for the structural elucidation. All isotopes with an odd number of protons and/or neutrons exhibit an intrinsic magnetic moment. Therefore, the exposure of a sample containing non-zero spin (NMR-active, e.g. $^{1}H$, $^{13}C$, or $^{15}N$) nuclei to a strong constant magnetic field results in a polarization of their magnetic spins. By excitation with an electro-magnetic pulse perpendicular to the constant magnetic field, the local magnetic spins of the nuclei are perturbed. The required perturbation frequency (resonance frequency) of each nucleus depends on the local strength of the constant magnetic field, which is mainly influenced by shielding of surrounding shells of electrons of nearby nuclei. Furthermore, the resonance frequency depends on the gyromagnetic ratio, which describes the ratio between the magnetic dipole moment of the nucleus towards the spin. The detected amplitude is directly proportional to the concentration of the respective NMR-active nucleus. As both, the frequency as well as the amplitude, can be detected with a high degree of accuracy, NMR is a powerful technique for precise structural elucidation of molecules.[16] NMR measurements were conducted on a 400 MHz Bruker Avance III HD spectrometer.

## 2.6 THERMOGRAVIMETRIC ANALYSIS (TGA)

Thermogravimetric analysis (TGA) is very useful to characterize the composition and the thermal stability of an investigated sample. Therefore, the sample is exactly weighed in a non-reactive crucible (metal or metal-plated steel) and heated with a defined rate under a selected gas flow. The detected mass change occurs due to combustion, decomposition, dehydration, solvent evaporation or reduction/oxidation (phase transitions) in the course of time or depending on the temperature and is specific for the investigated system. Usually, either an inert gas (e.g. nitrogen or argon) or a synthetic air mixture as oxidant is used. In addition, a differential scanning calorimetry (DSC) can give information about enthalpy changes within the sample, independent of mass changes. Therefore, the energy is measured that is needed to heat or cool the sample in comparison to an inert reference in another crucible under the same conditions. By this investigation, it is possible to distinguish between endothermic processes (evaporation, phase transformation) and exothermic processes (combustion, recrystallization).[18]

The synthesized COFs were characterized by TGA to determine their thermal stability on a NETZSCH STA 440 C TG/DSC (heating rate of 10 °C $min^{-1}$ in a stream of synthetic air or nitrogen of about 25 mL $min^{-1}$).

## 2.7 UV/VIS SPECTROSCOPY

To measure the absorbance of a sample in the ultraviolet (10 – 400 nm) and in the visible light region (400 - 700 nm), ultraviolet-visible (UV-Vis) spectroscopy is used.[19] The electromagnetic UV-Vis radiation interacts with absorbing matters resulting in electronic transitions (electrons become excited from the ground state to a higher energy state). Besides liquid samples, solids can be investigated quantitatively as well as qualitatively by absorption. Therefore, the intensity of light passing through the sample cell ($I$) and a reference cell ($I_0$) is measured for each wavelength, respectively. The transmittance $T$ in % is the quotient of the intensities of $I$ divided by $I_0$. From $T$ the absorbance $A$ can be directly calculated according to Equation 2.4.

$$A = -log_{10}\frac{I_0}{I} \tag{2.4}$$

In contrast, the absorption (X) can be calculated by measuring the transmittance and the reflection ($R$) of films grown on a non-absorbing substrate like quartz, as described in Equation 2.5.

$$X = 100 - R - T \tag{2.5}$$

In this thesis UV-Vis spectroscopy was used to measure the absorbance, reflectance and the transmittance of powders and films on quartz. For the powder measurement, pure barium sulfate was used as a reference standard for diffused reflectance. For the measurement a small amount of the sample was ground with barium sulfate to access a measurable mixture. The samples were measured on a PerkinElmer Lambda 1050 spectrophotometer equipped with an integrating sphere (films) or a Praying Mantis (powders).

## 2.8 STEADY STATE PHOTOLUMINESCENCE

Photo-excitation of an electron in a semiconductor or in a chromophore results in an excitation from the ground state to an excited state energy level. Through non-radiative relaxation, for example dissipation as heat, the vibrational ground state of the excited state will be occupied. The comparably larger energy difference between ground state and excited state (band gap) will most probably be overcome by emission of a photon (Figure 2.8). This emission can be detected as steady state photoluminescence (ssPL) and is very informative concerning the energy levels of the sample.[20]

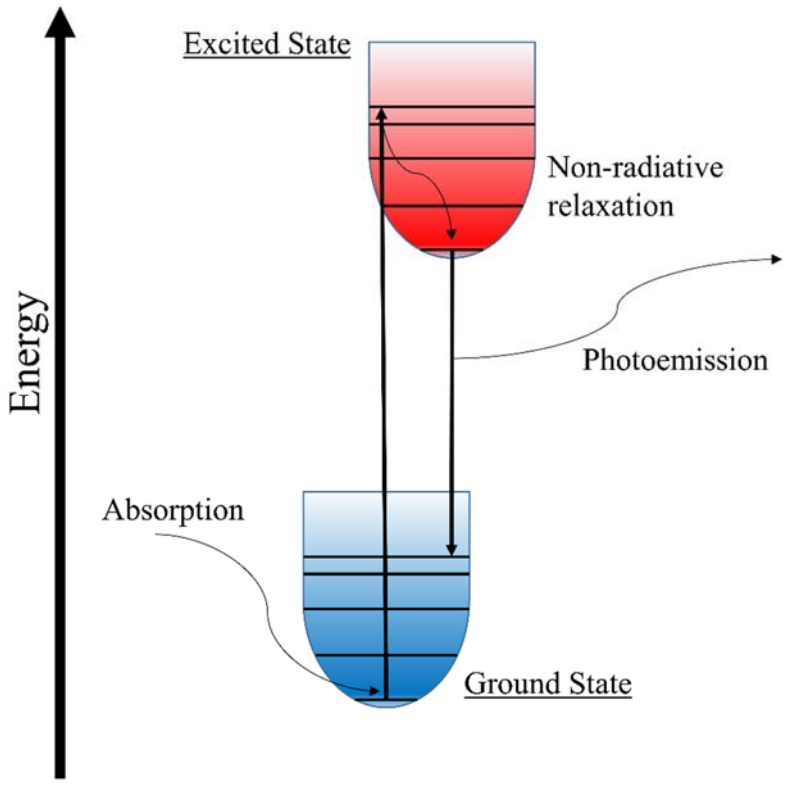


Figure 2.8: Schematic representation of photoemission induced by absorption and relaxation processes.

## 2.9 TIME CORRELATED SINGLE PHOTON COUNTING

As for ssPL, time correlated single photon counting (TCSPC), is used to detect photoluminescence. While ssPL only allows for gaining information about the intensity and the absolute energy of the emitted photons, with TCSPC time-resolved kinetics of the photo-emission of the band-edge can be recorded. The sample is excited by a pulsed laser source. The time between pulse and detection of a photon can be precisely and repetitively measured. With this measurement technique, lifetimes of the excited species can be connected to a statistical analysis. The energy of the laser must be weak enough to result in not more than one photoemission per pulse. The laser usually is pulsed at frequencies between 100 kHz and 80 MHz resulting in a multitude of individual single photon emissions and detections. Every decay time is measured and sorted in a histogram (Figure 2.9). The usually exponential decay over time can be fitted with an appropriate matching function to gain the half-life time of the different lifetime components.[21]

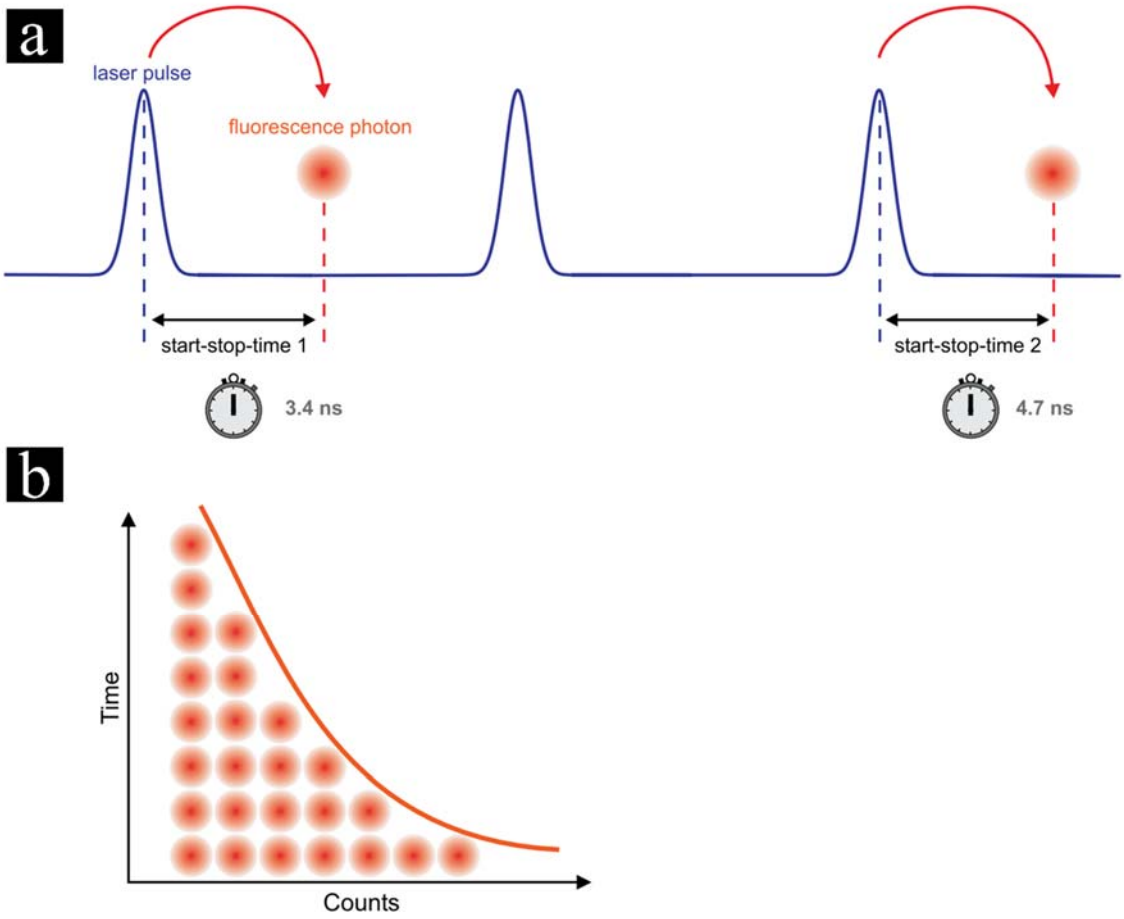


Figure 2.9: Schematic representation of a) time-resolved fluorescence measurement with TCSPC with start and stop times and b) resulting histogram of start-stop times in a time-resolved fluorescence measurement with TCSPC.[21]

Time-resolved PL measurements were acquired using a time correlated single photon counting (TCSPC) setup (FluoTime 300, PicoQuant GmbH). The samples were photo-excited using lasers with suitable wavelengths according to the sample absorption, i.e. 378 nm, 403 nm or 507 nm wavelengths (LDH-P-C-375, LDH-P-C-405, and LDH-P-C-510, respectively, all from PicoQuant GmbH) pulsed at 500 kHz, with a pulse duration of ~100 ps and fluence of ~ 300 nJ $cm^{-2}$/pulse. The samples were exposed to the pulsed light source set at 3 μJ $cm^{-2}$/pulse fluence for ~ 10 minutes prior to measurement to ensure stable sample emission. The PL was collected using a high-resolution monochromator and photomultiplier detector assembly (PMA-C 192-N-M, PicoQuant GmbH).

Photoluminescence (ssPL) measurements were performed using a home-built setup consisting of a Horiba Jobin Yvon iHR 320 monochromator equipped with a photomultiplier tube and a liquid $N_2$-cooled InGaAs detector. The samples were illuminated with a pulsed (83 Hz) 365 nm or 405 nm LED at a light intensity of 500 mW $cm^{-2}$.

# 2.10 REFERENCES

(1) Spiess, L. T., G.; Schwarzer, R.; Behnken, H.; Genzel, C., *Moderne Röntgenbeugung - Röntgendiffraktometrie für Materialwissenschaftler, Physiker und Chemiker*. Vieweg+Teubner Verlag: 2009; Vol. 2, p 321.

(2) Waseda, Y.; Matsubara, E.; Shinoda, K., *X-Ray Diffraction Crystallography*. Springer-Verlag Berlin Heidelberg: 2011.

(3) Holzwarth, U.; Gibson, N., *Nat Nanotechnol* **2011**, *6*, 534.

(4) Scherrer, P., *Nachrichten von der Gesellschaft der Wissenschaften zu Göttingen, Mathematisch-Physikalische Klasse* **1918**.

(5) Levine, J. R.; Cohen, J. B.; Chung, Y. W.; Georgopoulos, P., *J. Appl. Crystallogr.* **1989**, *22*, 528-532.

(6) Metzger, T. H.; Kegel, I.; Paniago, R.; Lorke, A.; Peisl, J.; Schulze, J.; Eisele, I.; Schittenhelm, P.; Abstreiter, G., *Thin Solid Films* **1998**, *336*, 1-8.

(7) Williams, D. B. C., Berry Carter, C., *Transmission Electron Microscopy - A Textbook for Materials Science*. Springer US: 2009; Vol. 2nd, p 775.

(8) Nishiyama, H.; Ohshima, T.; Shinada, H., *Appl. Surf. Sci.* **1999**, *146*, 382-386.

(9) Fultz, B.; Howe, J. M., *Transmission Electron Microscopy and Diffractometry of Materials*. Springer-Verlag Berlin Heidelberg: 2013; Vol. 4.

(10) Brandon, D. K., W. D., *Microstructural Characterization of Materials*. 2008; p 550.

(11) Goodhew, P. J., *Electron Microscopy and Analysis, Third Edition*. 3 ed.; Crc press: 2000; p 264.

(12) http://www.ammrf.org.au/myscope/images/sem/volumes08.png.

(13) Goldstein, J. I.; Newbury, D. E.; Michael, J. R.; Ritchie, N. W. M.; Scott, J. H. J.; Joy, D., *Scanning Electron Microscopy and X-Ray Microanalysis*. 4 ed.; Springer-Verlag: New York, 2018; p 550.

(14) Reimer, L., *Scanning Electron Microscopy - Physics of Image Formation and Microanalysis*. Springer-Verlag Berlin Heidelberg: 1998; Vol. 45, p 529.

(15) Thommes, M.; Kaneko, K.; Neimark, A. V.; Olivier, J. P.; Rodriguez-Reinoso, F.; Rouquerol, J.; Sing, K. S. W., *Pure Appl. Chem.* **2015**, *87*, 929-1069.

(16) Hesse, M. M., Herbert; Zeeh, Bernd, *Spektroskopische Methoden in der organischen Chemie*. Thieme: Stuttgart, 2005; Vol. 7, p 468.

(17) Hollas, J. M., *Modern Spectroscopy*. John Wiley & Sons Ltd: Chichester, 2004; Vol. 4, p 482.

(18) Skoog, D. A. H., F. J.; Crouch, S. R., *Principles of Instrumental Analysis*. Thomson Brooks/Cole: 2007; p 1039.

(19) Clark, B. J. F., T.; Russell, M. A., *UV Spectroscopy - Techniques, instrumentation and data handling*. Springer Netherlands: 1993; Vol. 1, p 146.

(20) Lacowicz, J. R., *Principles of Fluorescence Spectroscopy*. Springer US: 2006; p 954.

(21) Wahl, M. *Technical Note: Time-Correlated Single Photon Counting (TCSPC)*; 2014.

# 3. FROM HIGHLY CRYSTALLINE TO OUTER SURFACE FUNCTIONALIZED COVALENT ORGANIC FRAMEWORKS – A MODULATION APPROACH

This chapter is based on the following publication:

Mona Calik, ‡ Torben Sick, ‡ Mirjam Dogru, Markus Döblinger, Stefan Datz, Harald Budde, Achim Hartschuh, Florian Auras, Thomas Bein*

*J. Am. Chem. Soc.* **2016**, *138* (4), 1234–1239.

## 3.1 ABSTRACT

Crystallinity and porosity are of central importance for many properties of covalent organic frameworks (COFs) including adsorption, diffusion, and electronic transport. We have developed a new method for strongly enhancing both aspects through the introduction of a modulating agent in the synthesis. This modulator competes with one of the building blocks during the solvothermal COF growth, resulting in highly crystalline frameworks with greatly increased domain sizes reaching several hundreds of nanometers. The obtained materials feature fully accessible pores with an internal surface area of over 2000 $m^2g^{-1}$. Compositional analysis via NMR spectroscopy revealed that the COF-5 structure can form over a wide range of boronic acid to catechol ratios, spanning from highly boronic acid-deficient frameworks to networks with catechol voids. Visualization of an -SH functionalized modulating agent via iridium staining revealed that the COF domains are terminated by the modulator. Using functionalized modulators, this synthetic approach thus also provides a new and facile method for the external surface functionalization of COF domains, providing accessible sites for post-synthetic modification reactions. We demonstrate the feasibility of this concept by covalently attaching fluorescent dyes and hydrophilic polymers to the COF surface. We anticipate that the realization of highly crystalline COFs with the option of additional surface functionality will

render the modulation concept beneficial for a range of applications including gas separations, catalysis, and optoelectronics.

## 3.2 INTRODUCTION

Covalent organic frameworks (COFs) represent an emerging class of crystalline, porous materials exhibiting unique structural and functional diversity. By combining multidentate building blocks via covalent bonds, two- or three-dimensional frameworks with defined pore size and high specific surface area in conjunction with appreciable thermal and chemical stability can be constructed.[1-2] Depending on their topology and functionality, these reticular materials are promising candidates for various applications, such as gas adsorption[3-4], separation[5-6], catalysis[7-8], proton conduction[9], energy storage[10] and optoelectronics.[11-15]

In the context of the latter applications COFs consisting of two-dimensional layers (2D COFs) are of particular interest. These frameworks are realized by combining virtually planar building units into extended two-dimensional sheets, which assemble via dispersive forces (π-stacking) into highly anisotropic porous, crystalline materials. While the topology of a COF can be pre-designed via the geometry of its building blocks, the actual formation of a long-range ordered network relies on the reversibility of the covalent bond formation. Only if the reaction conditions are chosen such that the covalent bonds can be formed, broken and reformed at a sufficiently high rate, thus providing a functional 'self-healing' mechanism, will crystalline frameworks be obtained. COF syntheses have predominantly been realized through reversible condensation reactions, including the formation of B-O bonds (boroxines, boronic esters[16-18] and borosilicates[19]), imines[20-21], imides[22-23] and others[24-26].

While the optimization of the COF growth conditions can produce fairly crystalline frameworks, the realization of particularly well-ordered COFs with large domain sizes requires an even higher degree of synthetic control.

The effects of ligands on the nucleation, growth, and properties of materials have been studied extensively for metal[27] and inorganic semiconductor nanocrystals[28-29]. Also, nanoparticles of coordination polymers have been modified by the addition of surfactants and capping agents.[30] In the field of metal-organic frameworks (MOFs) modulation concepts, which utilize the competition between the bridging ligands and a mono-functionalized terminating ligand, have proven very successful. Enabling the adjustment of growth kinetics and energies of specific

crystal facets via selection of the modulator, this approach has been demonstrated to allow for the growth of highly crystalline MOFs with tailored morphology and domain sizes.[31-34]

Dichtel's group recently demonstrated that 3D COFs can be functionalized internally by adding truncated building blocks bearing functional groups to the synthesis mixture.[35-37] Growth rates of 2D COFs have been studied depending on the monomer reactivity and solvent mixtures.[38-40]

In this work, we transfer the modulation concept to the synthesis of a 2D COF. Applying monoboronic acids as a modulator in the solvothermal synthesis of the archetypical COF-5 we are able to influence and optimize the crystallinity, domain size, and porosity of the resulting framework. Moreover, the addition of phenylboronic acids bearing a functional group opens up a novel, convenient way for the surface functionalization of COF crystallites, which can be used for subsequent modifications, such as the attachment of dyes or polymers.

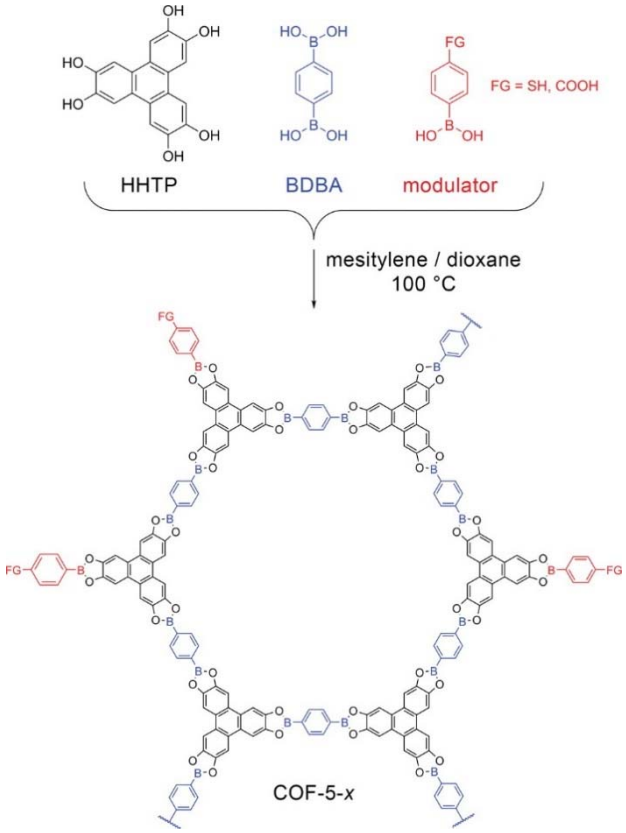


Figure 3.1: Synthesis of COF-5-x via a co-condensation reaction of benzene-1,4-diboronic acid (blue) and 2,3,6,7,10,11-hexahydroxytriphenylene (black) in the presence of 4-mercaptophenylboronic acid (red) as modulating agent.

## 3.3 RESULTS AND DISCUSSION

The hexagonal COF-5 was synthesized via a microwave-assisted co-condensation of 2,3,6,7,10,11 hexahydroxytriphenylene (HHTP) with 1.5 equivalents of benzene-1,4-diboronic acid (BDBA) in a 1:1 solvent mixture of mesitylene and 1,4-dioxane (Figure 3.1). When a modulating agent was used in the synthesis, 2 equivalents of the modulator (denoted as COF-5-x, where x is expressed in %) were substituted for a fraction x of BDBA, thus keeping the amount of boronic acid groups in the reaction mixture constant. In our study the degree of substitution was systematically varied from 0 to 70%.

As a first example for a modulating agent we chose 4-mercaptophenylboronic acid (MPBA), as its size, shape and solubility are similar to BDBA. Additionally, its thiol group provides a way of detecting the incorporated modulator (see below).

The influence of the modulator on the COF-5 crystallinity was monitored by powder X-ray diffraction (PXRD) analysis (Figure 3.2a). Successful formation of the COF-5 framework was observed up to x = 60. We found that the introduction of small amounts of the modulating agent led to an enhanced crystallinity of the resulting COF, as evidenced by a sharpening of the reflections. The COF-5-5 and COF-5-10 samples exhibit a series of particularly sharp reflections and a number of higher-order reflections, indicating the presence of large crystalline domains with a very low concentration of defects (Figure S 3.6). The XRD patterns can be indexed assuming a hexagonal P6/mmm-symmetry (Figure 3.2b and Figure S 3.4a). Small deviations from this idealized model, i.e. a tilt of the bridging phenyl groups (P-3, Figure S 3.4b) or a serrated rather than a fully eclipsed layer arrangement (Cmcm, Figure S 3.4c) would produce nearly identical patterns and thus cannot be identified based on the experimental data (Figure S 3.5). Pawley refinement of the experimental data applying the P6/mmm-symmetric model produced lattice parameters of a = b = 2.98 ± 0.02 nm and c = 0.35 ± 0.01 nm.

COF-5 has been reported to be highly porous with a Brunauer–Emmett–Teller (BET) surface area of up to 1590 $m^2g^{-1}$ and a pore volume of 0.998 $cm^3g^{-1}$ (Figure 3.2c).[1] Nitrogen sorption experiments carried out for the COF-5-x series reveal a close correlation of the surface area and pore volume with the crystallinity of the frameworks (Figure 3.2d,e). While in our hands the modulator-free synthesis produced frameworks with a surface area of 1200 $m^2g^{-1}$ and a pore volume of 0.64 $cm^3g^{-1}$, the substitution of the modulator for 10% of the BDDA increased the surface area to 2100 $m^2g^{-1}$ at a pore volume of 1.14 $cm^3g^{-1}$. This represents an increase of 32% in surface area when compared to literature values and 75% when compared to our own data

for the modulator-free COF-5-0. Moreover, these values are close to the theoretical Connolly surface area and pore volume (2130 $m^2g^{-1}$ and 1.21 $cm^3g^{-1}$, respectively), indicating the realization of a highly crystalline network with fully open and accessible pores. Furthermore, the distinct step in the sorption isotherms at $p/p^0 = 0.1$ underlines the very well-defined porosity of this material.[41-43] A further increase of the modulator content above x = 10 led to a gradual decrease in surface area and pore volume. The shape of the obtained isotherms also changes upon the substitution. COF-5-0 and the COF-5-10 exhibit the typical sharp increase at $p/p^0$ = 0.1 that is caused by the simultaneous pore condensation in the uniformly sized pores. The samples grown at a higher modulator concentration, COF-5-25, COF-5-50 and COF-5-60, however, display an increasingly broadened slope, suggesting less uniform pores and an increasing contribution of textural porosity. This trend is also reflected in the corresponding pore size distributions determined by quenched solid density functional theory (QSDFT) calculations (Figure S 3.10).

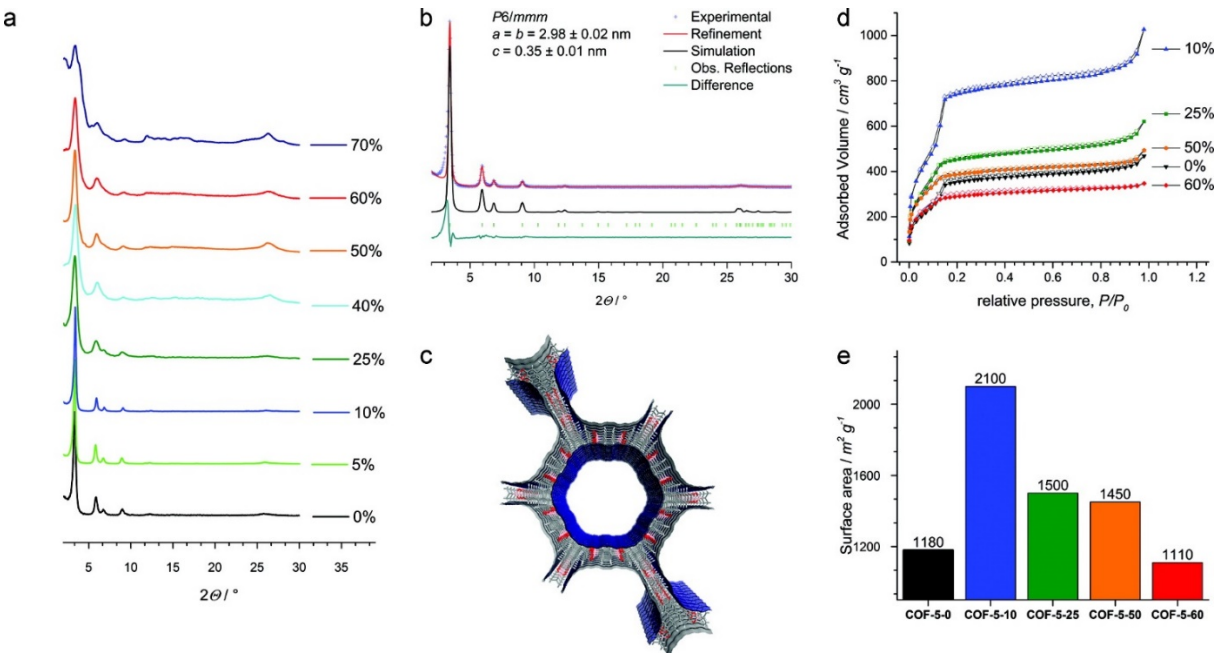


Figure 3.2: (a) Comparison of the PXRD patterns of the COF-5-x series. (b) Pawley refinement assuming P6/mmm symmetry (red) of the COF-5-10 PXRD pattern (blue), simulated pattern (black), reflection positions (green) and difference plot (dark green). (c) Illustration of COF-5 showing the hexagonal pores and the Connolly surface (blue). (d) Nitrogen sorption isotherms of the COF-5-x series recorded at 77 K. (e) BET surface areas obtained from the nitrogen sorption experiments.

Transmission electron microscopy (TEM) images of the COF grown at several modulator contents underline the influence of the MPBA on the resulting material. While COF-5-0 is composed of intergrown domains that are 30-50 nm in size (Figure 3.3a), the domains of COF-

5-10 can extend to hundreds of nanometers (Figure 3.3b). Depending on the orientation of a domain, either the hexagonal arrangement of the pores or straight porous channels are visible. Increased content of the modulator results in an apparent deterioration of the structural quality and a decrease of the domain size to only 15-20 nm for COF-5-25, which we attribute primarily to the depletion of the bridging diboronic acid in the reaction mixture (Figure 3.3c).

Based on these experimental findings we propose the following mechanism for the modulator-assisted COF growth:

The modulator acts as a capping agent for the developing COF, terminating the 2D sheets during lateral growth. By repetitive attachment and detachment, the modulator slows the COF formation. The COF crystals thus experience an increased number of precipitation and dissolution steps, thus facilitating the healing of defects and bringing the system closer to thermodynamic equilibrium. Moreover, the modulator can saturate point or line defects, such as partially unreacted building blocks and dislocations, thus reducing strain in the crystal and allowing for a more stable overall crystal conformation. Consequently, adding small amounts of the modulator enables the formation of very large and highly crystalline COF domains.

In order to gain further insights into the formation mechanism, we compared the growth kinetics of unmodulated and modulated COF-5 (Figure S 3.9). In absence of a modulator, the first reflections of the COF appear already after 0.5 h. After 4 h all of the starting material has been consumed and the crystallinity increases only moderately over the next 92 h (Figure S 3.9a). If 10 % MPBA is used in the synthesis, the COF formation is slowed down appreciably, while the reflections of the starting material disappear faster (Figure S 3.9b). First very weak reflections appear after 1 h but remain considerably weaker than the corresponding ones of the unmodulated sample for the next hours. Only after 16 h the same reflection intensity is reached, and the crystallinity of the modulated sample outperforms the unmodulated sample thereafter. The same trend was also observed for CPBA as modulator (Figure S 3.9c).

As the COF formation is thermodynamically favored over the precipitation of oligomers that might block the porous channels, we expect the modulator-assisted synthesis to produce COFs with very high porosity. Indeed, the surface area and pore volume are the highest for the modulator contents that yield the most crystalline COFs. Also, porosity values that are close to the theoretical maximum were achieved without an activation procedure, during which precipitated reactants and oligomers are digested and washed away.

From the above considerations, some of the modulator is expected to incorporate into the crystal structure at high modulator concentration. For a quantitative compositional analysis, the COF-5 samples grown at different modulator concentrations were dissolved by adding pinacol in deuterated DMSO. The proton NMR signals of HHTP, pinacol-terminated BDBA and the pinacol-terminated modulators (MPBA or CPBA) were found to be sufficiently separated to allow for a quantification of the COF constituents.

For the highly ordered COF-5-x samples ($x \leq 10$) no modulator was detected (Figure S 3.1 – S 3.3). As the surface to volume ratio is very small for the relatively large domains of COF-5-5 and COF-5-10, the amount of modulator that could be attached to the outer surface would be below the detection limit of this method. Starting from $x = 25$ we observe an advancing incorporation of the modulator into the structure, reaching a BDBA:MPBA ratio of 1:1 for $x = 60$ (SI, Table S4).

The HHTP:BDBA ratio reveals striking deviations from the expected 2:3 molecular composition of the idealized COF-5 structure. In the absence of the modulator, we observe a 6:4.3 ratio of the aryl proton integrals, corresponding to a 1:1.1 molar ratio of the two building blocks. This BDBA deficiency requires a significant amount of voids to be incorporated into the COF structure. Indeed, the pore size distribution of COF-5-0 features an additional contribution of smaller pores around 20 Å (Figure S 3.11).

The composition of COF-5-10, which exhibits the highest degree of order, was found to be very close to the theoretical HHTP:BDBA molar ratio. In line with this observation, this material does not possess any porosity in addition to the hexagonal porous channels.

Increasing the modulator content in the reaction mixture leads to a gradual decrease of the incorporated BDBA, which is, however, fully balanced by the increasing incorporation of the modulator. The overall HHTP:boronic acid group ratio remains constant at 1:3, indicating that all OH groups were saturated in the framework (SI, Table S4). As the space occupied by the diboronic acid in the framework is too small to accommodate two molecules of the modulator, the observed amount of modulator can only be incorporated alongside with HHTP voids (Figure S 3.12). This would cause additional small pores inside the COF walls, which are indeed observed in the pore size distributions of COF-5-25, -50, and -60 (Figure S 3.11).

In addition to the non-specific incorporation at high modulator concentration in the synthesis mixture, we expect the modulator, acting as capping agent for the growing crystal domains, to accumulate at grain boundaries. Due to the instability of the framework at large TEM probe

currents, a direct determination of the –SH distribution inside the framework via energy-dispersive X-ray (EDX) analysis was not possible. Therefore, an indirect method was chosen, where the –SH groups that are pointing into free space were stained with iridium clusters (Figure S 3.10a) and visualized by scanning TEM in high angle annular dark field mode (STEM-HAADF) imaging.[44] (for further information see the SI, Section 2). In STEM-HAADF images, the intensity distribution is approximately proportional to the square of the atomic number. By overlaying the STEM-HAADF images and TEM images, recorded at the same sample positions, an accumulation of Ir-clusters at grain boundaries, with respect to the crystal domains, was observable as white dots (Figure 3.3d-f). A COF-5-0 sample that does not feature the -SH functionalization did not show any preferred localization of the iridium clusters but a random distribution within the network (Figure S 3.17).

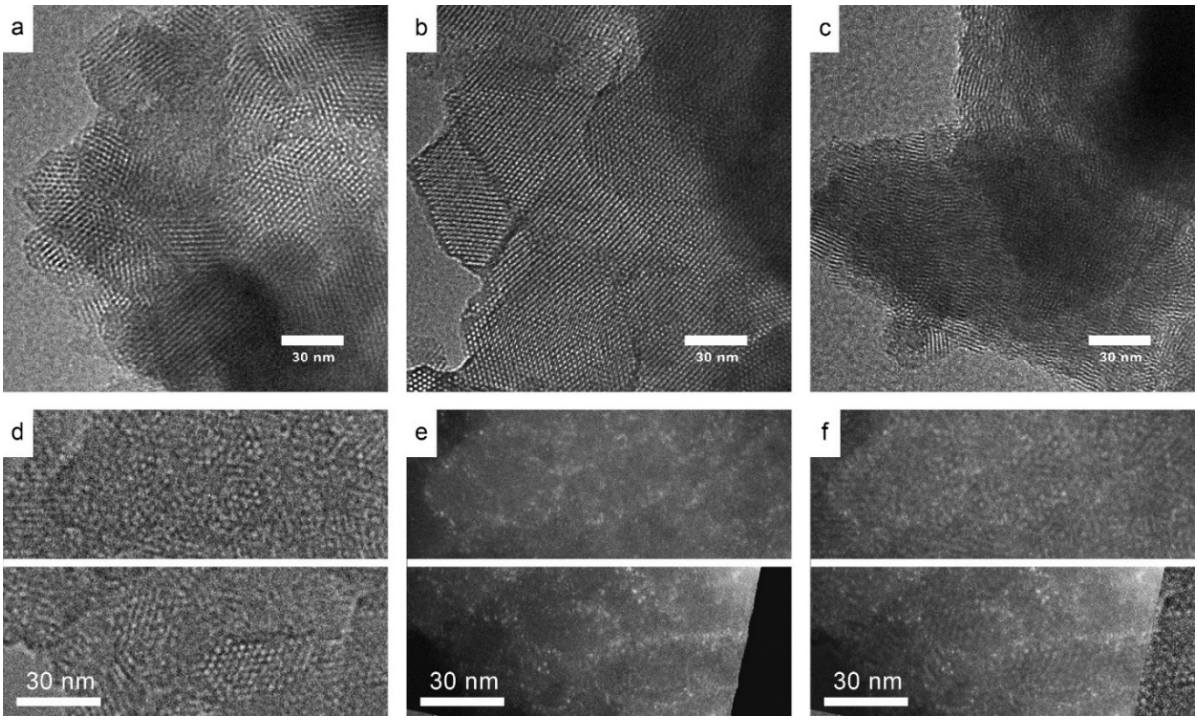


Figure 3.3: TEM micrographs of (a) COF-5-0, (b) COF-5-10 and (c) COF-5-25. (d)TEM micrographs of COF-5-10 stained with iridium at two different sample positions. (e) Corresponding scanning transmission electron microscopy (STEM) micrographs of the same sample positions (f) Overlay of TEM and STEM micrographs of COF-5-10 showing the increased Ir occurrence at the grain boundaries of the crystallite domains.

Having studied the effect of substituting an -SH functionalized modulator for a fraction of the diboronic acid, we asked whether a similar effect on the COF crystallization was also achievable with phenylboronic acids bearing other functional groups. Introducing carboxyphenyl boronic acid (CPBA) as modulating agent resulted in the same increase in

domain size up to x = 10 followed by a gradual decrease as the modulator content was increased beyond 10% (Figure S 3.7). The application of the non-functionalized phenylboronic acid as modulator, however, did not produce crystalline COFs, possibly due to a different solubility and polarity.

The above substitution approach proved to be very sensitive to the modulator concentration and led to small domains for x > 10, which we attribute primarily to an increasingly unfavorable ratio between the bridging diboronic acid and the terminating monoboronic acid. In order to allow for high modulator contents, thus ensuring optimal reaction control, but at the same time provide enough diboronic acid to form extended networks, we tested the addition of variable amounts of the modulating agent to a stoichiometric reaction mixture of HHTP and BDBA. The addition of CPBA to a 2:3 mixture of HHTP and BDBA resulted in improved crystallinity with the optimal modulator:BDBA ratio being at 3:10 (Figure S 3.8). Optimal crystallinity of the COF was achieved at slightly higher modulator:BDBA ratio than for the substitution approach (i.e. 2:9 corresponding to 10 % substitution), while the resulting domain sizes and the general trends were very similar.

Post-functionalization of framework materials typically includes the risk of sample decomposition or the loss of crystallinity. In the case of 2D COFs, the delamination of the π-stacked, and thus comparably weakly interacting layers can be an issue of particular importance. Moreover, sterically demanding functional groups might prove very difficult to incorporate into close-packed 2D COFs and to convert in post-modification reactions. In cases where a modification on the outer surface of a COF domain is sufficient, the use of functionalized modulators during the COF synthesis can provide a convenient and versatile alternative. As discussed above the modulator is expressed at the outer surface of individual COF crystallites. Thus, the functional group of a para-substituted modulator, such as MPBA or CPBA, will be pointing away from the COF, rendering it easily accessible for subsequent reactions.

As a first example for illustrating this concept we chose the attachment of a fluorescent dye to the carboxylic acid functionalized CPBA-modulated COF-5-10 surface. The N-ethyl-N'-(3-dimethylaminopropyl)carbodiimide hydrochloride (EDC) activated -COOH groups were found to react readily at room temperature with the amino functionalized ATTO633 dye. Any unreacted, not covalently bound dye was removed by extensive washing prior to the measurements. PXRD measurements confirmed that the crystallinity had been fully retained during this process (Figure S 3.10b). The newly formed amide bond was identified via IR spectroscopy (Figure S 3.13a). Moreover, the presence of the dye was confirmed via UV-VIS

diffuse reflectance measurements (Figure S 3.15). While the COF-5-COOH absorbs strongly at wavelengths below 400 nm, its absorption in the visible range is very low and free of spectral features. The attachment of the dye gives rise to an increased absorption between 400 and 600 nm with a distinct absorption feature at 643 nm. The successful attachment of the dye was further confirmed via photoluminescence measurements (Figure S 3.16). Upon excitation with a HeNe laser at 633 nm the ATTO633 modified COF exhibits a broad emission centered at 766 nm. As expected for a dye that is immobilized at a surface both the absorption and emission spectra are broadened and red-shifted versus the respective spectra of the dye in solution.[45]

This strategy can also be used to coat the COF crystallites with a shell of a different material, thus altering properties like stability, dispersibility, or bio-compatibility. Methoxypolyethylene glycol maleimide (PEG-maleimide) was successfully attached to MPBA-modified COF-5-10 via a Michael-type addition (Figure S 3.13b).[46] While the bare COF-5-x is not stable towards alcohols, the PEG-modified material was found to retain its crystallinity upon soaking in ethanol. The corresponding PXRD pattern does not show any loss in crystallinity, whereas the non-functionalized COF-5-10 sample degrades rapidly (Figure S 3.10c).

## 3.4 CONCLUSION

We have developed a modulation strategy for the growth of highly crystalline COFs with large domains and very high porosity. The competition between the bridging COF building block and the terminating modulation agent was found to influence the dynamic equilibrium during framework formation, slowing down the COF growth and supporting the self-healing of crystal defects. Under optimized conditions, the crystal domains of the boronic ester-linked COF-5 reached several hundreds of nanometers. The pores of the framework were found to be open and fully accessible even without any activation procedure, which is reflected by a surface area close to the theoretical maximum and a very narrow pore size distribution.

Compositional analysis via NMR revealed that the COF-5 structure forms over a wide range of molecular compositions, from highly diboronic acid-deficient frameworks to networks comprising an excess of the linear building block.

The use of functionalized modulating agents furthermore provides a new strategy for functionalizing the outer surface of COF crystallites. These functional groups were found to be accessible for the subsequent covalent attachment of molecules or polymers, allowing for further modification of the chemical, physical, or electronic properties of the COF.

The combination of an enhanced degree of crystallinity and the option for an outer surface post-modification of COF domains might prove beneficial for a range of applications, such as gas separation, catalysis, superresolution imaging, and optoelectronics.

# 3.5 SUPPORTING INFORMATION

Abbreviations

BET = Brunauer, Emmett, Teller; BDBA = Benzene-1,4-diboronic acid; CC = column chromatography; CPBA = 4-carboxyphenylboronic acid; FT = Fourier transform; FWHM = full width at half maximum; HHTP = 2,3,6,7,10,11-hexahydroxytriphenylene; MPBA = 4-mercaptophenylboronic acid; PXRD = powder X-ray diffraction; QSDFT = quenched solid density functional theory; rcf = relative centrifugal force; RT = room temperature; THF = tetrahydrofuran.

**Section 1: Materials and Methods**

All reagents and solvents were obtained from commercial suppliers and used as received.

Benzene-1,4-diboronic acid (BDBA, ≥95%, Sigma-Aldrich), 4-carboxyphenylboronic acid (CPBA, Sigma-Aldrich), 2,3,6,7,10,11-hexahydroxytriphenylene hydrate (HHTP, >95%, TCI) and 4-mercaptophenylboronic acid (MPBA, 90%, Sigma-Aldrich) were used without further purification.

**Nuclear magnetic resonance (NMR)** spectra were recorded on Bruker AV 400 and AV 400 TR spectrometers. Proton chemical shifts are expressed in parts per million (δ scale) and are calibrated using residual undeuterated solvent peaks as an internal reference (DMSO-d6: 2.50).

**Infrared (IR)** spectra were recorded on a Perkin Elmer Spectrum BX II FT-IR system and a Thermo Scientific Nicolet™ 6700 FT-IR spectrometer in transmission mode. IR data are reported in wavenumbers ($cm^{-1}$).

**UV-Vis spectra** were recorded using a Perkin-Elmer Lambda 1050 spectrometer equipped with a 150 mm integrating sphere. Diffuse reflection measurements of COF powders were performed with a Harrick Praying Mantis accessory and referenced to $BaSO_4$.

For the **photoluminescence measurements** the COF powder was deposited on a glass slide. A 60x oil immersion objective with high numerical aperture (NA=1.49) was used in backscattering geometry to focus the laser beam onto the sample and to collect the emitted light. The samples were excited using a linearly polarized HeNe laser (λexc = 632.8 nm). Photoluminescence spectra were recorded using a multichannel spectrometer equipped with a 633 nm longpass filter.

**Nitrogen sorption isotherms** were recorded on a Quantachrome Autosorb 1 at 77 K within a pressure range from $p/p^0$ = 0.001 to 0.98. Prior to the measurement of the sorption isotherms the samples were heated for 24 h at 120°C under turbo-pumped vacuum. For the evaluation of the surface area the BET model was applied between 0.05 and 0.2 $p/p^0$. Pore size distributions were calculated using the QSDFT equilibrium model with a carbon kernel for cylindrical pores.

**X-ray diffraction (XRD)** measurements were performed using a Bruker D8 Discover with Ni-filtered Cu Kα radiation and a LynxEye position-sensitive detector.

**Transmission electron microscopy (TEM)** and **scanning transmission electron microscopy (STEM)** were performed on a Titan Themis at 300 kV. For STEM-HAADF, a camera length of 130 mm and a semi-convergence angle of 16.6. mrad were chosen.

## Section 2: Syntheses

### COF-5 Modulation with MPBA - COF-5-x (SH)

A 10 mL microwave glass tube was equipped with BDBA, HHTP and MPBA according to Table S1. The reagents were suspended in 4 mL of a mixture of 1,4-dioxane and mesitylene (2 mL : 2 mL). The reaction mixture was sonicated for 5 min. Afterwards, the sealed flask was placed in a microwave and heated for 1 h at 100 °C with 300 W. The gray solid product was isolated by filtration, washed with 1,4-dioxane and dried under vacuum. For the gas sorption measurement, the product was heated to 120 °C for 1 d under dynamic vacuum.

**Table 3.1** Applied initial weights for the syntheses of COF-5-x with MPBA as modulator.

| x [%] | molar ratios | BDBA [mg] | BDBA [mmol] | HHTP [mg] | HHTP [mmol] | MPBA [mg] | MPBA [mmol] |
|---|---|---|---|---|---|---|---|
| **0** | 3.00 : 2 : 0.0 | 18.7 | 0.113 | 24.3 | 0.075 | 0.0 | 0.000 |
| **5** | 2.85 : 2 : 0.3 | 17.7 | 0.107 | 24.3 | 0.075 | 1.7 | 0.011 |
| **10** | 2.70 : 2 : 0.6 | 16.8 | 0.101 | 24.3 | 0.075 | 3.5 | 0.023 |
| **25** | 2.25 : 2 : 1.5 | 14.0 | 0.084 | 24.3 | 0.075 | 6.9 | 0.056 |
| **40** | 1.80 : 2 : 2.4 | 13.1 | 0.068 | 24.3 | 0.075 | 10.4 | 0.090 |
| **50** | 1.50 : 2 : 3.0 | 9.30 | 0.056 | 24.3 | 0.075 | 17.3 | 0.112 |
| **60** | 1.20 : 2 : 3.6 | 7.5 | 0.045 | 24.3 | 0.075 | 20.8 | 0.135 |
| **70** | 0.90 : 2 : 4.2 | 5.6 | 0.034 | 24.3 | 0.075 | 24.3 | 0.158 |

### COF-5 Modulation with CPBA - COF-5-x (COOH)

The synthesis of COF-5-x in the presence of CPBA as modulating agent was carried out following the procedure described above. BDBA, HHTP and CPBA were added to the reaction tube according to Table S2. The gray products were isolated by filtration and after washing with 1,4-dioxane dried under vacuum.

**Table 3.2** Applied initial weights for the syntheses of COF-5-x with CPBA as modulator.

| x [%] | molar ratios | BDBA [mg] | BDBA [mmol] | HHTP [mg] | HHTP [mmol] | CPBA [mg] | CPBA [mmol] |
|---|---|---|---|---|---|---|---|
| **0** | 3.00 : 2 : 0.0 | 18.7 | 0.113 | 24.3 | 0.075 | 0.0 | 0.000 |
| **5** | 2.85 : 2 : 0.3 | 17.7 | 0.107 | 24.3 | 0.075 | 1.9 | 0.011 |
| **10** | 2.70 : 2 : 0.6 | 16.8 | 0.101 | 24.3 | 0.075 | 3.7 | 0.023 |
| **15** | 2.55 : 2 : 0.9 | 15.9 | 0.096 | 24.3 | 0.075 | 5.6 | 0.034 |
| **20** | 2.40 : 2 : 1.2 | 14.9 | 0.090 | 24.3 | 0.075 | 7.5 | 0.045 |
| **30** | 2.10 : 2 : 1.8 | 13.1 | 0.079 | 24.3 | 0.075 | 11.2 | 0.068 |
| **40** | 1.80 : 2 : 2.4 | 11.2 | 0.068 | 24.3 | 0.075 | 14.9 | 0.090 |
| **50** | 1.50 : 2 : 3.0 | 9.3 | 0.056 | 24.3 | 0.075 | 18.7 | 0.113 |
| **60** | 1.20 : 2 : 3.6 | 7.5 | 0.045 | 24.3 | 0.075 | 22.4 | 0.135 |

**Modulation synthesis of COF-5 by the addition of CPBA**

The synthesis of COF-5-x in the presence of CPBA was as well carried out with addition of CPBA to a constant amount of BDBA instead of substituting BDBA, according to Table S3.

**Table 3.3** Applied initial weights for the synthesis of COF-5 with the addition of CPBA as modulator.

| **BDBA : CPBA Ratio** | **molar ratios** | **BDBA [mg]** | **BDBA [mmol]** | **HHTP [mg]** | **HHTP [mmol]** | **CPBA [mg]** | **CPBA [mmol]** |
|---|---|---|---|---|---|---|---|
| **0 : 0** | 3.00 : 2 : 0.00 | 18.7 | 0.113 | 24.3 | 0.075 | 0.0 | 0.0 |
| **0 : 0.05** | 3.00 : 2 : 0.15 | 18.7 | 0.113 | 24.3 | 0.075 | 0.93 | 0.007 |
| **0 : 0.1** | 3.00 : 2 : 0.30 | 18.7 | 0.113 | 24.3 | 0.075 | 1.85 | 0.011 |
| **0 : 0.2** | 3.00 : 2 : 0.60 | 18.7 | 0.113 | 24.3 | 0.075 | 3.71 | 0.023 |
| **0 : 0.3** | 3.00 : 2 : 0.90 | 18.7 | 0.113 | 24.3 | 0.075 | 5.56 | 0.034 |
| **0 : 0.4** | 3.00 : 2 : 1.20 | 18.7 | 0.113 | 24.3 | 0.075 | 7.42 | 0.045 |
| **0 : 0.5** | 3.00 : 2 : 1.50 | 18.7 | 0.113 | 24.3 | 0.075 | 9.27 | 0.056 |
| **0 : 0.6** | 3.00 : 2 : 1.80 | 18.7 | 0.113 | 24.3 | 0.075 | 11.13 | 0.068 |

**Post-modification of COF-5-10-SH**

To a suspension of 1 mg thiol-functionalized COF-5-10 material in 1 mL 1,4-dioxane, 1 µL of methoxypolyethylene glycol maleimide (0.5 mg/mL in DMF) was added and reacted for 1 h. After several washing steps with 1,4-dioxane, the obtained solid was collected by centrifugation (4 min, 16873 rcf).

**Treatment of COF-5-10-SH / COF-5 with $IrCl_3$**

To a suspension of 1 mg COF (COF-5-10-SH or COF-5) in 1 mL 1,4-dioxane, 100 µL of a 0.1 M ethanolic solution of $IrCl_3$ was added and reacted for 3 h. The solid was collected after several washing steps with 1,4-dioxane by centrifugation (4min, 16873 rcf).

**Post-modification of COF-5-10-COOH**

1 mg as-synthesized COOH-functionalized COF-5-10 material was mixed with 3 µL 1-ethyl-3-(3-dimethylaminopropyl)carbodiimide (EDC) in 1 mL 1,4-dioxane. After 1 h, 1 µL Atto633-$NH_2$ (0.5 mg/mL in DMF) was added. The material was collected (4 min, 16873 rcf) and washed several times with 1,4-dioxane until no dye could be detected in the supernatant. The modification led to a slightly blue solid.

**Section 3: Compositional Analysis by NMR**

For the compositional analysis by NMR the COFs were digested by the addition of a stoichiometric amount of pinacol in deuterated DMSO.

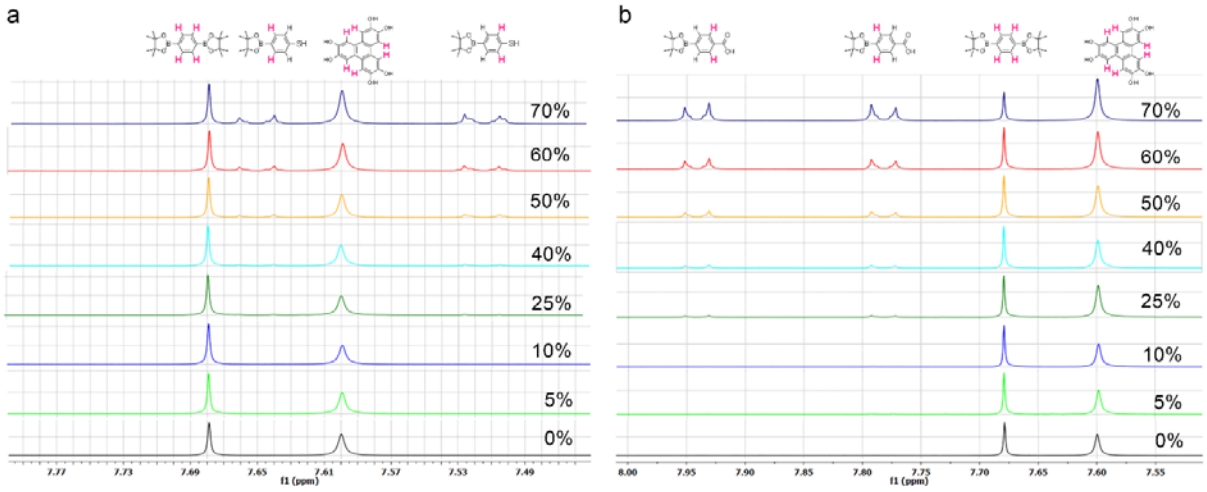


Figure S 3.1: Overview of the NMR spectra of a) COF-5-x (SH) and b) COF-5-x (COOH) showing the additional signals arising from the incorporation of the modulator at higher degrees of substitution. Up to a modulator content of 10 % in the reaction mixture the amount of incorporated modulator is below the detection limit.

**Table 3.4** Molecular composition of the MPBA-modulated COF-5 samples analyzed by NMR.

| **Modulator in reaction mixture [%]** | **HHTP aryl protons integral** | **BDBA protons integral** | **MPBA protons integral** | **HHTP molar ratio** | **BDBA molar ratio** | **MPBA molar ratio** | **Total boronic acid groups** |
|---|---|---|---|---|---|---|---|
| **0** | 6 | 4.25 | 0 | 1 | 1.06 | 0 | 2.12 |
| **5** | 6 | 4.95 | 0 | 1 | 1.24 | 0 | 2.48 |
| **10** | 6 | 5.82 | 0 | 1 | 1.46 | 0 | 2.92 |
| **25** | 6 | 5.40 | 0.24 | 1 | 1.35 | 0.12 | 2.82 |
| **40** | 6 | 5.00 | 0.77 | 1 | 1.25 | 0.39 | 2.89 |
| **50** | 6 | 4.41 | 1.50 | 1 | 1.10 | 0.75 | 2.95 |
| **60** | 6 | 3.81 | 1.82 | 1 | 0.95 | 0.91 | 2.81 |
| **70** | 6 | 3.13 | 3.01 | 1 | 0.78 | 1.51 | 3.06 |

**Table 3.5** Molecular composition of the CPBA-modulated COF-5 samples analyzed by NMR.

| **Modulator in reaction mixture [%]** | **HHTP aryl protons integral** | **BDBA protons integral** | **CPBA protons integral** | **HHTP molar ratio** | **BDBA molar ratio** | **CPBA molar ratio** | **Total boronic acid groups** |
|---|---|---|---|---|---|---|---|
| **0** | 6 | 4.22 | 0 | 1 | 2.11 | 0 | 2.11 |
| **5** | 6 | 4.48 | 0 | 1 | 2.22 | 0 | 2.22 |
| **10** | 6 | 4.74 | 0.11 | 1 | 2.37 | 0.06 | 2.43 |
| **25** | 6 | 3.46 | 0.38 | 1 | 1.73 | 0.19 | 1.92 |
| **40** | 6 | 3.90 | 0.91 | 1 | 1.95 | 0.46 | 2.41 |
| **50** | 6 | 3.74 | 1.62 | 1 | 1.87 | 0.81 | 2.68 |
| **60** | 6 | 2.06 | 2.95 | 1 | 1.03 | 1.48 | 2.51 |
| **70** | 6 | 1.83 | 3.09 | 1 | 0.92 | 1.55 | 2.47 |

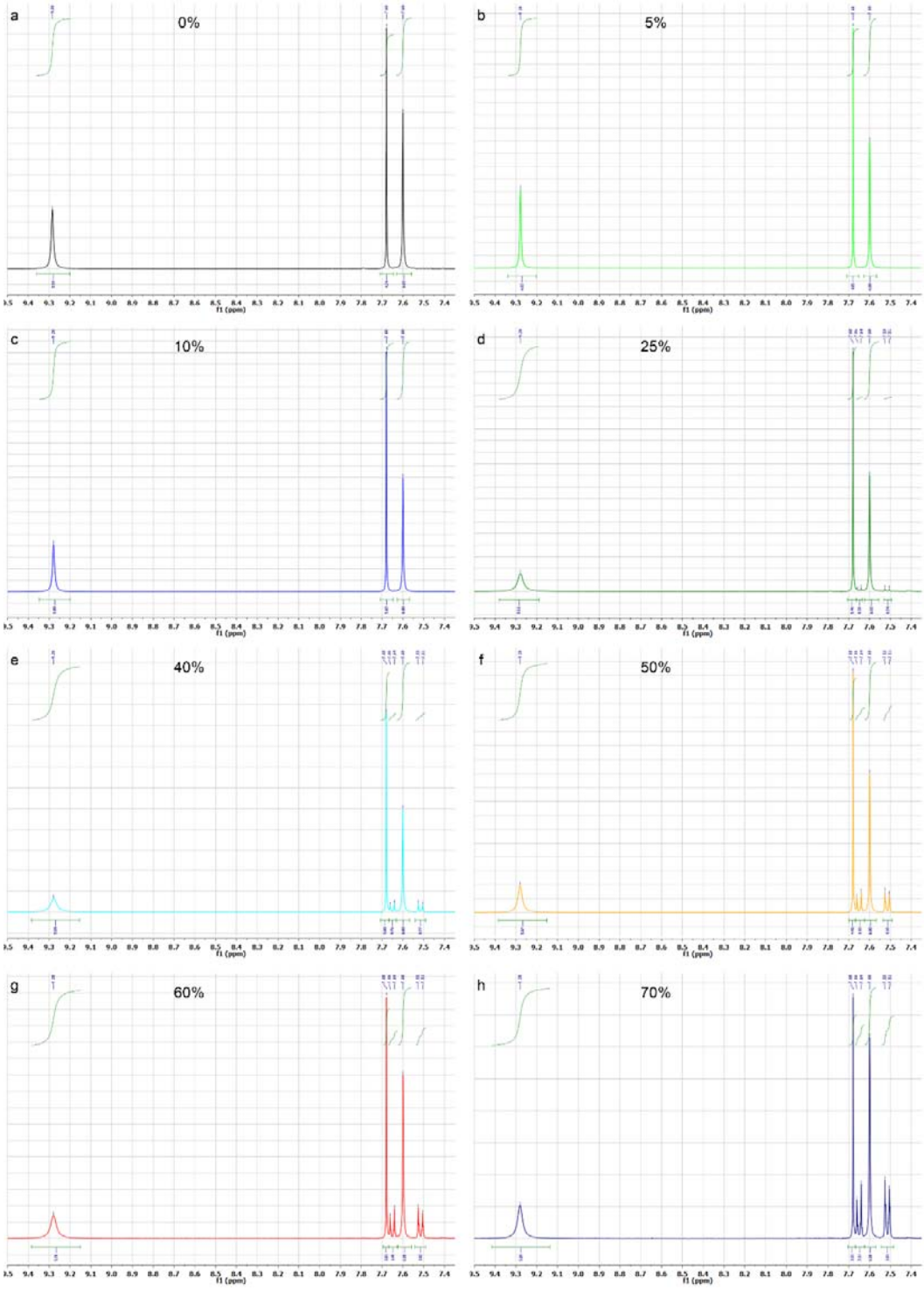


Figure S 3.2: NMR spectra of COF-5-x (SH) grown with different modulator contents. The integrals were referenced to the signal at 7.6 ppm arising from the HHTP protons. As expected for fully hydrolyzed HHTP, the ratio between the aryl and the –OH protons at 9.28 ppm is constant at 1:1 in all samples. The ratio between the HHTP and BDBA protons, however, deviates considerably from the theoretical ratio depending on the modulator content in the reaction mixture. Only at a modulator content of 10 % the ratio between the trigonal and the linear building block reaches the expected theoretical ratio, i.e. 2:3, corresponding to a 1:1 proton ratio.

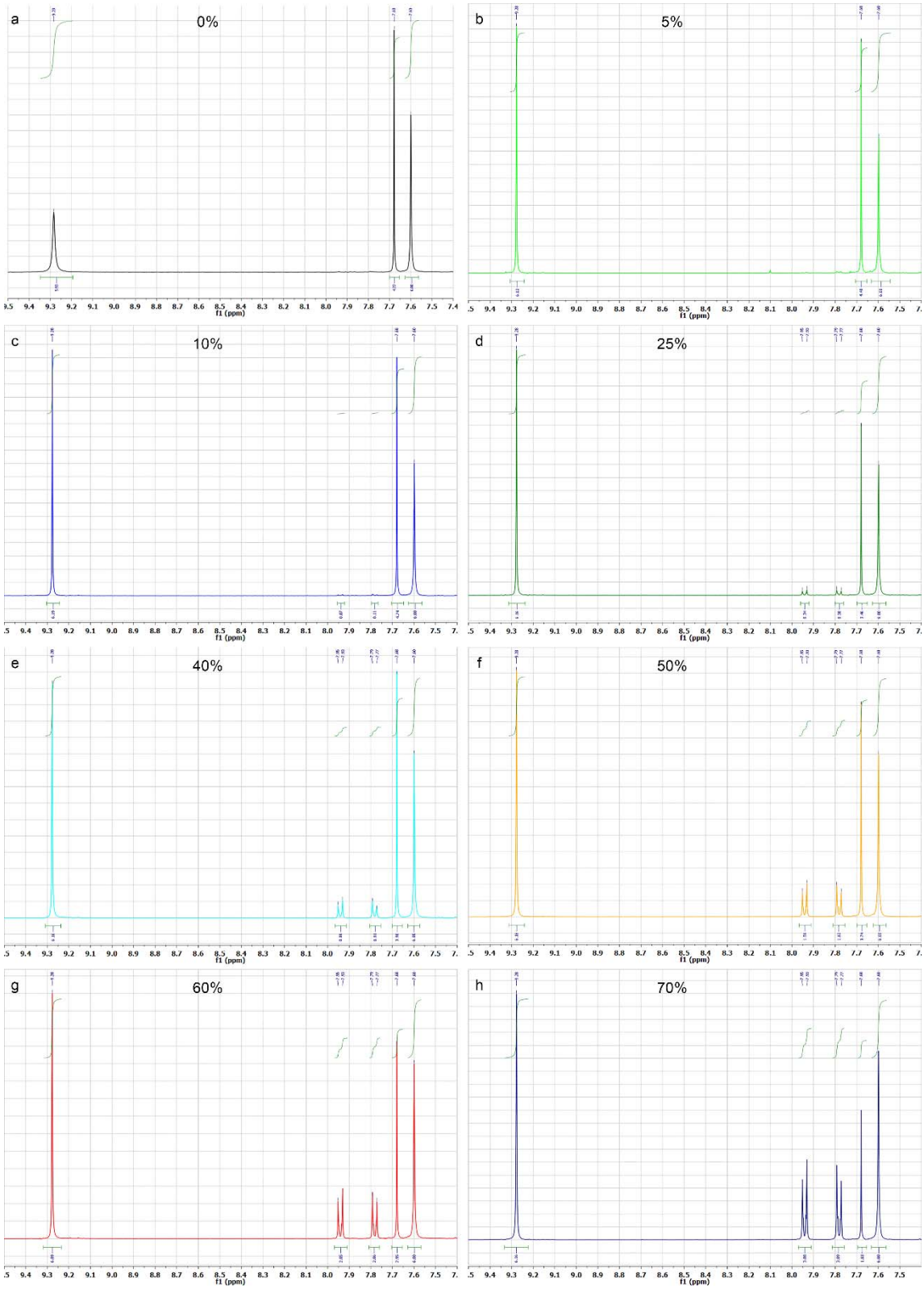


Figure S 3.3: NMR spectra of COF-5-x (COOH) grown with different modulator contents. The integrals were referenced to the signal at 7.6 ppm arising from the HHTP protons. Similar to the –SH modulated COF-5, the ratio between the HHTP and BDBA protons deviates considerably from the theoretical ratio depending on the modulator content in the reaction mixture. At a modulator content of 5-10 % the ratio between the trigonal and the linear building block is closest to the expected theoretical ratio, i.e. 2:3, corresponding to a 1:1 proton ratio.

## Section 4: Simulation of the COF-5 Crystal Structures

Structure simulations were carried out using force-field methods with the Accelrys Materials Studio software package.

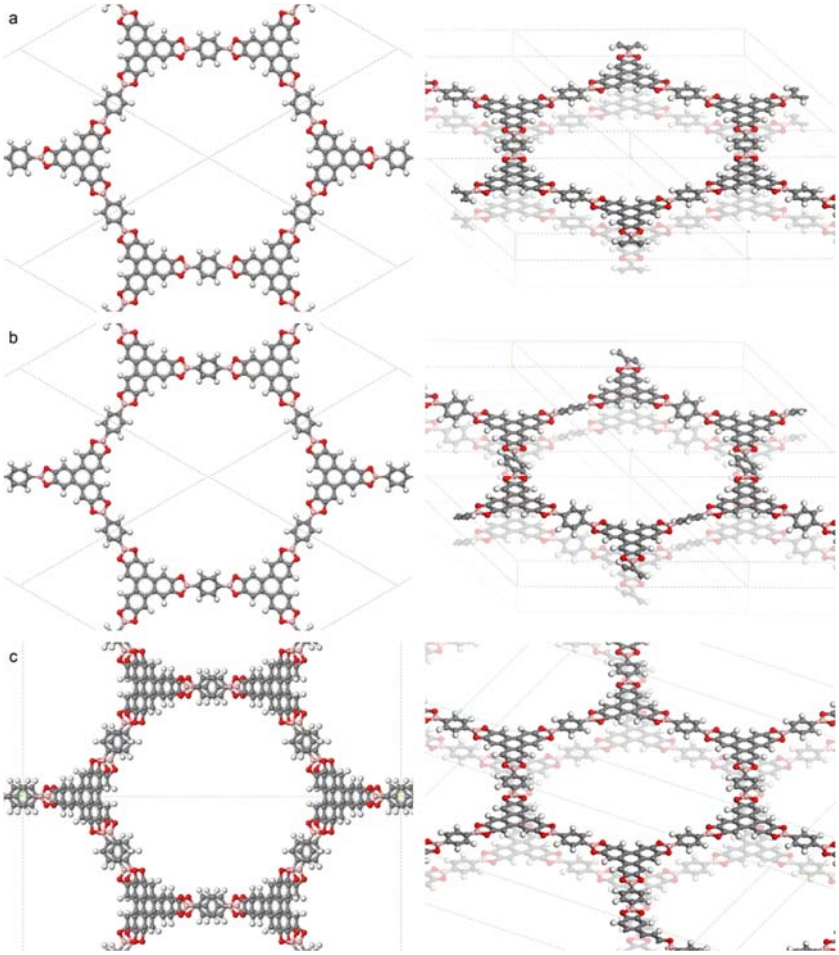


Figure S 3.4: Simulation of the COF-5 structure assuming (a) P6/mmm, (b) P-3, and (c) Cmcm symmetry.

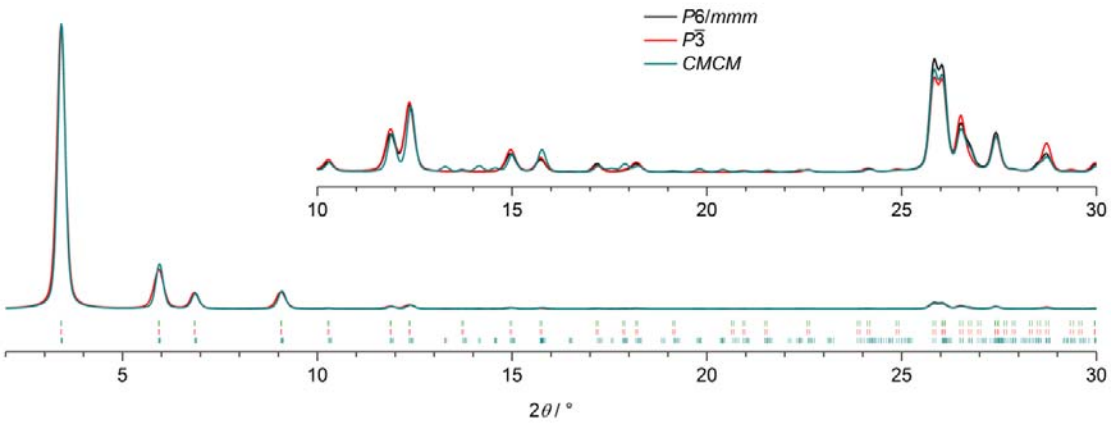


Figure S 3.5: Simulated PXRD patterns (lines) and Bragg positions (symbols) using the structures displayed in Figure 3.1. Inset: Enlarged plot of the 10-30 ° 2θ range.

**Section 5: X-Ray Diffraction Analysis of Modulated COF-5-x**

**COF-5 Modulation with MPBA - COF-5-x (SH)**

For XRD analysis in reflection mode a small amount of powder was flattened on top of a glass substrate. Domain sizes were estimated from the broadening of the 100 reflection using the Scherrer formula (Equation 3.1)

$$FWHM(2\theta) = \frac{K\,\lambda}{L\,cos(\theta)} \tag{3.1}$$

with $K = 0.9$ (assuming spherical particles), $\lambda = 0.15418$ nm, $\theta$ being the diffraction angle, and L being the domain size. The observed FWHM was corrected for the instrument broadening of 0.11 °.

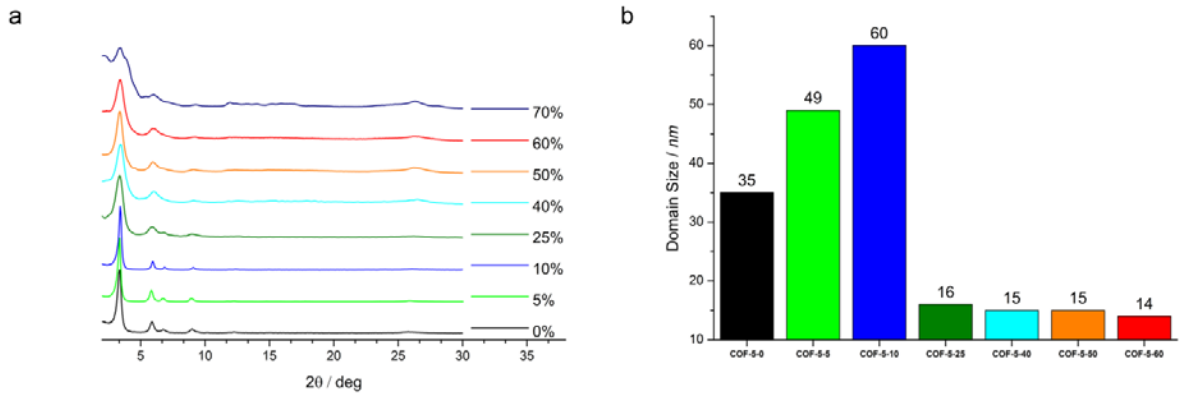


Figure S 3.6: a) Comparison of XRD pattern of COF-5-x modulated by substituting BDBA with MPBA (with x = 0, 5, 10, 25, 40, 50, 60 and 70%). b) Calculated domain sizes of COF-5-x using the FWHM of the 100 reflection at 3.4° 2θ.

## COF-5 Modulation with CPBA - COF-5-x (COOH)

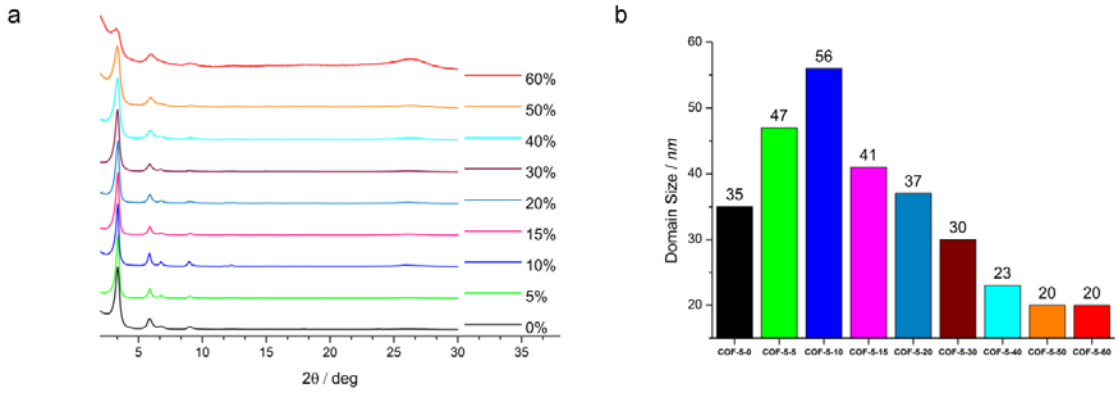


Figure S 3.7: a) Comparison of XRD patterns of COF-5-x modulated by substituting BDBA with CPBA (with x = 0, 5, 10, 15, 20, 30, 40, 50 and 60%). b) Calculated domain sizes of COF-5-x using the FWHM of the 100 reflection at 3.4° 2θ.

## Modulation synthesis of COF-5 by the addition of CPBA

In a different approach neither of the starting materials were substituted but the modulating agent CPBA was added to the reaction mixture. Upon addition an increase in crystallinity and domain size could be observed. This technique was found to be less sensitive concerning the used modulator amount (compare to Figure S 3.7).

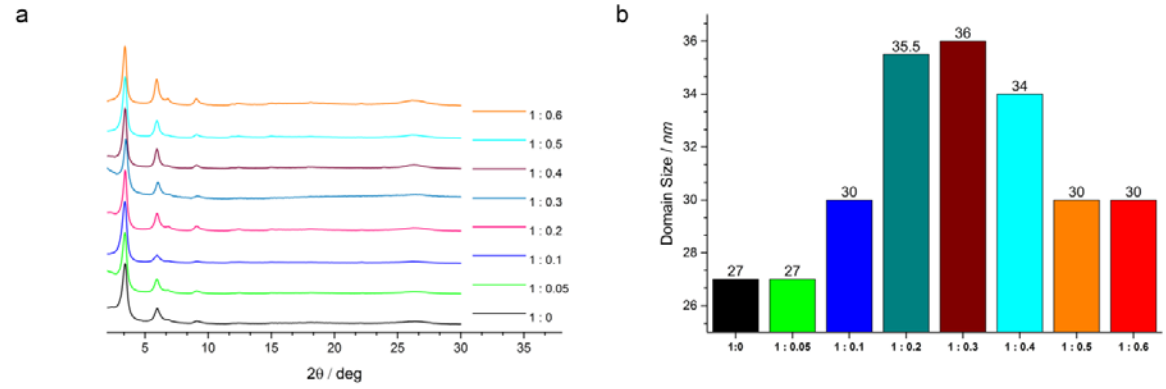


Figure S 3.8: a) XRD pattern for COF-5 modulated by adding CPBA to the reaction mixture. BDBA to CPBA ratios were varied from 1:0 up to 1:0.6. b) Calculated domain sizes of COF-5-x using the FWHM of the 100 reflection at 3.4° 2θ.

**Growth kinetics**

For studying the COF growth kinetics, the samples were prepared and handled as described in the synthesis section, except that the reactions were carried out by heating at 100 °C in a conventional oven. This way, the reaction was sufficiently slow to be able to monitor the framework formation. In all cases, the final products after 96 h were comparable to the products from the microwave-assisted syntheses. All samples were measured with identical instrument and scan settings.

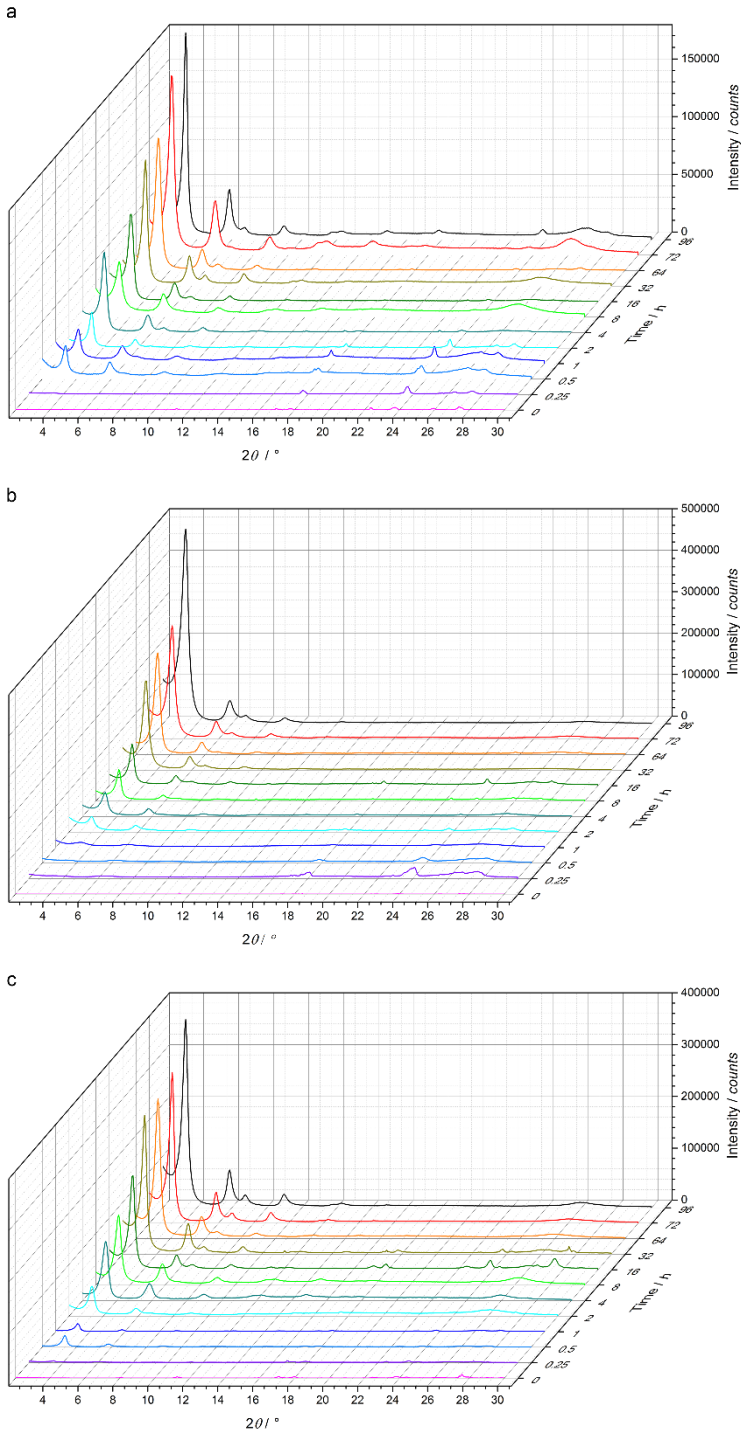


Figure S 3.9: Time evolution of the COF formation. a) in absence of a modulator, b) with 10 % MPBA and c) 10 % CPBA. At identical scan settings, the peak intensities are more than doubled for the samples grown in the presence of a modulator.

**Post-modification of COF-5-10**

Regardless of the modulating agent, COF-5-10 samples showed the highest crystallinity with the largest domain sizes. Therefore, these samples were used for post-modifications. COF-5-10-SH was treated with an $IrCl_3$ solution to promote the formation of Ir-S-clusters. The comparison of the PXRD data of the treated and untreated sample confirms that the crystallinity is retained (Figure S 3.10a).

Furthermore, COOH functionalized COF-5-10 was post-modified by the attachment of an ATTO633 dye. The PXRD pattern of COF-5-10-ATTO reveals the intact crystallinity of the framework (Figure S 3.10b).

To a thiol-functionalized COF-5-10 sample maleimide bearing polyethyleneglycol was added. The attachment of these PEG-groups was found to stabilize COF-5 towards EtOH. After dispersing COF-5-S-PEG in ethanol for 3 h the PXRD pattern confirms the completely maintained crystallinity of the framework (Figure S 3.10c).

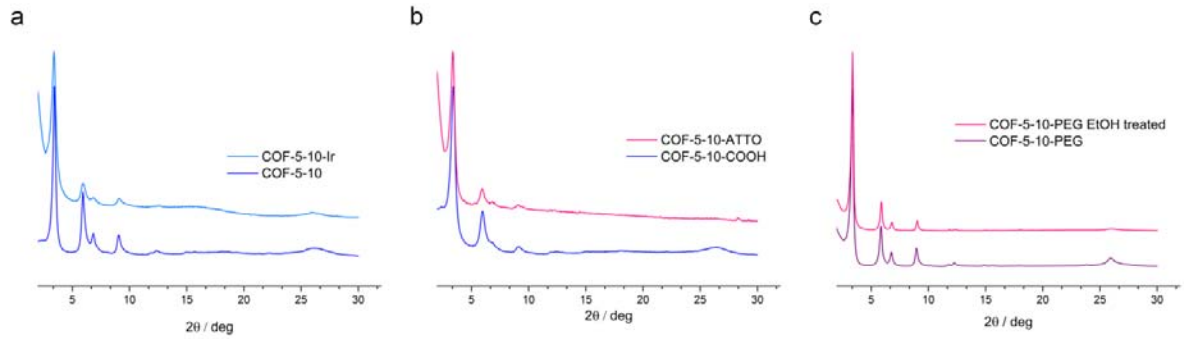


Figure S 3.10: Comparison of COF-5-10 before and after post-modifications. a) COF-5-10-SH and COF-5-10-Ir showing the retained crystallinity of the framework after the addition of $IrCl_3$. b) COF-5-10-COOH and ATTO633 labeled COF-5-10 (COF-5-10-ATTO) and c) COF-5-10-S-PEG and COF-5-10-S-PEG after dispersing the sample in EtOH for 3 h.

## Section 6: Pore Size Distribution Analysis

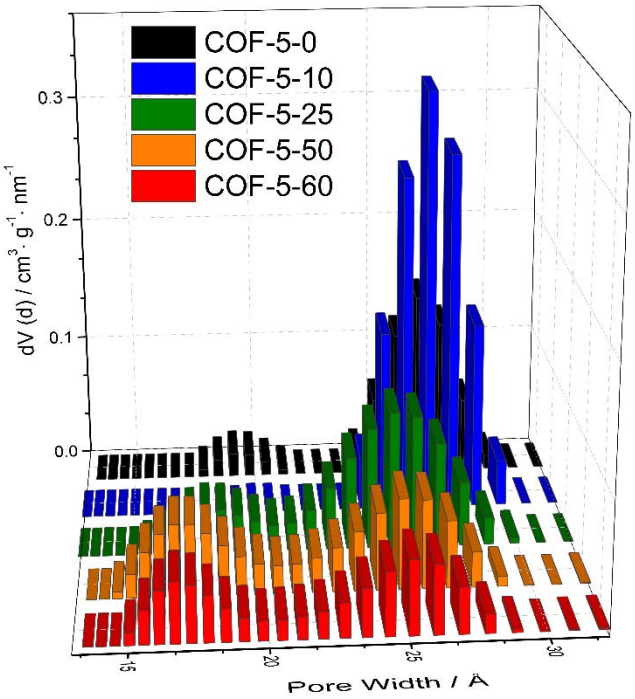


Figure S 3.11: Bar chart of pore size distributions calculated for COF-5-x (MPBA) (with x = 0, 10, 25, 50 and 60) samples using a QSDFT equilibrium model with a carbon kernel for cylindrical pores. The pore size distribution for COF-5-10 shows the highest intensity with the narrowest distribution of all compared samples. At higher substitution degrees a broadening in the pore size distribution and the occurrence of smaller pore sizes can be observed, being indicative for the existence of blocked or narrowed pores.

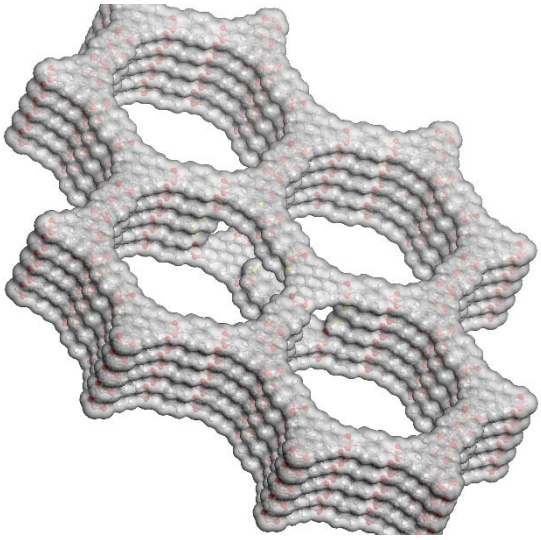

Figure S 3.12: Illustration of the additional porosity arising from the incorporation of the modulator into the COF that is accompanied by HHTP voids.

**Section 7: IR spectroscopy**

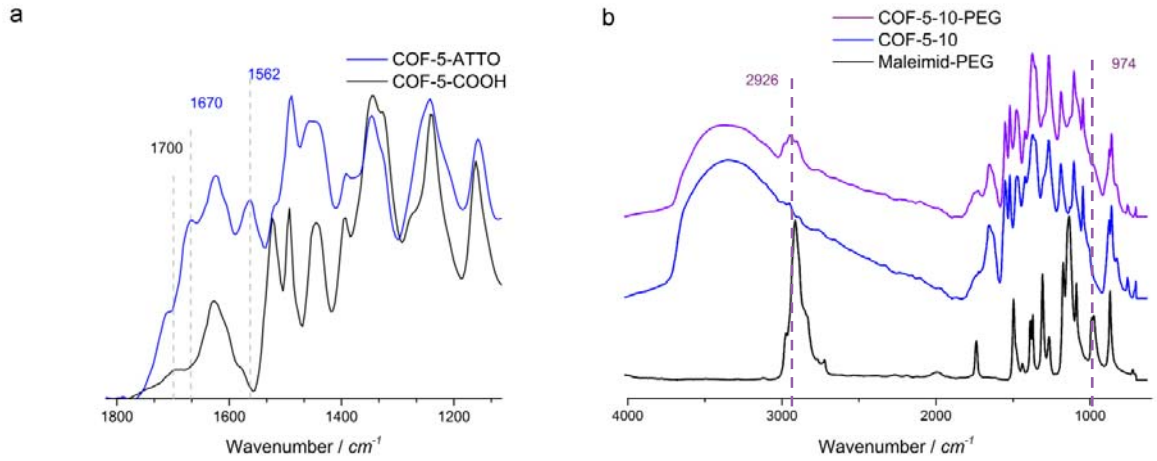


Figure S 3.13: IR spectra of a) COF-5-COOH powder and ATTO labeled COF-5-COOH (COF-5-ATTO) showing the characteristic signals of the C=O stretching vibration at 1700 $cm^{-1}$ of the carboxylic acid, the amide I C=O stretching vibration at 1670 $cm^{-1}$ and amide II N-H deformation vibration at 1562 $cm^{-1}$ and b) COF-5-10 and COF-5-10-PEG in comparison with maleimide-PEG showing the typical CH-stretching vibrations of methyl groups at 2926 $cm^{-1}$ and CH-vibration of polyenes at 974 $cm^{-1}$.

## Section 8: Thermal gravimetric analysis (TGA)

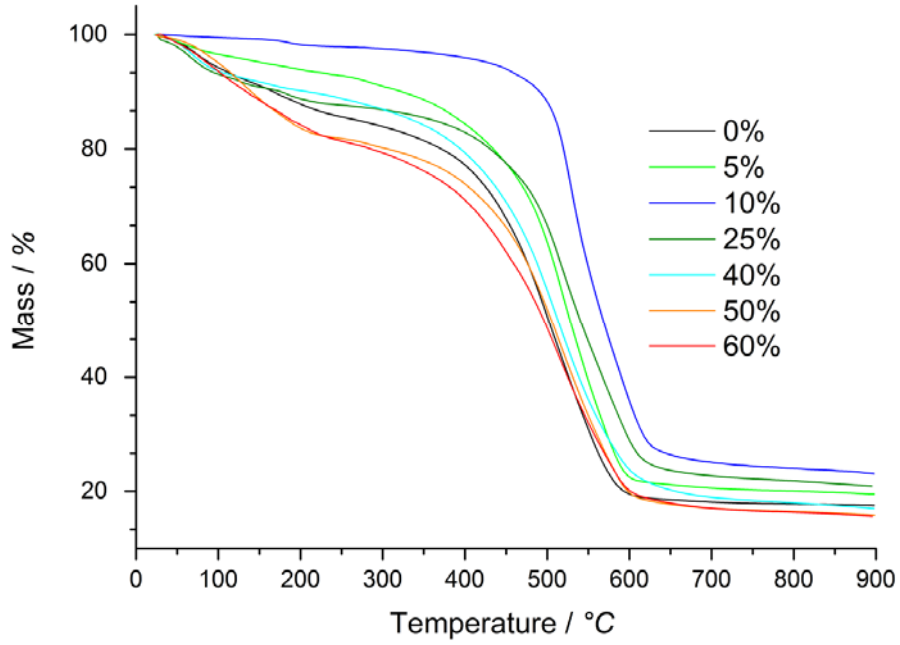


Figure S 3.14: Comparison of different COF-5-x (MPBA) (with x = 0, 10, 25, 50 and 60) samples investigated by TGA. The most crystalline sample (COF-5-10) exhibits the best-defined step at 450-500 °C, indicating a very well-ordered framework without residual starting material or oligomers in the pores.

## Section 8: UV-Vis Spectroscopy

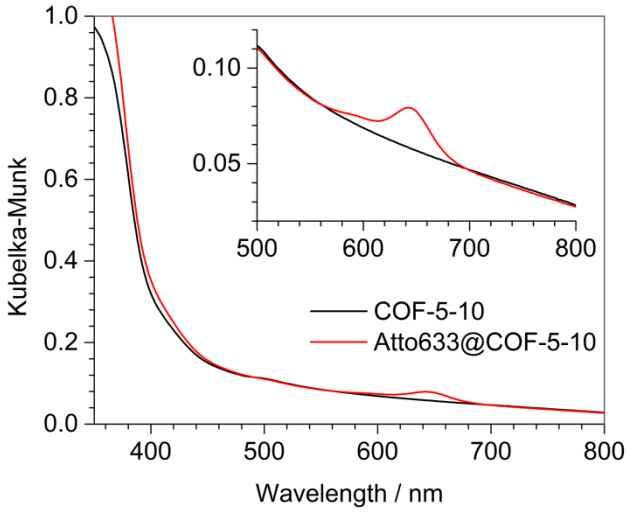


Figure S 3.15: Diffuse reflectance spectra of -COOH-functionalized COF-5-10 (black) and the same sample after covalent attachment of the Atto633 dye (red). The inset shows a magnified cut-out of the spectrum, highlighting the characteristic absorption of the attached dye.

## Section 9: Fluorescence Spectroscopy

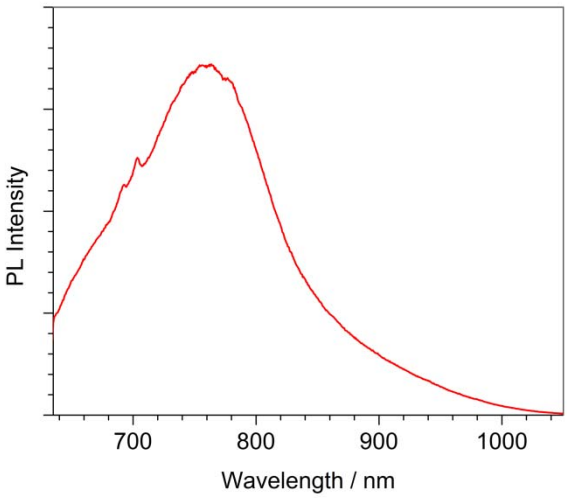


Figure S 3.16: Photoluminescence spectrum of the Atto633-modified COF-5-10 upon excitation with a 632.8 nm laser. The spectral features around 700 nm are artefacts from the setup.

## Section 10: Transmission Electron Microscopy / STEM

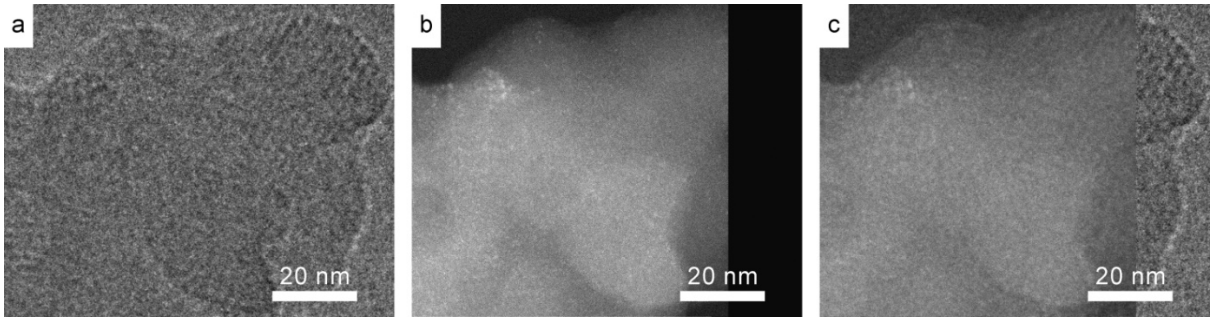


Figure S 3.17: (a) TEM micrograph of COF-5-0 stained with iridium. (b) Corresponding scanning transmission electron microscopy (STEM) micrograph of the same sample position. (c) Overlay of TEM and STEM micrographs of COF-5 showing a random distribution of iridium within the COF-5 network.

## 3.6 REFERENCES

(1) Cote, A. P.; Benin, A. I.; Ockwig, N. W.; O'Keeffe, M.; Matzger, A. J.; Yaghi, O. M., *Science* **2005**, *310*, 1166-1170.

(2) Uribe-Romo, F. J.; Hunt, J. R.; Furukawa, H.; Klöck, C.; O'Keeffe, M.; Yaghi, O. M., *J. Am. Chem. Soc.* **2009**, *131*, 4570-4571.

(3) Furukawa, H.; Yaghi, O. M., *J. Am. Chem. Soc.* **2009**, *131*, 8875-8883.

(4) Doonan, C. J.; Tranchemontagne, D. J.; Glover, T. G.; Hunt, J. R.; Yaghi, O. M., *Nat. Chem.* **2010**, *2*, 235-238.

(5) Oh, H.; Kalidindi, S. B.; Um, Y.; Bureekaew, S.; Schmid, R.; Fischer, R. A.; Hirscher, M., *Angew. Chem. Int. Ed. Engl.* **2013**, *52*, 13219-13222.

(6) Ma, H.; Ren, H.; Meng, S.; Yan, Z.; Zhao, H.; Sun, F.; Zhu, G., *Chem Commun (Camb)* **2013**, *49*, 9773-9775.

(7) Xu, H.; Chen, X.; Gao, J.; Lin, J.; Addicoat, M.; Irle, S.; Jiang, D., *Chem Commun (Camb)* **2014**, *50*, 1292-1294.

(8) Ding, S.-Y.; Gao, J.; Wang, Q.; Zhang, Y.; Song, W.-G.; Su, C.-Y.; Wang, W., *J. Am. Chem. Soc.* **2011**, *133*, 19816-19822.

(9) Chandra, S.; Kundu, T.; Kandambeth, S.; BabaRao, R.; Marathe, Y.; Kunjir, S. M.; Banerjee, R., *J. Am. Chem. Soc.* **2014**, *136*, 6570-6573.

(10) DeBlase, C. R.; Silberstein, K. E.; Truong, T.-T.; Abruña, H. c. D.; Dichtel, W. R., *J. Am. Chem. Soc.* **2013**, *135*, 16821-16824.

(11) Dogru, M.; Handloser, M.; Auras, F.; Kunz, T.; Medina, D.; Hartschuh, A.; Knochel, P.; Bein, T., *Angew. Chem. Int. Ed. Engl.* **2013**, *52*, 2920-2924.

(12) Calik, M.; Auras, F.; Salonen, L. M.; Bader, K.; Grill, I.; Handloser, M.; Medina, D. D.; Dogru, M.; Löbermann, F.; Trauner, D.; Hartschuh, A.; Bein, T., *J. Am. Chem. Soc.* **2014**, *136*, 17802-17807.

(13) Medina, D. D.; Werner, V.; Auras, F.; Tautz, R.; Dogru, M.; Schuster, J.; Linke, S.; Doblinger, M.; Feldmann, J.; Knochel, P.; Bein, T., *ACS Nano* **2014**, *8*, 4042-4052.

(14) Feng, X.; Chen, L.; Honsho, Y.; Saengsawang, O.; Liu, L.; Wang, L.; Saeki, A.; Irle, S.; Seki, S.; Dong, Y.; Jiang, D., *Adv. Mater.* **2012**, *24*, 3026-3031.

(15) Jin, S.; Ding, X.; Feng, X.; Supur, M.; Furukawa, K.; Takahashi, S.; Addicoat, M.; El-Khouly, M. E.; Nakamura, T.; Irle, S.; Fukuzumi, S.; Nagai, A.; Jiang, D., *Angew. Chem. Int. Ed. Engl.* **2013**, *52*, 2017-2021.

(16) Cote, A. P.; El-Kaderi, H. M.; Furukawa, H.; Hunt, J. R.; Yaghi, O. M., *J. Am. Chem. Soc.* **2007**, *129*, 12914-12915.

(17) Spitler, E. L.; Dichtel, W. R., *Nat. Chem.* **2010**, *2*, 672-677.

(18) Ding, X.; Guo, J.; Feng, X.; Honsho, Y.; Guo, J.; Seki, S.; Maitarad, P.; Saeki, A.; Nagase, S.; Jiang, D., *Angew. Chem. Int. Ed.* **2011**, *50*, 1289-1293.

(19) Hunt, J. R.; Doonan, C. J.; LeVangie, J. D.; Cote, A. P.; Yaghi, O. M., *J. Am. Chem. Soc.* **2008**, *130*, 11872-11873.

(20) Chen, X.; Addicoat, M.; Irle, S.; Nagai, A.; Jiang, D., *J. Am. Chem. Soc.* **2013**, *135*, 546-549.

(21) Zhang, Y.-B.; Su, J.; Furukawa, H.; Yun, Y.; Gándara, F.; Duong, A.; Zou, X.; Yaghi, O. M., *J. Am. Chem. Soc.* **2013**, *135*, 16336-16339.

(22) Fang, Q.; Zhuang, Z.; Gu, S.; Kaspar, R. B.; Zheng, J.; Wang, J.; Qiu, S.; Yan, Y., *Nat. Commun.* **2014**, *5*, 4503.

(23) Fang, Q.; Wang, J.; Gu, S.; Kaspar, R. B.; Zhuang, Z.; Zheng, J.; Guo, H.; Qiu, S.; Yan, Y., *Journal of the American Chemical Society* **2015**, *137*, 8352-8355.

(24) Uribe-Romo, F. J.; Doonan, C. J.; Furukawa, H.; Oisaki, K.; Yaghi, O. M., *J. Am. Chem. Soc.* **2011**, *133*, 11478-11481.

(25) Dalapati, S.; Jin, S.; Gao, J.; Xu, Y.; Nagai, A.; Jiang, D., *J. Am. Chem. Soc.* **2013**, *135*, 17310-17313.

(26) Jackson, K. T.; Reich, T. E.; El-Kaderi, H. M., *Chem Commun (Camb)* **2012**, *48*, 8823-8825.

(27) Yu, W. W.; Wang, Y. A.; Peng, X., *Chem. Mater.* **2003**, *15*, 4300-4308.

(28) Leff, D. V.; Ohara, P. C.; Heath, J. R.; Gelbart, W. M., *The Journal of Physical Chemistry* **1995**, *99*, 7036-7041.

(29) Tao, A. R.; Habas, S.; Yang, P., *Small* **2008**, *4*, 310-325.

(30) Uemura, T.; Kitagawa, S., *Chem. Lett.* **2005**, *34*, 132-137.

(31) Diring, S. p.; Furukawa, S.; Takashima, Y.; Tsuruoka, T.; Kitagawa, S., *Chem. Mater.* **2010**, *22*, 4531-4538.

(32) Tsuruoka, T.; Furukawa, S.; Takashima, Y.; Yoshida, K.; Isoda, S.; Kitagawa, S., *Angew. Chem. Int. Ed. Engl.* **2009**, *48*, 4739-4743.

(33) Schaate, A.; Roy, P.; Godt, A.; Lippke, J.; Waltz, F.; Wiebcke, M.; Behrens, P., *Chemistry* **2011**, *17*, 6643-6651.

(34) Biemmi, E.; Darga, A.; Stock, N.; Bein, T., *Microporous Mesoporous Mater.* **2008**, *114*, 380-386.

(35) Bunck, D. N.; Dichtel, W. R., *Angew. Chem. Int. Ed.* **2012**, *51*, 1885-1889.

(36) Bunck, D. N.; Dichtel, W. R., *Chem. Commun.* **2013**, *49*, 2457-2459.

(37) Brucks, S. D.; Bunck, D. N.; Dichtel, W. R., *Polymer* **2014**, *55*, 330-334.

(38) Smith, B. J.; Dichtel, W. R., *J. Am. Chem. Soc.* **2014**, *136*, 8783-8789.

(39) Smith, B. J.; Hwang, N.; Chavez, A. D.; Novotney, J. L.; Dichtel, W. R., *Chem. Commun.* **2015**, *51*, 7532-7535.

(40) Colson, J. W.; Mann, J. A.; DeBlase, C. R.; Dichtel, W. R., *J. Polym. Sci. Part A* **2015**, *53*, 378-384.

(41) Sing, K. S. W., *Pure Appl. Chem.* **1985**, *57*, 603-619.

(42) Thommes, M.; Smarsly, B.; Groenewolt, M.; Ravikovitch, P. I.; Neimark, A. V., *Langmuir* **2006**, *22*, 756-764.

(43) Thommes, M.; Cychosz, K. A., *Adsorption* **2014**, *20*, 233-250.

(44) Jesson, D. E.; Pennycook, S. J., *Proceedings of the Royal Society of London A: Mathematical, Physical and Engineering Sciences* **1995**, *449*, 273-293.

(45) ATTO 633. http://www.atto-tec.com/fileadmin/user_upload/Katalog_Flyer_Support/ATTO_633.pdf.

(46) Northrop, B. H.; Frayne, S. H.; Choudhary, U., *Polymer Chemistry* **2015**, *6*, 3415-3430.

# 4. MOLECULAR DOCKING SITES DESIGNED FOR THE GENERATION OF HIGHLY CRYSTALLINE COVALENT ORGANIC FRAMEWORKS

This chapter is based on the following publication:

Laura Ascherl, Torben Sick, Johannes T. Margraf, Saul H. Lapidus, Mona Calik, Christina Hettstedt, Konstantin Karaghiosoff, Markus Döblinger, Timothy Clark, Karena W. Chapman, Florian Auras, Thomas Bein

*Nat. Chem. 2016, 8, 310-316.*

I have provided the following contributions:

- Initiation of the project
- Synthesis of ETTA
- IR measurements
- Sorption measurements and data evaluation

# 4.1 ABSTRACT

Crystallinity and porosity are of central importance for many properties of covalent organic frameworks (COFs) including adsorption, diffusion, and electronic transport. We have developed a new method for strongly enhancing both aspects through the introduction of a modulating agent in the synthesis. This modulator competes with one of the building blocks during the solvothermal COF growth, resulting in highly crystalline frameworks with greatly increased domain sizes reaching several hundreds of nanometers. The obtained materials feature fully accessible pores with an internal surface area of over 2000 $m^2$ $g^{-1}$. Compositional analysis via NMR spectroscopy revealed that the COF-5 structure can form over a wide range of boronic acid to catechol ratios, spanning from highly boronic acid-deficient frameworks to networks with catechol voids. Visualization of an -SH functionalized modulating agent via iridium staining revealed that the COF domains are terminated by the modulator. Using functionalized modulators, this synthetic approach thus also provides a new and facile method for the external surface functionalization of COF domains, providing accessible sites for post-synthetic modification reactions. We demonstrate the feasibility of this concept by covalently attaching fluorescent dyes and hydrophilic polymers to the COF surface. We anticipate that the realization of highly crystalline COFs with the option of additional surface functionality will render the modulation concept beneficial for a range of applications including gas separations, catalysis, and optoelectronics.

## 4.2 INTRODUCTION

Controlling the crystallization of organic materials has remained challenging, particularly if a long-range ordered network is to be formed entirely from covalent bonds, as in the case of covalent organic frameworks (COFs). COFs have recently come into the limelight as gas storage or separation materials-[1-2], as new materials for applications in catalysis[3] and as promising candidates for realizing new optoelectronic-device concepts[4-5]. COFs linked in two dimensions (2D COFs) are of great interest, especially for optoelectronic devices. π-Stacking between the COF layers enables charge-carrier transport along selfassembled molecular columns[6-7] and the formation of oriented host channels, which can be used to incorporate functional guest molecules[8]. COFs are realized via a reversible mechanism of covalent-bond formation, the most prominent linkage modes being boronic ester formation[9-14], imine[15-17] and imide[18] condensation and trimerization processes based on borazine[19] and triazine[20]. The reversibility of the bond formation allows for constant self-healing during COF growth and is of key importance to obtain a highly crystalline product. Although 3D imine-linked COFs, such as COF-300 or molecular imine cages, can exhibit a rather high degree of order[15, 21-22], most 2D COFs are of moderate crystallinity, which possibly limits the accessible surface area and electronic transport in the framework.

Methods to enhance the crystallinity of layered COFs have focused mostly on the control of the intralayer interactions and layer planarity via the introduction of hydrogen bonds[23-24]. Although these concepts have an indirect influence on the layer stacking, a direct and deterministic control of the stacking is highly desirable. Theoretical investigations of the layer stacking in these frameworks have established that a lateral offset between adjacent COF layers is energetically favorable, and results in inclined or serrated rather than fully eclipsed structures[25-26]. Owing to the inherent symmetry of the layers, however, this offset will happen with the same probability along all the symmetry-equivalent directions. Consequently, if a successive COF layer nucleates at more than one location, the lateral offset of the growing islands is very likely to be in different directions, and so possibly causes lattice strain and defects, and in turn compromises crystallinity (Figure 4.1a).

To preclude this error-prone network formation, we developed a concept to control 3D spatial relationships during the formation of COFs, in which the molecular conformation of the building blocks unambiguously defines the position of each building unit within adjacent COF layers (Figure 4.1b). We surmised that multidentate central units with a lock-and-key-like

molecular conformation could be used to guide the attachment of the successive layers (Figure 4.1c). To implement this concept, we synthesized a set of highly crystalline hexagonal COFs with eclipsed 2D structures.

## 4.3 RESULTS AND DISCUSSION

Inspired by stackable objects, we looked for screw- or propeller shaped molecules that can lock into each other and thereby fix the lateral position for the attachment of successive COF layers (Figure 4.1c). As a first example for realizing this concept with imine-linked COFs we chose 1,1,2,2-tetrakis(4-aminophenyl)ethene (1). 1 is expected to yield fourfold connected and thus very stable COF structures, whereby a star-shaped, dual-pore arrangement of the COF seems to be favoured[27]. To study the molecular arrangement of the 1,1,2,2-tetraphenylethene (4PE) central unit inside a possible COF network, we first synthesized a molecular model system (2) by the fourfold imine condensation of 1 with benzaldehyde (Figure 4.1d (for experimental details, see the Supplementary Information)). Single-crystal X-ray data confirm that the 4PE unit adopts the desired propeller-like arrangement (Figure 4.1e) with both a left- and a right-turning entity present in the crystal structure (Figure S 4.1).

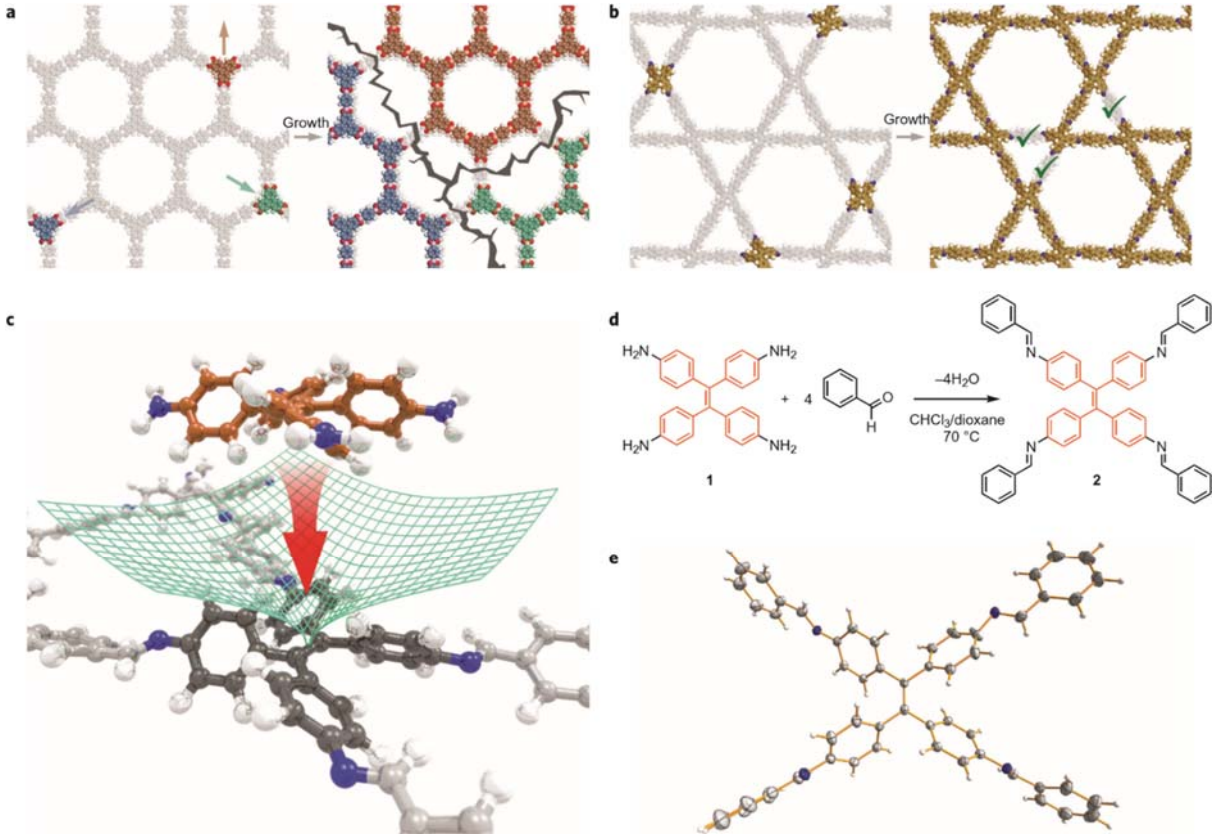


Figure 4.1: The self-repeating lock-and-key motif of propeller-shaped building blocks. a, simultaneous nucleation of a successive COF layer (at three moieties for which the carbon atoms are shown in orange, blue and green, respectively; oxygen, red; hydrogen, white) at several positions over an initial COF layer (shown in light grey for clarity, with hydrogen atoms in white) offset in symmetry-equivalent directions (indicated by the orange, blue and green arrows) can lead to strain and lattice defects (visualized by cracks) during COF growth. b, If a successive COF layer (C, yellow; N, blue; H, white) nucleates at unique attachment sites exactly over the nodes of the initial COF layer (shown in light grey with hydrogen atoms in white), the islands formed from these nucleation sites in the early steps of COF growth can merge into a defect-free layer (visualized by green ticks). c, Illustration of the guided attachment of the 4PE-based building blocks (C, dark grey for the four core aromatic rings, light grey for the other carbons; N, blue; H, white). The molecular conformation of this building block (dark grey) causes a single minimum in the potential-energy hypersurface (green grid) for lateral displacement, which allows the successive layer (C, orange; N, blue; H, white) to lock in position (visualized by the red arrow). d, Synthesis of a 4PE-based molecular model system via condensation of 1 with benzaldehyde. e, Asymmetric unit of the single-crystal X-ray structure of 2 that shows the solid-state geometry of the 4PE unit. Blue, N; grey, C; white, H. The co-crystallized solvent molecule is omitted for clarity.

We then applied 1 as a building block in a series of imine-linked COFs (Figure 4.2a), co-condensing the four-armed building block with linear dialdehydes. As to the choice of the linear building units, we decided to start with weakly interacting non-rigid molecules to avoid the layer stacking being dominated by these linear building blocks. We therefore selected biphenyl-4,4′-dicarboxaldehyde (2P) and, to achieve different pore sizes, the shorter terephthalaldehyde

(1P) and its elongated homologue p-terphenyl-4,4″-dicarboxaldehyde (3P). To study whether the concept could also be transferred to linkers with stronger electronic interactions, we chose thieno[3,2-*b*]thiophene-2,5-dicarboxaldehyde (TT) as a further dicarboxaldehyde building block. A thienothiophene-bridged diboronic acid had already been applied successfully in previous COF studies by our group[4].

The corresponding 4PE-1P, 4PE-2P, 4PE-3P and 4PE-TT COFs were obtained via acid catalysis under solvothermal conditions (see Methods). In a way similar to molecular imine cages[28], the 4PE COFs possess very high physicochemical stabilities. The frameworks are stable in ambient air and were found to retain their crystallinity on stirring in a variety of protic and aprotic organic solvents and in boiling water (Figure S 4.6 and S 4.7).

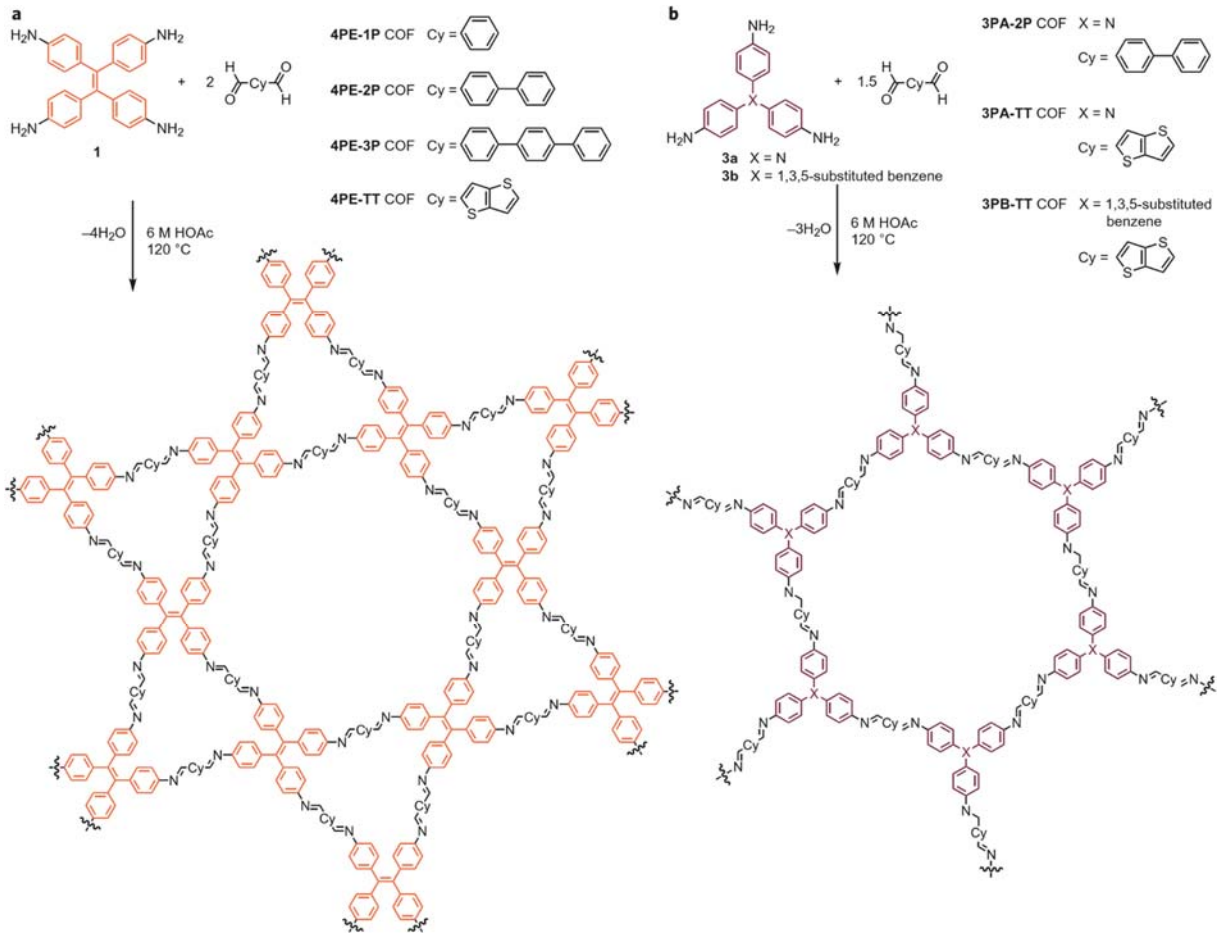


Figure 4.2: Synthetic scheme for the construction of the imine-linked COFs that comprise propeller-shaped building blocks. a, Construction of star-shaped, dual-pore 4PE-based COFs via co-condensation of 1 with the linear dialdehyde bridging units 1P, 2P, 3P and TT. b, Synthesis of the hexagonal 3PA- and 3PB-based COFs in combination with the linear dialdehyde bridging units 2P and TT.

Powder X-ray diffraction (PXRD) data from both high-resolution and high-energy synchrotron-based measurements confirmed the formation of highly crystalline frameworks (Figure 4.3a–c and Figure S 4.3). In particular, the diffraction patterns of the new 4PE-2P, 4PE-3P and 4PE-TT COFs display a large number of well-defined higher-order reflections (insets of Figure 4.3a–c). The high-energy data collected using an area detector provided an improved signal-to-noise ratio for the higher-angle reflections. For each COF, structural analysis via a Rietveld refinement was performed against both data sets simultaneously using density functional theory/local density approximation (DFT/LDA)-optimized structures as the starting models (Figure 4.3d–f). The Rietveld method refines the atom positions of these models to find the best match between the theoretical pattern and the experimental data. Refinements were undertaken in the *P*6 space group, as this was the highest symmetry predicted from the DFT modelling. The *a* lattice parameter was well constrained by the data. However, this sample illustrates the

classic problem of a dominant zone with fewer and broad peaks corresponding to *hkl* reflections for $l \neq 0$. As such the *c* lattice dimension was defined less precisely. Bond lengths were constrained to the DFT-optimized values as the torsion between rigid moieties, such as rotations of the aromatic rings, was allowed to refine. The optimized models provide an excellent fit to the measured diffraction intensities (Figure 4.3). The unit-cell parameter a ranges from 4.12 nm for the 4PE-TT COF to 5.48 nm for the 4PE-3P COF. The c axis was found to be almost identical at 0.46-0.48 nm for all the 4PE-based COFs, which indicates a similar layer stacking in all cases despite the differences in stiffness and electronic interactions between the 2P, 3P and TT building blocks.

Pair-distribution functions (PDFs) calculated for the optimized structure models provided an excellent match to the experimental data, and further confirmed the local structure (Figure S 4.2). The best match between the experimental and simulated PDFs was achieved when the a lattice dimension was allowed to expand, which is in line with the systematic underestimation of bond lengths by the LDA method we used to build the starting models. The atomic displacement parameters perpendicular to the layers were significantly larger than those in the layer direction, which reflects the presence of an increased static and dynamic disorder in this non-bonded direction.

According to our simulations and the X-ray structure of the molecular fragment 2, the four core phenylene groups assume a screw-like arrangement, and thus allow the 4PE building block of a successive COF layer to lock in a single, well-defined lateral position. To vindicate the locking mechanism, DFT calculations were performed using the CASTEP code with the generalized gradient approximation PBE functional and applying a correction for dispersion interactions[29-33]. The simulation of the potential energy surface for the displacement of two 4PE-2P layers confirms that the eclipsed structure is, indeed, thermodynamically favored (Figure S 4.8). Furthermore, the potential-energy hypersurface is steepest around the minimum and levels off considerably for displacements higher than 0.04 nm in any direction.

To understand the nature of these interactions, it is instructive to compare the potential-energy hypersurfaces obtained from pure and dispersion-corrected PBE calculations (Figure S 4.9). The two methods predict the same qualitative features, most importantly the steep descent for displacements below 0.04 nm. As the PBE functional describes permanent multipole–multipole interactions only, without accounting for London-type interactions, the lock-and-key principle is primarily based on permanent electrostatic interactions between the aromatic rings. If dispersion interactions are included, the eclipsed structure is additionally stabilized by over 0.5

eV relative to the most-displaced geometry we considered. Furthermore, these interactions tilt the potential-energy hypersurface towards the minimum, which drives the key into the lock. This becomes particularly important for displacements beyond 0.04 nm, where the uncorrected PBE hypersurface is almost flat.

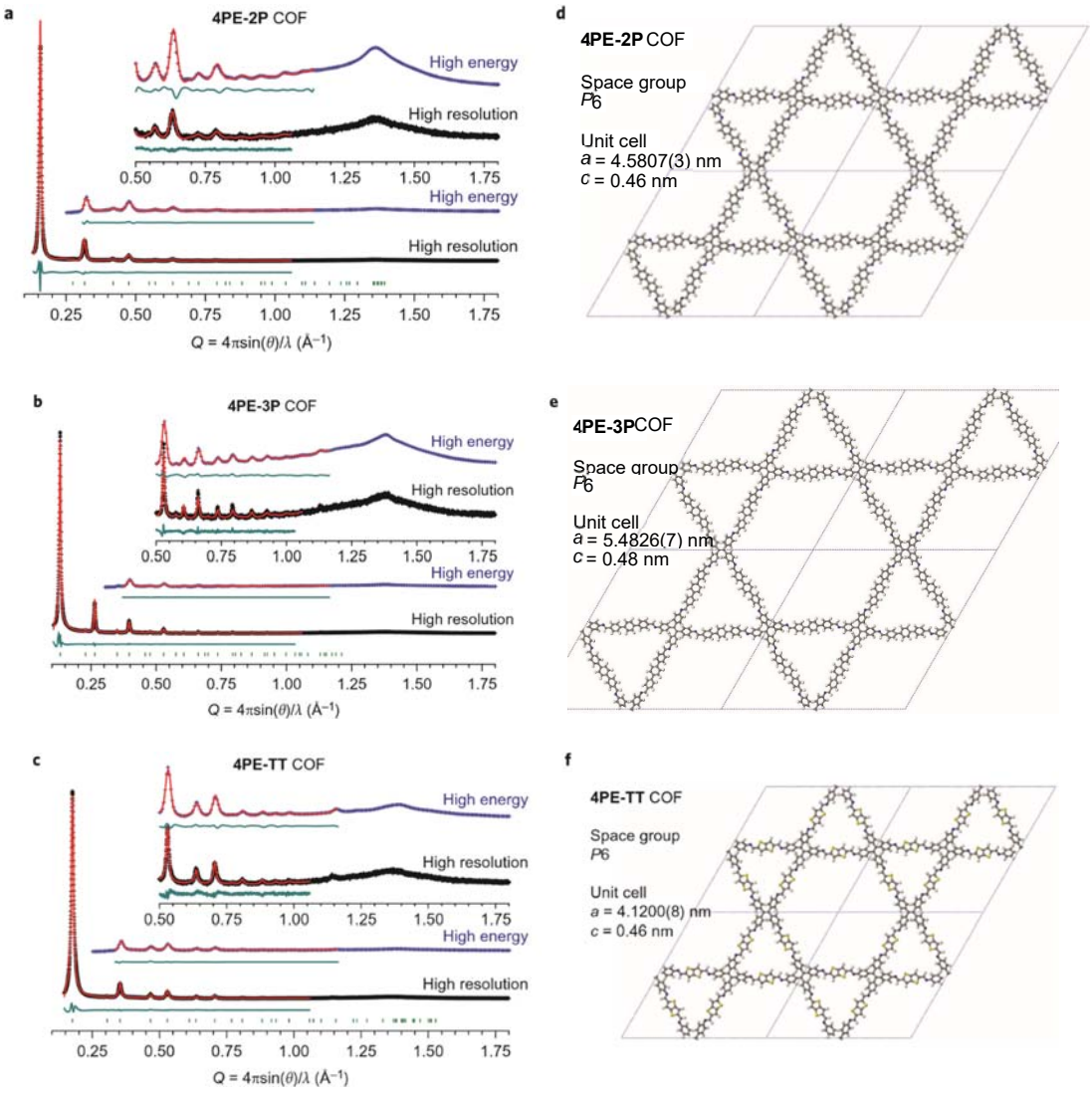


Figure 4.3: PXRD patterns and the corresponding Rietveld-refined structures illustrate the high degree of order within the 4PE-based COF networks. a–c, Experimental synchrotron PXRD data (black, high-resolution X-ray scattering; blue, high-energy X-ray total scattering) of the 4PE-2P COF (a), 4PE-3P COF (b) and 4PE-TT COF (c). Simultaneous Rietveld refinements of the high-resolution and high-energy data sets (red lines) provide good fits to the experimental data with only minimal differences (the green lines show the difference plots between the experimental PXRD patterns and those obtained by Rietveld refinements). Bragg positions are indicated by light green ticks. λ = 0.41417 Å for the high-resolution data (black) and 0.2114 Å for the high-energy data (blue). Insets, magnified views onto the $Q > 0.5$ Å$^{-1}$ region show well-defined higher-order reflections. d–f, The corresponding Rietveld-refined COF structures of the 4PE-2P (a), 4PE-3P (b) and 4PE-TT (c) COFs assuming P6 symmetry (available as Supplementary Information).

Regarding the interlayer distance (that is, the c lattice vector), the dispersion-corrected PBE calculations predict a value of 0.46 nm for both 4PE-2P and 4PE-TT, in excellent agreement with the experiments. This confirms that this dimension is governed by interactions between the 4PE units, and is relatively independent of the bridging moiety.

A perfectly defect-free crystal domain of P6 symmetry would be built up by 4PE units that all have the same direction of rotation (Figure 4.4). As the introduction of even a single 4PE column of the 'wrong' propeller enantiomer would cause considerable strain in the framework, synchronizing the molecular conformation of all the 4PE units throughout a COF domain appears to be of key importance. We propose that this synchronization can only be achieved if the linear bridging unit is able to transmit information on the molecular configuration between adjacent 4PE units during COF growth.

Dividing the COF in a 'thought experiment' into phenylene– bridge–phenylene fragments we find a C2 axis in the center of the bridging unit (inset of Figure 4.4). Based on this consideration we can anticipate well-ordered systems for linear building blocks with a strong tendency to adopt a C2-symmetric configuration, whereas mirror-symmetric bridging units cannot synchronize the 4PE units.

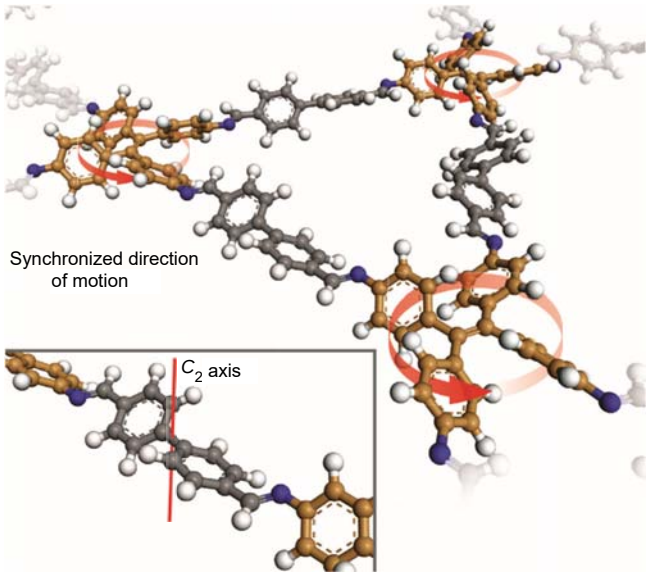


Figure 4.4: Fragment of the 4PE-2P COF structure. The direction of rotation (red arrows) of 4PE entities (C, orange; N, blue; H, white) is synchronized via the molecular conformation of the linear bridging unit (C, grey; H, white). Inset, a cut-out showing the $C_2$-symmetric bridging unit that is crucial for transmitting information on the molecular conformation of the 4PE entities.

Indeed, the 2P and 3P units seem to be able to transfer this information efficiently, possibly via the tilt of their terminal phenylenes. If the bridging unit, however, is reduced to a single aromatic ring, as in the case of the 4PE-1P COF, this mechanism might not be operational. In a *P*6-symmetric setting the rigid 1P would be required to assume an intermediate position, that is be co-planar with the ab plane. As both the cis and trans configurations of the terminal aldehydes have approximately the same energy, the 1P building block cannot impose a synchronized direction of rotation on all the 4PE entities, which possibly results in an increased defect density. Indeed, we observed a lower crystallinity for the 4PE-1P COF compared with that of its larger homologues (Figure S 4.3). Even though the relative ratios of the peak intensities correspond well to those of the proposed model, the broader and strongly asymmetrically shaped peaks could not be modelled so well by the data, which indicates the presence of considerably more disorder in this framework.

The TT bridging unit, on the other hand, proved to be capable of generating very well-ordered frameworks. Although this rigid building block is also expected to be co-planar with the ab plane in a P6-symmetric COF, the inherent C2 symmetry of this molecule and its stronger electronic interaction with the imine bonds seem to provide a functional path for directing the conformation of adjacent 4PE units.

Given their well-defined geometries, the new COFs are expected to form porous structures with two precisely defined pore sizes. The nitrogen sorption isotherms recorded at 77 K exhibit a type IV isotherm with two sharp steps and an H1 hysteresis loop (Figure 4.5a).

Quenched-solid DFT calculations using an equilibrium model and assuming a cylindrical pore geometry show the existence of two types of pores with narrow size distributions in each of the COFs (Figure 4.5b)[34-35]. The obtained pore diameters of 2.9, 3.8, 4.5 and 3.2 nm for the large hexagonal pores of the 4PE-1P, 4PE-2P, 4PE-3P and 4PE-TT COFs, respectively, are in very good agreement with the simulated pore sizes of 2.9, 3.8, 4.5 and 3.3 nm, respectively. For the smaller trigonal pores we obtained pore sizes of 1.6, 1.7, 1.8 and 1.6 nm, which are consistent with those of the simulated structures. The Brunauer–Emmett–Teller surface areas of the four COFs are 2140 ± 50 $m^2 g^{-1}$ (4PE-1P), 2070 ± 50 $m^2 g^{-1}$ (4PE-2P), 1000 ± 50 $m^2 g^{-1}$ (4PE-3P) and 1990 ± 50 $m^2 g^{-1}$ (4PE-TT) with total pore volumes of 1.31 $cm^3 g^{-1}$, 1.53 $cm^3 g^{-1}$, 0.844 $cm^3 g^{-1}$ and 1.24 $cm^3 g^{-1}$ , respectively. Some of these surface areas are among the highest reported surface areas for imine-linked COFs[2, 27].

Transmission electron microscopy (TEM) images of 4PE-3P COF powder samples reveal the nanoscale morphology of individual COF crystallites (Figure 4.5c). Typical domain sizes range

from 50 to 100 nm. Straight porous channels that extend through entire crystal domains can be observed. Domains oriented with their ab plane perpendicular to the viewing direction show the highly ordered hexagonal arrangement of the mesopores and exhibit clearly observable hexagonal facets, which highlights the crystallinity of this material. To the best of our knowledge this is the first time that such faceting has been observed for COF nanocrystals.

Having demonstrated that highly crystalline frameworks can be obtained for combinations of 1 with different linear building blocks, we decided to test the generality of our approach by extending our study to other propeller-shaped building blocks (Figure 4.2b). Triphenylamine (3PA) can be seen as a trigonal complement to 4PE with comparable steric interactions between its aromatic rings. Although the terminal phenylenes of triphenylbenzene (3PB) are expected to interact less strongly with each other, the preferred conformation of this building block is propeller-like as well. We employed both trigonal building blocks terminated with amino groups (3a and 3b) in the synthesis of imine-linked COFs using 2P and TT as their linear counterparts. The resulting frameworks exhibited a very high crystallinity with sharp and well-defined higher-order reflections similar to those of the 4PE COFs (Figure S 4.4 and S 4.5). Pawley refinement of the 3PA- and 3PB-containing COFs based on P6-symmetric structure models produced the lattice parameters listed in Table 4.2.

Similar to the case of the 4PE COFs, the c axis seems to be determined by the nature of the propeller-shaped building block. The smaller tilt angle of the terminal aromatic rings of 3PB compared with that of 4PE (30° versus 44° according to our DFT simulations of the COFs) seems to allow for a closer layer stacking, and thus a reduced length of the c axis. Still, the high order caused by a single, well-defined lateral position is retained.

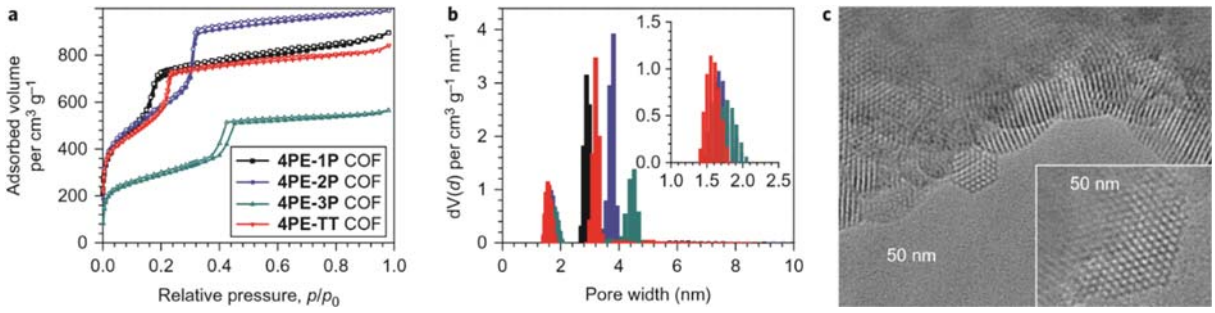


Figure 4.5: Porosity and real-space images of the 4PE-based COFs. a, Nitrogen sorption isotherms of the 4PE-1P (black), 4PE-2P (blue), 4PE-3P (green) and 4PE-TT (red) COFs exhibit type IV isotherms. Filled symbols, adsorption; open symbols, desorption. b, Corresponding pore-size distributions indicate the presence of both micro- and mesopores. Inset, enlargement of the microporous region. c, TEM images of 4PE-3P COF that show the faceted COF crystallites with a hexagonal arrangement of the mesopores. Inset, magnified view onto a single COF crystallite.

## 4.4 CONCLUSION

In this study, we utilized the inherent molecular conformation of rigid, propeller-shaped building units to define self-repeating docking sites for the attachment of consecutive COF layers. In this way, we were able to realize COFs that feature, to the best of our knowledge, an as yet unmatched degree of crystallinity and well-defined crystal facets.

Studying a series of COFs that comprise bridging units of different molecular symmetry and conformational flexibility enabled us to gain insights into the conveyance of configurational information during the COF formation, and highlights the importance of designing intra- and interlayer interactions. With the generality of this approach demonstrated for a number of combinations of different building blocks and bridging units, we expect this concept to be applicable to a broad variety of functional building blocks and to promote the establishment of COFs in catalysis and organic electronics.

**Methods**

4PE-1P COF. 1 (5.9 mg, 15 μmol, 1 equiv.) and 1P (4.0 mg, 30 μmol, 2 equiv.) were suspended in a mixture of 1,4-dioxane (149 μl) and mesitylene (33 μl). The resulting mixture was vortexed until complete dissolution of the reactants was achieved. Aqueous acetic acid (6 M, 18 μl) was added and the mixture kept in a glass tube at 120 °C for four days. The resulting bright-yellow precipitate was collected by filtration, washed with 1,4-dioxane and dried under reduced pressure. Analysis (calculated, found for $C_{126}H_{84}N_{12}$): C (85.29, 83.92), H (5.23, 4.78), N (9.47, 9.31).

4PE-2P COF. 1 (5.9 mg, 15 μmol, 1 equiv.) and 2B (6.3 mg, 30 μmol, 2 equiv.) were suspended in 1,4-dioxane (273 μl). The resulting mixture was vortexed until complete dissolution of the reactants was achieved. Aqueous acetic acid (6 M, 27 μl) was added and the mixture kept in a glass tube at 120 °C for four days. The resulting light-orange precipitate was collected by filtration, washed with 1,4-dioxane and dried under reduced pressure. Analysis (calculated, found for $C_{162}H_{108}N_{12}$): C (87.22, 86.30), H (5.24, 4.97), N (7.53, 7.44).

4PE-3P COF. 1 (5.9 mg, 15 μmol, 1 equiv.) and 3P (8.1 mg, 30 μmol, 2 equiv.) were suspended in a mixture of 1,4-dioxane (149 μl) and mesitylene (33 μl). The mixture was vortexed and aqueous acetic acid (6 M, 18 μl) added. The mixture was kept in a glass tube at 120 °C for four days to yield an ochre precipitate. The product was filtered, washed with 1,4-dioxane and dried

under reduced pressure. Analysis (calculated, found for $C_{198}H_{132}N_{12}$): C (88.49, 86.33), H (5.25, 5.04), N (6.25, 6.27).

4PE-TT COF. Under argon, 1 (11.7 mg, 30 µmol, 1 equiv.) and TT (11.8 mg, 60 µmol, 2 equiv.) were dissolved in 1 ml of a 1:9 v/v mixture of mesitylene and benzyl alcohol at 120 °C. The solution was cooled to room temperature and aqueous acetic acid (6 M, 100 µl) added. The mixture was kept in a glass tube at 120 °C for three days. The resulting red precipitate was collected by filtration, washed with DMF and dried under reduced pressure. Analysis (calculated, found for $C_{126}H_{72}N_{12}S_{12}$): C (70.76, 70.12), H (3.39, 3.72), N (7.86, 7.87), S (17.99, 17.30).

# 4.5 SUPPORTING INFORMATION

## Abbreviations

BET Brunauer-Emmett-Teller

DFT density functional theory

DMSO dimethyl sulfoxide

PDF pair distribution function

PXRD powder X-ray diffraction

QSDFT quenched solid density functional theory

TEM transmission electron microscopy

THF tetrahydrofuran

### A. Materials and methods

Unless stated otherwise, all reactions were performed in oven dried glassware under ambient atmosphere. All reagents and solvents were obtained from commercial suppliers and used as received.

1,1,2,2-Tetrakis-(4-nitrophenyl)ethylene and 1,1,2,2-tetrakis(4-aminophenyl)ethylene were synthesized following published procedures.[36]

**Nuclear magnetic resonance** (NMR) spectra were recorded on Bruker AV 400 and AV 400 TR spectrometers. Proton chemical shifts are expressed in parts per million ($\delta$ scale) and are calibrated using residual undeuterated solvent peaks as an internal reference (DMSO-$d_6$: 2.50). Data for $_1$H NMR spectra are reported in the following way: chemical shift ($\delta$ ppm) (multiplicity, coupling constant/Hz, integration). Multiplicities are reported as follows: s = singlet, d = doublet, t = triplet, q = quartet, m = multiplet, br = broad, or combinations thereof.

**Infrared** (IR) **spectra** were recorded on a Thermo Scientific Nicolet™ 6700 FTIR spectrometer in transmission mode. IR data are reported with a wavenumber ($cm^{-1}$) scale.

**UV-Vis spectra** were recorded using a PerkinElmer Lambda 1050 spectrometer equipped with a 150 mm InGaAs integrating sphere. Diffuse reflectance spectra were collected with a Praying Mantis (Harrick) accessory and were referenced to barium sulfate powder as white standard.

**Photoluminescence** (PL) measurements were performed using a home-built setup consisting of a Horiba Jobin Yvon iHR 320 monochromator equipped with a photomultiplier tube and a liquid $N_2$-cooled InGaAs detector. The samples were illuminated with a pulsed (83 Hz) 365 nm LED at a light intensity of 500 mW $cm^{-2}$.

**Thermogravimetric analysis** (TGA) measurements were performed on a Netzsch Jupiter ST 449 C instrument equipped with a Netzsch TASC 414/4 controller. The samples were heated from room temperature to 900 °C under a synthetic air atmosphere at a heating rate of 1 K/min.

The **nitrogen sorption** isotherms were recorded on a Quantachrome Autosorb 1 at 77 K in a pressure range from $p/p^0$ = 0.001 to 0.98. Prior to the measurement of the sorption isotherm the samples were outgassed for 24 h at 120°C under high vacuum. For the evaluation of the surface area the BET model was applied between 0.05 and 0.2 $p/p^0$. The calculations of the pore size distribution were performed using the QSDFT equilibrium model with a carbon kernel for cylindrical pores.

**Powder X-ray diffraction** (PXRD) measurements were performed using a Bruker D8 Discover with Ni-filtered Cu $K_\alpha$ radiation and a LynxEye position-sensitive detector. Background correction was performed using spline-interpolated and intensity-adapted measurements of the empty sample holder.

The initial **structure models of the COFs** were built using the Forcite module of the Accelrys Materials Studio software package. We applied the space group with the highest possible symmetry, i.e. *P*6, taking into account the propeller-like conformation of the central building blocks. Using this coarse model we determined the unit cell parameters via Pawley refinement of our PXRD data. In order to obtain a more realistic picture of the local molecular arrangement, we then performed DFT geometry optimizations based on the refined unit cell parameters using the CASTEP module and the LDA/CA-PZ functional. These models were suitable for subsequent Rietveld refinements.

**Synchrotron X-ray scattering** measurements were undertaken for capillary-loaded samples at the Advanced Photon Source at Argonne National Laboratory. High-resolution powder X-ray diffraction data were collected at ambient temperature and at 100 K at beamline 11-BM with the use of a 12-detector/analyzer system, with the data from the detectors corrected and merged into a single diffraction pattern. Samples were spun at 90 Hz to ensure good powder averaging.

High energy X-ray total scattering data suitable for diffraction and **pair distribution function** (PDF) analysis were collected at beamline 11-ID-B using high energy X-rays (58 keV, 0.2114 Å wavelength) in combination with a large amorphous-Si based area detector from Perkin-Elmer. The two-dimensional scattering images were reduced to one-dimensional data within Fit2d. PDF's, $G(r)$, were extracted from the data within PDFgetX2, subtracting contributions from the background and inelastic scattering before Fourier transforming the data to $Q_{max}$ = 19.8 Å$^{-1}$. There was no evidence for preferred orientation effects in the diffraction images. PDFs were calculated for the diffraction-optimized structural models within PDFgui.

Structural analysis of the powder diffraction data (both high resolution and high energy data) were undertaken by **Rietveld refinement**, as implemented within TOPAS. The high energy data collected using an area detector provided improved signal-to-noise for the higher angle reflections. The DFT-optimized structures were used as starting models for the structural refinements. Refinements were undertaken in the *P*6 space group, as this was the highest symmetry predicted from the DFT calculations.

**Single-crystal X-ray diffraction** data were collected with an Xcalibur3 diffractometer equipped with a Spellman generator (voltage 50 kV, current 40 mA) and a Kappa CCD detector, and using Mo K$_\alpha$ radiation ($\lambda$ = 0.71073 Å). The data collection was performed with the CrysAlis CCD software[37] and the data reduction was achieved with the CrysAlis RED software.[38] The structure was solved with SIR-92, refined with SHELXL-97 and checked using PLATON.[39-43] The absorptions were corrected by the SCALE3 ABSPACK multiscan method.[44] Crystallographic data for the structure have been deposited with the Cambridge Crystallographic Data Centre, CCDC, 12 Union Road, Cambridge CB21EZ, UK. Copies of the data can be obtained free of charge on quoting the depository number CCDC 1055083 (http://www.ccdc.cam.ac.uk).

**DFT calculations** were performed with the CASTEP code using the generalized-gradient-approximation PBE functional. The energy cutoff for the planewave basis-set was set to 310.0 eV, ions were represented with ultrasoft pseudopotentials and k-point sampling was performed with a 1x1x4 Monkhorst-Pack grid (1x1x2 for the double layer structures). To account for dispersion interactions, we used the correction scheme of Tkatchenko and Scheffler.

**Transmission electron microscopy** (TEM) was performed on an FEI Titan Themis equipped with a field emission gun operated at 300 kV.

## B. Synthetic procedures

1,1,2,2-Tetrakis(4-nitrophenyl)ethene (4)

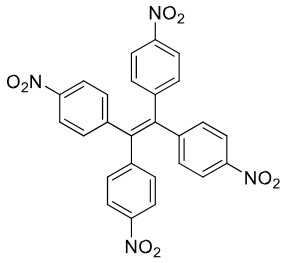


A mixture of 30 mL fuming nitric acid and 30 mL glacial acetic acid was cooled to 0°C. 1,1,2,2,-Tetraphenylethene (3.00 g, 9.00 mmol) was added in small portions and the mixture was allowed to warm to room temperature. After stirring for 3 h the solution was poured into ice water. The resulting precipitate was filtered off, washed with water and recrystallized from 1,4-dioxane to yield bright yellow crystals of **4** (2.05 g, 4.00 mmol, 44.4 %).

$^1$H NMR (400 MHz, DMSO-$d_6$): 8.11 (d, $J$ = 8.00 Hz, 8 H), 7.37 (d, $J$ = 8.00 Hz, 8 H).

**1,1,2,2-Tetrakis(4-aminophenyl)ethene (1)**

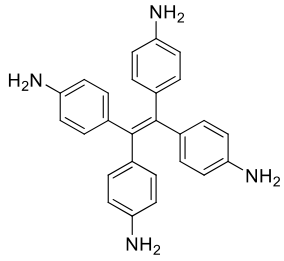


Under nitrogen, compound **4** (1.00 g, 1.95 mmol) was dissolved in 20 mL of THF. Raney Nickel (ca. 4 g) and hydrazine monohydrate (1.30 mL, 26.7 mmol) were added to the solution and the mixture was refluxed for 2 h. The solution was allowed to cool to 55 °C and the Raney Nickel was filtered off. All volatiles were evaporated under reduced pressure, yielding the title compound (0.75 g, 1.92 mmol, 98 %) as a yellow powder.

$^1$H NMR (400 MHz, DMSO-$d_6$): 6.57 (d, $J$ = 8.00 Hz, 8 H), 6.26 (d, $J$ = 8.00 Hz, 8 H), 4.85 (s, 8 H).

**4PE(benzaldehyde)$_4$ (2)**

In an argon atmosphere, dry benzaldehyde (53 mg, 0.5 mmol, 5 equiv.) was added to a suspension of **1** (39.2 mg, 0.10 mmol, 1 equiv.) in anhydrous 1,4-dioxane (0.5 mL) and $CHCl_3$ (2 mL). After addition of 5 beads of 3 Å molecular sieve, the reaction mixture was heated at 70 °C for 16 h. Upon slow cooling yellow needles formed, which were isolated by filtration and dried under reduced pressure. Crystals suitable for X-ray structure analysis were grown from a THF/1,2-dichloroethane (1:1 *v*:*v*) solution.

**3PA-2P COF**

Under argon, tris(4-aminophenyl)amine **3a** (8.7 mg, 30 µmol, 1 equiv.) and biphenyl-4,4'-dicarboxaldehyde (9.5 mg, 45 µmol, 1.5 equiv.) were dissolved in 500 µL of a 19:1 *v*:*v* mixture of anisole and 1,4-dioxane at 120 °C. Upon cooling to room temperature, aqueous acetic acid (6 M, 50 µL) was added and the reaction mixture was kept at 100 °C for 3 days, yielding an orange precipitate. The product was isolated via filtration.

**3PA-TT COF**

In an argon atmosphere, tris(4-aminophenyl)amine **3a** (8.7 mg, 30 µmol, 1 equiv.) and thieno[3,2-*b*]thiophene-2,5-dicarboxaldehyde (8.8 mg, 45 µmol, 1.5 equiv.) were dissolved in 500 µL of a 9:1 *v*:*v* mixture of mesitylene and benzyl alcohol at 120 °C. After cooling to room temperature, aqueous acetic acid (6 M, 50 µL) was added. The reaction mixture was kept at 120 °C for 4 days, yielding a dark purple precipitate. The product was isolated via filtration.

**3PB-TT COF**

In an argon atmosphere, tris(4-aminophenyl)benzene **3b** (14.1 mg, 40 µmol, 1 equiv.) and thieno[3,2-*b*]thiophene-2,5-dicarboxaldehyde (11.8 mg, 60 µmol, 1.5 equiv.) were suspended in 1 mL of a 9:1 *v*:*v* mixture of anisole and ethanol. Aqueous acetic acid (6 M, 100 µL) was added and the resulting reaction mixture was kept at 100 °C for 5 days. The resulting yellow precipitate was isolated via filtration.

## C. Single crystal structure of compound 2

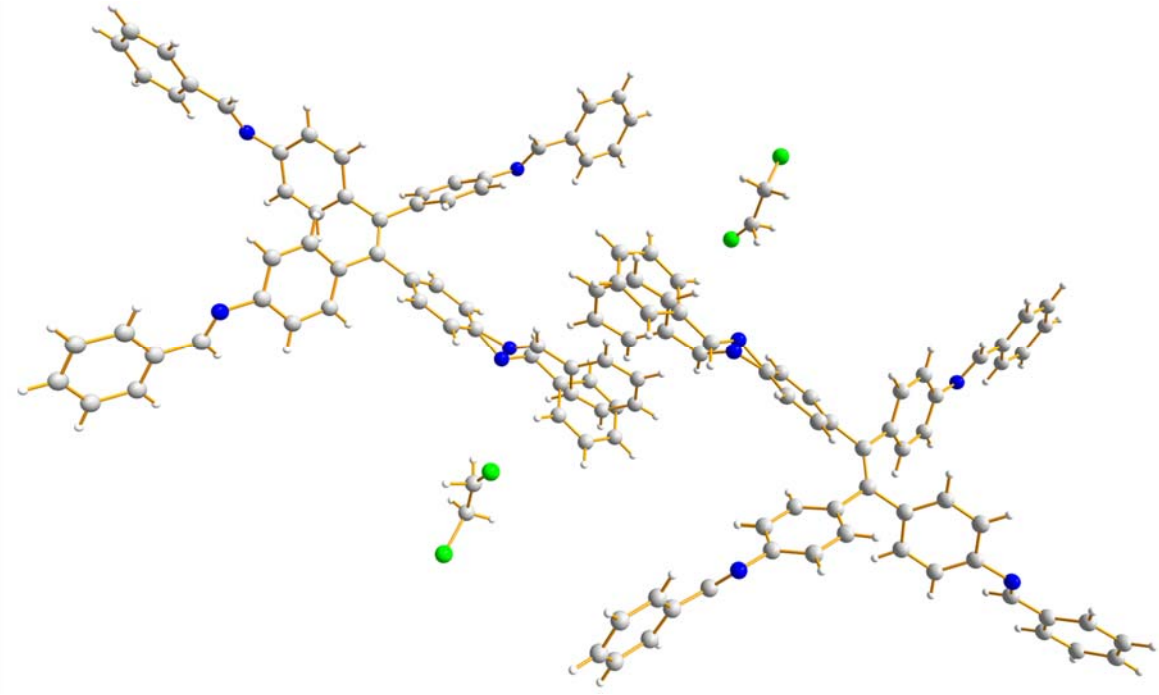

Figure S 4.1: Single-crystal X-ray structure of compound 2. Color scheme: carbon (grey), hydrogen (white), chlorine (green), nitrogen (blue). The structure contains one right-turning and one left-turning molecule per unit cell. The branches closest to the other molecule were refined having two positions with 50% occupancy each.

Table 4.1: Crystal structure data of compound **2**.

| | |
|---|---|
| Formula | $C_{56}H_{44}Cl_2N_4$ |
| M | 843.85 |
| T / K | 173(2) |
| Colour, habit | yellow block |
| Cryst. Size / mm | 0.2 x 0.2 x 0.1 |
| Crystal system | triclinic |
| Space group | *P*–1 |

| | |
|---|---|
| $\rho_{calcd}$ / g cm$^{-3}$ | 1.254 |
| $\mu$ / mm$^{-1}$ | 0.188 |
| Irradiation / Å | 0.71073 |
| *F* (000) | 884 |
| Index ranges | $-11 \leq h \leq 10$ |
| | $-18 \leq k \leq 18$ |
| | $-20 \leq l \leq 19$ |

| | |
|---|---|
| $a$ / Å | 9.3210(5) |
| $b$ /Å | 15.2640(9) |
| $c$ / Å | 16.6530(7) |
| $\alpha$ / ° | 74.721(4) |
| $\beta$ / ° | 84.365(4) |
| $\gamma$ / ° | 78.162(4) |
| $V$ / Å$^3$ | 2234.5(2) |
| $Z$ | 2 |
| | |
| | |

| | |
|---|---|
| Reflns. collected | 17004 |
| Reflns. unique | 8138 |
| Reflns. obsd. | 5453 |
| $R_{int}$ | 0.0330 |
| Params. refined | 669 |
| $\theta$ range / ° | 4.098 - 25.350 |
| $R_1$, $wR_2$ [I > 2$\sigma$(I)] | 0.0526, 0.1212 |
| $R_1$, $wR_{2\ (all\ data)}$ | 0.0874, 0.1422 |
| GooF | 1.022 |
| $\delta p_{max}$, $\delta p_{min}$ / e nm$^{-3}$ | 0.431, −0.335 |

When the final .cif file for compound 2 was checked using the IUCr checkCIF routine, a B-level alert appeared in the output.

PLAT910_ALERT_3_B Missing # of FCF Reflection(s) Below Th(Min) ... 34 Report.

This is attributed to the fact that, due to the large unit cell of this compound, some reflections (34) appear below $\theta_{min}$ and were thus masked by the beamstop. However, considering the large number of collected reflections (17004), the quality and reliability of the structure solution are not dependent on the reflections below $\theta_{min}$.

## D. Pair distribution analysis

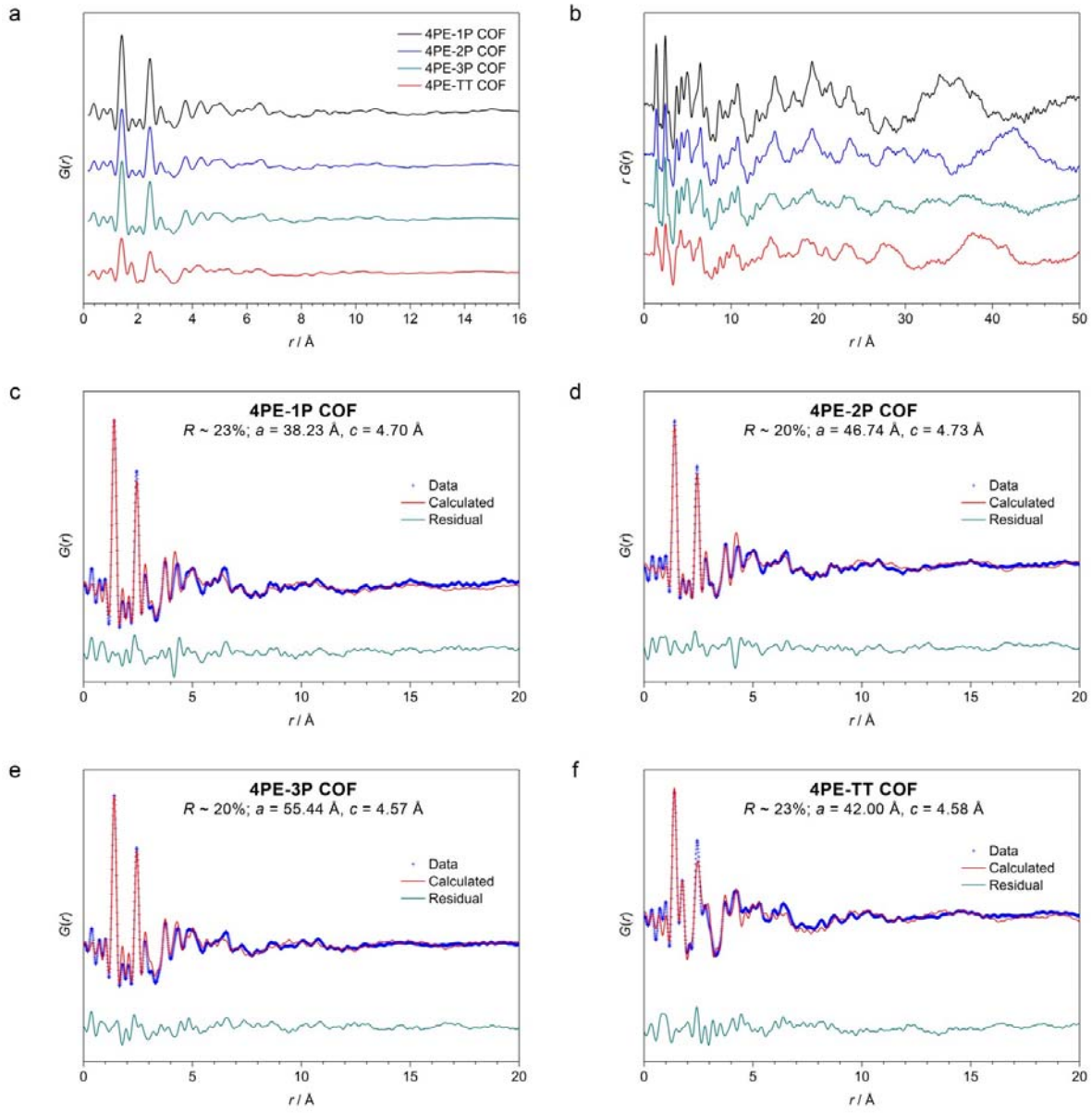


Figure S 4.2: The PDF data for the COFs. a, PDF, G(r), and b, the r-multiplied G(r), which highlights features at longer distance. c, d, e, f, Fits of the structural models to the PDF data.

## E. PXRD analysis and structure simulations of the 4PE-1P COF

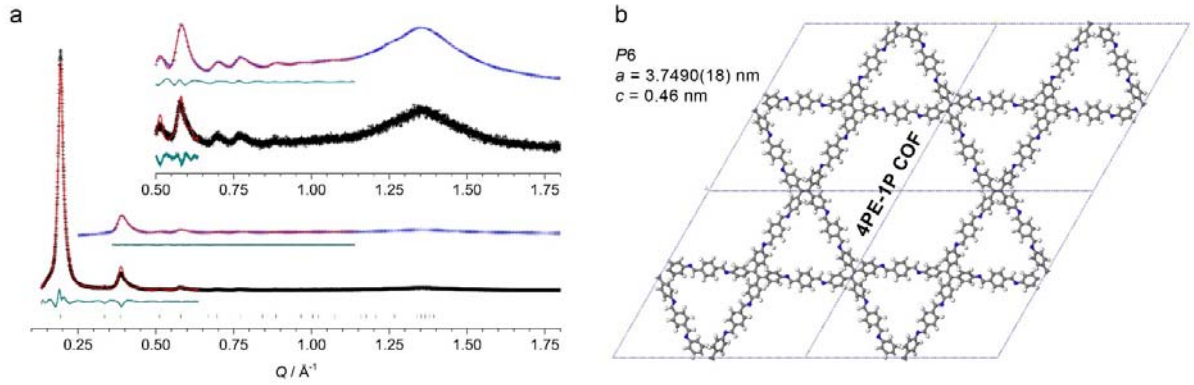


Figure S 4.3: PXRD patterns and Rietveld-refined structure of the 4PE-1P COF. a, Experimental synchrotron PXRD data (black: High-resolution X-ray scattering, blue: High energy X-ray total scattering) and Rietveld-refined patterns (red), difference plots (green) and Bragg positions (vertical ticks). Insets, magnified view onto the Q > 0.5 Å-1 region. b, Corresponding Rietveld-refined COF structure.

## F. PXRD analysis and simulated structures of the 3PA- and 3PB-based COFs

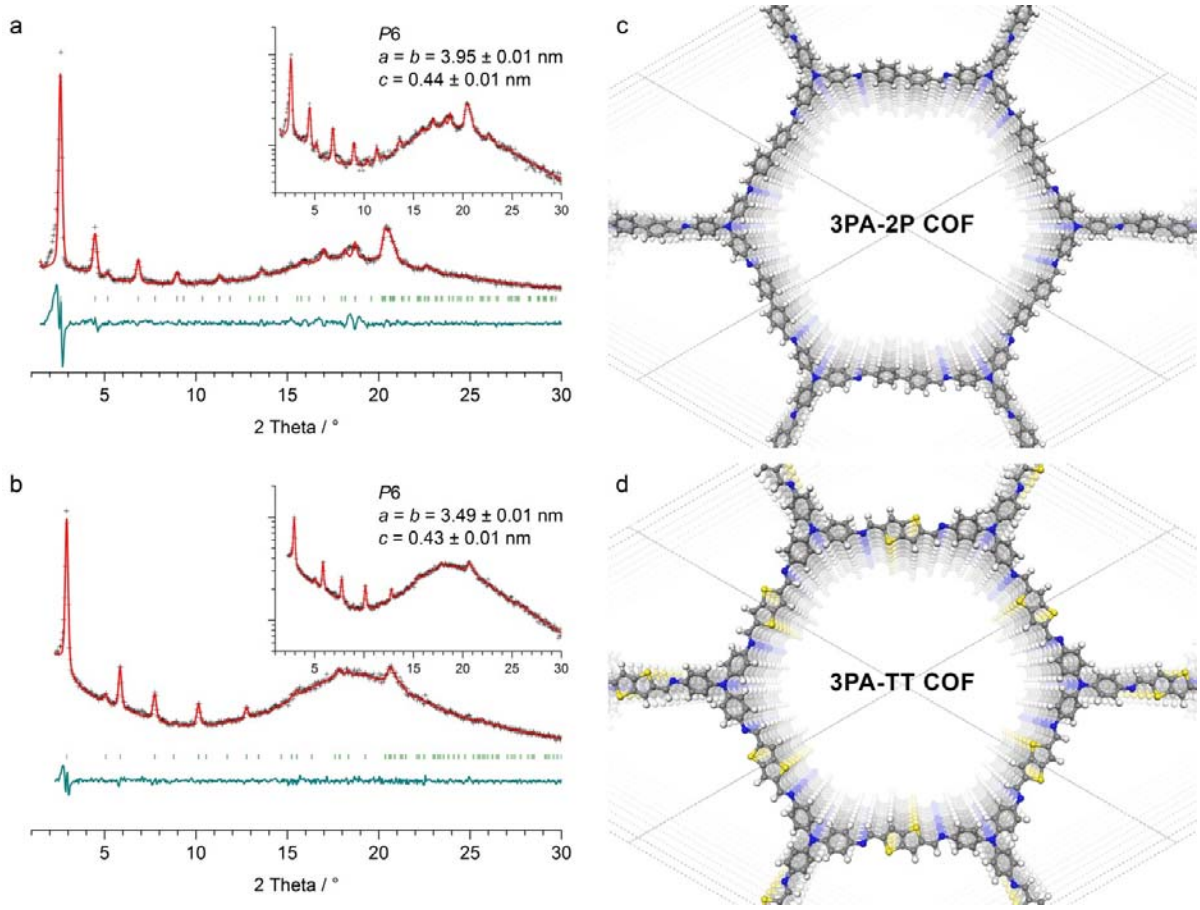


Figure S 4.4: PXRD patterns of the triphenylamine (3PA) containing COFs and the corresponding simulated structures. a, b, Experimental (black symbols) and Pawley-refined (red) PXRD patterns, Bragg positions (green symbols) and difference plots (green) of the 3PA-2P COF (a) and 3PA-TT COF (b). c, d Simulated structures of the 3PA-2P COF (c) and 3PA-TT COF (d).

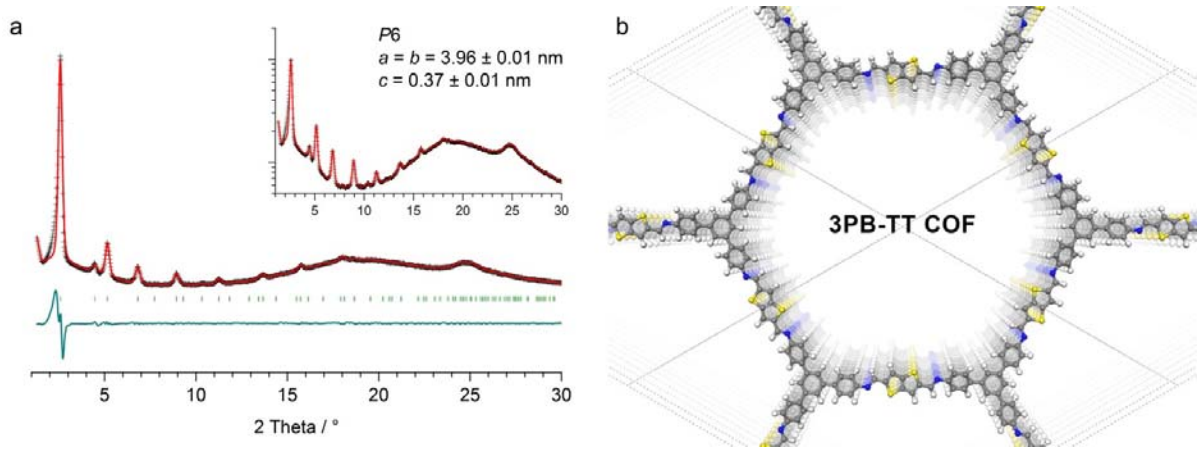


Figure S 4.5: PXRD pattern of the triphenylbenzene (3PB) containing 3PB-TT COF and the corresponding simulated structure. a, Experimental (black symbols) and Pawley-refined (red) PXRD pattern, Bragg positions (green symbols) and difference plot (green). b, Simulated structure of the 3PB-TT COF.

Table 4.2: Lattice parameters of the 3PA- and 3PB-based COFs.

| COF | *a*, *b* / nm | *c* / nm |
|---|---|---|
| **3PA-2P** | 3.95 ± 0.01 | 0.44 ± 0.01 |
| **3PA-TT** | 3.49 ± 0.01 | 0.43 ± 0.01 |
| **3PB-TT** | 3.96 ± 0.01 | 0.37 ± 0.01 |

## G. Stability tests

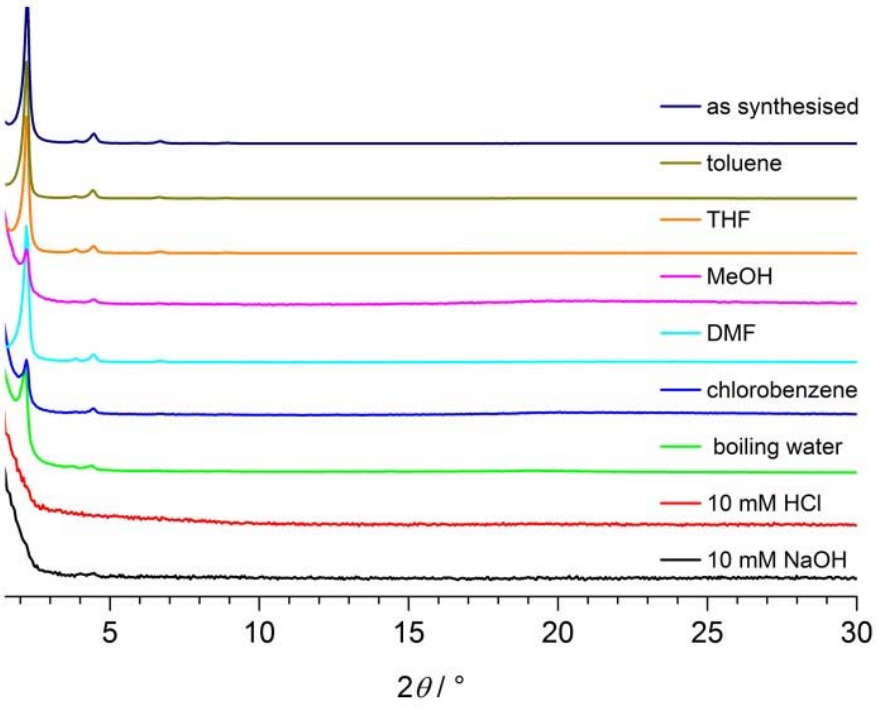


Figure S 4.6: Stability tests of the 4PE-2P COF. Immersing the 4PE-2P COF in common organic solvents or boiling water reveals the high physicochemical stability of the new COF. The immersion times were 24 h for organic solvents and 4 h for water, acid and base, respectively.

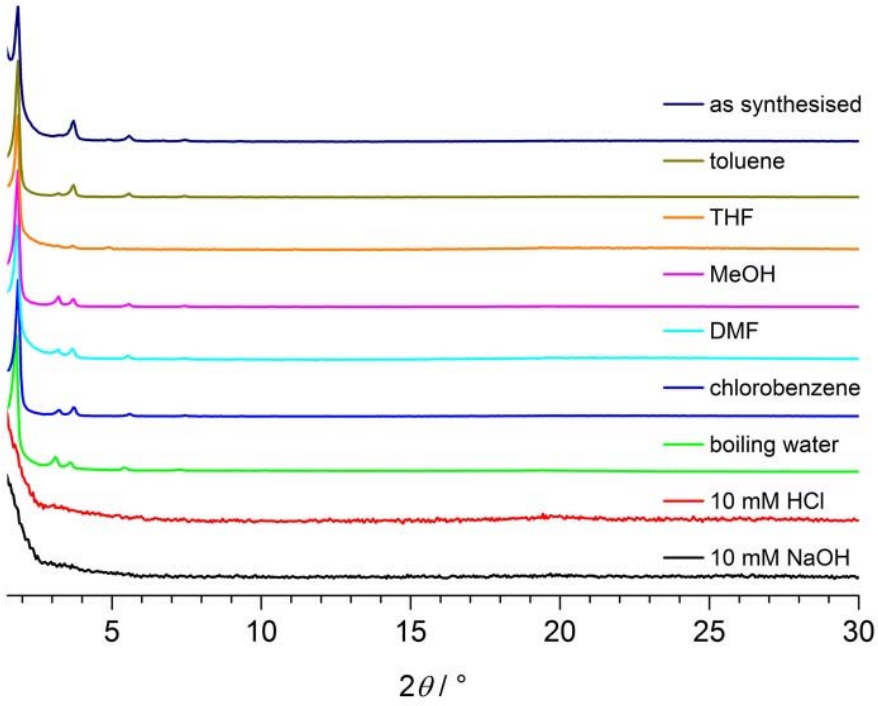


Figure S 4.7: Stability tests of the 4PE-3P COF. The 4PE-3P COF shows high physicochemical stability towards common organic solvents or boiling water. The immersion times were 24 h for organic solvents and 4 h for water, acid and base, respectively.

**H. DFT simulations**

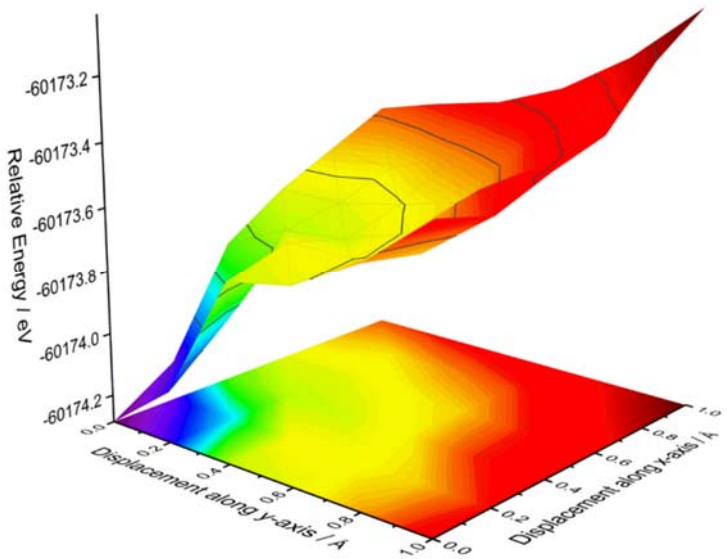


Figure S 4.8: PBE+D potential energy surface for the horizontal displacement of two 4PE-2P layers relative to each other.

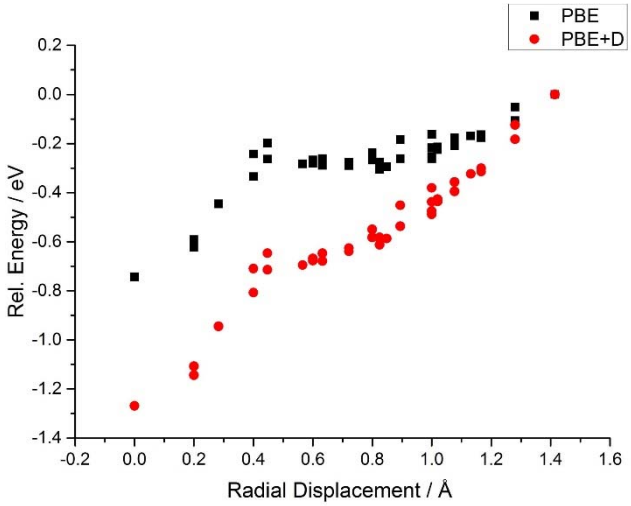


Figure S 4.9: Comparison of the potential energy surfaces obtained from pure and dispersion-corrected PBE calculations. Plot of radial displacement versus relative energy for dispersion corrected (PBE+D) and uncorrected potential energy surface scans.

## I. Optical spectroscopy

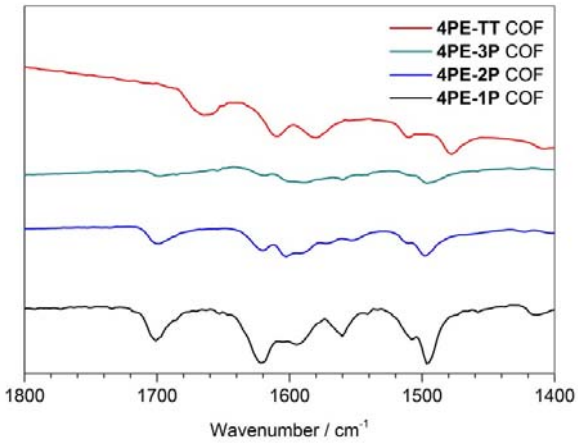


Figure S 4.10: FT-IR spectra of the 4PE-based COFs. Enlargement of the fingerprint region below 1800 $cm^{-1}$ showing the signals of the characteristic C=N stretching vibration (wavenumbers are given in the following Table 4.3).

Table 4.3: C=N stretching vibrations of the 4PE-based COFs.

| | C=N / $cm^{-1}$ |
|---|---|
| **4PE-P** COF | 1618 |
| **4PE-2P** COF | 1620 |
| **4PE-3P** COF | 1620 |
| **4PE-TT** COF | 1608 |

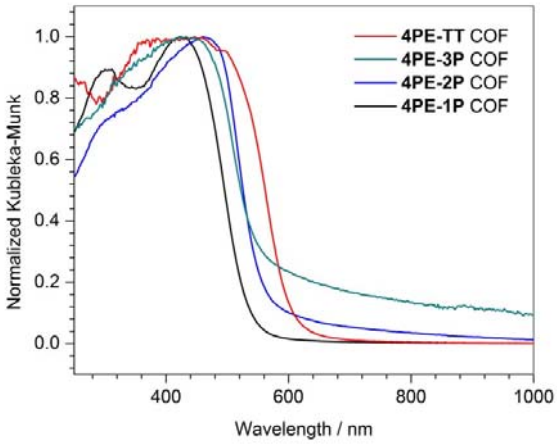


Figure S 4.11: UV-vis diffuse reflectance spectra of the 4PE-containing COFs. The data are expressed in Kubelka-Munk units and normalized to the strongest absorption.

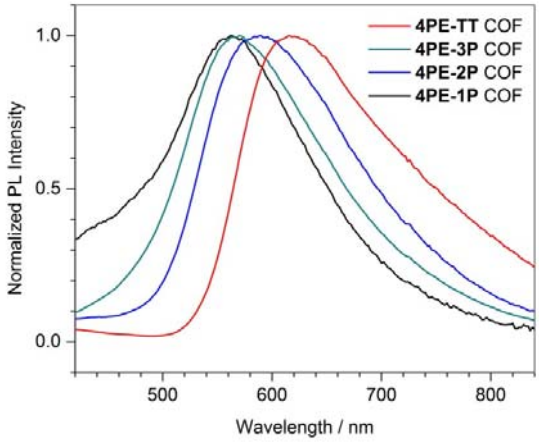


Figure S 4.12: Photoluminescence emission spectra of the 4PE-based COFs. The COFs were measured as optically dense powders using 365 nm illumination.

## K. Thermogravimetric analysis

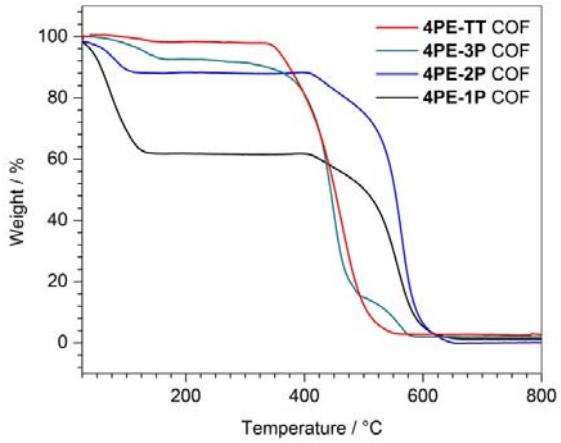


Figure S 4.13: Thermogravimetric analysis of the 4PE-containing COFs. The samples were heated at 1 K min-1 in a constant flow of synthetic air.

## L. NMR spectroscopy

**Compound 4** 400 MHz, DMSO-$d_6$

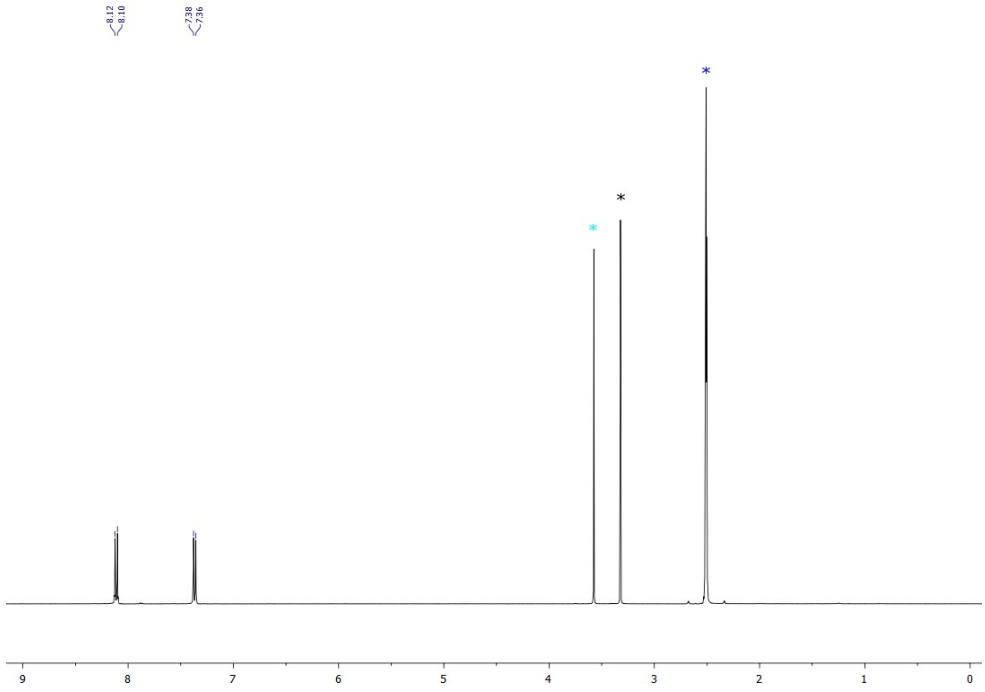


Solvent residues: 1,4-dioxane (cyan), water (black), DMSO (blue).

**Compound 1** 400 MHz, DMSO-$d_6$

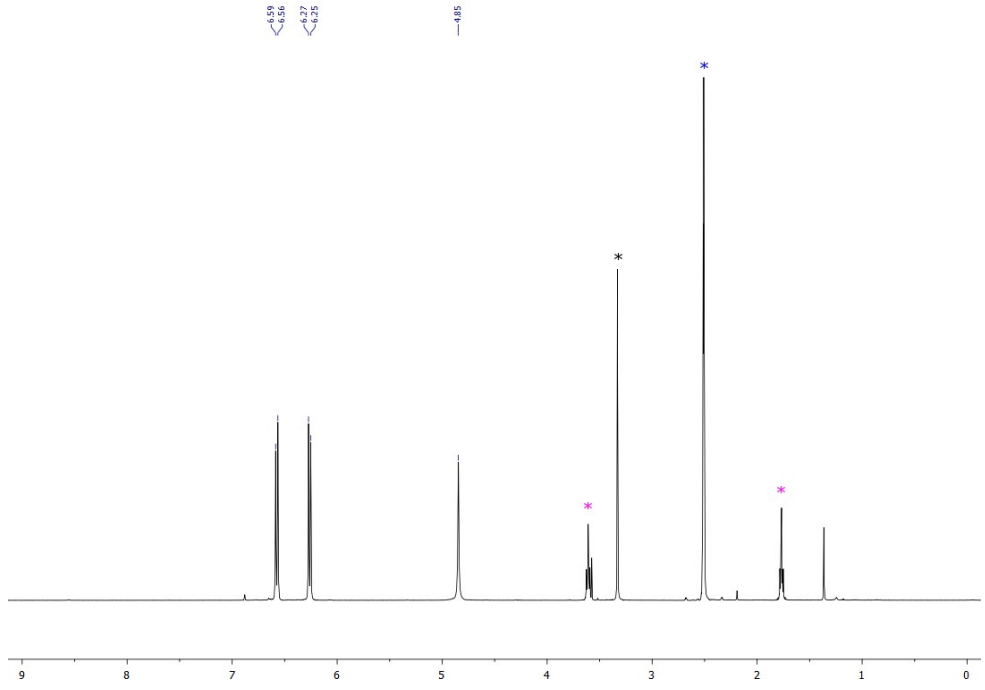


Solvent residues: THF (pink), water (black), DMSO (blue).

## 4.6 REFERENCES

(1) Doonan, C. J.; Tranchemontagne, D. J.; Glover, T. G.; Hunt, J. R.; Yaghi, O. M., *Nat. Chem.* **2010**, *2*, 235-238.

(2) Rabbani, M. G.; Sekizkardes, A. K.; Kahveci, Z.; Reich, T. E.; Ding, R.; El-Kaderi, H. M., *Chemistry* **2013**, *19*, 3324-3328.

(3) Ding, S. Y.; Gao, J.; Wang, Q.; Zhang, Y.; Song, W. G.; Su, C. Y.; Wang, W., *J. Am. Chem. Soc.* **2011**, *133*, 19816-19822.

(4) Dogru, M.; Handloser, M.; Auras, F.; Kunz, T.; Medina, D.; Hartschuh, A.; Knochel, P.; Bein, T., *Angew. Chem. Int. Ed. Engl.* **2013**, *52*, 2920-2924.

(5) Calik, M.; Auras, F.; Salonen, L. M.; Bader, K.; Grill, I.; Handloser, M.; Medina, D. D.; Dogru, M.; Lobermann, F.; Trauner, D.; Hartschuh, A.; Bein, T., *J. Am. Chem. Soc.* **2014**, *136*, 17802-17807.

(6) Patwardhan, S.; Kocherzhenko, A. A.; Grozema, F. C.; Siebbeles, L. D. A., *J. Phys. Chem. C* **2011**, *115*, 11768-11772.

(7) Jin, S.; Ding, X.; Feng, X.; Supur, M.; Furukawa, K.; Takahashi, S.; Addicoat, M.; El-Khouly, M. E.; Nakamura, T.; Irle, S.; Fukuzumi, S.; Nagai, A.; Jiang, D., *Angew. Chem. Int. Ed. Engl.* **2013**, *52*, 2017-2021.

(8) Bertrand, G. H.; Michaelis, V. K.; Ong, T. C.; Griffin, R. G.; Dinca, M., *Proc Natl Acad Sci U S A* **2013**, *110*, 4923-4928.

(9) Cote, A. P.; Benin, A. I.; Ockwig, N. W.; O'Keeffe, M.; Matzger, A. J.; Yaghi, O. M., *Science* **2005**, *310*, 1166-1170.

(10) Spitler, E. L.; Dichtel, W. R., *Nat. Chem.* **2010**, *2*, 672-677.

(11) Dogru, M.; Sonnauer, A.; Gavryushin, A.; Knochel, P.; Bein, T., *Chem Commun (Camb)* **2011**, *47*, 1707-1709.

(12) Spitler, E. L.; Colson, J. W.; Uribe-Romo, F. J.; Woll, A. R.; Giovino, M. R.; Saldivar, A.; Dichtel, W. R., *Angew. Chem. Int. Ed. Engl.* **2012**, *51*, 2623-2627.

(13) Medina, D. D.; Werner, V.; Auras, F.; Tautz, R.; Dogru, M.; Schuster, J.; Linke, S.; Doblinger, M.; Feldmann, J.; Knochel, P.; Bein, T., *ACS Nano* **2014**, *8*, 4042-4052.

(14) Medina, D. D.; Rotter, J. M.; Hu, Y.; Dogru, M.; Werner, V.; Auras, F.; Markiewicz, J. T.; Knochel, P.; Bein, T., *J. Am. Chem. Soc.* **2015**, *137*, 1016-1019.

(15) Uribe-Romo, F. J.; Hunt, J. R.; Furukawa, H.; Klock, C.; O'Keeffe, M.; Yaghi, O. M., *J. Am. Chem. Soc.* **2009**, *131*, 4570-4571.

(16) Wan, S.; Gándara, F.; Asano, A.; Furukawa, H.; Saeki, A.; Dey, S. K.; Liao, L.; Ambrogio, M. W.; Botros, Y. Y.; Duan, X.; Seki, S.; Stoddart, J. F.; Yaghi, O. M., *Chem. Mater.* **2011**, *23*, 4094-4097.

(17) Guo, J.; Xu, Y.; Jin, S.; Chen, L.; Kaji, T.; Honsho, Y.; Addicoat, M. A.; Kim, J.; Saeki, A.; Ihee, H.; Seki, S.; Irle, S.; Hiramoto, M.; Gao, J.; Jiang, D., *Nat. Commun.* **2013**, *4*, 2736.

(18) Fang, Q.; Zhuang, Z.; Gu, S.; Kaspar, R. B.; Zheng, J.; Wang, J.; Qiu, S.; Yan, Y., *Nat. Commun.* **2014**, *5*, 4503.

(19) Jackson, K. T.; Reich, T. E.; El-Kaderi, H. M., *Chem Commun (Camb)* **2012**, *48*, 8823-8825.

(20) Kuhn, P.; Antonietti, M.; Thomas, A., *Angew. Chem. Int. Ed. Engl.* **2008**, *47*, 3450-3453.

(21) Zhang, Y. B.; Su, J.; Furukawa, H.; Yun, Y.; Gandara, F.; Duong, A.; Zou, X.; Yaghi, O. M., *J. Am. Chem. Soc.* **2013**, *135*, 16336-16339.

(22) Jones, J. T.; Hasell, T.; Wu, X.; Bacsa, J.; Jelfs, K. E.; Schmidtmann, M.; Chong, S. Y.; Adams, D. J.; Trewin, A.; Schiffman, F.; Cora, F.; Slater, B.; Steiner, A.; Day, G. M.; Cooper, A. I., *Nature* **2011**, *474*, 367-371.

(23) Kandambeth, S.; Shinde, D. B.; Panda, M. K.; Lukose, B.; Heine, T.; Banerjee, R., *Angew. Chem. Int. Ed. Engl.* **2013**, *52*, 13052-13056.

(24) Shinde, D. B.; Kandambeth, S.; Pachfule, P.; Kumar, R. R.; Banerjee, R., *Chem Commun (Camb)* **2015**, *51*, 310-313.

(25) Spitler, E. L.; Koo, B. T.; Novotney, J. L.; Colson, J. W.; Uribe-Romo, F. J.; Gutierrez, G. D.; Clancy, P.; Dichtel, W. R., *J. Am. Chem. Soc.* **2011**, *133*, 19416-19421.

(26) Dogru, M.; Bein, T., *Chem Commun (Camb)* **2014**, *50*, 5531-5546.

(27) Zhou, T. Y.; Xu, S. Q.; Wen, Q.; Pang, Z. F.; Zhao, X., *J. Am. Chem. Soc.* **2014**, *136*, 15885-15888.

(28) Hasell, T.; Schmidtmann, M.; Stone, C. A.; Smith, M. W.; Cooper, A. I., *Chem Commun (Camb)* **2012**, *48*, 4689-4691.

(29) Monkhorst, H. J.; Pack, J. D., *Physical Review B* **1976**, *13*, 5188-5192.

(30) Perdew, J. P.; Burke, K.; Ernzerhof, M., *Phys. Rev. Lett.* **1996**, *77*, 3865-3868.

(31) Clark, S. J.; Segall, M. D.; Pickard, C. J.; Hasnip, P. J.; Probert, M. I. J.; Refson, K.; Payne, M. C., *Zeitschrift für Kristallographie - Crystalline Materials* **2005**, *220*.

(32) McNellis, E. R.; Meyer, J.; Reuter, K., *Physical Review B* **2009**, *80*.

(33) Tkatchenko, A.; Scheffler, M., *Phys. Rev. Lett.* **2009**, *102*, 073005.

(34) Sing, K. S. W., *Pure Appl. Chem.* **1985**, *57*, 603-619.

(35) Thommes, M., *Chem. Ing. Tech.* **2010**, *82*, 1059-1073.

(36) Lu, J.; Zhang, J., *J. Mater. Chem. A* **2014**, *2*, 13831-13834.

(37) *CrysAlis CCD*, 1.171.27p5 beta; Oxfordshire, U. K., 2005.

(38) *CrysAlis RED*, 1.171.27p5 beta; Oxfordshire, U.K., 2005.

(39) Altomare, A.; Burla, M. C.; Camalli, M.; Cascarano, G. L.; Giacovazzo, C.; Guagliardi, A.; Moliterni, A. G. G.; Polidori, G.; Spagna, R., *J. Appl. Crystallogr.* **1999**, *32*, 115-119.

(40) Altomare, A.; Cascarano, G.; Giacovazzo, C.; Guagliardi, A., *J. Appl. Crystallogr.* **1993**, *26*, 343-350.

(41) Sheldrick, G. M. *SHELXL-97, Program for the Refinement of Crystal Structures*, University of Göttingen: Göttingen, 1999.

(42) Sheldrick, G. M. *SHELXS-97, Program for Crystal Structure Solution*, Universit of Göttingen: Göttingen, 1997.

(43) Spek, L. A. *PLATON, A Multipurpose Crystallographic Tool*, University of Utrecht: Utrecht, 1999.

(44) *SCALE3 ABSPACK - An Oxford Diffraction program*, 1.0.4, gui: 1.0.3; Oxford Diffraction Ltd.: Oxford, 200

# 5. ORIENTED FILMS OF CONJUGATED 2D COVALENT ORGANIC FRAMEWORKS AS PHOTOCATHODES FOR WATER SPLITTING

This chapter is based on the following publication:

Torben Sick,‡ Alexander G. Hufnagel,‡

Jonathan Kampmann,‡ Ilina Kondofersky,

Mona Calik, Julian M. Rotter, Austin M. Evans,

Markus Döblinger, Simon Herbert, Kristina Peters,

Daniel Boehm, Paul Knochel, Dana D. Medina,

Dina Fattakhova-Rohlfing*, Thomas Bein*

*J. Am. Chem. Soc.* **2017**, *138* (4), 1234–1239.

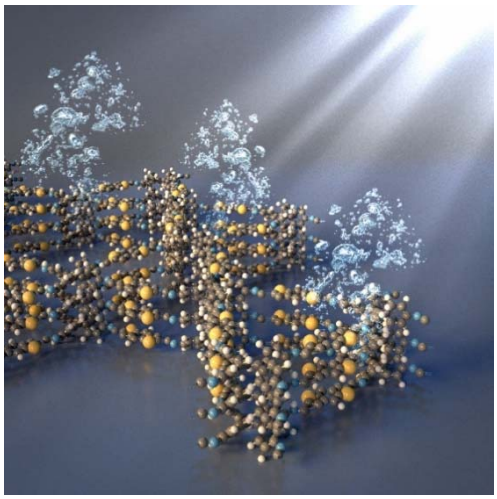

Light-driven water electrolysis at a semiconductor surface is a promising way to generate hydrogen from sustainable energy sources, but its efficiency is limited by the performance of available photoabsorbers. Here we report the first time investigation of covalent organic frameworks (COFs) as a new class of photoelectrodes. The presented 2D COF structure is assembled from aromatic amine-functionalized tetraphenylethylene and thiophene dialdehyde building blocks to form conjugated polyimine sheets, which π-stack in the third dimension to create photoactive porous frameworks. Highly oriented COF films absorb light in the visible range to generate photo-excited electrons that diffuse to the surface and are transferred to the electrolyte resulting in proton reduction and hydrogen evolution. The observed photoelectrochemical activity of the 2D COF films and their photocorrosion stability in water pave the way for a novel class of photoabsorber materials with versatile optical and electronic properties that are tunable through the selection of appropriate building blocks and their three-dimensional stacking.

# 5.1 INTRODUCTION

Photoelectrochemical (PEC) water splitting is an attractive way to generate hydrogen using renewable energy. Due to the potential of directly converting solar power into a chemical fuel or process feedstock, this process has attracted broad research interest. An ideal photoabsorber will combine efficient light harvesting with suitable band energies for water oxidation and reduction, fast interfacial charge transfer kinetics to the electrolyte, and corrosion stability under operating conditions.[1] However, the performance of known systems is modest, being primarily limited by photoabsorber material properties. On the one hand, metal oxides tend to be stable under operation (i.e. resistant against photocorrosion) but exhibit poor semiconductor properties such as short charge carrier diffusion lengths and fast recombination, which can be partially compensated by nanostructuring.[2-4] On the other hand, Si and III-V semiconductors offer favorable charge transport properties and high photocurrents but are prone to photocorrosion unless protected by overlayers.[5-6] For this reason, the discovery of new photoabsorber materials is urgent and currently the focus of combinatorial synthetic and computational research.[7-10] In this work we explore covalent organic frameworks (COFs) as photoelectrodes for light-driven water splitting. COFs are an emerging class of crystalline polymers composed of organic units linked via covalent bonds to form porous networks. By using multidentate building blocks, two- or three-dimensional frameworks with a defined pore size and high specific surface area in conjunction with appreciable thermal and chemical stability can be obtained. In 2D COFs, covalently bonded units form two- dimensional (2D) sheets, which stack due to dispersive forces (π-stacking) in the third dimension to construct extended open porous frameworks. The π-stacking mediates electronic interactions between the functional units, thereby providing another possible path for charge carrier transport in addition to transfer within the covalent sheets. The selection of appropriate building blocks, linkage motifs (from unconjugated boroxines, boronic esters and borosilicates[11-14] to conjugated imines[15-19], imides[20-21] and others[22-24]), as well as their stacking mode all provide ways to tailor the optical and electronic properties of COF structures, thereby opening the way for the discovery of novel materials for optoelectronic systems. COFs have found applications in gas storage[25-26], catalysis[27-28], separation[29-31], energy storage[32] and proton conduction[33]. Zeolitic imidazolate frameworks (ZIFs)[34], carbon nitrides (CNs)[35-40], phenyl triazine oligomers (PTOs)[41], poly-(azomethine) networks (ANWs)[42], triazine containing organic frameworks and even covalent organic frameworks (CTFs and COFs)[43-50] were found to be active in photocatalysis and photocatalytic hydrogen evolution reactions, where photogenerated charge

separation was achieved by adding noble metal co-catalysts and/or sacrificial electron donors. Fabricated as oriented COF thin films, COFs have already found use as active materials in optoelectronic devices[51-54].

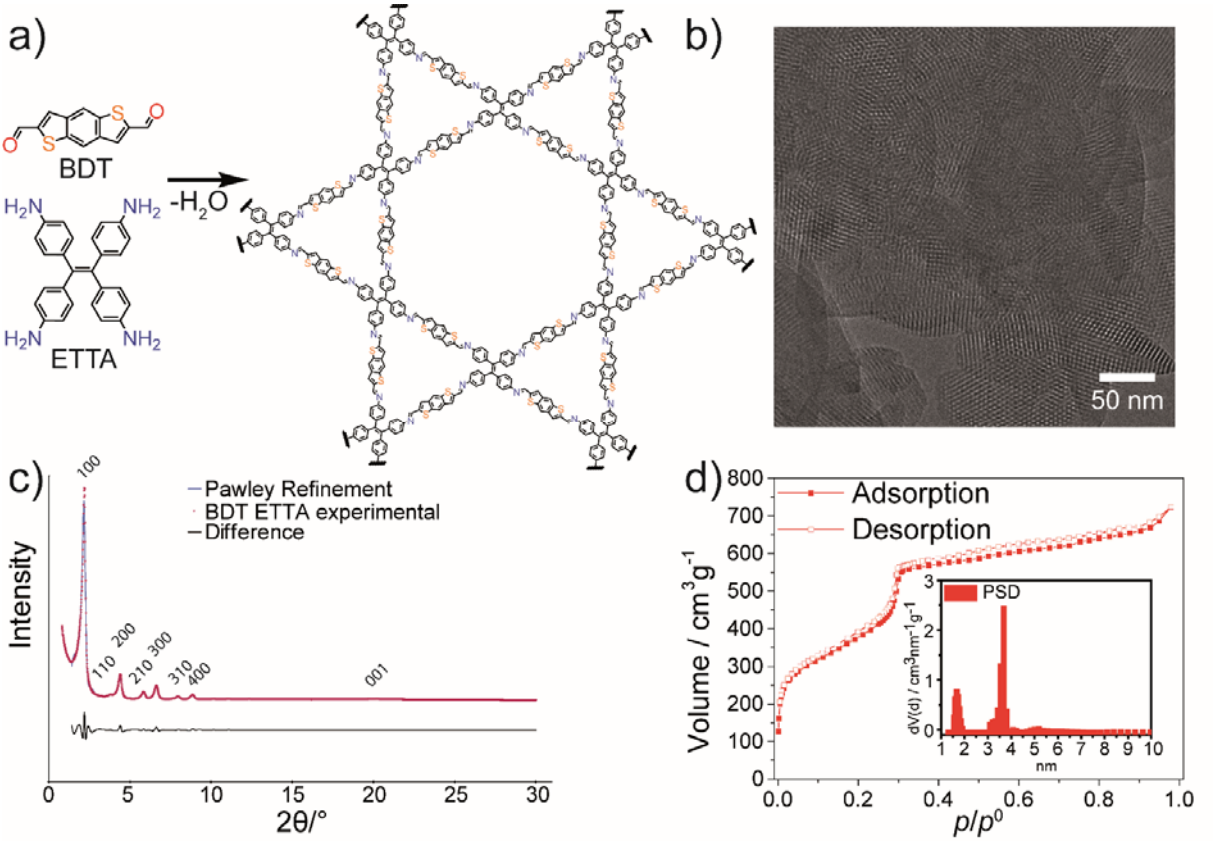


Figure 5.1: a) Synthetic approach for the formation of BDT-ETTA COF with a structural overview of the resulting 2D layers. Due to π-interactions the sheets stack in the third dimension to form the final hexagonal AA eclipsed framework b) TEM image of the resulting powder. c) PXRD of BDT-ETTA (red), comparison to a Pawley-refined pattern (blue) and difference (black line). d) Nitrogen physisorption isotherm of BDT-ETTA with a pore size distribution revealing two distinct pore sizes.

However, COF films being utilized as photoelectrodes for direct water splitting have yet to be reported. Herein, we demonstrate the use of an imine-based COF, grown as oriented films on transparent, conducting substrates serving as a light-absorbing material. This is the first report of a COF acting as a photoelectrode to enable photoelectrochemical water splitting in aqueous electrolytes without the use of a co-catalyst or sacrificial agent. In addition, we demonstrate a four-fold increase in the obtained photocurrent by the application of a Pt nanoparticle hydrogen evolution catalyst.

## 5.2 RESULTS AND DISCUSSION

**Synthesis of COF systems**

For the possible use as photocathodes in photoelectrochemical water splitting devices, we investigated a 2D COF built from aromatic amino- and thiophene-based units. The use of nearly planar p-type functional building units linked via polarizable imine bonds is expected to result in conjugated p-type semiconductors, whose optoelectronic properties can be varied via the structure of the building units and the nature of their stacking in the third dimension. One building unit is a conjugated aromatic and four-fold amine-functionalized tetraphenylethylene (1,1',2,2'-tetra-*p*-aminophenylethylene, ETTA). The ETTA monomer has been investigated in 2D imine COF powders[55], where it was shown to have a strong impact on geometry, shape, crystallinity and on the stacking distance of adjacent layers. The other component is the linear dialdehyde benzo[1,2-*b*:4,5-*b*']dithiophene-2,6-dicarboxaldehyde (BDT), which is a donor-type dithiophene (Figure 5.1a).

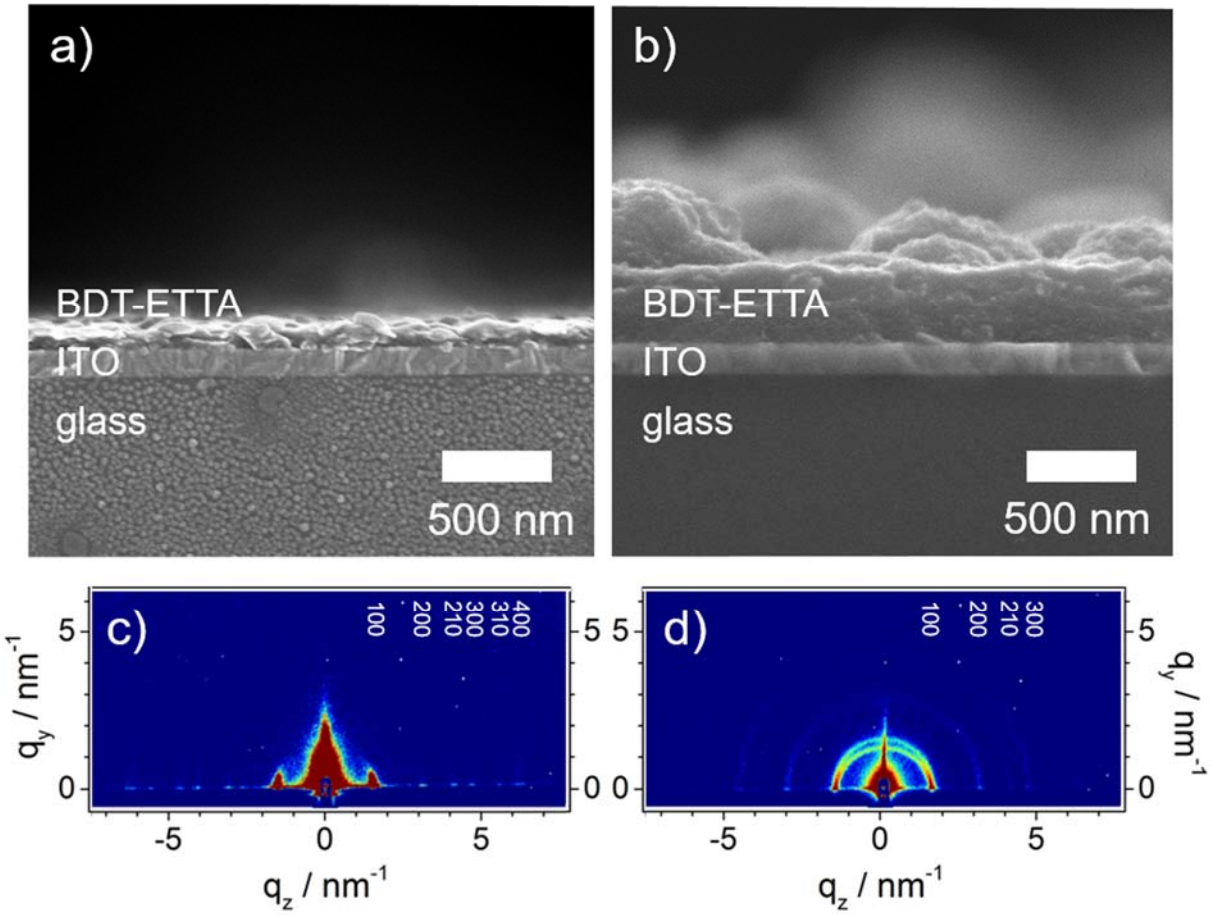


Figure 5.2: Thin (ca. 100 nm) (a, c) and thick (ca. 500 nm) (b, d) BDT-ETTA films grown on ITO substrates: SEM images (cross-section) (a, b) and grazing incidence diffraction (GID) patterns (c, d) revealing a high degree of film orientation.

For use as electrodes in photoelectrochemical cells, the COFs were grown as films on transparent conducting FTO or ITO substrates. We found that high concentrations of reactants resulted in homogeneous nucleation and growth of bulk COF powders, whereas dilute solutions promote heterogeneous film growth on a substrate. To avoid nucleation and precipitation of COF powders on the substrate, the substrates were placed with the FTO or ITO side downwards in a PTFE film holder in a mesitylene-benzyl alcohol (V:V = 1:1) solution in an autoclave. After adding a catalytic amount of 6 M acetic acid, the films were grown for 72 h at 120 °C. Intensely orange-colored BDT-ETTA COF films were obtained on FTO or ITO substrates. Cross-sectional SEM images of BDT-ETTA films (Figure 5.2 a, b) with different thicknesses demonstrate that COF films can be grown in a thickness range between 100 to 500 nm and that they adhere well to the substrate. The surface exhibits some roughness, which is notably less pronounced in the case of thinner films (compare Figure 5.2a).

The BDT-ETTA COF is crystalline, as established by an intense and sharp 100 reflection and the presence of well-defined higher-order reflections in the PXRD pattern (Figure 5.1). The reflection at around 20° 2θ represents the π-stacking distance, which corresponds to 0.44 nm. The obtained PXRD pattern agrees well with the simulated pattern calculated for an AA eclipsed layer stacking model for a hexagonal structure in P6 symmetry (Figure 5.1 and Figure S 5.14). The π-stacking distance is high in comparison to other COF systems, which can be explained by the strong contribution of the propeller-shaped (i.e. non-planar) ETTA motif to the final geometry compared to the planar thiophene linker.[19] Notably, both the XRD measurements in reflection mode (Figure S 5.12) as well as grazing incidence diffraction (GID) patterns (Figure 5.4c, d) provide strong evidence for oriented growth of the COF films on the substrates. The orientation in c-direction is evident from the intense reflections at q(y)=0 originating from COF layers oriented parallel to the substrate and correspond to the reflections of the BDT-ETTA COF (compare PXRD in Figure 5.1). A weak diffuse arc arises from randomly distributed COF particles present on top of the highly-oriented film (see Figure S 5.10 and S 5.12). For the electrochemical investigations we used the thinner films as they constitute a well-defined system with less non-oriented COF material.

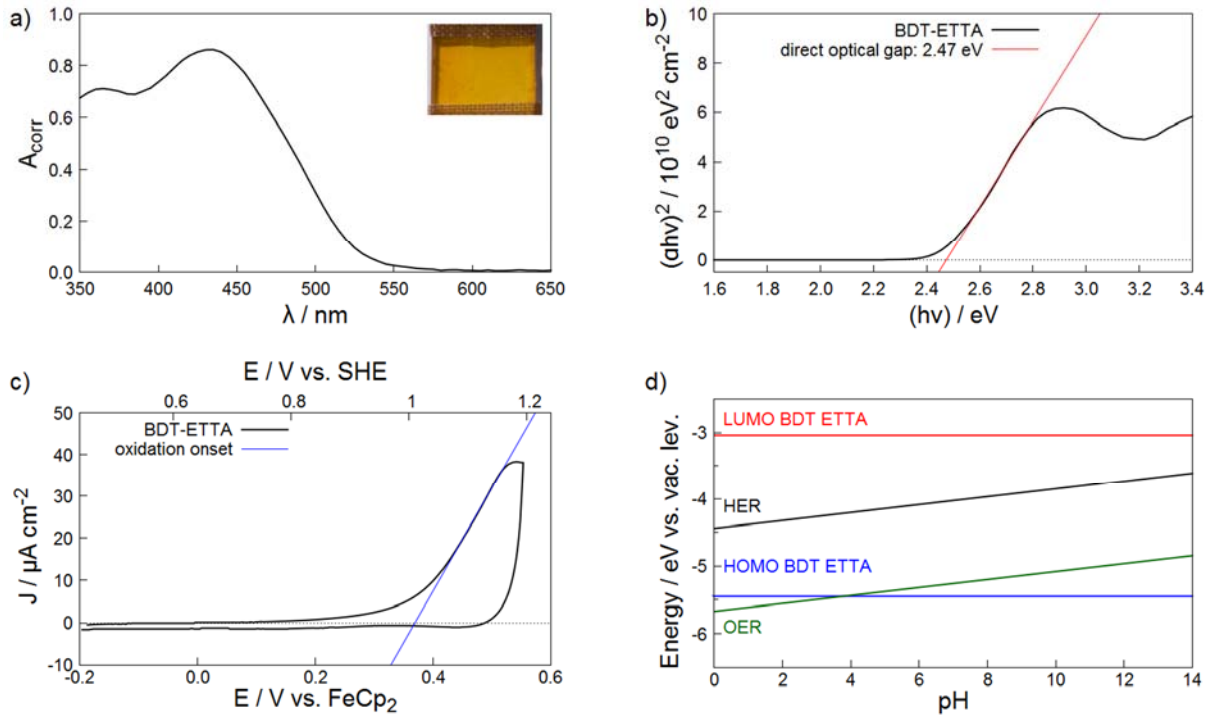


Figure 5.3: a) Absorbance spectrum of a BDT-ETTA thin film on ITO with a photograph of a representative sample masked with a PFTE adhesive tape (inset). b) Tauc plot analysis of a BDT-ETTA film on ITO showing a direct optical band gap of 2.47 eV. c) Cyclic voltammogram of a BDT-ETTA electrode in non-aqueous electrolyte. d) Calculated alignment between the HOMO and LUMO of BDT-ETTA and the water splitting redox couples.

The nitrogen physisorption isotherms of the COF powder demonstrate that the BDT-ETTA COF forms a porous structure with clearly distinguishable micro- and mesopores (Figure 5.1). The BET surface areas and total pore volumes for COF bulk material was calculated to be 1360 $m^2g^{-1}$ and 1.0 $cm^3g^{-1}$, respectively. The bimodal pore size distribution shows pores of 1.67 nm and 3.68 nm in diameter. The pore sizes match the predicted values for the geometry of an AA eclipsed framework. The TEM image of BDT-ETTA (Figure 5.1b) reveals a high degree of crystallinity and order, as demonstrated by the large domain sizes. 2D honeycomb-type facets are visible, where the *ab* plane is oriented perpendicular to the viewing direction. In other viewing directions, channels indicate the growth orientation, highlighting the crystallinity of the COF material with domain sizes of 50-100 nm.

**Photoelectrochemical properties of COF films**

The remarkable stability of the obtained BDT-ETTA in different solvents, including water in a pH range from 3 to 14 (see Figure S 5.13 for further details), and strong absorption of visible light suggested that the novel BDT-ETTA COF structure would be an interesting example of a

photoabsorber material for water splitting applications. Therefore we measured the photochemical activity at pH 7.

The absorption spectrum is shown in Figure 5.3. BDT-ETTA films strongly absorb light in the visible range with an absorption threshold of around 550 nm and two absorbance maxima at 360 and 430 nm (Figure 5.3a). The Tauc plot analysis of BDT-ETTA thin films (Figure 5.3b) reveals a direct optical band gap of 2.47 eV, which is favorable for photoelectrochemical water splitting.[2]

To determine the absolute positions of the conduction and valence band edges of BDT-ETTA films (corresponding to their LUMO and HOMO energies, respectively), electrochemical measurements in a non-aqueous electrolyte (0.1 M $NBu_4PF_6$ in anhydrous acetonitrile) were performed. The cyclic voltammogram of a BDT-ETTA film electrode (Figure 5.3c) shows an anodic peak with an onset at 0.37 V vs. ferrocene/ferrocenium (FOC), which we attribute to the expected oxidation of thiophene moieties. From this, the approximate position of the HOMO can be calculated to be -5.51 eV (see SI for further details).

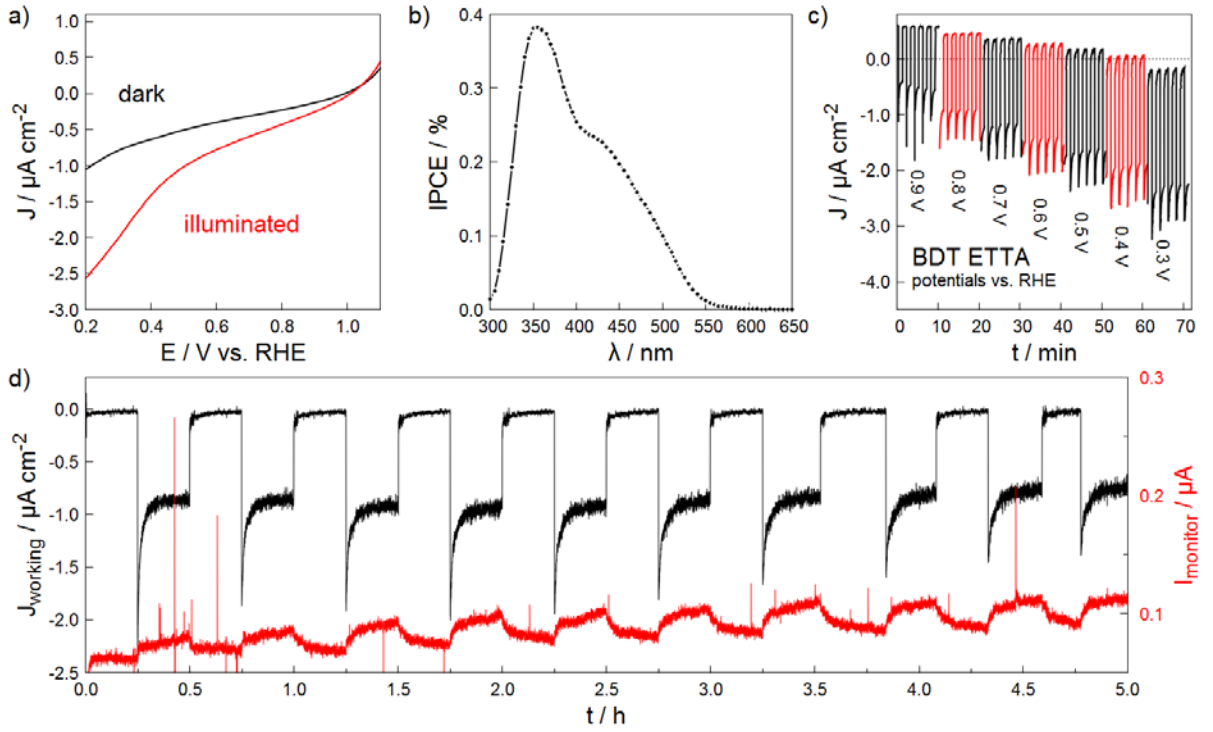


Figure 5.4: a) Linear sweep voltammograms of BDT-ETTA films on ITO performed in the dark (black) and under AM 1.5 illumination through the substrate (red). b) The corresponding IPCE spectrum quantifies the photoresponse of the COF electrodes in the visible spectral range. c) Chronoamperometric data of a BDT-ETTA film collected under chopped illumination (8.3 mHz, 455 nm, 1017 $s^{-1}$) demonstrating the photocurrent response at different potentials. d) Chronoamperometric data recorded on a BDT-ETTA film at 0.4 V vs. RHE (black) under chopped AM 1.5 illumination. Oxidation current recorded simultaneously on a platinum mesh indicator electrode (red) indicating the formation of hydrogen under illumination (see SI for experimental details).

Using the optical bandgap of 2.47 eV determined above, the LUMO position is approximately -3.34 eV. The absolute energy of the HOMO and LUMO of BDT-ETTA as well as the $H_2O/H_2$ (hydrogen evolution reaction, HER) and $O_2/H_2O$ (oxygen evolution reaction, OER) redox couples are plotted in Figure 5.3d. If we assume that the HOMO and LUMO positions do not change significantly due to protonation or deprotonation of the COF structure, the LUMO is higher in energy than the $H_2O/H_2$ redox pair in solution over the entire pH range, which means that photoexcited electrons at the COF surface should be able to spontaneously transfer to the electrolyte, resulting in proton reduction and hydrogen evolution. The driving force, i.e. the potential difference between the LUMO of the COF and the HER is significant, particularly in acidic solutions. In alkaline solutions, the HOMO energy lies below that of the OER redox couple, which would also render photoelectrochemical water oxidation and thus bias-free one-photon water splitting is thermodynamically feasible. However, the potential difference is limited to approximately 0.5 V, which approaches the minimum overpotential needed to drive

the OER. Therefore, in the absence of an efficient OER catalyst, this reaction is not expected to yield significant currents. The photoelectrochemical performance of 100 nm BDT-ETTA films was characterized by linear sweep voltammetry in nitrogen-purged 0.1 M $Na_2SO_4$ aqueous electrolyte under AM 1.5 illumination through the substrate in the potential range between 0.9 and 0.3 V vs. RHE (Figure 5.4a). The photoelectrode shows an early HER onset potential of 0.8 V vs. RHE reaching currents of up to 1.5 μA $cm^{-2}$ at 0.3 V vs. RHE. We note that thicker (500 nm) films with a less homogeneous orientation (cf. Figure 5.2b) show a higher current density of 4.3 μA $cm^{-2}$ at 0.3 V vs. RHE, demonstrating that the PEC performance of the COF films can be improved (Figure S 5.2). However, due to the well-defined geometry of the highly oriented thin (100 nm) films, we have chosen these as a system for further photoelectrochemical study. The incident-photon-to-current-efficiency (IPCE) of these thin films was determined to examine the photoelectrochemical performance of the COF electrode at different wavelengths (Figure 5.4b). The BDT-ETTA COF showed light-to-current conversion activity over a broad spectral range below 530 nm, reaching a maximum IPCE of 0.38 % at 355 nm. Stability of the photoabsorber is a key requirement for achieving energy payback via photoelectrochemical hydrogen generation.[56] To investigate this issue, we performed chronoamperometric measurements under chopped illumination (8.3 mHz, 455 nm, $10^{17}$ $s^{-1}$) at different potentials between 0.9 and 0.3 V vs. RHE for 10 min each (Figure 5.4c). BDT-ETTA films showed a stable photocurrent response over the entire potential range while the absolute values of current density followed the trend of the linear sweep voltammograms. Further, we investigated the stability of the COF photoelectrode for an extended period of time at 0.4 V vs. RHE. At this potential, the BDT-ETTA films showed stable behavior with a negligible dark current density and good photoactivity. Chronoamperometric data was recorded at this potential for 5 hours (Figure 5.4d, black). The sample was alternatingly kept in the dark and under illumination with AM 1.5 simulated sunlight for 15 minutes at a time. After the initial switch-on transient a steady-state photocurrent density of 0.9 μA $cm^{-2}$ was reached in each illumination step. To ensure that the resulting photocurrent arises from the water reduction, we designed a four-electrode setup enabling the continuous monitoring of the hydrogen evolution during this stability test (see experimental details and Figure S 5.5 for further information). A platinum indicator electrode was placed next to the photocathode and polarized at 1.1 V vs. RHE to oxidize dissolved hydrogen in the electrolyte. An oxidation current recorded at this electrode indicates hydrogen evolution in the system although quantification of the hydrogen amount via this method is challenging due to a low collection efficiency of the indicator electrode (Figure S 5.7). Prior to measurements the indicator electrode was polarized without

illumination until a stable background current of 0.06 µA was reached (Figure S 5.6). Illumination of the COF film resulted in a photocurrent detected at the photoelectrode (Figure 5.4d, black) and a simultaneous rise in the hydrogen oxidation current at the indicator electrode (Figure 5.4d, red). Switching off the light results in a decay of the photocurrent as well as the oxidation current. This behavior is stable and repeatable over the course of the measurement, indicating stability of the material under photoelectrochemical operating conditions. In order to rule out that the oxidative current observed in Figure 5.4d results from any other species than photoelectrochemically evolved hydrogen, we quantified the product with a hydrogen microsensor (Unisense A/S H2-NPLR) with a hydrogen-selective silicone membrane. At a static potential on the COF film of 0.4 V vs. RHE, a direct correlation between the hydrogen evolution and the illumination of the sample with AM 1.5 simulated sunlight is evident (Figure S 5.9). The long-term stability demonstrated by the COF photoelectrode shows that no components of the COF material are dissolved by photocorrosion. This demonstrates that a BDT-ETTA covalent organic framework can be used as a stable photocathode for PEC water reduction. The conversion efficiency of photoelectrodes can be enhanced by a number of methods, including the application of a co-catalyst which facilitates the charge transfer to the electrolyte. We demonstrate that this is a viable approach for COF photocathodes by decorating the COF film with platinum nanoparticles. As shown in Figure 5.5, the BDT-ETTA/Pt films show a four-fold increase in photocurrent compared to bare BDT-ETTA photocathodes. Hence, we have established the potential to improve the efficiency of COF photoelectrodes by combining them with suitable co-catalysts.

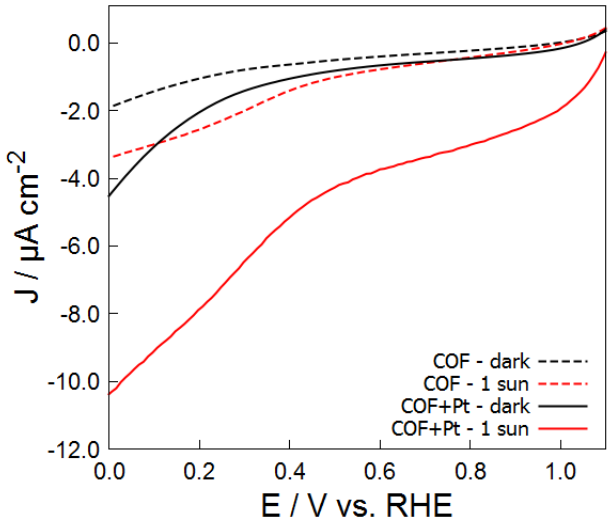


Figure 5.5: Linear sweep voltammograms of BDT-ETTA films on ITO performed in the dark (black) and under AM 1.5 illumination through the substrate (red). The combination of BDT-ETTA with platinum nanoparticles (solid lines) leads to an increased photocurrent over the whole potential range compared to bare BDT-ETTA films (dashed lines).

## 5.3 CONCLUSION

Our results show that BDT-ETTA COF films are viable photocathodes for light-driven water reduction. The material meets the requirements for this application, which include efficient light harvesting, suitable band positions, and stability. The polyimine framework BDT-ETTA is the first to be investigated in this context, representing an unexplored field of applications for COFs. Given the enormous diversity of molecular building units that can be employed in the construction of COFs, both the development of new framework structures and fine-tuning the properties of existing ones is possible. We envision that future research on combinations of building blocks and stacking modes and the combination of the photoabsorber with suitable co-catalysts will allow for further optimizing charge carrier lifetimes, long term stability, and charge transfer kinetics in order to improve the conversion efficiency obtainable from COF-based photoelectrodes.

# 5.4 EXPERIMENTAL SECTION

All reagents and solvents were obtained from commercial suppliers and used as received. Benzo(1,2-*b*:4,5-*b*')dithiophene (BDT, >98%, TCI), benzyl alcohol (BnOH, anhydrous, Sigma-Aldrich), mesitylene (Mes, anhydrous, Sigma-Aldrich), tetrahydrofuran (THF, extra dry, stabilized, Acros Organics and anhydrous, inhibitor-free, Sigma-Aldrich), acetonitrile (Sigma-Aldrich), ITO glass substrates (Visiontek, 12 Ω/sq). FTO- coated glass substrates (Pilkington, 7 Ω/sq).

**General procedure for BDT-ETTA COF films**

Under argon, BDT (7.88 mg, 0.032 mmol) and ETTA (6.28 mg, 0.016 mmol) were finely ground, added to a PTFE autoclave, and suspended in a mixture of benzyl alcohol and mesitylene (V/V 1:1, 2000 µL). A glass slide holder, containing ITO or FTO slides, was introduced to the liner with the conducting side downwards. Acetic acid (6 M, 200 µL) was added, the autoclave was sealed, and the mixture was kept at 120 °C for 3 days. The resulting orange film was rinsed with anhydrous THF and dried under reduced pressure. COF bulk material that precipitated beneath the film substrate holder was filtered and purified in a Soxhlet extractor for 24 h with anhydrous THF.

**Structural characterization**

$^{1}$H NMR spectra were recorded on Bruker AV 400 and AV 400 TR spectrometers. Proton chemical shifts are expressed in parts per million ($\delta$ scale) and are calibrated using residual non deuterated solvent peaks as an internal reference (e.g. DMSO-$d_6$: 2.50 ppm). Ultraviolet–vis–infrared diffuse reflectance spectra (Kubelka–Munk spectrum) of the films on quartz glass were recorded on a Perkin-Elmer Lambda 1050 spectrometer equipped with a 150 mm integrating sphere. Thin film absorbance spectra were measured by illuminating the sample through the substrate side and correcting for reflection.[57] Scanning electron microscopy (SEM) images were recorded with a JEOL 6500F and an FEI Helios NanoLab G3 UC scanning electron microscope equipped with a field emission gun operated at 3-5 kV. Transmission electron microscopy (TEM) was performed on an FEI Titan Themis equipped with a field emission gun operated at 300 kV. X-ray diffraction (XRD) measurements were performed using a Bruker D8 Discover with Ni-filtered Cu K$\alpha$ radiation and a LynxEye position-sensitive detector. Experimental XRD data were used for Pawley refinement to optimize the hypothetical structure. The initial structure models of the COFs were built using the Forcite module of the Accelrys Materials Studio software package. We applied the space group with the highest possible symmetry, i.e.

*P*6, taking into account the propeller-like conformation of the central building blocks. Using this coarse model we determined the unit cell parameters via Pawley refinement of the PXRD data. Nitrogen sorption isotherms were recorded on a Quantachrome Autosorb 1 at 77 K within a pressure range from $p/p^0$ = 0.001 to 0.98. Prior to the measurement of the sorption isotherms the samples were heated for 24 h at 120°C under turbo-pumped vacuum. For the evaluation of the surface area the BET model was applied between 0.05 and 0.2 $p/p^0$. Pore size distributions were calculated using the QSDFT equilibrium model with a carbon kernel for cylindrical pores.

# 5.5 SUPPORTING INFORMATION

**Section 1: Materials and Methods**

All reagents and solvents were obtained from commercial suppliers and used as received. Benzo(1,2-*b*:4,5-*b*')dithiophene (BDT, >98%, TCI), benzyl alcohol (BnOH, anhydrous, Sigma-Aldrich), mesitylene (Mes, anhydrous, Sigma-Aldrich), tetrahydrofuran (THF, extra dry, stabilized, Acros Organics), ITO glass substrates (Visiontek, 12 Ω/sq). FTO-coated glass substrates (Pilkington, 7 Ω/sq).

**Nuclear magnetic resonance (NMR) spectra** were recorded on Bruker AV 400 and AV 400 TR spectrometers. Proton chemical shifts are expressed in parts per million ($\delta$ scale) and are calibrated using residual non-deuterated solvent peaks as internal reference (e.g. DMSO-$d_6$: 2.50 ppm).

**Infrared (IR) spectra** were recorded on a Perkin Elmer Spectrum BX II FT-IR system and a Thermo Scientific Nicolet™ 6700 FT-IR spectrometer in transmission mode. IR data are reported in wavenumbers ($cm^{-1}$).

**UV-Vis** spectra were recorded using a Perkin-Elmer Lambda 1050 spectrometer equipped with a 150 mm integrating sphere. The reflectance-corrected absorbance $A_{corr}$ was calculated according to Equation 5.1, where $T_{sample}$, $T_{substrate}$, $R_{sample}$ and $R_{substrate}$ denote the transmittance and reflectance of the sample (substrate with COF film) and bare substrate, respectively.[57]

$$A_{corr} = -\log_{10}\left(\frac{\frac{T_{sample}}{T_{substrate}}}{1-\frac{R_{sample}-R_{substrate}}{T_{substrate}^2}}\right) \quad (5.1)$$

**Nitrogen sorption isotherms** were recorded on a Quantachrome Autosorb 1 at 77 K within a pressure range of $p/p_0$ = 0.001 to 0.98. Prior to the measurement of the sorption isotherms the samples were heated for 24 h at 120°C under turbo-pumped vacuum. For the evaluation of the surface area the BET model was applied between 0.05 and 0.2 $p/p_0$. Pore size distributions were calculated using the QSDFT equilibrium model (desorption branch) with a carbon kernel for cylindrical pores.

**Thermogravimetric analysis** (TGA) measurements were performed on a Netzsch Jupiter ST 449 C instrument equipped with a Netzsch TASC 414/4 controller. The samples were heated from room temperature to 900 °C under a synthetic air flow (25 mL $min^{-1}$) at a heating rate of 1 K $min^{-1}$.

**Powder X-ray diffraction** (PXRD) measurements were performed using a Bruker D8 Discover with Ni-filtered Cu-K$\alpha$ radiation and a LynxEye position-sensitive detector. (scan speed of 4 s per 0.01 degree 2θ) Experimental XRD data were used for Pawley refinement to optimize the hypothetical structure.

The initial **structure models of the COFs** were built using the Forcite module of the Accelrys Materials Studio software package. We applied the space group with the highest possible symmetry, i.e. *P*6, taking into account the propeller-like conformation of the central building blocks. Using this coarse model we determined the unit cell parameters via Pawley refinement of our PXRD data.

**Transmission electron microscopy (TEM)** was performed on an FEI Titan Themis equipped with a field emission gun operated at 300 kV.

**Scanning electron microscopy (SEM)** images were recorded with a JEOL 6500F and an FEI Helios NanoLab G3 UC scanning electron microscope equipped with a field emission gun operated at 3-5 kV.

## Section 2: Synthetic procedures

**1,1,2,2-Tetra(*p*-nitrophenyl)ethylene (TNPE)** (adapted from Gorvin[58])

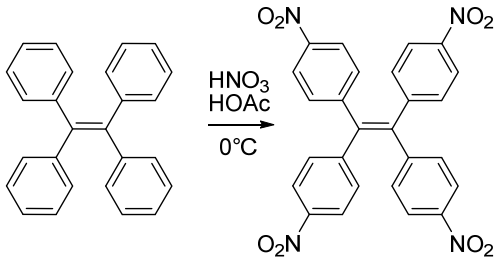


1,1,2,2-Tetraphenylethylene (3.0 g, 9.0 mmol) was slowly added with stirring at 0 °C to a mixture of 30 mL nitric acid (≥ 99%) and 30 mL glacial acetic acid. After 3 h at room temperature the solution was diluted with cold water. The resulting precipitate was filtered and dried under reduced pressure. Recrystallization from 1,4-dioxane, filtration and drying resulted in a yellow solid of TNPE with 69% yield. $^1$H NMR (400 MHz, $CDCl_3$) δ (ppm): 8.055-8.100 (m, 8H), 7.16-7.21 (m, 8H).

**1,1,2,2-Tetra(*p*-aminophenyl)ethylene (ETTA)** (adapted from Lu *et al*.[59])

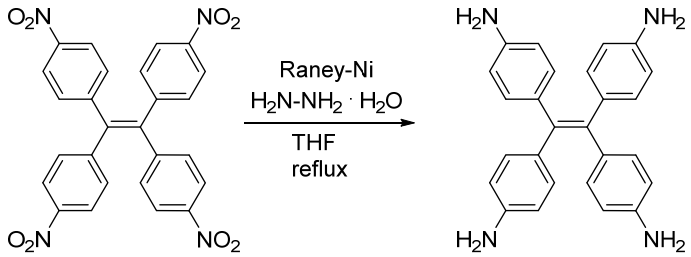


TNPE (1.0 g, 1.9 mmol) was dissolved in 20 mL of anhydrous THF in a 100 mL flask under nitrogen atmosphere. Approximately 4 g of Raney-nickel catalyst slurry was added to the mixture with stirring. Hydrazine monohydrate (1.3 mL, 26 mmol) was then added dropwise to the stirred mixture. The resulting solution was heated to reflux for two hours. The solution was allowed to cool to room temperature and filtered. The filtrate was dried under reduced pressure, giving a yellow solid with 79% yield. $^1$H NMR (400 MHz, DMSO-$d_6$) δ (ppm): 6.60-6.55 (m, 8H), 6.29-6.24 (m, 8H), 4.84 (s, 8H).

**Benzo[1,2-*b*:4,5-*b*']dithiophene-2,6-dicarboxaldehyde (BDT)** (adapted from Koßmehl *et al*.[60])

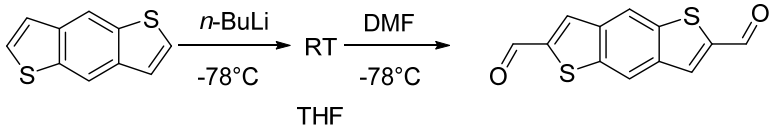

Benzo[1,2-*b*:4,5-*b*']dithiophene (1.0 g, 5.3 mmol) was dissolved in 100 mL anhydrous, inhibitor-free THF in an outgassed 250 mL flask under nitrogen atmosphere. The stirred solution was cooled to -78°C in a dry ice/acetone cooling bath. A solution of *n*-butyl lithium (5.0 mL, 2.5 M in *n*-hexane, 12.5 mmol) was added dropwise within 10 minutes. The solution was stirred for 30 minutes at -78°C and after removal of the cooling bath for 1 h at room temperature. The solution was then cooled again to -78°C and DMF (1.0 mL, 13.0 mmol) was added dropwise. After stirring overnight, the solution was poured into ice water and filtered. The yellow precipitate was washed with water several times and further treated with small amounts of MeOH and $Et_2O$. The solid was dried under reduced pressure, giving a yellow solid with 46% yield. $^1$H NMR (400 MHz, DMSO-$d_6$) δ (ppm): 8.53 (s, 2H), 8.89 (s, 2H), 10.20 (s, 2H); $^{13}$C NMR (100 MHz, DMSO-$d_6$) δ (ppm): 121.6, 135.3, 138.4, 138.9, 144.9, 186.6.

**BDT-ETTA COF synthesis:**

Benzo[1,2-*b*:4,5-*b'*]dithiophene-2,6-dicarboxaldehyde (BDT, 4.94 mg, 0.0201 mmol) and 1,1,2,2-tetra(*p*-aminophenyl)ethylene (ETTA, 3.94 mg, 0.0100 mmol) were finely ground and suspended in a mixture of benzyl alcohol and mesitylene (V/V 9:1, 500 µL). The resulting mixture was sonicated until complete dissolution of the educts was achieved. Acetic acid (6 M, 50 µL) was added and the mixture was kept in a culture tube at 120 °C for 3 days. The resulting orange precipitate was suction filtered, treated with anhydrous THF to remove the less volatile solvent, further purified by using a Soxhlet extraction apparatus with THF and dried under reduced pressure.

**BDT-ETTA Films:**

Benzo[1,2-*b*:4,5-*b'*]dithiophene-2,6-dicarboxaldehyde (BDT, 7.88 mg, 0.0320 mmol) and 1,1,2,2-tetra(*p*-aminophenyl)ethylene (ETTA, 6.28 mg, 0.0160 mmol) were finely ground, added to a PTFE autoclave, and suspended in a mixture of benzyl alcohol and mesitylene (V/V 1:1, 2000 µL). A glass slide holder, containing ITO or FTO glass slides in the horizontal position with the ITO/FTO side downwards, was transferred into the autoclave. Acetic acid (6 M, 200 µL) was added, the liner was sealed, and the mixture was kept at 120 °C for 3 days. The as-synthesized COF films were rinsed with THF to remove residues of the reaction mixture. COF bulk material precipitated beneath the film substrate holder was collected by filtration and purified in a Soxhlet extractor for 24 h with anhydrous THF.

**Platinum nanoparticles**

$PtCl_2$ (4.7 mg, 17,7 µmol) was dispersed in 14 mL *tert*-butanol, transferred into a Teflon-lined steel autoclave and heated in a laboratory oven at 175°C for 24 h. The metallic grey product was separated by centrifugation (15 min, 15000 rpm) and dispersed in 6 mL ethanol. 50 µL of the resulting dispersion were dropcasted on a BDT-ETTA COF thin film and dried at room temperature before the electrode was used for photoelectrochemical characterization.

**Section 3: Electrochemical measurements**

**Non-aqueous photoelectrochemistry**

The non-aqueous photoelectrochemical experiments were performed in a sealed borosilicate glass cell in a three-electrode configuration with the COF film as the working electrode, a Pt foil counter electrode and a silver wire as the reference. This cell was assembled in an argon-filled glove box ($c(O_2) < 0.1$ ppm, $c(H_2O) < 0.1$ ppm). The electrolyte was 0.1 M $NBu_4PF_6$ (Aldrich, 99.9 %) in acetonitrile (Aldrich, anhydrous); it was prepared under the same conditions and dried further using 3 Å molecular sieves. The COF films were degassed in vacuum at 120 °C for several hours prior to use. The potential of the Ag reference vs. ferrocene (Aldrich, 95 % resublimed) was established to be -200 mV in a control experiment with a blank ITO substrate. A Metrohm Autolab PGStat302N was used for the measurements. Cyclic voltammetry was performed at potentials between -0.2 and 0.5 V vs. FOC and a scan rate of 20 mV $s^{-1}$. The absolute energy of the HER can be calculated according to Equation 3.1.

$$E_{RHE,abs} = -4.5\ eV + 0.059\ eV \cdot pH \qquad (3.1)$$

The FOC redox couple in this electrolyte is at 641 mV vs. SHE[61] with an absolute energy of the SHE of -4.5 eV[62], this results in an absolute energy of the FOC redox couple of -5.14 eV relative to the vacuum level.

**Aqueous photoelectrochemistry**

Aqueous photoelectrochemistry experiments were carried out in a custom build, airtight cell with quartz glass window (Präzisions Glas & Optik GmbH, UV-Grade Fused Silica) under constant nitrogen purging to remove any dissolved oxygen in the electrolyte (Figure S 5.1). The electrolyte was 0.1 M $Na_2SO_4$ (Aldrich) in deionized water (Millipore Q grade, 18.2 MΩ cm) at pH 6.8. In the case of light exposure, all samples were illuminated through the substrate by an AM1.5 solar simulator (Solar Light Model 16S) at 100 mW $cm^{-2}$ or a 455 nm LED with a photon flux of 1017 $s^{-1}$ at the sample position.

Figure S 5.1: Photograph of the custom build, airtight cell with quartz glass window and nitrogen purging used for all photoelectrochemical measurements in aqueous electrolyte.

**Cyclic voltammetry (CV) and chronoamperometry (CA)**

CV and CA measurements were performed with a Metrohm μ-Autolab III potentiostat with FRA2 impedance analyzer with a platinum wire counter electrode and a $Hg/Hg_2SO_4$ reference electrode in order to apply a potential range of 0.3 – 1.0 V vs. reference hydrogen electrode (RHE). Prior to each measurement, the potential of the $Hg/Hg_2SO_4$ electrode was determined against RHE. The active area of the COF films was selected by masking the films with PFTE adhesive tape to expose a film area of 0.212 $cm^2$. CV measurements were performed by scanning from positive to negative potentials either in the dark or under illumination at a sweep rate of 20 mV $s^{-1}$.

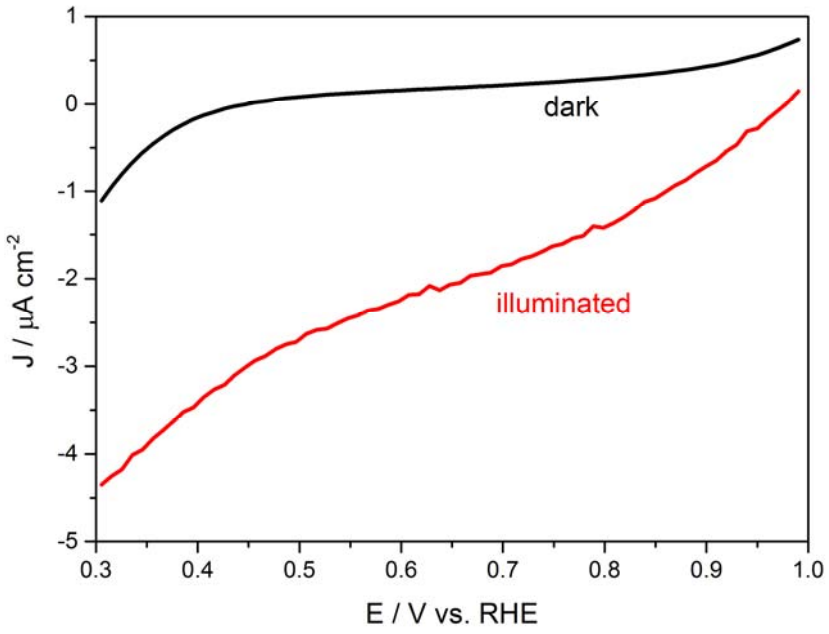


Figure S 5.2: Linear sweep voltammograms of a rough, 500 nm thick BDT-ETTA film on ITO performed in the dark (black) and under AM 1.5 illumination through the substrate (red).

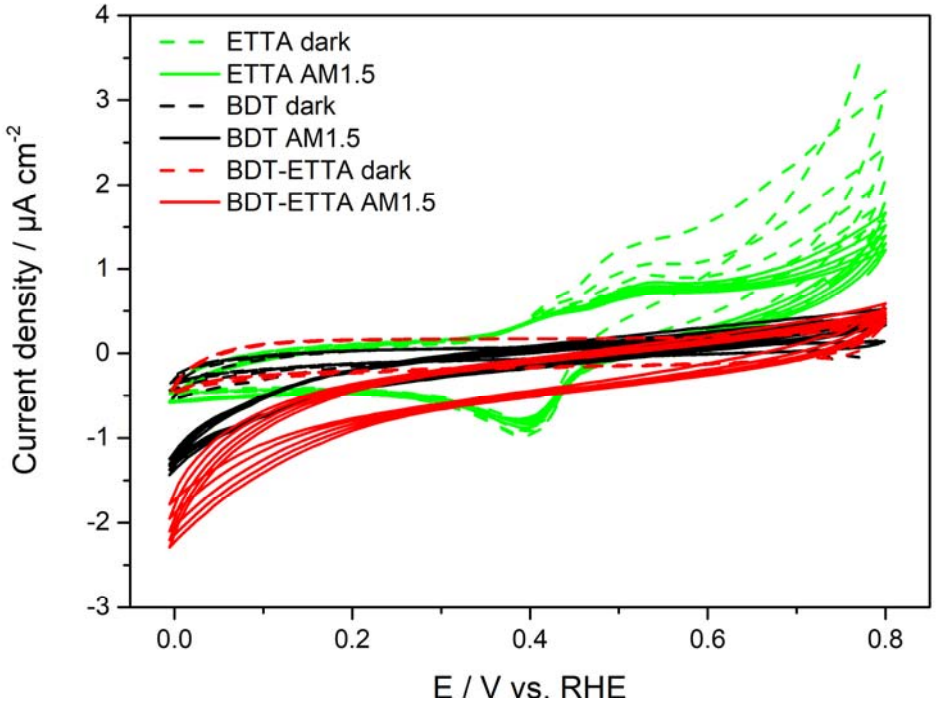


Figure S 5.3: Cyclic voltammograms of the BDT-ETTA COF electrode (red) in the dark (dashed lines) and under AM1.5 substrate illumination (solid lines). The BDT-ETTA COF is compared with the corresponding monomers BDT (black) and ETTA (green) dropcasted on ITO substrate (2 mg monomer in 500 µL of EtOH/Acetone (v/v 1:1), respectively). We assume that the photoactivity arises from the BDT part, but the total photocurrent can be doubled for the case of a crystalline BDT-ETTA COF. In contrast, the ETTA part shows no photoactivity itself. Therefore, the formation of a COF material from photoactive building blocks like BDT allows the deposition of electrochemical stable thin film electrodes on TCO substrates.

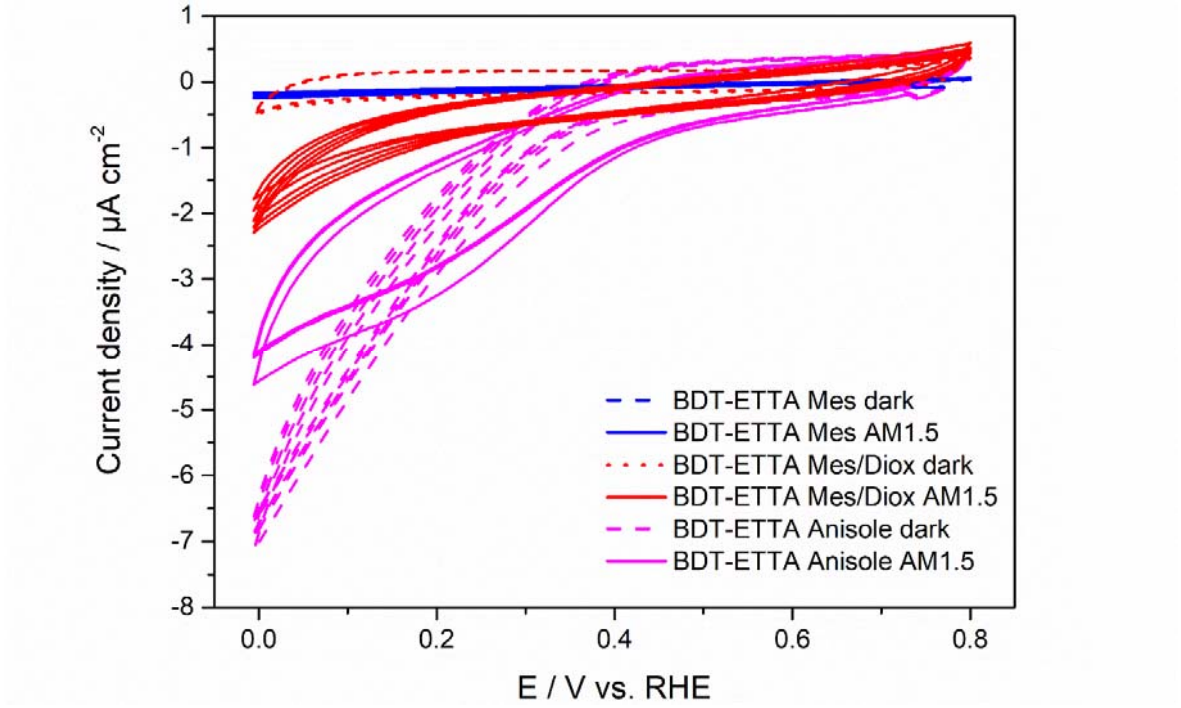


Figure S 5.4: The oriented grown BDT-ETTA electrode (red) is compared to amorphous, not oriented grown BDT-ETTA film electrodes. To achieve amorphous COF films instead of crystalline and oriented films, the synthesis was varied in the used solvents only, while amount of starting materials, the total volume of the reaction mixture and the added catalyst (acetic acid, 6 M) were kept the same. If the COF is grown in mesitylene (blue), it shows no activity at all. BDT-ETTA grown in Anisole (magenta) shows a high dark current onset potential which can be indicated as sign for poor stability. This is confirmed by the second measurement under illumination, where the electrode shows significantly lower current densities. Therefore we emphasize that crystallinity and orientation are key factors for the application of BDT-ETTA as photocathode material.

**Incident Photon-to-Current conversion Efficiency (IPCE)**

The IPCE measurement was performed under low-frequency chopped monochromatic light (1 Hz). A 150 W xenon lamp equipped with a monochromator and order-sorting filters was used as a light source. The sample was simultaneously illuminated by an AM1.5 solar simulator (Solar Light Model 16S) with OD3 filter (Thorlabs). The light intensity reaching the electrode was calibrated using a certified Fraunhofer ISE silicon reference cell equipped with a KG5 filter. All measurements were performed at 0.4 V vs. RHE under illumination through the substrate.

**Hydrogen detection**

Hydrogen detection measurements were performed in a four electrode setup with a Metrohm Autolab PGStat302N potentiostat, a platinum wire counter electrode and a $Hg/Hg_2SO_4$ reference electrode, whose potential was determined against a reversible hydrogen electrode within the applied measurement conditions. The exposed area of the COF thin film electrode was masked to 1.1 $cm^2$ (first working electrode) and a platinum mesh electrode was placed at a distance of 5 mm from the photoabsorber surface as second working electrode (Figure S 5.3). In a first step prior to the hydrogen detection measurement, 1.1 V vs. RHE was applied on the platinum mesh in a three electrode mode for 1.5 hours to remove any residues which can be oxidized and therefore determine the background current (Figure S 5.4). To drive the hydrogen evolution reaction, a potential of 0.4 V vs. RHE was applied to the COF photocathode and a potential of 1.1 V vs. RHE was set on the platinum mesh to oxidize the produced hydrogen. During the five-hour experiment, the AM1.5 illumination was manually chopped at intervals of 15 minutes. On average, the total hydrogen oxidation current increased over time (Figure S 5.7). Reference measurements with constant hydrogen evolution on blank ITO substrates with a comparable exposed area showed that it is possible to quantify only a fraction of the produced hydrogen, which was calculated from the oxidative current (Figure S 5.5). The remaining amount is either dissolved in the electrolyte and therefore distributed over the whole volume of the measuring cell or escapes the liquid due to the moderate nitrogen purging. For these reasons, the absolute amount of produced hydrogen could not be determined. However, the observation that the oxidation current rises and falls with the photocurrent proves that the oxidized species is produced exclusively in the photoelectrochemical process at the COF film.

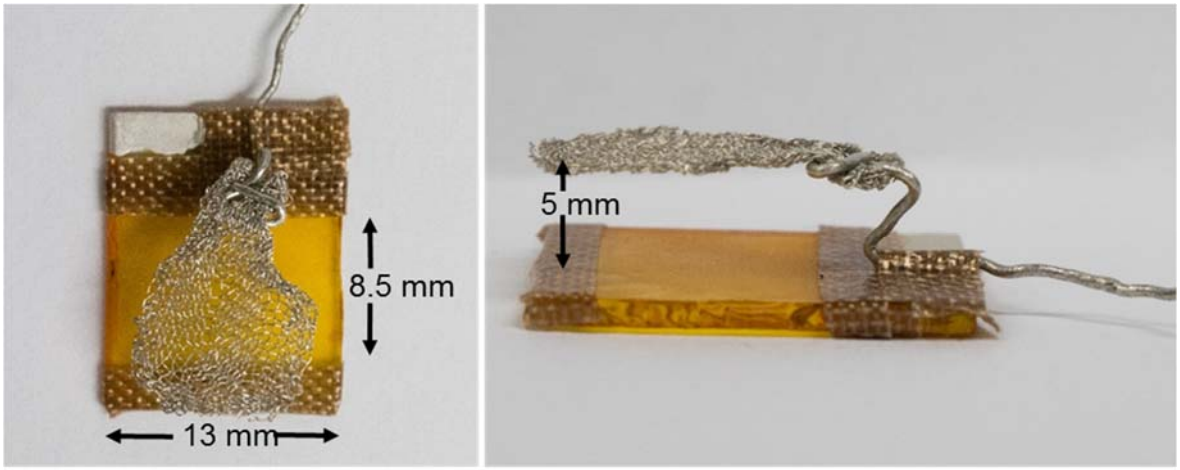


Figure S 5.5: Photographs of a sample used for a hydrogen detection measurement: The masked COF film is contacted with silver paint (first working electrode) and a platinum mesh is placed in 5 mm distance to the film surface to oxidize the produced hydrogen.

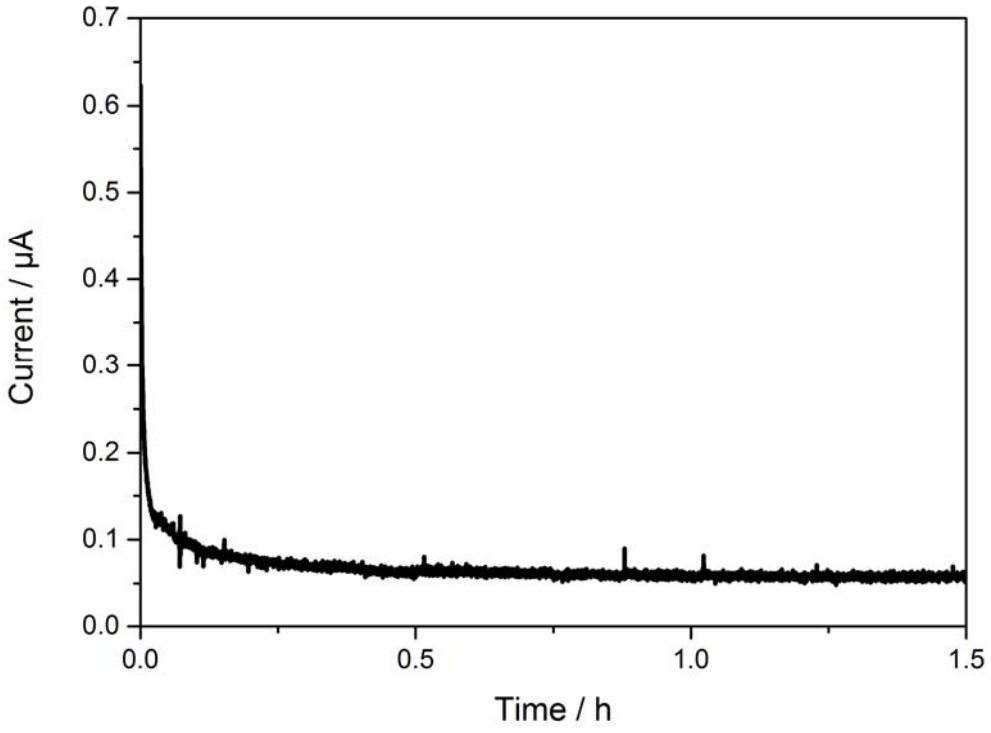


Figure S 5.6: Any residues in the electrolyte were oxidized at 1.1 V vs. RHE on a platinum mesh prior to the hydrogen detection measurement.

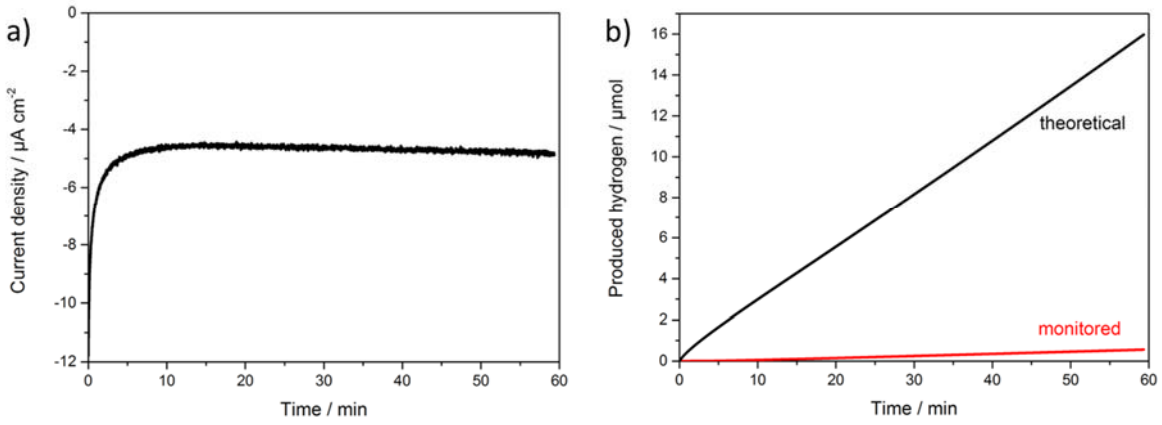


Figure S 5.7: a) A potentiostatic measurement performed at -1.2 V vs. $Hg/Hg_2SO_4$ on a blank ITO substrate was used to evolve hydrogen with a current density of 5 µA $cm^{-2}$. b) The cumulative amount of hydrogen detected was calculated from the oxidative current at the platinum mesh. The mismatch between monitored and theoretical values shows that the collection efficiency of this experimental setup is about 3.5% after 60 minutes.

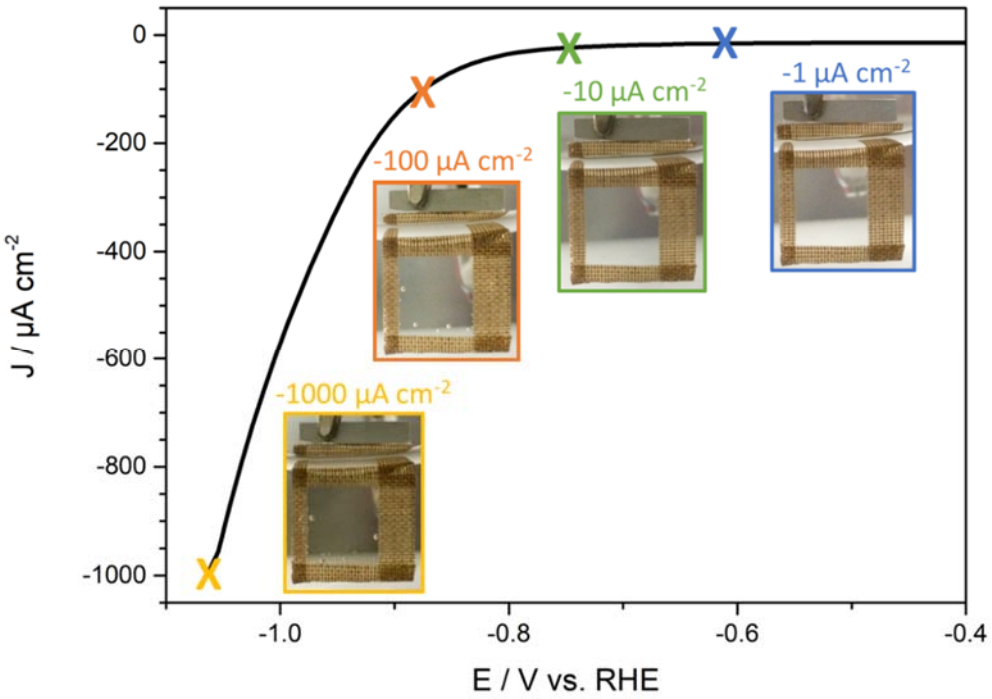


Figure S 5.8: Cyclic voltammogram of a FTO electrode without illumination. The electrode was masked with Teflon adhesive tape to obtain an uncovered area of 1 $cm^2$. Afterwards, rising current densities of 1 – 1000 µA $cm^{-2}$ were applied to the FTO electrode for 15 minutes each. No hydrogen formation is visible for current densities up to 10 µA $cm^{-2}$, as can be indicated from the pictures (insets). We assume that the produced hydrogen is directly dissolved in the electrolyte. With current densities above 100 µA $cm^{-2}$, the hydrogen gas is produced fast enough on the electrode surface to form bubbles.

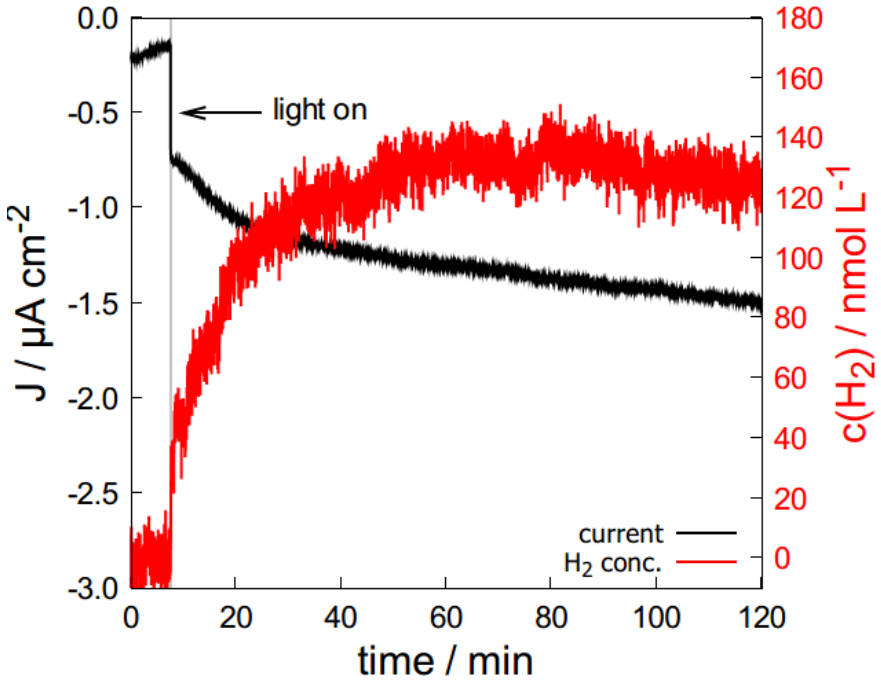


Figure S 5.9: The hydrogen evolution on a BDT-ETTA COF electrode was quantified with a hydrogen microsensor (Unisense A/S H2-NPLR) with selective silicone membrane at a static potential of 0.4 V vs. RHE. Illumination of the sample with AM1.5 simulated sunlight results in a photocurrent (black) and in the production of hydrogen (red).

**Section 4: SEM**

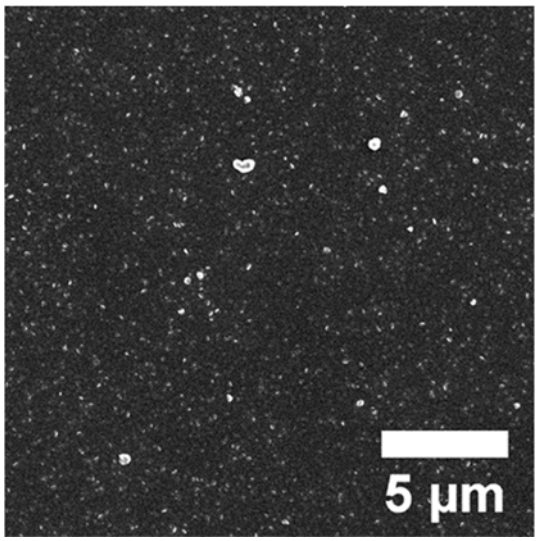


Figure S 5.10: Top-view SEM images of BDT-ETTA film on ITO.

The morphology of the COF bulk material was examined by SEM (Figure S 5.11). SEM analysis reveals a comparable morphology of COF particles for BDT-ETTA with a spherical and intergrown rod morphology.

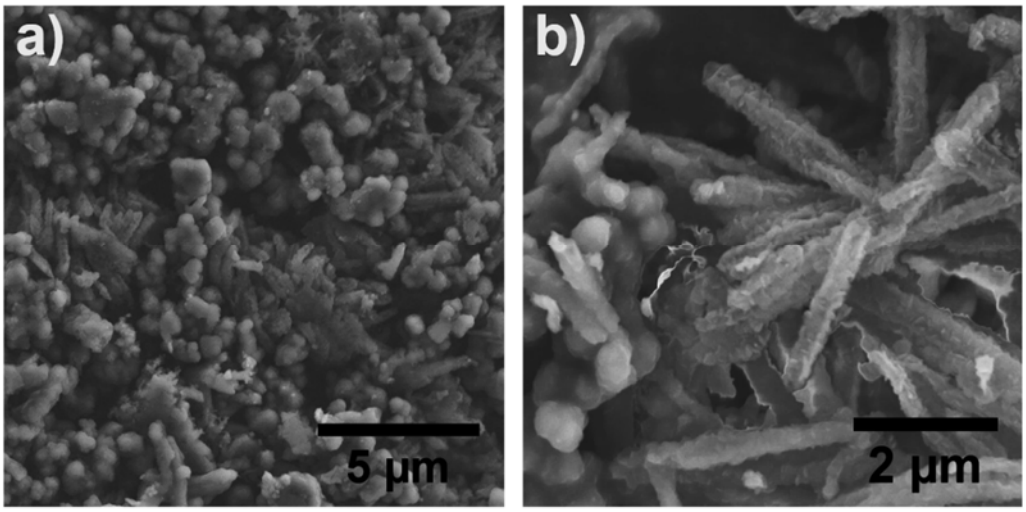


Figure S 5.11: SEM images of BDT-ETTA bulk material (a, b). Besides a spherical morphology, BDT-ETTA COF consists of rod-shaped structures.

**Section 5: X-Ray Diffraction Analysis**

Induced by steric hindrance of close-by phenyl protons in ETTA, a propeller-like shape of the building unit is favored. In contrast to more planar building units, this results in an increased stacking distance of adjacent layers. Also, this twist leads to a lock-and-key-like molecular stacking. The conformation of the first layer leads to a predetermined conformation and alignment of the growing second layer.[19] For COFs without this locking mechanism, AA eclipsed stacking of adjacent layers would still be most suitable. Nevertheless, a slight lateral offset of the layers can be expected and is energetically favorable for planar building blocks, especially with incorporated heteroatoms.[63-64] This lateral offset would induce peak broadening not distinguishable from the AA eclipsed stacking by PXRD. In the case of ETTA, adjacent layers are guided by the position of ETTA in previous layers, resulting in energetically favored lateral positions and extension of oriented crystalline domains.

Due to the fact that the 001 reflection of the COF films (20.1 °2θ for BDT-ETTA) coincides with an ITO reflection (21.56 °2θ), we also grew films on FTO under the same conditions to distinguish the reflections of COF and substrate.

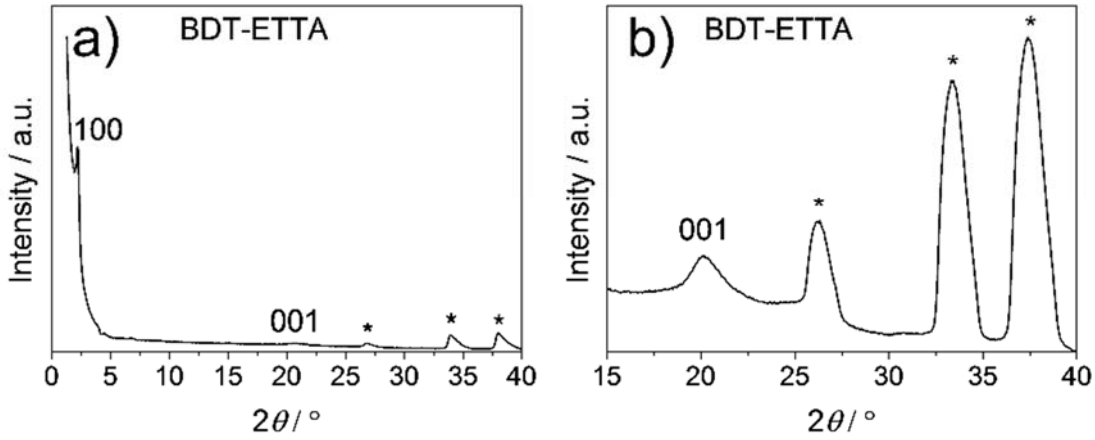


Figure S 5.12: a) XRD of BDT-ETTA COF films on FTO in detector scan mode. 100 reflections result from less oriented COF particles on top of the film. The 001 reflection from the COF and the FTO reflections (*) are distinguishable. The 001 reflection in b) is related to π–stacking, which can be clearly distinguished from FTO reflections in the zoom-in.

**Stability tests**

For stability tests, the COF powder samples were Soxhlet-extracted with anhydrous THF for 3 d. The COF materials were then suspended in different solvent mixtures for 24 h. After washing with anhydrous THF, the samples were vacuum-dried, and their crystallinity was investigated.

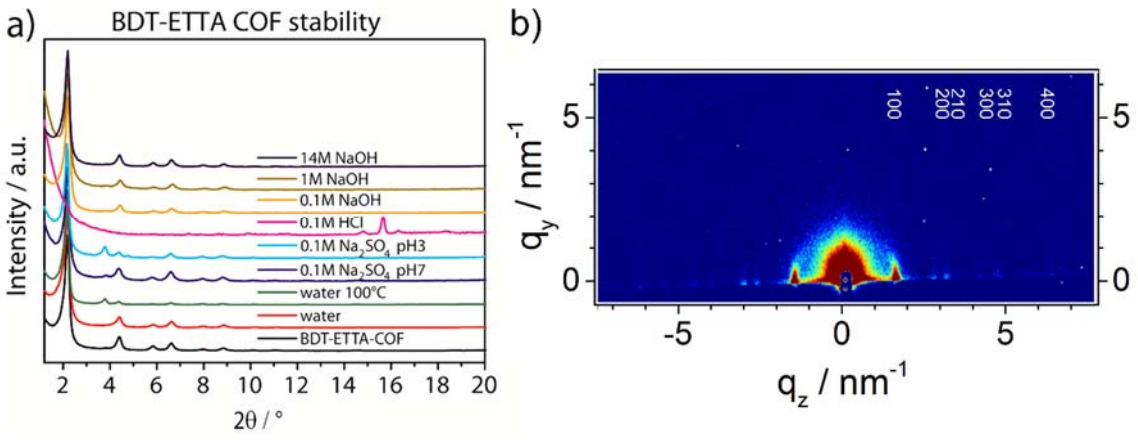


Figure S 5.13: a) Stability of BDT-ETTA (5 mg) powder exposed to 1 mL of different solvent mixtures for 24 h. If no temperature is noted, the experiments were performed at room temperature. In most cases, the crystallinity was maintained. An exception was the exposure to strongly acidic solutions. b) GID of a BDT-ETTA COF film after potentiostatic measurements. The still preserved crystallinity and orientation is represented by an intense first 100 reflection as well as higher order reflections visible only in the z-direction.

**Section 6: Sorption**

The first steep uptake at very low $p/p^0$ in Figure 5.1 indicates the micropore filling, while the second one ($p/p^0$ = 0.2 to 0.3) represents the capillary condensation within the mesopores. Due to the comparably small size of the mesopores (≤ 4 nm), a type IVb physisorption isotherm without a hysteresis loop is obtained.[65] The pore size distribution was calculated from QSDFT with a carbon kernel for cylindrical pore geometry.

**Section 7: Structural simulations of BDT-ETTA COF**

Space group: P*6* with an AA-hexagonal eclipsed stacking (AA-H).

**Table 4.5.1:** Fractional atomic coordinates for the unit cell of AA-H calculated with the Materials Studio v7.0 modeling program.

| P*6* (168) – hexagonal | | | |
|---|---|---|---|
| a = b = 4.6413(4) nm, c = 0.4465(5) nm | | | |
| α = β = 90°, γ = 120° | | | |
| **Atom** | **x/a** | **y/b** | **z/c** |
| C1 | 0.48474 | 1.48621 | 0.48266 |
| C2 | 0.51973 | 0.54732 | 0.47664 |
| C3 | 0.54629 | 0.51248 | 0.47792 |
| C4 | 0.57161 | 0.53280 | 0.30656 |
| C5 | 0.60077 | 0.53204 | 0.29905 |
| C6 | 0.60521 | 0.51088 | 0.46405 |
| C7 | 0.58018 | 0.49066 | 0.63439 |
| C8 | 0.55131 | 0.49185 | 0.64410 |
| C9 | 0.45948 | 0.42899 | 0.65637 |

| **Atom** | **x/a** | **y/b** | **z/c** |
|---|---|---|---|
| C10 | 0.45516 | 0.39750 | 0.65108 |
| C11 | 0.47177 | 0.38927 | 0.46800 |
| C12 | 0.49166 | 0.41258 | 0.28206 |
| C13 | 0.49551 | 0.44380 | 0.28614 |
| N14 | 0.53262 | 0.64303 | 0.47056 |
| C15 | 0.51035 | 0.64986 | 0.40028 |
| N16 | 0.63409 | 0.50822 | 0.45469 |
| C17 | 0.66312 | 0.53199 | 0.40099 |
| C18 | 0.48289 | 0.31631 | 0.40351 |
| S19 | 0.44186 | 0.28140 | 0.43759 |
| C20 | 0.46043 | 0.25631 | 0.4118 |
| C21 | 0.49408 | 0.27411 | 0.38466 |
| C22 | 0.50649 | 0.30898 | 0.3780 |
| C23 | 0.51274 | 0.25870 | 0.3691 |
| C24 | 0.49620 | 0.22457 | 0.37936 |
| C25 | 0.46247 | 0.20668 | 0.40062 |
| C26 | 0.44382 | 0.22213 | 0.4188 |
| C27 | 0.45019 | 0.17178 | 0.40583 |
| C28 | 0.47411 | 0.16473 | 0.39422 |
| S29 | 0.51516 | 0.19982 | 0.37111 |

| **Atom** | **x/a** | **y/b** | **z/c** |
|---|---|---|---|
| H30 | 0.44682 | 0.43498 | 0.80183 |
| H31 | 0.43934 | 0.37966 | 0.79306 |
| H32 | 0.50381 | 0.40660 | 0.13152 |
| H33 | 0.51072 | 0.46140 | 0.14393 |
| H34 | 0.53208 | 0.32700 | 0.35554 |
| H35 | 0.53905 | 0.27265 | 0.3512 |
| H36 | 0.41753 | 0.20819 | 0.43888 |
| H37 | 0.42456 | 0.15359 | 0.42127 |
| H38 | 0.44342 | 0.11098 | 0.37202 |
| H39 | 0.51389 | 0.36941 | 0.34694 |
| H40 | 0.61941 | 0.54735 | 0.16036 |
| H41 | 0.56868 | 0.54908 | 0.17619 |
| H42 | 0.58314 | 0.47404 | 0.76138 |
| H43 | 0.53260 | 0.47604 | 0.77652 |

**Table 4.5.2:** Space groups and cell parameters of AA-H and AB-H COFs constructed from BDT and ETTA.

| Structure | Crystal System | Space group | Cell parameters |
|---|---|---|---|
| AA-H | hexagonal | P*6* | a=b= 4.6413 nm, c = 0.45 nm, α=β=90°, γ=120° |
| AB-H | hexagonal | P*63* | a=b= 4.6413 nm, c = 0.76 nm, α=β=90°, γ=120° |

For comparison, an XRD pattern of an eclipsed structure in P*6* indexed as AA-hexagonal (AA-H) and a staggered structure in P*63* indexed as AB-hexagonal (AB-H) were simulated (Figure S 5.14a) and b)). The simulated XRD patterns coincide in several reflection positions, although the significant differences in intensities show a mismatch between the simulated structure (AB-H) and the experimental data.

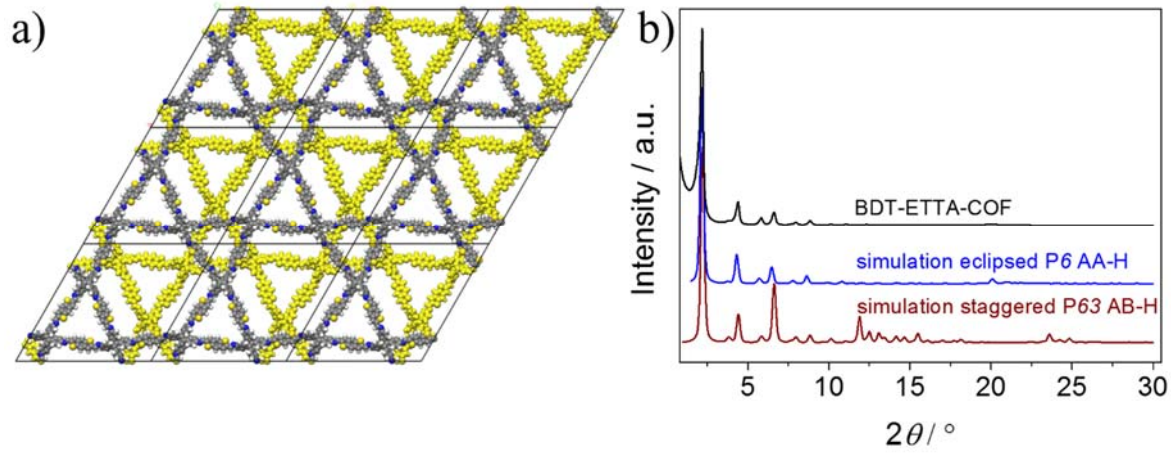


Figure S 5.14: a) Staggered structure of BDT-ETTA in P63 symmetry AB-hexagonal (AB-H). b) Resulting simulated XRD pattern of the eclipsed AA-H with P6 and the staggered AB-H with P63 symmetry. The reflection intensities in the staggered simulation differ significantly from the experimental data.

**Section 9: IR Spectroscopy**

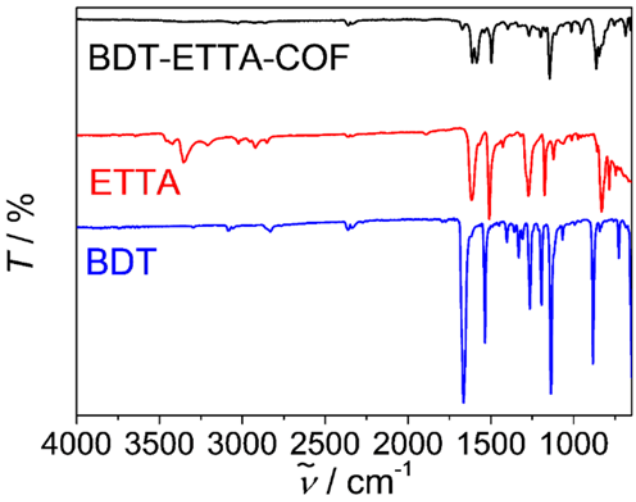


Figure S 5.15: IR spectra of BDT-ETTA COF powder (black) and starting materials (ETTA, red and BDT, blue).

## Section 10: Thermogravimetric Analysis

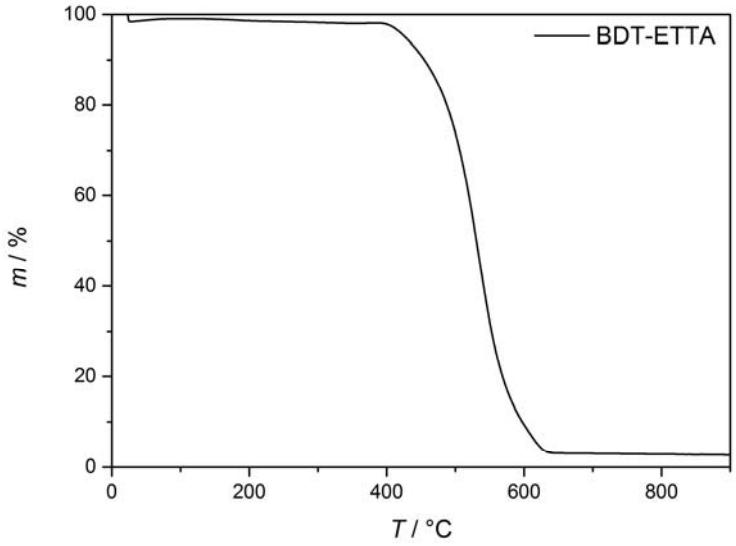


Figure S 5.16: Thermogravimetric analysis of BDT-ETTA COF.

## Section 11: Elemental Analysis

Table 5.3: Elemental analysis of BDT-ETTA COF bulk material compared with the calculated mass percentages.

| **Element** | **BDT-ETTA** | |
|---|---|---|
| | Theoretical percentage | Measured percentage |
| **N** | 6.89 | 6.69 |
| **C** | 73.86 | 70.00 |
| **H** | 3.47 | 3.68 |
| **S** | 15.78 | 14.06 |

The deviations of theoretical and measured atomic percentages are tentatively attributed to COF structures having a certain number of defects (missing building blocks).

## Section 12: NMR Spectra

### TNPE

$^1$H, 400 MHz, DMSO-$d_6$

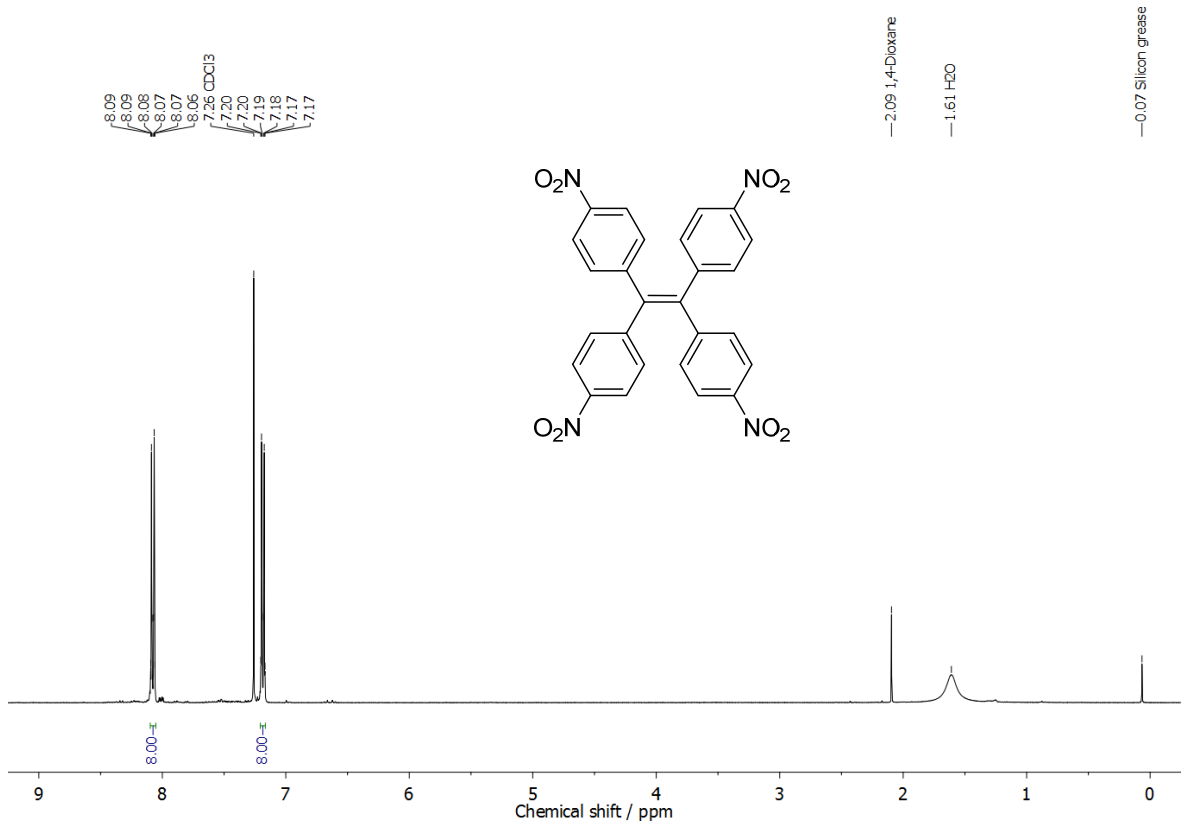


Figure S 5.17: $^1$H NMR spectrum of TNPE.

**ETTA**

$^1$H, 400 MHz, DMSO-$d_6$

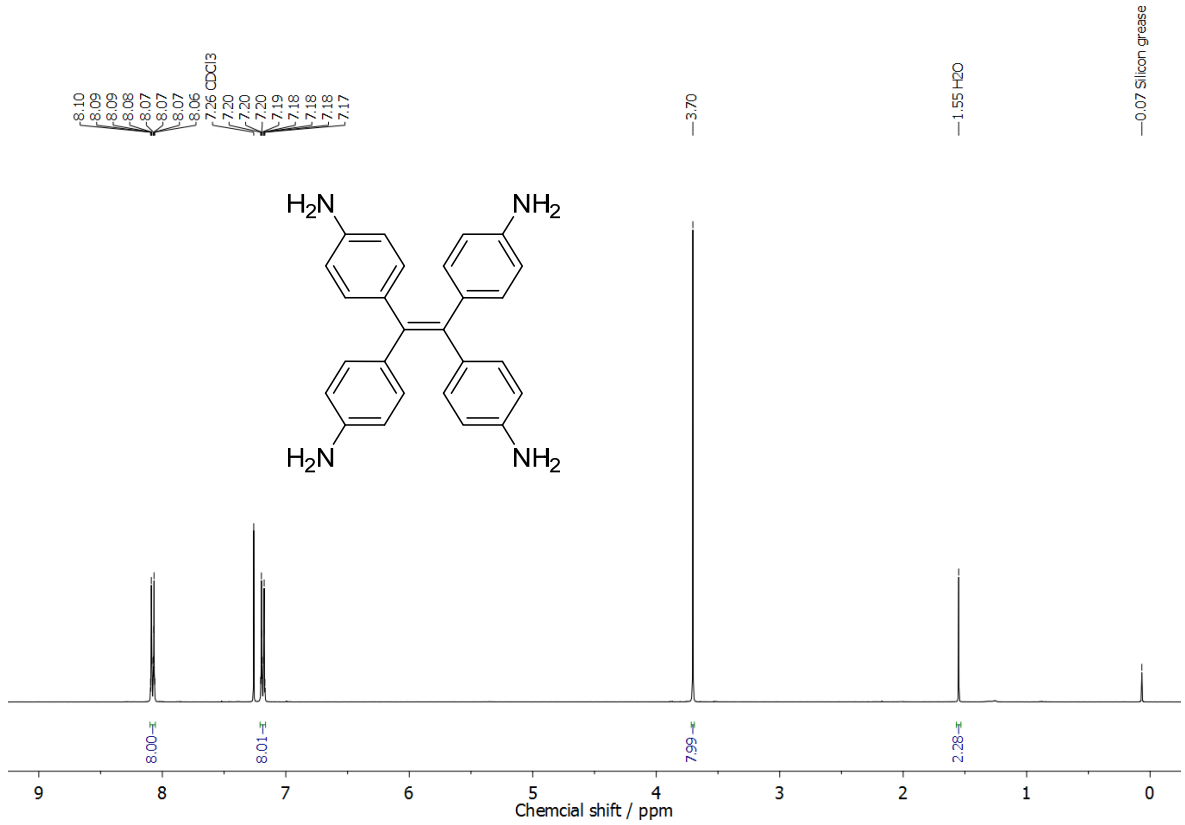


Figure S 5.18: $^1$H NMR spectrum of ETTA.

**BDT**

$^1$H, 400 MHz, DMSO-$d_6$

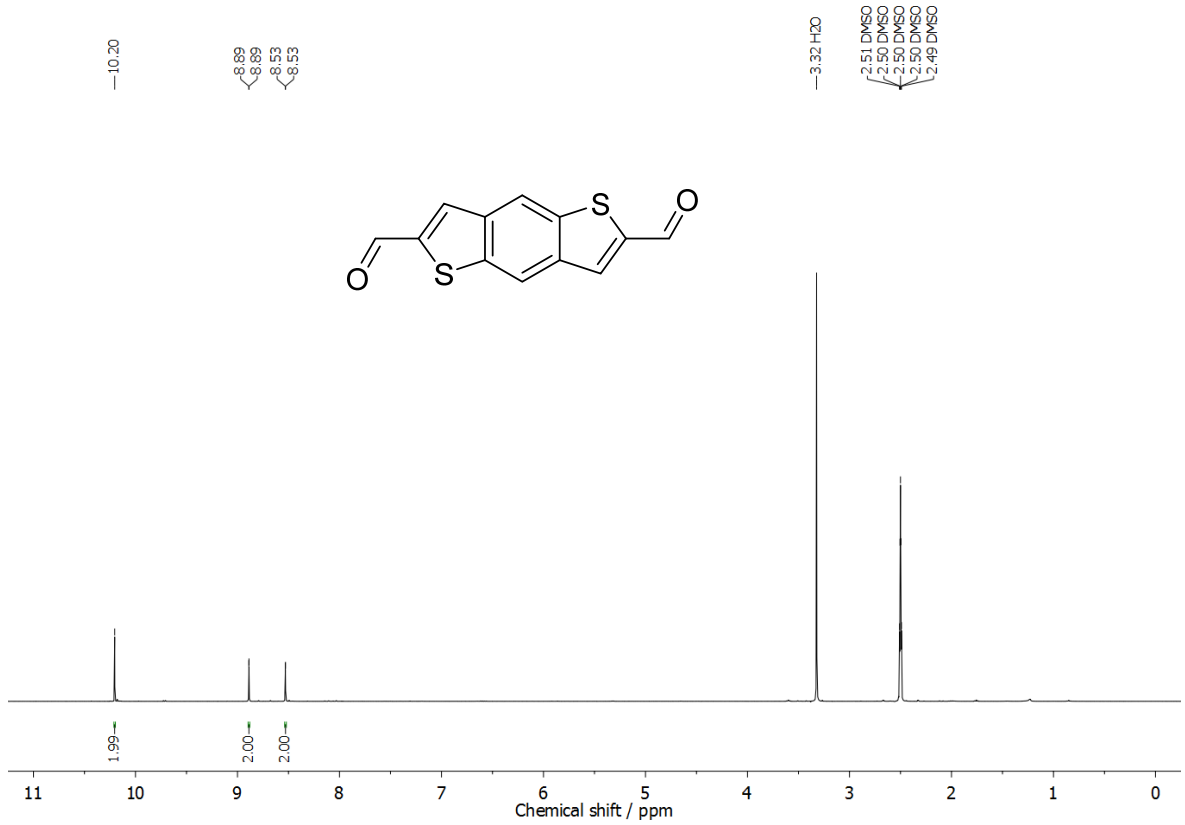


Figure S 5.19: $^1$H NMR spectrum of BDT.

$^{13}$C, 100 MHz, DMSO-$d_6$

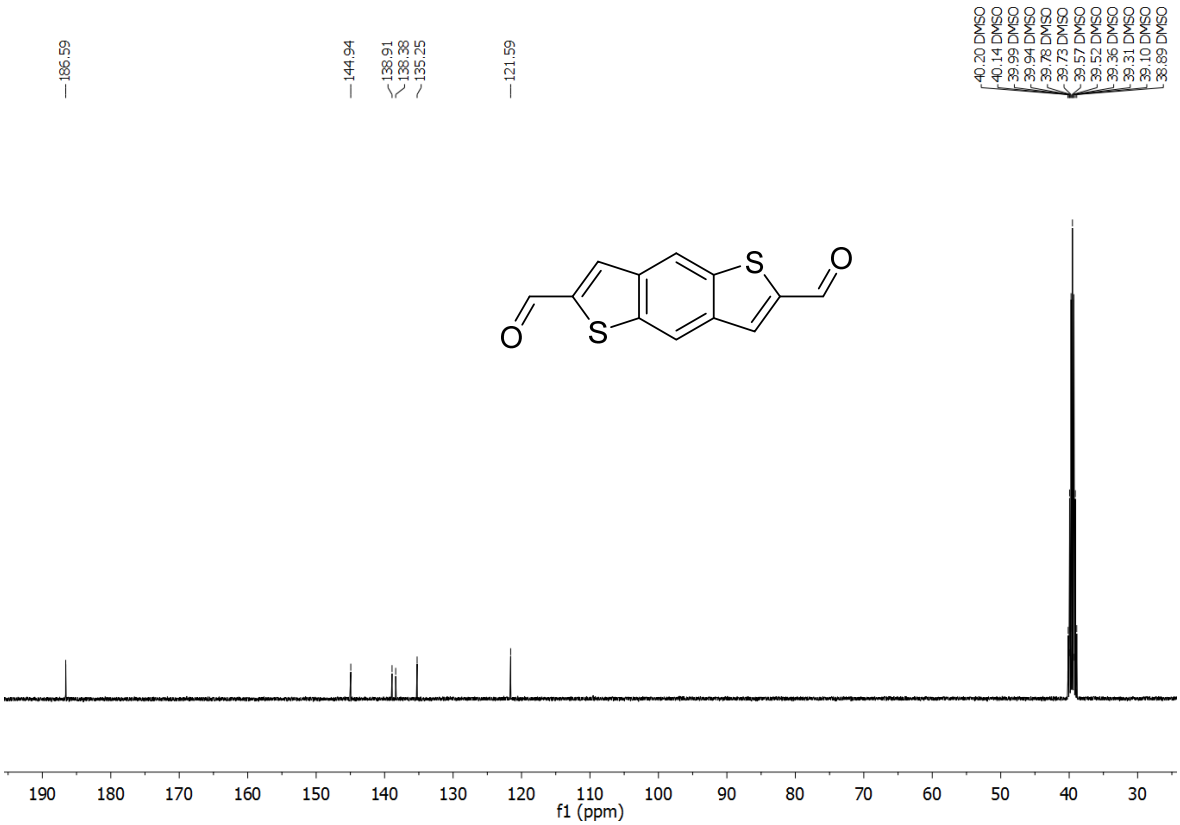


Figure S 5.20: $^{13}$C NMR spectrum of BDT.

# 5.6 REFERENCES

(1) Peter, L. M. J. *Solid State Electrochem*. **2012**, *17*, 315-326.

(2) van de Krol, R.; Liang, Y.; Schoonman, J. *J. Mater. Chem.* **2008**, *18*, 2311-2320.

(3) Sivula, K.; Le Formal, F.; Gratzel, M. *ChemSusChem* **2011**, *4*, 432-449.

(4) Dunn, H. K.; Feckl, J. M.; Muller, A.; Fattakhova-Rohlfing, D.; Morehead, S. G.; Roos, J.; Peter, L. M.; Scheu, C.; Bein, T. *Phys. Chem. Chem. Phys.* **2014**, *16*, 24610-24620.

(5) Hu, S.; Shaner, M. R.; Beardslee, J. A.; Lichterman, M.; Brunschwig, B. S.; Lewis, N. S. *Science* **2014**, *344*, 1005-1009.

(6) Reece, S. Y.; Hamel, J. A.; Sung, K.; Jarvi, T. D.; Esswein, A. J.; Pijpers, J. J.; Nocera, D. G. *Science* **2011**, *334*, 645-648.

(7) Woodhouse, M.; Parkinson, B. A. *Chem. Soc. Rev.* **2009**, *38*, 197-210.

(8) Woodhouse, M.; Parkinson, B. A. *Chem. Mater.* **2008**, *20*, 2495-2502.

(9) Singh, A. K.; Mathew, K.; Zhuang, H. L.; Hennig, R. G. *J. Phys. Chem. Lett.* **2015**, *6*, 1087-1098.

(10) Castelli, I. E.; Olsen, T.; Datta, S.; Landis, D. D.; Dahl, S.; Thygesen, K. S.; Jacobsen, K. W. *Energy Environ. Sci.* **2012**, *5*, 5814-5819.

(11) Hunt, J. R.; Doonan, C. J.; LeVangie, J. D.; Côté, A. P.; Yaghi, O. M. *J. Am. Chem. Soc.* **2008**, *130*, 11872-11873.

(12) Côte, A. P.; Benin, A. I.; Ockwig, N. W.; O'Keeffe, M.; Matzger, A. J.; Yaghi, O. M. *Science* **2005**, *310*, 1166-1170.

(13) Calik, M.; Sick, T.; Dogru, M.; Döblinger, M.; Datz, S.; Budde, H.; Hartschuh, A.; Auras, F.; Bein, T. *J. Am. Chem. Soc.* **2016**, *138*, 1234-1239.

(14) Lohse, M. S.; Rotter, J. M.; Margraf, J. T.; Werner, V.; Becker, M.; Herbert, S.; Knochel, P.; Clark, T.; Bein, T.; Medina, D. D. *CrystEngComm* **2016**, *18*, 4295-4302.

(15) Medina, D. D.; Rotter, J. M.; Hu, Y.; Dogru, M.; Werner, V.; Auras, F.; Markiewicz, J. T.; Knochel, P.; Bein, T. *J. Am. Chem. Soc.* **2015**, *137*, 1016-1019.

(16) Uribe-Romo, F. J.; Hunt, J. R.; Furukawa, H.; Klöck, C.; O'Keeffe, M.; Yaghi, O. M. *J. Am. Chem. Soc.* **2009**, *131*, 4570-4571.

(17) Chen, X.; Addicoat, M.; Irle, S.; Nagai, A.; Jiang, D. *J. Am. Chem. Soc.* **2013**, *135*, 546-549.

(18) Zhang, Y.-B.; Su, J.; Furukawa, H.; Yun, Y.; Gándara, F.; Duong, A.; Zou, X.; Yaghi, O. M. *J. Am. Chem. Soc.* **2013**, *135*, 16336-16339.

(19) Ascherl, L.; Sick, T.; Margraf, J. T.; Lapidus, S. H.; Calik, M.; Hettstedt, C.; Karaghiosoff, K.; Döblinger, M.; Clark, T.; Chapman, K. W.; Auras, F.; Bein, T. *Nat. Chem.* **2016**, *8*, 310-316.

(20) Fang, Q.; Zhuang, Z.; Gu, S.; Kaspar, R. B.; Zheng, J.; Wang, J.; Qiu, S.; Yan, Y. *Nat. Commun.* **2014**, *5*, 4503-4510.

(21) Fang, Q.; Wang, J.; Gu, S.; Kaspar, R. B.; Zhuang, Z.; Zheng, J.; Guo, H.; Qiu, S.; Yan, Y. *J. Am. Chem. Soc.* **2015**, *137*, 8352-8355.

(22) Uribe-Romo, F. J.; Doonan, C. J.; Furukawa, H.; Oisaki, K.; Yaghi, O. M. *J. Am. Chem. Soc.* **2011**, *133*, 11478-11481.

(23) Dalapati, S.; Jin, S.; Gao, J.; Xu, Y.; Nagai, A.; Jiang, D. *J. Am. Chem. Soc.* **2013**, *135*, 17310-17313.

(24) Jackson, K. T.; Reich, T. E.; El-Kaderi, H. M. *Chem. Commun.* **2012**, *48*, 8823-8825.

(25) Furukawa, H.; Yaghi, O. M. *J. Am. Chem. Soc.* **2009**, *131*, 8875-8883.

(26) Doonan, C. J.; Tranchemontagne, D. J.; Glover, T. G.; Hunt, J. R.; Yaghi, O. M. *Nat. Chem.* **2010**, *2*, 235-238.

(27) Xu, H.; Chen, X.; Gao, J.; Lin, J.; Addicoat, M.; Irle, S.; Jiang, D. *Chem. Commun.* **2014**, *50*, 1292-1294.

(28) Ding, S.-Y.; Gao, J.; Wang, Q.; Zhang, Y.; Song, W.-G.; Su, C.-Y.; Wang, W. *J. Am. Chem. Soc.* **2011**, *133*, 19816-19822.

(29) Oh, H.; Kalidindi, S. B.; Um, Y.; Bureekaew, S.; Schmid, R.; Fischer, R. A.; Hirscher, M. *Angew. Chem. Int. Ed.* **2013**, *52*, 13219-13222.

(30) Ma, H.; Ren, H.; Meng, S.; Yan, Z.; Zhao, H.; Sun, F.; Zhu, G. *Chem. Commun.* **2013**, *49*, 9773-9775.

(31) Lohse, M. S.; Stassin, T.; Naudin, G.; Wuttke, S.; Ameloot, R.; De Vos, D.; Medina, D. D.; Bein, T. *Chem. Mater.* **2016**, *28*, 626-631.

(32) DeBlase, C. R.; Silberstein, K. E.; Truong, T.-T.; Abruña, H. D.; Dichtel, W. R. *J. Am. Chem. Soc.* **2013**, *135*, 16821-16824.

(33) Chandra, S.; Kundu, T.; Kandambeth, S.; BabaRao, R.; Marathe, Y.; Kunjir, S. M.; Banerjee, R. *J. Am. Chem. Soc.* **2014**, *136*, 6570-6573.

(34) Flugel, E. A.; Lau, V. W.; Schlomberg, H.; Glaum, R.; Lotsch, B. V. *Chem. Eur. J.* **2016**, *22*, 3676-3680.

(35) Schwinghammer, K.; Tuffy, B.; Mesch, M. B.; Wirnhier, E.; Martineau, C.; Taulelle, F.; Schnick, W.; Senker, J.; Lotsch, B. V. *Angew. Chem. Int. Ed.* **2013**, *52*, 2435-2439.

(36) Schwinghammer, K.; Mesch, M. B.; Duppel, V.; Ziegler, C.; Senker, J.; Lotsch, B. V. *J. Am. Chem. Soc.* **2014**, *136*, 1730-1733.

(37) Lau, V. W.; Mesch, M. B.; Duppel, V.; Blum, V.; Senker, J.; Lotsch, B. V. *J. Am. Chem. Soc.* **2015**, *137*, 1064-1072.

(38) Caputo, C. A.; Gross, M. A.; Lau, V. W.; Cavazza, C.; Lotsch, B. V.; Reisner, E. *Angew. Chem. Int. Ed.* **2014**, *53*, 11538-11542.

(39) Zhang, J.; Chen, X.; Takanabe, K.; Maeda, K.; Domen, K.; Epping, J. D.; Fu, X.; Antonietti, M.; Wang, X. *Angew. Chem. Int. Ed. Engl.* **2010**, *49*, 441-444.

(40) Wang, X.; Maeda, K.; Thomas, A.; Takanabe, K.; Xin, G.; Carlsson, J. M.; Domen, K.; Antonietti, M. *Nat. Mater.* **2009**, *8*, 76-80.

(41) Schwinghammer, K.; Hug, S.; Mesch, M. B.; Senker, J.; Lotsch, B. V. *Energy Environ. Sci.* **2015**, *8*, 3345-3353.

(42) Schwab, M. G.; Hamburger, M.; Feng, X.; Shu, J.; Spiess, H. W.; Wang, X.; Antonietti, M.; Mullen, K. *Chem. Commun.* **2010**, *46*, 8932-8934.

(43) Vyas, V. S.; Haase, F.; Stegbauer, L.; Savasci, G.; Podjaski, F.; Ochsenfeld, C.; Lotsch, B. V. *Nat. Commun.* **2015**, *6*, 8508-8516.

(44) Stegbauer, L.; Schwinghammer, K.; Lotsch, B. V. *Chem. Sci.* **2014**, *5*, 2789-2793.

(45) Bi, J.; Fang, W.; Li, L.; Wang, J.; Liang, S.; He, Y.; Liu, M.; Wu, L. *Macromol. Rapid Commun.* **2015**, *36*, 1799-1805.

(46) Kuecken, S.; Acharjya, A.; Zhi, L.; Schwarze, M.; Schomacker, R.; Thomas, A. *Chem Commun (Camb)* **2017**, *53*, 5854-5857.

(47) Chen, X.; Addicoat, M.; Jin, E.; Zhai, L.; Xu, H.; Huang, N.; Guo, Z.; Liu, L.; Irle, S.; Jiang, D. *J. Am. Chem. Soc.* **2015**, *137*, 3241-3247.

(48) Haase, F.; Banerjee, T.; Savasci, G.; Ochsenfeld, C.; Lotsch, B. V. *Faraday Discuss.* **2017**, *201*, 247-264.

(49) He, S.; Rong, Q.; Niu, H.; Cai, Y. *Chem. Commun.* **2017**, *53*, 9636-9639.

(50) Banerjee, T.; Haase, F.; Savasci, G.; Gottschling, K.; Ochsenfeld, C.; Lotsch, B. V. *J. Am. Chem. Soc*. **2017**, *139*, 16228-16234.

(51) Dogru, M.; Handloser, M.; Auras, F.; Kunz, T.; Medina, D.; Hartschuh, A.; Knochel, P.; Bein, T. *Angew. Chem. Int. Ed.* **2013**, *52*, 2920-2924.

(52) Calik, M.; Auras, F.; Salonen, L. M.; Bader, K.; Grill, I.; Handloser, M.; Medina, D. D.; Dogru, M.; Löbermann, F.; Trauner, D.; Hartschuh, A.; Bein, T. *J. Am. Chem. Soc.* **2014**, *136*, 17802-17807.

(53) a) Medina, D. D.; Werner, V.; Auras, F.; Tautz, R.; Dogru, M.; Schuster, J.; Linke, S.; Döblinger, M.; Feldmann, J.; Knochel, P.; Bein, T. *ACS Nano* **2014**, *8*, 4042-4052. b) Medina, D. D., Petrus, M. L., Jumabekov, A. N., Margraf, J. T., Weinberger, S., Rotter, J. M., Clark, T., Bein, T. *ACS Nano* **2017**, *11* (3), 2706-2713.

(54) Jin, S.; Ding, X.; Feng, X.; Supur, M.; Furukawa, K.; Takahashi, S.; Addicoat, M.; El-Khouly, M. E.; Nakamura, T.; Irle, S.; Fukuzumi, S.; Nagai, A.; Jiang, D. *Angew. Chem. Int. Ed.* **2013**, *52*, 2017-2021.

(55) Zhou, T. Y.; Xu, S. Q.; Wen, Q.; Pang, Z. F.; Zhao, X. *J. Am. Chem. Soc.* **2014**, *136*, 15885-15888.

(56) Sathre, R.; Scown, C. D.; Morrow, W. R.; Stevens, J. C.; Sharp, I. D.; Ager, J. W.; Walczak, K.; Houle, F. A.; Greenblatt, J. B. *Energy Environ. Sci.* **2014**, *7*, 3264-3278.

(57) Klahr, B. M.; Martinson, A. B. F.; Hamann, T. W. *Langmuir* **2011**, *27*, 461-468.

(58) Gorvin, J. H., *J. Chem. Soc.* **1959**, 678-682.

(59) Lu, J.; Zhang, J., *J. Mater. Chem. A* **2014**, *2*, 13831-13834.

(60) Koßmehl, G.; Beimling, P.; Manecke, G., *Makromol. Chem.* **1983**, *184*, 627-650.

(61) Connelly, N. G.; Geiger, W. E., *Chem. Rev.* **1996**, *96*, 877-910.

(62) Bard, A. J.; Faulkner, L. R., *Electrochemical Methods: Fundamentals and Applications*. 2nd ed.; Wiley: New York, 2001.

(63) Spitler, E. L.; Koo, B. T.; Novotney, J. L.; Colson, J. W.; Uribe-Romo, F. J.; Gutierrez, G. D.; Clancy, P.; Dichtel, W. R., *J. Am. Chem. Soc.* **2011**, *133*, 19416-19421.

(64) Dogru, M.; Bein, T., *Chem. Commun.* **2014**, *50*, 5531-5546.

(65) Thommes, M.; Kaneko, K.; Neimark, A. V.; Olivier, J. P.; Rodriguez-Reinoso, F.; Rouquerol, J.; Sing, K. S. W., *Pure Appl. Chem.* **2015**, *87*, 929-1069

# 6. SWITCHING ON CRYSTALLINITY AND PERMANENT POROSITY IN FRAGILE COVALENT ORGANIC FRAMEWORKS

Torben Sick[1], Sharath Kandambeth[1], Julian M. Rotter[1], Nicolai N. Bach[1], Markus Döblinger[1], Peter Mayer[1], Julia Merz[2], Austin Evans[1], Olaf A. von Mankowski[3], Todd B. Marder[2], Tim Clark[4], Dana D. Medina[1] and Thomas Bein[1]*

[1] Department of Chemistry and Center for NanoScience (CeNS), University of Munich (LMU), Butenandtstraße 5-13, 81377 Munich, Germany

[2] Department of Chemistry, University of Würzburg

[3] Department of Chemistry, University of Munich (LMU)

[4] Department of Chemistry and Pharmacy, Friedrich Alexander University Erlangen-Nürnberg, Germany

## 6.1 ABSTRACT

Covalent organic frameworks (COFs) attract great interest owing to their well-defined, tunable pore systems and very high surface areas. One of the central challenges regarding their possible integration into devices is the sensitivity of many 2D COF materials towards external stimuli. Many of the 2D COF materials have a fragile framework structure and they can instantly lose crystallinity and porosity upon the action of external stimuli such as solvent treatment. Herein, we systematically studied the sensitivity of 2D imine COFs on a molecular level. We observed that the sensitivity of the 1,3,5-tri(4-aminophenyl)benzene (TAPB)-based 2D COFs mainly arises from weak π-stacking of the linear dialdehyde linker between adjacent COF layers. COFs with enlarged π-systems or alkoxy functionalities in the linear linkers are more robust towards the external stimuli, while COFs with unsubstituted linkers feature only weak π-attractive interactions and instantly lose their crystallinity and porosity upon exposure to solvents or vapors. As the spatial control of stacking allows for tuning key enabling properties such as open porosity and crystallinity, stabilizing fragile COFs is an open challenge. Here we introduce treatment in supercritical carbon dioxide ($scCO_2$) as a highly efficient means to transform non-porous fragile COFs into highly crystalline and open porous frameworks. Strikingly, the framework structure of TAPB-COFs responds dynamically to such chemical stimuli,

demonstrating that their porosity and crystallinity can be reversibly controlled by solvent stimuli and $scCO_2$ treatment.

## 6.2 INTRODUCTION

Covalent organic frameworks (COFs) are a class of organic crystalline porous materials obtained by connecting organic building units through covalent bonds.[1] The dynamic nature of the formed covalent bonds, comprising mainly boroxines[2-3], boronic esters[4-9], imines[10-13], azines[14-15], imides[16-17], hydrazones[18-20] and triazines[21-24], and the defined geometries of the COF building blocks are two essential criteria for attaining ordered 2D or 3D framework structures.[7, 25] In 2D COF materials, extended molecular sheets interact through weak attractive forces to form defined molecular stacks and open pores. Therefore, the π-stacking interactions between adjacent COF layers play a pivotal role in achieving long-range order, accessible surface area, and structural stability.[2] For all new COF structures, the isolation of a crystalline and porous product from the reaction mixture can be challenging and the final quality of the product is highly dependent on the post-synthetic treatment.[16, 26-29] Crystalline 2D COFs with weak π-stacking interactions are prone to exfoliation into individual 2D layers upon exposure to different solvents and solvent mixtures during sonication[19,30-32] or by mechanical exfoliation.[33-34] The reason for the exfoliation in solution is still to be revealed, nevertheless it is believed that intercalation of solvent molecules might be the trigger.[19] COFs featuring enhanced π-stacking interactions were reported to be highly stable towards post-synthetic solvent treatment. Robust 2D COFs are usually constructed by reinforcing the π-stacking interactions between the COF layers, by methods such as intra-molecular hydrogen bonding[35], alkoxy group incorporation[36], defined docking of propeller moieties[37] and armchair building blocks[38], or by minimizing the dipole moments between COF layers.[39] Jiang and coworkers introduced a strategy to use arene/perfluoroarene-subunits to influence adjacent layers' polarities, yielding highly crystalline, alternatingly stacked frameworks.[41] However, the above strategies are typically based on tailoring the structural properties of the building blocks prior to the COF synthesis. As these building blocks are suitable only for specific types of COF structures, generating a potent post-synthesis protocol that assists in preserving and accessing the full potential of the COF properties is highly desirable. Beyond that, a reversible activation and deactivation protocol for the crystallinity and porosity of COFs could open the way for novel applications in size-selective sieving, membranes, catalysis and sensing, as 2D COFs generate their order and porosity in a highly dynamic process.

Herein, we report the synthesis of a series of hexagonal-pore COFs featuring a wide range of structural robustness. The COFs were synthesized through an acetic acid-catalyzed Schiff base condensation reaction of 1,3,5-tri(4-aminophenyl)benzene (TAPB) as a central building block with a variety of linear dialdehydes. Using unsubstituted linear dialdehydes, namely terephthalaldehyde (TA), thieno[3,2-*b*]thiophene-2,5-dicarboxaldehyde (TT) and benzo[1,2-*b*:4,5-*b*']dithiophene-2,6-dicarboxaldehyde (BDT) resulted in COFs with moderate crystallinity, limited pore accessibility and moderate structural stability towards a variety of external stimuli. These COFs were therefore classified as 'fragile'. Structural robustness of the BDT-core TAPB-COFs was achieved by employing BDT alkoxy analogues as building blocks, such as 4,8-dimethoxybenzo[1,2-*b*:4,5-*b*']dithiophene-2,6-dicarbaldehyde (BDT-OMe), 4,8-diethoxybenzo[1,2-*b*:4,5-*b*']dithiophene-2,6-dicarbaldehyde (BDT-OEt) and 4,8-dipropoxybenzo[1,2-*b*:4,5-*b*']dithiophene-2,6-dicarbaldehyde (BDT-OPr). Alternatively, structural robustness was achieved by a significant enlargement of the stacking interactions using a pyrene-2,7-dicarboxaldehyde (Pyrene-2,7). In contrast to the above fragile COFs, these frameworks display long-range structural order and high surface area even after long exposure to organic solvents and solvent vapors.

We developed a fast, simple and efficient post-synthetic activation protocol using supercritical carbon dioxide ($scCO_2$) to transform the above fragile COFs with moderate crystallinity and no porosity into highly crystalline and open porous frameworks. The fragile $scCO_2$ activated crystalline and open porous COFs were found to be highly sensitive towards a large variety of organic solvents and vapors. In contrast, the robust $scCO_2$ activated COFs showed stability towards external stimuli except 1,4-dioxane exposure. Depending on the fragility of the COF, a significant reduction in long-range order and porosity was already recorded upon short incubation times (24 h) of the COFs in solvent atmosphere. Remarkably, alternating $scCO_2$ activation and solvent vapor exposure cycles allowed for the reversible turning-on and -off of the COFs' crystallinity and porosity.

## 6.3 RESULTS AND DISCUSSION

COFs containing the TAPB building units were reported to exhibit excellent structural properties such as long range order and accessible surface areas.[16, 39, 42-52] To explore the stability and crystallinity of TAPB-based frameworks, we synthesized a family of TAPB-COFs with linear counterparts featuring a π-system such as TA, TT, BDT and Pyrene-2,7. In addition, we synthesized TAPB-COFs of substituted BDT cores exhibiting different alkoxy side chain lengths, namely BDT-OMe, BDT-OEt, and BDT-OPr. The series of these imine-linked TAPB-COFs was synthesized under solvothermal conditions. Briefly, 1 eq of TAPB (0.02 to 0.06 mmol) and 1.5 eq of linear dialdehyde (0.03 to 0.09 mmol) were suspended in a mixture of 1,4-dioxane and mesitylene (1.0 mL, 8:1 v:v) in a 6 mL glass tube under argon. The reaction mixture was sonicated for 2 min to obtain a highly dispersed suspension of precursors. After addition of acetic acid catalyst (100 µL, 6 M) the reaction tube was sealed and placed in a preheated oven at 100 °C for 72 h. The as-synthesized precipitates were isolated by filtration under reduced pressure. Subsequently, the crystallinity of the obtained powders was studied without further purification by employing powder X-ray diffraction (PXRD) analysis. The PXRD spectra revealed that the as-synthesized, filtered powders exhibit moderate to limited crystallinity (Figure S 6.3 – 6.5). To improve the structural features of the obtained COFs, namely the long-range order, different isolation and purification procedures were employed. Attempts at removing residual monomers, catalyst agents and solvents solely by vacuum-drying and heat activation did not lead to the desired improvement in crystallinity. Surprisingly, when employing solvent rinsing of the COF powders with the main reaction solvent, namely 1,4-dioxane, all the investigated TAPB-COFs showed low stability towards this purification procedure and lost their structural order (Figure S 6.2).

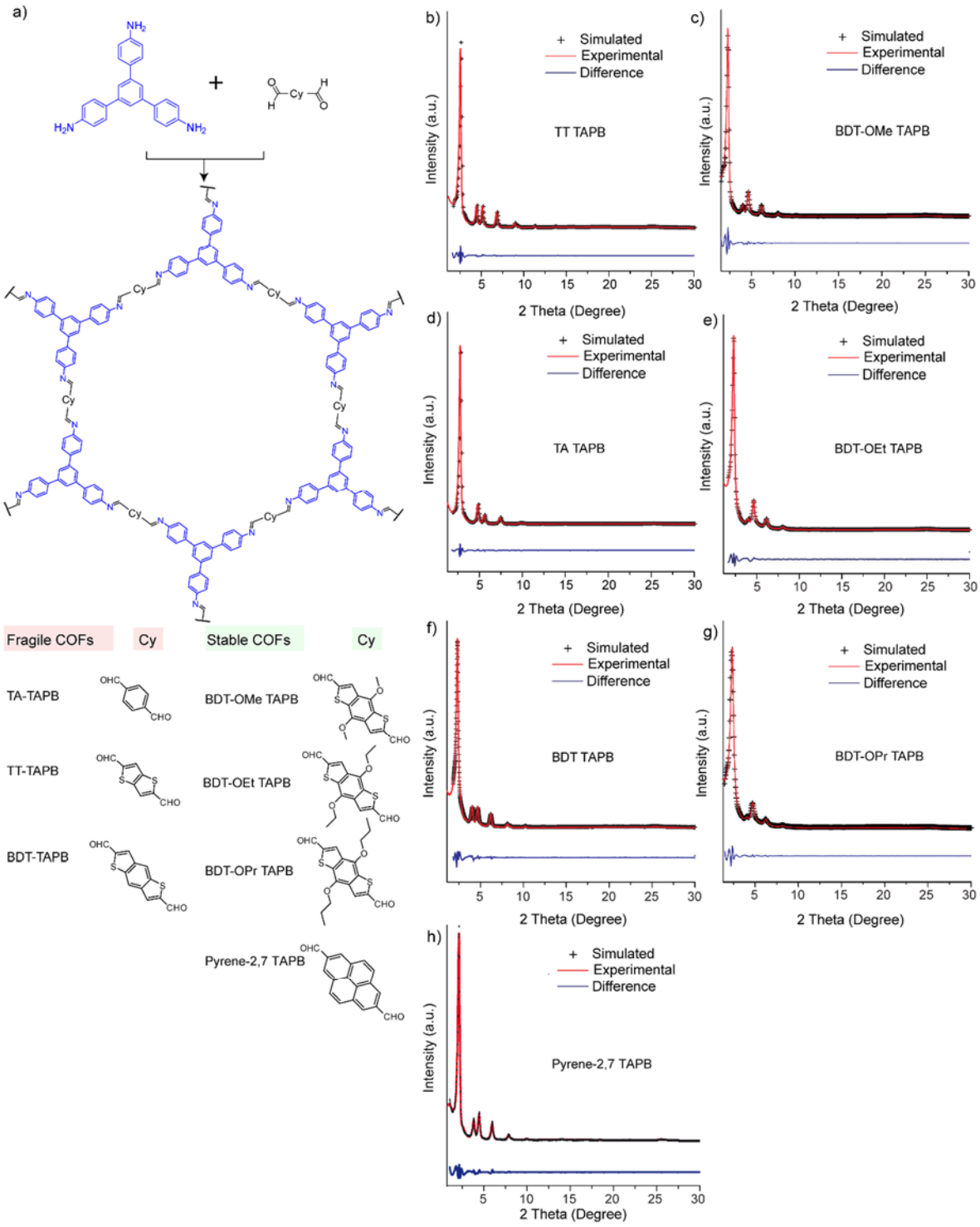


Figure 6.1: a) Schematic representation of the syntheses of 2D imine COFs from C3 and C2 building blocks. b)-h) Comparison of the experimental (red) and refined simulated PXRD pattern (black), the difference plot is given in blue for the different TAPB COFs.

Further solvent stability screenings were carried out to identify the optimal conditions for a suitable recovery and isolation procedure yielding highly crystalline products. We chose common commercially available solvents with a polarity gradient ranging from water to toluene

and submersed the COF powders for 24 h (5 mg/ml) in the respective solvent to allow for a mild solvent exchange process. Here, we could observe a relation between the structural stability of the COFs and the extension of the π-system of the linear building unit. The TA TAPB-COF, comprising a comparably short π-system, showed instability towards all the employed solvents, whereas the TT and BDT TAPB-COFs showed a certain degree of stability towards toluene and ethanol, respectively (Figure S 6.4). Nevertheless, the general stability observed towards solvent exchange for all three COFs was moderate (Figure S 6.3a and Figure S 6.4). Investigation of the accessible porosity of TT and BDT TAPB-COFs revealed non-porous or moderately porous frameworks, respectively (Figure S 6.45) Therefore, these unsubstituted COF structures were classified as "fragile" (Figure 6.1). In contrast, the alkoxy substituted COFs BDT-OMe, BDT-OEt and BDT-OPr TAPB-COFs as well as the Pyrene-2,7 TAPB-COF were found to be highly stable towards the solvent exchange treatment with acetone, ethanol, and toluene. Furthermore, these COFs could even be Soxhlet extracted with toluene and exhibited substantially higher crystallinity compared to the as-synthesized powders, indicating a sufficient elution of residual agents along with retention of the structure (Figure S 6.3b and Figure S 6.5). These findings are in accordance with the substantial open porosity of these TAPB-COFs (Figure S 6.41 and Figure S 6.43), which thereby were classified as "robust" (Figure 6.1).

In the search for a general isolation method that is suitable for both fragile and robust TAPB-COFs we employed a supercritical fluid activation method using supercritical carbon dioxide. In principle, the supercritical fluid activation is based on the action of a liquid-like substance above its critical point on a target material. Above the critical point, the liquid-like matter exhibits very low surface tension and thereby capillary forces acting on the walls of the extracted material are significantly reduced. This activation procedure is well established for obtaining highly porous materials[53-57] and was already reported to be useful for the recovery of imine based-COFs.[26, 46, 52, 58-59] In a typical $scCO_2$ activation process employed in our work, freshly filtered COF powders exhibiting low to moderate crystallinity were transferred to a metal holder and placed in an autoclave, which was then tightly closed and cooled to 5 °C. Subsequently, $CO_2$ was flushed through the system and finally the closed autoclave was heated to 40 °C, while adjusting the pressure to 85 bar to establish supercritical $CO_2$ conditions (see experimental part for further details). After 2 h the pressure was slowly reduced and the $scCO_2$ activated powders were recovered.

### 6.3.1 STRUCTURAL CHARACTERIZATION

The crystallinity of $scCO_2$ activated fragile and robust COF samples was investigated by PXRD (Figure 6.1). Strikingly, for all the structures studied, a very intense and sharp reflection for low 2 theta values in the PXRD patterns corresponding to the 100 plane was observed, indicating high crystalline order. For the TA and TT TAPB-COF this reflection appears at $2\theta = 2.53°$, d = 34.9 Å and $2\theta = 2.73°$, d = 32.3 Å respectively. The unsubstituted and substituted BDT TAPB-COFs (BDT TAPB-COF, BDT-OMe TAPB-COF, BDT-OET TAPB-COF, BDT-OPr TAPB-COF) exhibit the 100 reflection at $2\theta = 2.30°$, corresponding to a *d*-spacing value of 38.4 Å. For the Pyrene-2,7 TAPB-COF the 100 reflection appears at $2\theta = 2.28°$, corresponding to the largest unit cell of the TAPB-COF series with a *d*-spacing value of 38.7 Å. The intense 100 reflection is followed by weaker higher order reflections that are attributed to the *110, 200, 210, 220, 230, 310*, and *001* planes. We modeled the COF structures in the *P*6 space group, corresponding to a fully overlapped AA eclipsed stacking model. The unit cell parameters of the COFs were determined by performing Pawley refinements with respect to the obtained experimental diffraction patterns (Figure 6.1). The comparison between the experimental and the simulated PXRD patterns shows close matching for all reflection positions (Figure 6.1b-g). The *d*-spacing values corresponding to the broad 001 reflections positioned at $2\theta = 24\text{-}27°$ with maxima at about $2\theta = 25.1°$ were calculated to be around 3.55 Å and are attributed to the COFs' interlayer distances. As an exception, Pyrene-2,7 TAPB-COF exhibits a 001 reflection being positioned at $2\theta = 25.7°$ corresponding to a comparably closer stacking distance of adjacent layers of 3.46 Å. In our previous report, the TAPB was shown to be a key factor for obtaining highly crystalline frameworks.[37] Due to its inherent propeller structure induced by steric constraints, it allows for spatial control and a precise arrangement of adjacent layers and influences the stacking distance of the adjacent COF layers. Here, we reveal that the interlayer distances can be controlled through the nature of the linear counterparts. Using a linear pyrene linker between the TAPB building units results in a closer stacking distance of adjacent COF-layers, demonstrating that the TAPB propeller has a certain degree of flexibility.

The long-range order established by employing the $scCO_2$ activation process was monitored over the course of several months. The $scCO_2$ activated fragile and the robust TAPB-COFs maintained their highly crystalline character during this time, rendering these COFs stable in ambient conditions and exhibiting long shelf life. (Figure S 6.15).

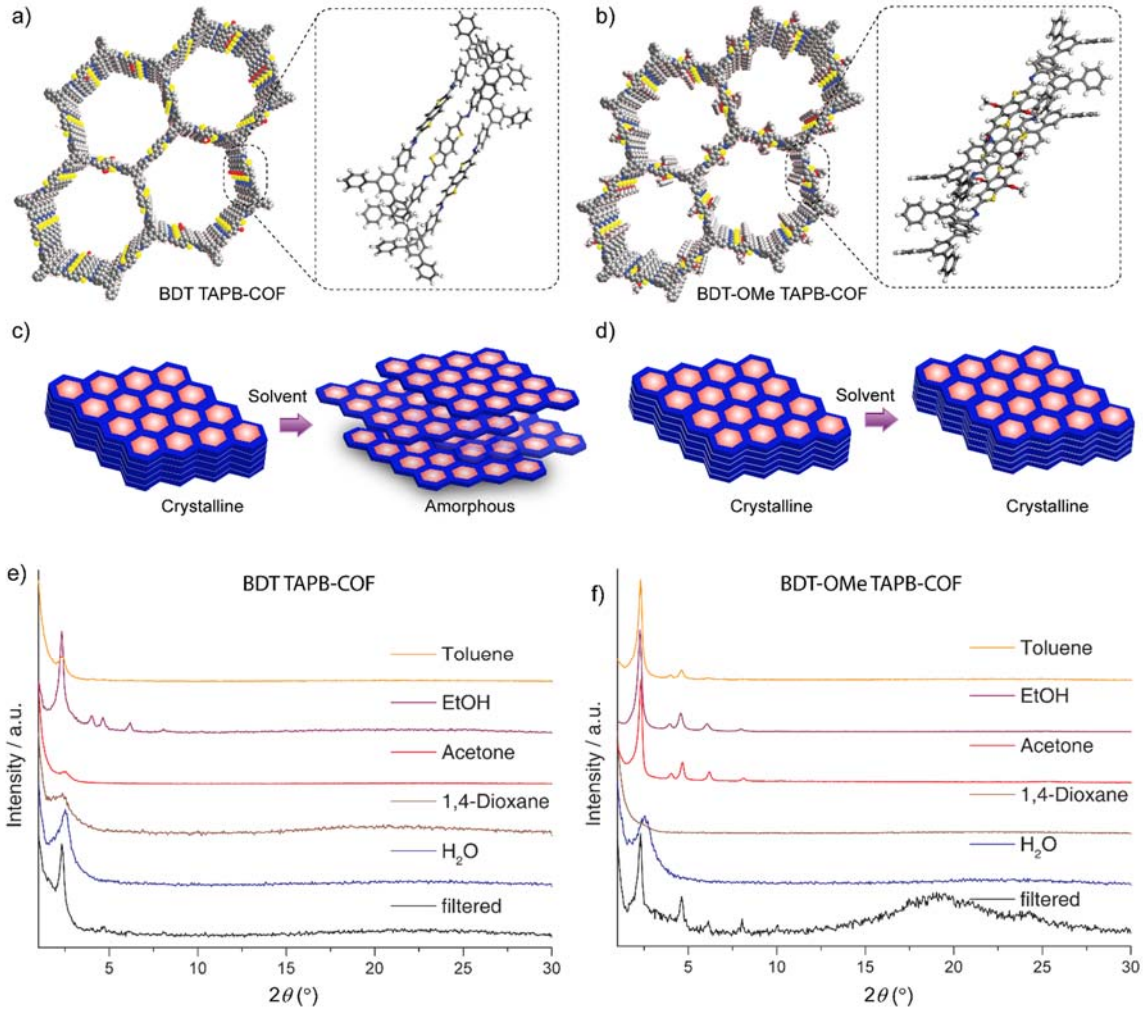


Figure 6.2: a) Space filling model showing the hexagonal pore channels of (a) BDT TAPB-, and (b) BDT-OMe TAPB-COF. The ball and stick model (insert) shows the T-shaped and parallel-displaced π-π stacking interaction existing in the crystallized fragments of BDT TAPB-COF and BDT-OMe TAPB-COF. (c) Schematic representation of framework deformation of (c)BDT TAPB-COF and (d) BDT-OMe TAPB-COF upon solvent treatment. (e) PXRD of the BDT TAPB-COF upon solvent treatment and subsequent vacuum drying. (f) PXRD of the BDT-OMe TAPB-COF upon solvent treatment and subsequent vacuum drying.

### 6.3.2 POROSITY

The porosity of the $scCO_2$ activated fragile and robust COF samples was investigated by nitrogen physisorption. The obtained type IVb isotherms are characteristic for mesoporous materials with pores smaller than 5 nm (Figure S 6.40 – 6.42).[60] For both $scCO_2$ fragile and robust COFs high surface areas of up to 2000 $m^2g^{-1}$ were determined, which illustrates the power of $scCO_2$ activation as a general method providing highly porous and crystalline COF materials (for details on BET surface areas, pore volumes and pore size distributions see Table 6.2 and Figure S 6.40 – 6.43).

### 6.3.3 MORPHOLOGY

Scanning electron micrographs (SEM) of the highly crystalline COF powders revealed either spherical or rod-like COF particle assemblies (Figure S 6.35 and Figure S 6.36). Among the different COFs, the TT TAPB-COF exhibits unique monodispersed spherical particles of about 5 μm in size (Figure S 6.35c). Furthermore, we investigated the morphological properties of TT TAPB-COF following a previously reported reaction scheme using anisole/ethanol as the solvent mixture.[37] Under these synthesis conditions, the obtained monodisperse TT TAPB-COF particles are 2 μm in diameter, and in some cases self-organization into larger spherical hollow superstructures was observed (Figure S 6.37).

Remarkably, the structural analysis of the unsubstituted COF powders via transmission electron microscopy (TEM) reveals long-range ordered crystallites with domain sizes of up to 500 nm (Figure S 6.38). Specifically, the Pyrene-2,7 TAPB-COF exhibits well-faceted hexagonally shaped crystals and the BDT TAPB-COF exhibits large domain sizes of up to 500 nm. To further illustrate the impact of the $scCO_2$ activation on the structural features, we characterized an as-synthesized and vacuum-dried fraction, a 1,4-dioxane treated fraction (24 h exposure to 1,4-dioxane vapor) and a $scCO_2$-activated fraction of the same sample of BDT TAPB-COF by TEM (Figure S 6.39). The $scCO_2$ activated BDT TAPB-COF sample shows enlarged crystalline domains of up to 100 nm (Figure S 6.39c). In contrast, the filtered and vacuum-dried as well as the 1,4-dioxane rinsed BDT TAPB-COF fractions only exhibit short-range ordered domains of up to 10 nm in size (Figure S 6.39a and b). Interestingly, the $scCO_2$ activated robust COFs show significantly smaller domain sizes of 20-80 nm (Figure S 6.38). This finding is in good agreement with our previous report on the incorporation of alkoxy side chains on a BDT-core in a boronic-ester COF and can be attributed to the sterically demanding side chains, which have a direct impact on the packing of the COF layers.[61]

## 6.3.4 STABILITY OF $SCCO_2$ ACTIVATED TAPB-COFS

### 6.3.4.1 Solvent exposure

After achieving structural stability and permanent porosity under ambient conditions by $scCO_2$ activation of the TAPB-COFs, their stability towards external solvent stimuli was investigated. To this end, the crystalline and porous $scCO_2$ activated COF powders were immersed for 24 h in the different solvents of the series described earlier (acetone, ethanol, toluene, water, 1,4-dioxane,5 mg/ml). Prior to PXRD analysis, the powders were filtered and vacuum-dried to remove residual guest molecules. In the case of the fragile COFs, a pronounced decrease in the long-range order was detected. However, concerning the PXRD analysis, in some cases, we observed a slightly higher tolerability towards this treatment in comparison to the as-synthesized COF powders (Figure S 6.6a and Figure S 6.7). But the powders of fragile TAPB-COFs still were not highly crystalline. In contrast, the robust TAPB-COFs maintained their crystallinity towards all the employed solvents excluding water and 1,4-dioxane (Figure S 6.6b and Figure S 6.8). To rule out the possibility of simple decomposition of the fragile COF samples during exposure to solvents, we conducted IR measurements of the $scCO_2$ activated and the 1,4-dioxane treated fragile BDT TAPB-COF and the robust BDT-OMe TAPB-COF samples (Figure S 6.33 and Figure S 6.34). All IR spectra of the treated COFs exhibit vibrational absorption bands comparable to the highly porous and crystalline $scCO_2$ activated samples, hence excluding decomposition or new bond forming processes.

### 6.3.4.2 Vapor exposure

Next, we examined the interactions of the $scCO_2$ activated crystalline frameworks with different solvent vapors. We anticipated that the vapor treatment would have a smaller impact on the COF structures compared to exposure to liquid solvents. For these experiments, the $scCO_2$ activated TAPB COF samples were placed for 24 h in a closed vapor chamber containing an open reservoir of the respective solvent. The resulting powders were subjected to reduced pressure ($1.0 \times 10^{-3}$ mbar) for 30 min to remove residual guest molecules located in the pores prior to the PXRD analysis (Figure S 6.9 – 6.11). Surprisingly, the fragile COFs were still strongly affected by the interaction with solvent vapors and suffered a reduction of long-range order (Figure S 6.9a and Figure S 6.10). In contrast, similar to the immersion in solvents, the robust TAPB-COFs maintained their crystallinity and were not affected by the exposure to vapors of acetone, ethanol and toluene but were highly affected by water and 1,4-dioxane vapors (Figure S 6.9b and Figure S 6.11). To investigate the strong impact of solvent vapors on the TAPB-COF structures, time-dependent PXRD measurements were conducted for a fragile

and for a robust TAPB-COF. As representative model systems BDT TAPB-COF (fragile) and BDT-OMe TAPB-COF (robust) were selected for these experiments and were exposed to different solvent vapors. We chose 1,4-dioxane and ethanol as solvent vapors, because both frameworks were highly affected by 1,4-dioxane immersion, while ethanol immersion did not lead to a complete amorphization in both cases. For these experiments, highly crystalline $scCO_2$ TAPB COF-powders spread on a silicon wafer were placed in a plastic bag and immobilized on the PXRD measuring stage, respectively. An open vessel filled with the respective solvent was included into the plastic bag, which then was tightly closed allowing for saturation with solvent vapor inside the bag. Subsequently, PXRD patterns of the COF powders were collected in a cyclic mode with intervals of 2.5 minutes. In these experiments we found that exposing both BDT and BDT-OMe TAPB-COF powders to 1,4-dioxane vapor resulted in poorly crystalline material. This is an interesting observation as 1,4-dioxane is the main solvent in the TAPB-COF bulk syntheses, aiding the progressive construction of the frameworks. The loss of structural order was observed by a steady decrease in the diffraction intensity of the 100 reflections in the course of increasing vapor exposure time. We did not observe changes in the diffraction reflection positions concerning 100 and higher order reflections in the *ab*-plane during these experiments (Figure 6.3c).

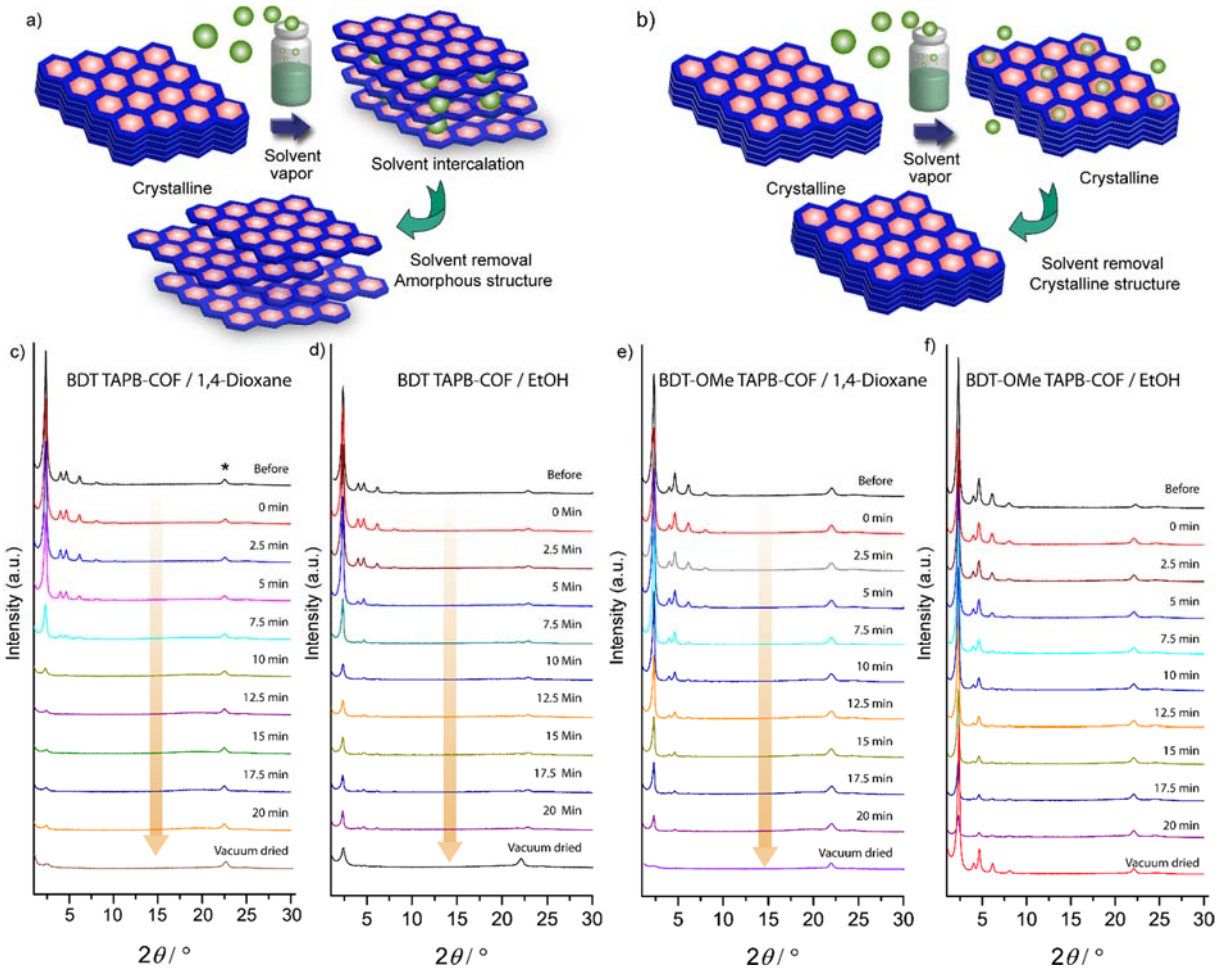


Figure 6.3: Schematic representation of the structural transformation of COF layers upon vapor treatment with 1,4-dioxane of (a) BDT TAPB-COF, and (b) BDT-OMe TAPB-COF. c) PXRD of the BDT TAPB-COF upon 1,4-dioxane vapor treatment. (d) PXRD of the BDT TAPB-COF upon ethanol vapor treatment. (e) PXRD of the BDT-OMe TAPB-COF upon 1,4-dioxane vapor treatment. (f) PXRD of the BDT-OMe TAPB-COF upon ethanol vapor treatment at different time intervals.

The amorphization process can be associated with a random displacement of the COF layers. In contrast to the exposure to 1,4-dioxane, both model systems showed a certain degree of tolerance towards exposure to ethanol vapor. Importantly, we detected a pronounced shift of the 001 reflection towards lower 2θ values corresponding to an increased stacking distance of the adjacent COF layers upon vapor penetration for both the fragile BDT TAPB-COF as well as the robust BDT-OMe TAPB-COF (Figure S 6.16). In combination with the IR investigations indicating a chemically intact imine polymer (Figure S 6.33 and Figure S 6.34), this observation points to a slow anisotropic displacement of the COF layers promoted by the weakening of the stacking interactions, thereby resulting in the loss of most structural features.

As the solvent vapors show a slowly progressing effect on the 001 reflections accompanied by a decrease in all reflection intensities, we decided to investigate the effect on the 001 reflections in further detail for both model systems with a small volume of different solvents, respectively. We therefore conducted PXRD measurements with $scCO_2$ activated TAPB-COF samples being wetted with a droplet of either ethanol, 1,4-dioxane or toluene to examine the immediate impact on the frameworks' stacking distances. Here, we detected distinct shifts of the 001 reflections towards smaller 2θ values (Figure S 6.18 – 6.19). For the fragile BDT TAPB-COF and a droplet of 1,4-dioxane we detected a shift from 25.1 to 22.7 °2θ corresponding to interlayer distances of 3.52 Å and 3.91 Å, respectively. In comparison, the 001 reflections of the robust BDT-OMe TAPB-COF shifted from 25.1 to 24.2 °2θ upon treatment with a droplet of 1,4-dioxane, corresponding to interlayer distances of 3.52 Å and 3.68 Å, respectively. The dynamic character of the layer distance enlargements can also be seen by comparison of the treatment with toluene droplets. For the robust BDT-OMe TAPB, the interlayer distance shifted from 25.1 to 24.4 °2θ, corresponding to interlayer distances of 3.52 Å and 3.64 Å upon exposure to toluene. The stacking distance of BDT TAPB-COF shifted upon the treatment with a droplet of toluene from 25.1 to 24.7 °2θ, corresponding to interlayer distances of 3.52 Å and 3.60 Å. These results underline the significant effect of solvents on the COFs' stacking distance and the amorphization.

Strikingly, by employing a $scCO_2$ reactivation process for the vapor and solvent treated samples, we were able to retrieve highly crystalline COFs featuring the close stacking distances observed prior to vapor and wetting experiments (Figure S 6.17 – 6.19). This illustrates that the process of gradual loss of structural order is reversible for all TAPB-COFs and that a poorly-crystalline TAPB-based polymer can be converted back into a highly crystalline COF by simply using the $scCO_2$ activation protocol. We therefore conclude that the TAPB-COF layers can be mobilized and shift in all three dimensions upon exposure to external stimuli such as solvent vapors. This "breathing" feature of the frameworks results in complete amorphization in the case of fragile TAPB-COFs, while the robust TAPB-COFs resist full amorphization with different solvents like acetone, toluene and ethanol. Retrieving the structural order for these robust COFs can be simply achieved by the removal of the solvents by common means such as employing reduced pressure.

Among the solvents used in this study, 1,4-dioxane stands out by exhibiting a profound role in two different processes. This solvent is essential for the formation of the TAPB-frameworks and is the main component in the solvent mixture for the synthesis of the bulk materials.

However, it has a strong impact on the long-range order when used post-synthetic for all the examined fragile or robust structures. As none of the investigated TAPB-COFs can withstand exposure to 1,4-dioxane, this becomes a general method for the amorphization of highly crystalline and open porous TAPB-COFs. Even more remarkable, this process is reversible for every used solvent or vapor by employing a $scCO_2$ reactivation workup where all TAPB-COFs regain their crystalline structure and their porosity (Table 6.3).

As the stacking of the TAPB-COFs can be controlled by employing solvent vapors and subsequent $scCO_2$ activation, we used 1,4-dioxane as external stimulus for multiple activation and amorphization cycles. In a typical cycle, a highly crystalline and open porous $scCO_2$ activated COF powder was immersed in 1,4-dioxane for 24 h, filtered and dried under reduced pressure, resulting in the amorphous non-porous state (Figure S 6.20). Later, the amorphous dried powder was $scCO_2$ reactivated following the developed protocol described earlier. For all the examined powders, the desired COF properties such as crystallinity and porosity were indeed restored in comparable quality by the $scCO_2$ activation (Figure 6.4). This cycle was repeated several times, as a result alternating between the crystalline, open porous and the amorphous, non-porous COF state. Attempts at replacing the $scCO_2$ activation protocol with other activation methods such as immersing the amorphous robust COFs in a weaker solvent for the cycling experiments failed to produce a powder with properties comparable to those resulting from the $scCO_2$ activation protocol (Figure S 6.13 and Figure S 6.14).

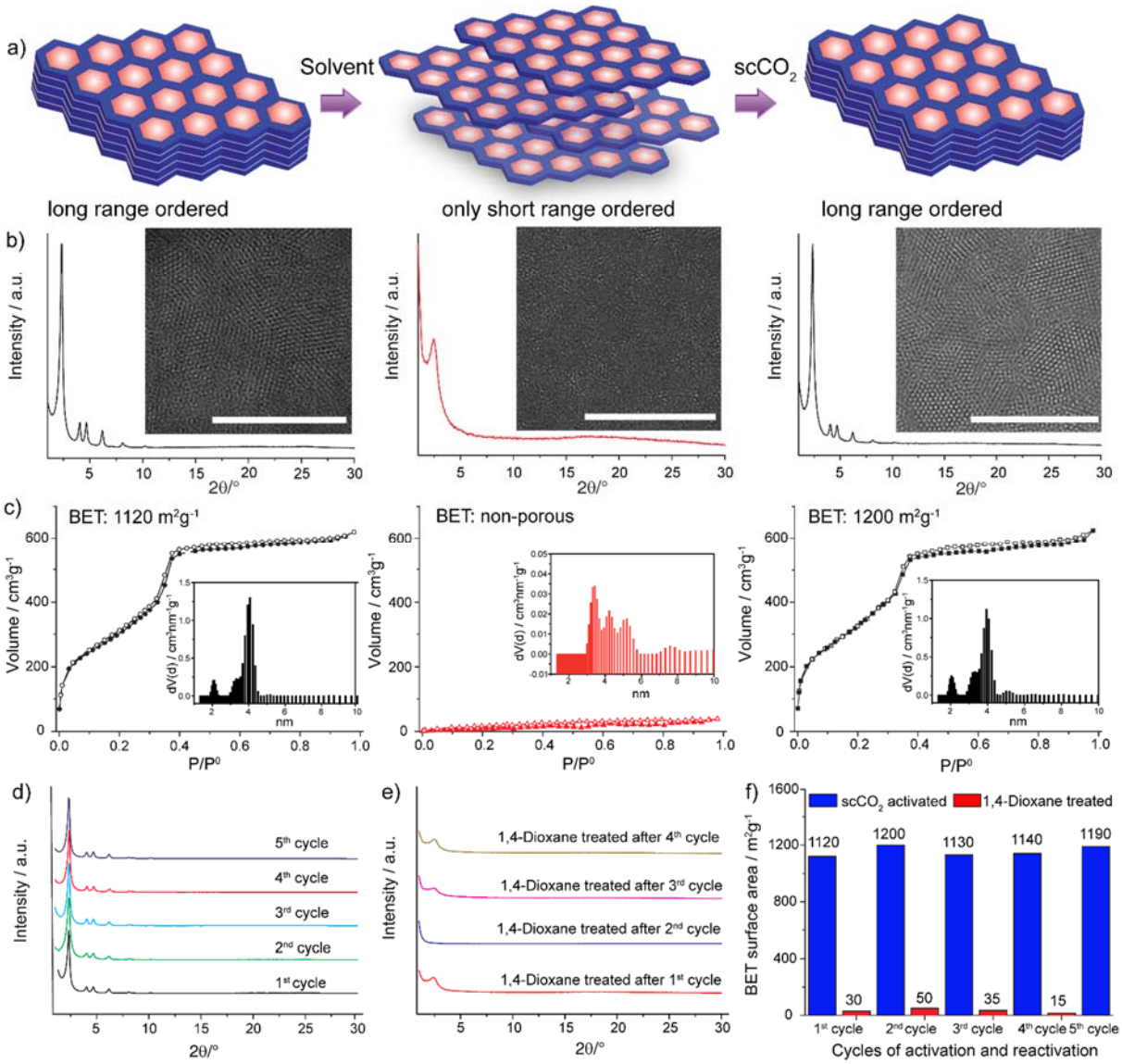


Figure 6.4: a) Model showing the destruction and restoration of the crystallinity of BDT TAPB-COF upon 1,4-dioxane treatment and $scCO_2$ reactivation. (b) and (c) show the changes in crystallinity and porosity upon the loss of order in this fragile framework during 1,4-dioxane treatment and subsequent $scCO_2$ reactivation. (d) PXRDs of the BDT TAPB-COF, reactivated by different cycles of $scCO_2$ activation. (e) PXRDs of the 1,4-dioxane treated BDT TAPB-COF in different cycles. (f) Bar chart showing the reversible change in surface area of BDT TAPB-COFs at different cycles of solvent treatment and $scCO_2$ reactivation.

To exclude the possibility that only the pressure and the temperature of the $scCO_2$ activation is relevant for successful (re-)activation, a BDT TAPB-COF (fragile) and a BDT-OMe TAPB-COF (robust) were treated with argon simulating the $CO_2$ treatment conditions. For these experiments, highly crystalline COF powders were initially obtained after the $scCO_2$ activation (40°C, 85 bar, 2 h). After immersion of these powders in 1,4-dioxane for 24 h, the COFs were dried under vacuum, resulting in the amorphous powder. Then, these powders were divided

into two portions. The first portions of the amorphous BDT TAPB and of the amorphous BDT-OMe TAPB samples were subjected to argon treatment (40°C, 85 bar, 2 h) and the second portions were subjected to the $scCO_2$ activation protocol. After these treatments, the PXRD analyses of the resulting powders revealed that the argon-activated powders remained amorphous while only the $scCO_2$ activated samples showed highly crystalline structures (Figure S 6.21).

Of special interest is the recovery of TAPB-COFs from aqueous media, which would allow for efficient removal of polar guests captured within the porous structure. To study the behavior of TAPB COFs in an aqueous medium, we immersed a $scCO_2$ activated, fragile BDT TAPB-COF sample in deionized water (15 mg/5 mL, pH 7) for a period of 24 h. After the treatment, the COF sample was filtered, dried under vacuum and examined by PXRD. Similar to the treatment with organic solvents, the PXRD of the water-treated sample showed a complete loss of long-range order. The amorphous powder was then subjected to the $scCO_2$ reactivation, resulting in the complete recovery of the COF structural order (Figure S 6.20). As with organic solvents, the robust TAPB-COFs showed higher resistance towards the water treatment. After 24 h in water, the crystallinity of these robust COFs was still high as indicated by the observed reflections (Figure S 6.6b and Figure S 6.8).

To gain further insights regarding the impact of the $scCO_2$ treatment on the TAPB frameworks, we studied the interaction of amorphous and crystalline COF powders with nitrogen and carbon dioxide by means of physisorption experiments. The porosity of the crystalline COF and of the corresponding amorphous analog of the fragile BDT TAPB-COF were analyzed by $N_2$ and $CO_2$ adsorption measurements at 273 K and 1 bar. The crystalline BDT TAPB-COF displayed $CO_2$ uptake of 1.41 mmol/g and $N_2$ uptake of 0.57 mmol/g at 273 K (Figure 6.5). The examined powder was immersed in 1,4-dioxane (5mg/mL) for 24 h to produce the amorphous BDT TAPB-COF analog after vacuum-drying. The amorphous BDT TAPB-COF showed a lower $N_2$ uptake of 0.364 mmol/g. This can be attributed to reduced surface area of the fragile COF due to fewer open pores. Interestingly, we observed that the amorphous COF analogue displayed a significant increase in $CO_2$ uptake (1.94 mmol/g at 273 K), which is higher than that of the crystalline COF (Figure 6.5). This indicates a high affinity of $CO_2$ to the amorphous framework and can possibly explain the effective activation of the COFs *via* $scCO_2$. We postulate that due to the smaller kinetic diameter of $CO_2$ (3.3 Å) compared to of $N_2$ (3.64 Å), $CO_2$ molecules are still able to access voids between displaced adjacent layers. An ideal adsorbed solution theory

(IAST) calculation revealed a $CO_2/N_2$ selectivity ratio of 6.2 for the amorphous COF, which is 2.3 times higher than that of the crystalline one (2.7) at 1 bar pressure (Figure S 6.46).

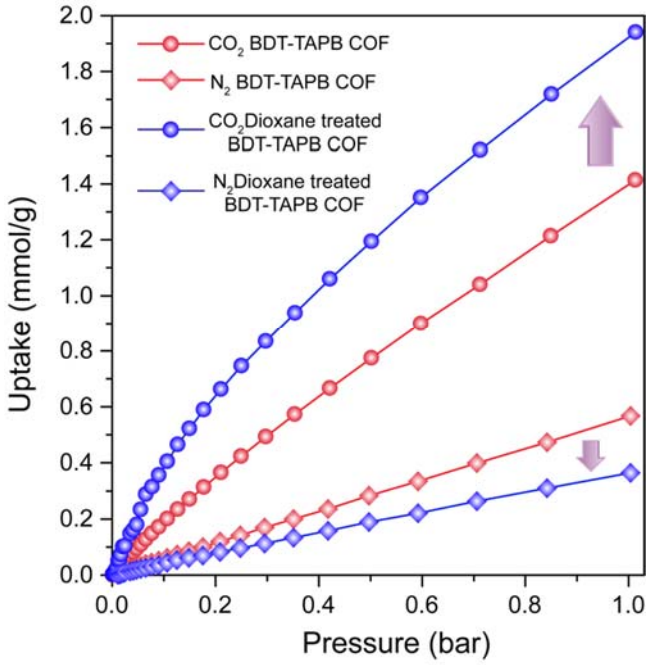


Figure 6.5: Switching of $N_2$ (diamond) and $CO_2$ (circle) storage properties of BDT TAPB-COF upon 1,4-dioxane vapor treatment at 273 K. Red represents crystalline COF sample before treatment, blue represents amorphous COF sample after the 1,4-dioxane vapor treatment.

To enhance understanding regarding the stacking interactions of the BDT-core leading to the observed structural fragility or stability in the TABP COFs, we performed DFT calculations on the unsubstituted and the substituted BDT cores' dimerization energies (Figure S 6.30). In the calculated structures of BDT, BDT-OMe and BDT-OEt, an AA stacking is favored compared to an AB stacking, where sulfur atoms could prevent close stacking. Overall, the dimerization of alkoxy-functionalized BDT cores is energetically favored compared to the non-functionalized BDT-core.

In addition, small molecular COF fragments serving as molecular models were synthesized. The model compounds consist of the respective linear linker bridging two monofunctionalized TAPB (MAPB) through imine bonds (Figure S 6.23). From the corresponding single crystal data (Figure S 6.24 – 6.28), we were able to determine the orientation of the imine bonds with regards to the sulfur heteroatom located in the linear TT and BDT linkers. This allows for the accurate modeling of the thiophene-core containing TAPB-COF structures, where the sulfur and the nitrogen atoms are relatively close to each other. This does not only affect the structural

simulations, but furthermore allows for predictions of charge distributions and orbitals. In addition, we observed a very close crystal packing in the case of functionalized BDT cores (BDT-OMe and BDT-OEt (Figure S 6.27 and Figure S 6.28), whereas the non-functionalized TT and BDT cores (Figure S 6.25 and Figure S 6.26) stack at larger distance with a T-shape-like stacking motif. These single crystal results hint at favorable interactions between adjacent substituted BDT layers, resulting in the structural stability observed for larger, self-assembled systems such as the COFs.

# 6.4 CONCLUSION

We have shown that hexagonal imine COFs consisting of TAPB and different linear dialdehyde linkers exhibit very different stabilities towards external stimuli. Freshly synthesized fragile TAPB-COFs instantly lose crystallinity and porosity upon exposure to solvents, heat or vacuum. We attribute the sensitivity of these COFs mainly to the weak π-π interactions of the linear dialdehydes between adjacent layers. We find that the fragile TAPB-COFs can be stabilized by the incorporation of alkoxy substituents on the BDT-cores. Alkoxy substituents reinforce the π-π stacking between the COF layers by minimizing the interlayer charge repulsion. While the usual extraction workup strategies for the fragile TAPB-COFs failed, we developed a successful workup scheme based on $scCO_2$ extraction for these fragile as well as the robust TAPB-COFs of our test series. The supercritical carbon dioxide extraction is not only a fast and efficient process, but it also minimizes the amount of solvents needed in the workup procedure.

Furthermore, we have established that successfully $scCO_2$-activated, highly crystalline and open porous COFs can be completely converted to amorphous and non-porous polymers by exposure to solvents in liquid and vapor phases. Intriguingly, this remarkable process is completely reversible by applying the $scCO_2$ activation approach, and the crystalline-amorphous switching cycle can be repeated many times. The dramatic transformation of fragile COFs from the crystalline to the amorphous state also leads to substantial changes in the gas adsorption behavior. Hence, the 1,4-dioxane treated, amorphous BDT TAPB-COF shows an almost doubled $CO_2/N_2$ selectivity for adsorption in comparison to the crystalline analog (Figure 6.5 and Figure S 6.46) at 1 bar pressure. Therefore, as $CO_2$ is still able to access the voids in-between amorphous COF layers, in its supercritical state it allows for a full reconstruction of the amorphous, non-porous polymer into a crystalline and open-porous COF. In view of our results, deeper insights regarding the decisive role of subtle interlayer interactions in COFs will provide access to intriguing new frameworks with ultra-high porosity, crystallinity, and novel functionalities.

# 6.5 SUPPORTING INFORMATION

## 6.5.1 METHODS

All reagents and solvents were obtained from commercial suppliers and used as received unless otherwise stated. Acetone (extra dry, AcroSeal, 99.5%, Acros), benzo(1,2-*b*:4,5-*b*')dithiophene (BDT, >98%, TCI), benzo(1,2-*b*:4,5-*b*')dithiophene-4,8-dione ($BDTO_2$, >98%, TCI), *n*-butyllithium solution (*n*-BuLi, 2.5 M in *n*-hexane), dichloromethane (DCM, in house supply), diethyl ether ($Et_2O$, in house supply), 1,4-dioxane (anhydrous, 99.8%, Sigma-Aldrich and in house supply), *N,N*-dimethylformamide (DMF, anhydrous, Sigma-Aldrich), ethanol (EtOH, extra dry, AcroSeal, 99.5%, Acros and in house supply), ethyl *p*-toluenesulfonate (98%, Sigma-Aldrich), glacial acetic acid (in house supply), mesitylene (Mes, anhydrous, Sigma-Aldrich), methanol (MeOH, anhydrous, 99.8%, Sigma-Aldrich), methyl *p*-toluenesulfonate (98%, Sigma-Aldrich), propyl *p*-toluenesulfonate (>98%, TCI), sodium hydroxide (NaOH, 97%; Sigma-Aldrich), terephthalaldehyde (TA, 99%, Sigma-Aldrich), tetrahydrofuran (THF, extra dry, stabilized, Acros Organics and anhydrous, >99.9%, inhibitor-free, Sigma-Aldrich), thieno[3,2-*b*]thiophene-2,5-dicarboxaldehyde (TT, >93%, TCI, recrystallized from DMF), 1,3,5-tris(4-aminophenyl)benzene (TAPB, >93%, TCI), zinc (dust, <10 µm, >98%, Sigma-Aldrich).

### 6.5.1.1 Synthesis of linkers

**a) BDT monomer**

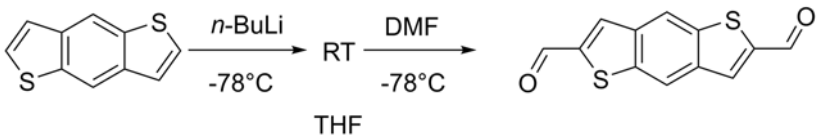


Benzo[1,2-*b*:4,5-*b*']dithiophene (1.0 g, 5.3 mmol) was dissolved in 100 mL anhydrous, inhibitor-free THF in an outgassed 250 mL flask under argon atmosphere. The stirred solution was cooled to -78°C in a dry ice/acetone cooling bath. A solution of *n*-butyl lithium (5.0 mL, 2.5 M in *n*-hexane, 12.5 mmol) was added dropwise within 10 minutes. The solution was stirred for 30 minutes at -78°C and after removal of the cooling bath for 1 h at room temperature. The solution was then cooled again to -78°C and DMF (1.0 mL, 13.0 mmol) was added dropwise. After stirring and slow warming overnight, the solution was poured into ice water and filtered. The yellow precipitate was washed with water several times (1000 mL) and further treated with small amounts of MeOH and $Et_2O$. The solid was dried under reduced pressure, giving a yellow solid with 46% yield.

MS-EI: calculated (m/z): 245.981, measured (m/z): 245.9806.

$^{1}$H NMR (400 MHz, DMSO-*d*$_6$) δ (ppm): 8.53 (s, 2H), 8.89 (s, 2H), 10.20 (s, 2H); $^{13}$C NMR (100 MHz, DMSO-*d*$_6$) δ (ppm): 186.6, 144.9, 138.9, 138.4, 135.3, 121.6.

**b) BDT-OMe monomer**

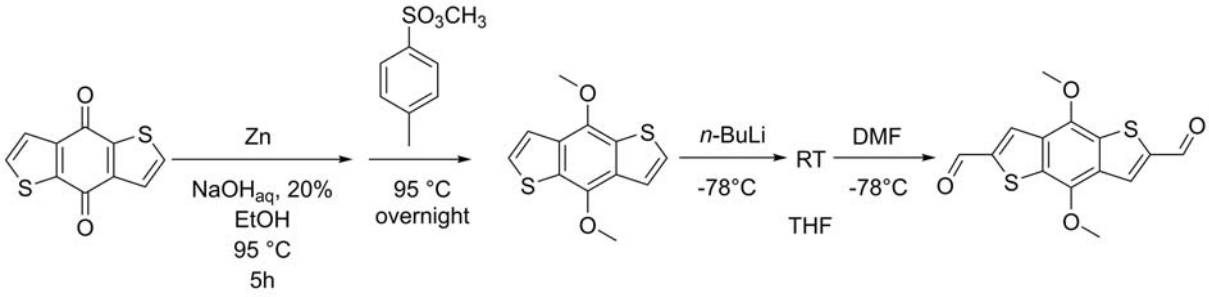


Under argon 1.55 g (7.04 mmol) of benzo[1,2-b:4,5-b']dithiophene-4,8-dione, 1.38 g (21.1 mmol) of zinc dust, 20 mL of an aqueous sodium hydroxide solution (20 %) and 20 mL of ethanol were heated at 95 °C for 5 h. To the hot solution 4.0 mL (26.5 mmol) of methyl *p*-toluenesulfonate was slowly added and the reaction solution was kept at 95 °C overnight. After the reaction solution had cooled down to room temperature, it was extracted with DCM (three times 50 mL) and phase separated. The combined organic layers were washed with brine (150 mL) and dried over $MgSO_4$. The obtained filtrate was evaporated under vacuum. 608.5 mg of a grey product was obtained corresponding to 35% yield.

Without further purification, under argon 500 mg (2.0 mmol) of the product was dissolved in 25 mL of anhydrous inhibitor-free THF and cooled down to -78 °C in an outgassed 250 mL flask. Afterwards, 3.6 mL (9.0 mmol, 2.5 M in *n*-hexane, 4.5 eq) of *n*-BuLi was slowly added and the reaction solution was stirred for 20 min at -78 °C. The solution was slowly warmed to RT to be stirred for 1 h. After cooling again to -78 °C, 2 mL (26 mmol) of DMF was added and the reaction solution was stirred overnight. It was poured on ice water and the precipitate was filtered and washed with an excess of water and small amounts of methanol. The highly insoluble solid was washed with hot ethanol, filtered and dried under vacuum before usage. The final amount of isolated product of 475.0 mg corresponds to 77% yield.

MS-EI: calculated (m/z): 306.002, measured (m/z): 334.0010.

$^{1}$H NMR (400 MHz, DMSO-*d*$_6$) δ (ppm): 10.20 (s, 2H), 8.71 (s, 2H), 4.22 (s, 6H). $^{13}$C NMR (100 MHz, DMSO-d6) δ (ppm): 186.32, 147.11, 143.91, 132.60, 131.90, 99.49, 61.70.

**c) BDT-OET monomer**

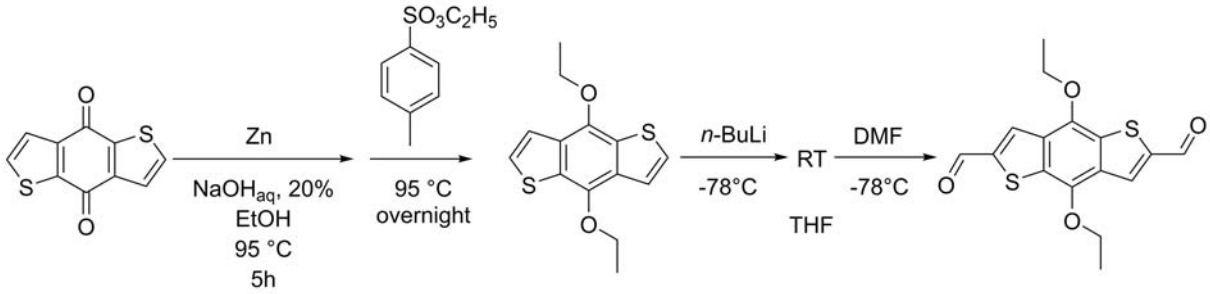


Under argon 1.10 g (4.99 mmol, 1.0 eq) of benzo[1,2-*b*:4,5-*b*']dithiophene-4,8-dione, 0.981 g (15.0 mmol, 3.0 eq) of zinc dust, 10 mL of an aqueous sodium hydroxide solution (20%) and 10 mL of ethanol were heated at 95 °C for 5 h. To the hot solution 2.56 mL (3.00 g, 15.0 mmol, 3.0 eq) of ethyl *p*-toluenesulfonate was slowly added and the reaction solution was kept at 95 °C overnight. After the reaction solution had cooled down to room temperature, it was extracted with DCM (three times 50 mL) and phase separated. The combined organic layers were washed with brine (150 mL) and dried over $Na_2SO_4$. The obtained filtrate was evaporated under vacuum. The crude product was purified by flash column chromatography (silica, isohexane/DCM = 3:1) to afford 0.675 g of a colorless solid, corresponding to 49% yield.

$^1$H NMR (400 MHz, $CDCl_3$) δ/ppm = 7.46 (d, J = 5.5 Hz, 2H), 7.35 (d, J = 5.5 Hz, 2H), 4.35 (q, J = 7.0 Hz, 4H), 1.47 (t, J = 7.0 Hz, 6H). $^{13}$C NMR (100 MHz, $CDCl_3$) δ/ppm = 144.3, 131.8, 130.4, 126.0, 120.3, 69.4, 16.1.

Under argon 500 mg (1.80 mmol) of 4,8-diethoxybenzo[1,2-*b*:4,5-*b*']dithiophene was dissolved in 25 mL of anhydrous inhibitor-free THF and cooled down to -78 °C. Afterwards, 3.6 mL (9.0 mmol, 2.5 M in *n*-hexane, 4.5 eq) of *n*-BuLi was slowly added and the reaction solution was stirred for 20 min at -78 °C. The solution was slowly warmed to RT to be stirred for 1 h. After cooling again to -78 °C, 2 mL (26 mmol) of DMF was added and the reaction solution was stirred overnight. It was poured on ice water and the precipitate was filtered and washed with excess of water (1000 mL). After drying under vacuum, 560 mg (1.67 mmol) of an orange product was obtained, corresponding to 93% yield.

MS-EI: calculated (m/z): 334.033, Measured (m/z): 334.0336.

$^1$H NMR (400 MHz, DMSO-$d_6$) δ (ppm): 10.18 (s, 2H), 8.65 (s, 2H), 4.45 (q, $J$ = 7.0 Hz, 4H), 1.45 (t, $J$ = 7.0 Hz, 6 H); $^{13}$C NMR (100 MHz, DMSO-$d_6$) δ (ppm): 186.38, 146.16, 143.89, 132.77, 132.70, 131.04, 70.27, 15.87.

**d) BDT-OPr monomer**

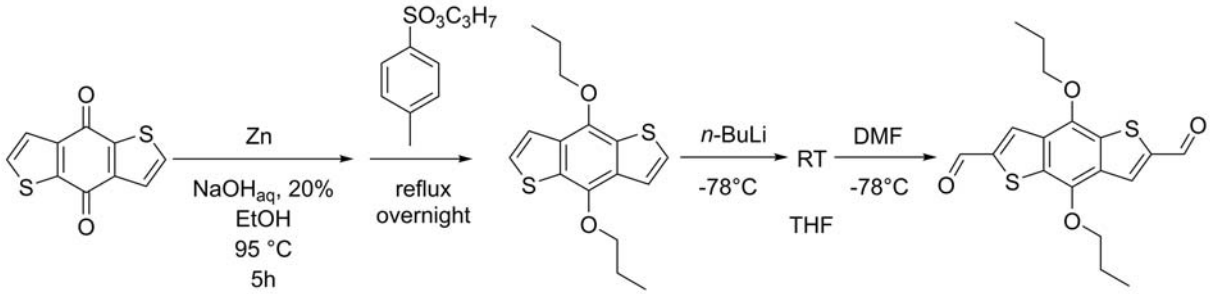


Under argon 1.1 g (5.0 mmol) of benzo[1,2-*b*:4,5-*b*']dithiophene-4,8-dione, 0.98 g (15 mmol) of zinc dust, 5.5 mL of an aqueous sodium hydroxide solution (20 %) and 4.4 mL of ethanol were refluxed for 5 h. To the hot solution 2.8 mL (15 mmol) of propyl *p*-toluenesulfonate was slowly added and the reaction solution was refluxed at 95 °C overnight. After the reaction solution had cooled down to room temperature, it was filtered and Soxhlet-extracted with toluene (50 mL). The obtained filtrate was concentrated under vacuum. 920 mg was obtained corresponding to 60% yield.

Without further purification, under argon 920 mg (3.0 mmol) of the product was dissolved in 25 mL of anhydrous inhibitor-free THF and cooled down to -78 °C. Afterwards, 3.6 mL (9.0 mmol, 2.5 M in *n*-hexane, 3 eq) of *n*-BuLi was slowly added and the brownish reaction solution was stirred for 20 min at -78 °C. The solution was slowly warmed to RT to be stirred for 1 h. After cooling again to -78 °C, 1.0 mL (13 mmol) of DMF was added and the reaction solution was stirred overnight. It was poured on ice water and the precipitate was filtered and washed with excess of water (1000 mL). After drying under vacuum, 883 mg (2.43 mmol) of red product was obtained, corresponding to 81% in yield.

MS-EI: calculated (m/z): 362.065, measured (m/z): 362.0659.

$^{1}$H NMR (400 MHz, DMSO-*d*$_6$) δ (ppm): 10.19 (s, 2H), 8.65 (s, 2H), 4.36 (t, *J* = 6.4 Hz, 4H), 1.82 – 1.91 (m, 4H), 1.10 (t, *J* = 7.4 Hz, 6H). $^{13}$C NMR (100 MHz, DMSO-*d*$_6$) δ (ppm): 186.42, 146.35, 143.86, 132.59, 132.45, 130.78, 76.01, 23.28, 10.39.

**e) Synthesis of pyrene-2,7-dicarboxaldehyde**

Under argon 1.00 g (2.78 mmol, 1 eq) of 2,7-dibromopyrene was suspended in 200 mL of anhydrous THF in a flame-dried flask. The suspension was stirred for 30 min in a cooling bath (acetone/ dry ice, -78 °C). After slow addition of 3.68 mL (6.25 mmol, 2.3 eq) of *t*-BuLi (1.7 M in *n*-pentane), the mixture was stirred for 2 h at -78 °C. 1.95 mL of anhydrous DMF (25.3 mmol, 9 eq) was slowly added. The cooling bath was removed, and the reaction mixture was stirred overnight. The mixture was quenched with 20 mL of aqueous hydrochloric acid (1.2 M). The solid was filtered, washed with $H_2O$, $Et_2O$, THF and dried under vacuum. The filtrate was extracted with DCM (three times 50 mL), the organic phases were combined and extracted with water (three times 50 mL) and brine (one time 50 mL). The organic phase was dried over $Na_2SO_4$, filtered and DCM was removed under vacuum. The crude product was purified by column chromatography (v/v 8/2 cyclohexane/EtOAc), combined with the washed solid and recrystallized from toluene to result in 0.50 g (1.94 mmol, 70% yield) of pyrene-2,7-dicarbaldehyde.

MS-EI: calculated (m/z): 258.068, measured (m/z): 258.0660.

$^{1}$H NMR (400 MHz, DMSO-$d_6$) δ (ppm): 10.48 (s, 2H), 8.89 (s, 4H), 8.47 (s, 4H).

$^{13}$C NMR (100 MHz, DMSO-$d_6$) δ (ppm): 193.63, 134.42, 131.69, 128.96, 126.32, 126.08.

#### 6.5.1.2 COF syntheses

**a) TA TAPB-COF:**

Under argon, a 6 mL glass tube was charged with TA (12.07 mg, 0.09 mmol, 1.5 eq) and TAPB (21.09 mg, 0.06 mmol, 1 eq). The reactants were suspended in 1 mL of an 8:1 (v/v) mixture of 1,4-dioxane/mesitylene. Aqueous acetic acid (6 M, 100 µl) was added, the tube was sealed, and the reaction mixture was heated at 100 °C for 72 h. The yellow precipitate was isolated by filtration and extracted with $CO_2$ under supercritical conditions for 2 h to yield 26.3 mg (88%). Details of the extractions are given below under (h). Analytically calculated for $N_6C_{72}H_{48}$: N, 8.43; C, 86.72; H, 4.85. Found: N, 8.29; C, 85.15; H, 4.92.

**b) TT TAPB-COF:**

Under argon, a 6 mL glass tube was charged with TT (11.77 mg, 0.06 mmol, 1.5 eq) and TAPB (14.06 mg, 0.04 mmol, 1 eq). The reactants were suspended in 1 mL of an 8:1 (v/v) mixture of 1,4-dioxane/mesitylene. Aqueous acetic acid (6 M, 100 µl) was added, the tube was sealed, and the reaction mixture was heated at 100 °C for 72 h. The brown precipitate was isolated by filtration and extracted with $CO_2$ under supercritical conditions for 2 h to yield 18.3 mg (77%). Analytically calculated for $N_6S_6C_{72}H_{42}$: N, 7.10; S, 16.26; C, 73.07; H, 3.58. Found: N, 6.97; S, 15.57; C, 72.12; H, 3.90.

**c) BDT TAPB-COF:**

Under argon, a 6 mL glass tube was charged with BDT (7.39 mg, 0.03 mmol, 1.5 eq) and TAPB (7.03 mg, 0.02 mmol, 1 eq). The reactants were suspended in 1 mL of an 8:1 (v/v) mixture of 1,4-dioxane/mesitylene. Aqueous acetic acid (6 M, 100 µl) was added, the tube was sealed, and the reaction mixture was heated at 100 °C for 72 h. The yellowish precipitate was isolated by filtration, washed with 1,4-dioxane and extracted with $CO_2$ under supercritical conditions for 2 h to yield 9.3 mg (70%) of COF. Analytically calculated for $N_6S_6C_{84}H_{48}$: N, 6.28; S, 14.38; C, 75.42; H, 3.92. Found: N, 6.07; S, 73.82; C, 73.82; H, 3.91.

**d) BDT-OMe TAPB-COF:**

Under argon, a 6 mL glass tube was charged with BDT-OMe (9.19 mg, 0.03 mmol, 1.5 eq) and TAPB (7.03 mg, 0.02 mmol, 1 eq). The reactants were suspended in 1 mL of an 8:1 (v/v) mixture of 1,4-dioxane/mesitylene. Aqueous acetic acid (6 M, 100 µl) was added, the tube was sealed, and the reaction mixture was heated at 100 °C for 72 h. The red precipitate was isolated by filtration, washed with 1,4-dioxane and extracted with $CO_2$ under supercritical conditions for 2 h to yield 11.4 mg (75%). Analytically calculated for $N_6O_6S_6C_{90}H_{60}$: N, 5.55; S, 12.71; C, 71.40; H, 4.00. Found: N, 5.44; S, 12.23; C, 70.45; H, 4.22.

**e) BDT-OEt TAPB-COF:**

Under argon, a 6 mL glass tube was charged with BDT-OEt (10.03 mg, 0.03 mmol, 1.5 eq) and TAPB (7.03 mg, 0.02 mmol, 1 eq). The reactants were suspended in 1 mL of an 8:1 (v/v) mixture of 1,4-dioxane/mesitylene. Aqueous acetic acid (6 M, 100 µl) was added, the tube was sealed, and the reaction mixture was heated at 100 °C for 72 h. The red precipitate was isolated by filtration, washed with 1,4-dioxane and extracted with $CO_2$ under supercritical conditions for 2 h to yield 9.3 mg (in 58%). Analytically calculated for $N_6O_6S_6C_{96}H_{72}$: N, 5.26; S, 12.04; C, 72.15; H, 4.54. Found: N, 5.32; S, 10.89; C, 71.61; H, 4.61.

**f) BDT-OPr TAPB-COF:**

Under argon, a 6 mL glass tube was charged with BDT-OPr (10.87 mg, 0.03 mmol, 1.5 eq) and TAPB (7.03 mg, 0.02 mmol, 1 eq). The reactants were suspended in 1 mL of an 8:1 (v/v) mixture of 1,4-dioxane/mesitylene. Aqueous acetic acid (6 M, 100 µl) was added, the tube was sealed, and the reaction mixture was heated at 100 °C for 72 h. The orange precipitate was isolated by filtration, washed with 1,4-dioxane and extracted with $CO_2$ under supercritical conditions for 2 h to yield 12.8 mg (76%). Analytically calculated for $N_6O_6S_6C_{102}H_{84}$: N, 5.00; S, 11.44; C, 72.83; H, 5.03. Found: N, 4.46; S, 10.36; C, 71.50; H, 5.57.

**g) Pyrene-2,7 TAPB-COF:**

Under argon, a 6 mL glass tube was charged with pyrene-2,7-dicarbaldehyde (7.75 mg, 0.03 mmol, 1.5 eq) and TAPB (7.03 mg, 0.02 mmol, 1 eq). The reactants were suspended in 1 mL of a 9:1 (v/v) mixture of benzyl alcohol/mesitylene. Aqueous acetic acid (6 M, 100 µl) was added, the tube was sealed, and the reaction mixture was heated at 120 °C for 72 h. The brownish precipitate was isolated by filtration, washed with 1,4-dioxane and extracted with $CO_2$ under supercritical conditions for 2 h to yield 9.5 mg (69%). Analytically calculated for $N_2C_{102}H_{60}$: N, 6.14; C, 89.45; H, 4.42. Found: N, 5.27; C, 75.73; H, 4.06.

**h) Supercritical fluid extraction with carbon dioxide**

Approximately 10 mg of the COF powder sample was suction filtered and rinsed with 1,4-dioxane (10 mL). The sample was transferred to a homemade $scCO_2$ extraction metal holder with sample chambers, which eventually were blocked by a filter paper. The holder was closed and tightened with a screw. The holder was placed in a sodium chloride/ice cooled autoclave (5 °C, Figure S 6.1) containing a temperature probe and a pressure indication (Anton Parr). The autoclave was tightly closed with screws and a circlip. Carbon dioxide (99.999%) from a gas bottle was passed in the autoclave until the pressure reached the maximum (45 bar). Leaving this valve open, gas was released by another valve until a temperature of 5 °C was reached within the autoclave. This temperature was kept for 30 s. Only the releasing valve was closed again. The temperature within the autoclave raised to approximately 10 to 12 °C. After the temperature reached 6 °C again, the valve, connecting gas bottle and autoclave, was tightly closed and afterwards the carbon dioxide cylinder valve. The autoclave was slowly heated to 40 °C by a heating jacket. When the pressure exceeded 100 bar, pressure was slowly released by a valve to 85 bar. This procedure was repeated until 40 °C and 85 bar were reached. After 2 h the pressure was slowly, entirely released, the powder was collected and dried under vacuum at 100 °C.

Figure S 6.1: Autoclave used for $scCO_2$ activation.

## 6.5.2 PXRD

### 6.5.2.1 Solvent treatment

Rinsing of freshly synthesized TAPB COFs with 1,4-dioxane, representing the main component of the reaction mixture, led to amorphization. The samples were vacuum-dried prior to PXRD measurements (Figure S 6.2).

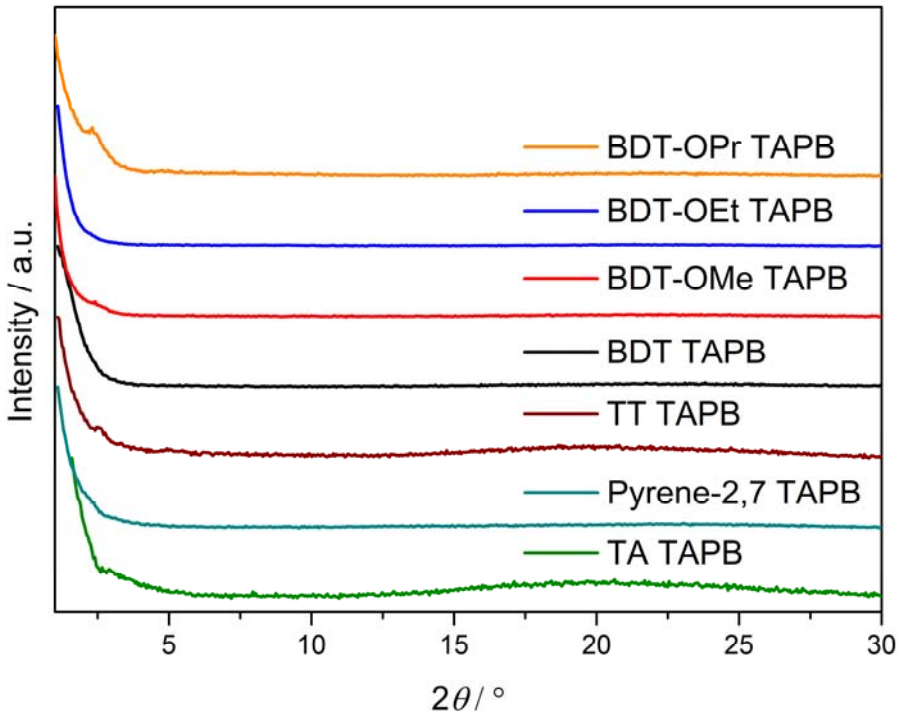


Figure S 6.2: PXRDs of TAPB-COFs rinsed with an excess of 1,4-dioxane and eventually vacuum-dried. No reflections that indicate a high degree of order could be detected.

In the following, we investigated freshly prepared COFs, which were rinsed with a solvent and finally solvent exchanged for 24 h prior to vacuum drying.

Solvent stability of the different COFs.

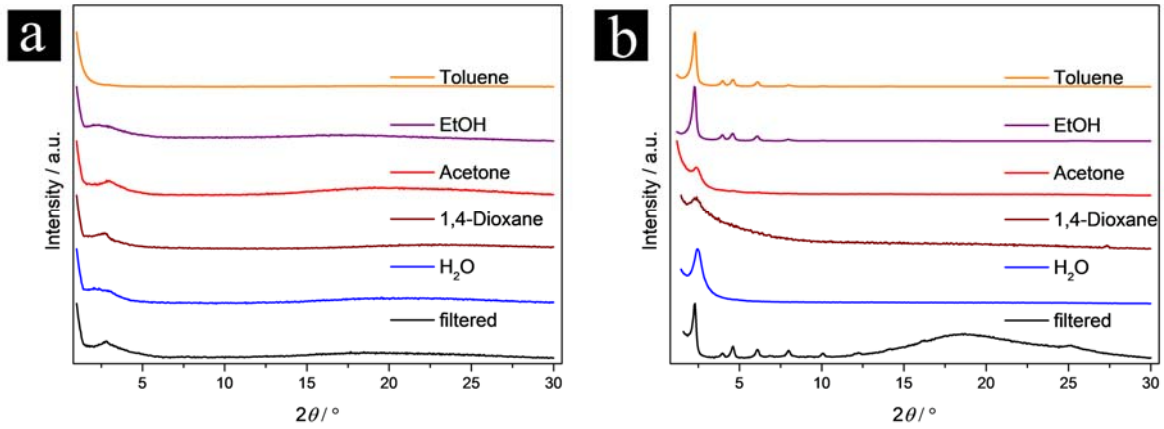


Figure S 6.3: a) PXRDs of TA TAPB-COF exposed for 24 h to different solvents. b) PXRDs of Pyrene-2,7 TAPB-COFs exposed for 24 h to different solvents. The samples were vacuum-dried after solvent exposure. In comparison, only filtered samples are shown in black.

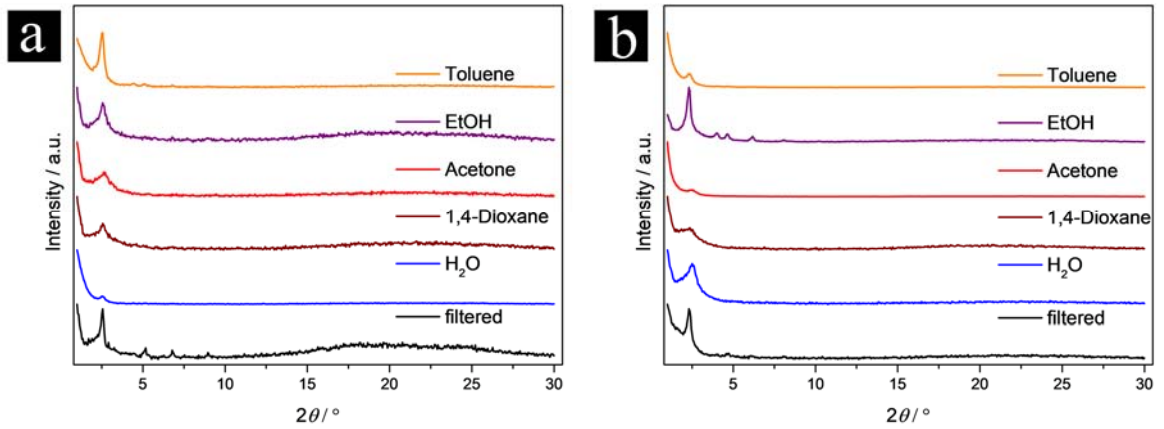


Figure S 6.4: a) PXRDs of TT TAPB-COF exposed for 24 h to different solvents. b) PXRDs of BDT TAPB-COFs exposed for 24 h to different solvents. The samples were vacuum-dried after solvent exposure. In comparison, only filtered samples are shown in black.

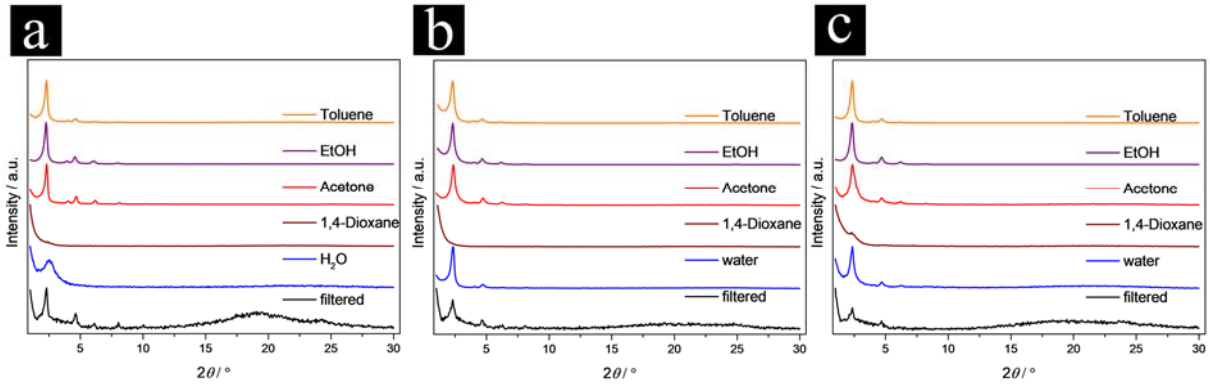


Figure S 6.5: a) PXRDs of BDT-OMe TAPB-COF exposed for 24 h to different solvents. b) PXRDs of BDT-OEt TAPB-COFs exposed for 24 h to different solvents. c) PXRDs of BDT-OPr TAPB-COF exposed for 24 h to different solvents. The samples were vacuum-dried after solvent exposure. In comparison, only filtered samples are shown in black.

#### 6.5.2.2 Solvent treatment after $scCO_2$ activation

In the following section, we investigated the $scCO_2$ activated COF samples regarding their stability towards solvent treatments. The $scCO_2$ activated COFs were solvent exchanged for 24 h (5 mg/mL) and finally dried under vacuum for 30 min.

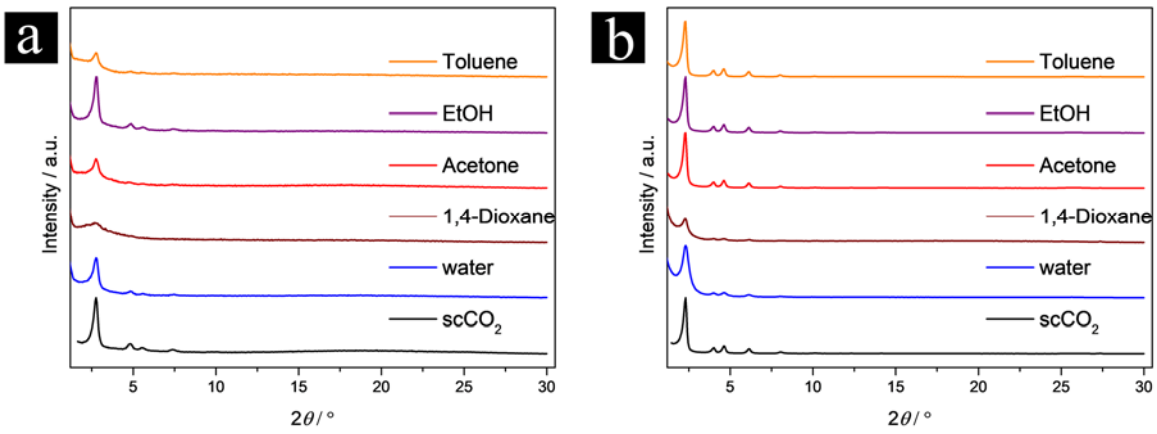


Figure S 6.6: a) PXRDs of $scCO_2$ activated TA TAPB-COF (black) exposed for 24 h to different solvents. b) PXRDs of $scCO_2$ activated Pyrene-2,7 TAPB-COF (black) exposed for 24 h to different solvents. The samples were vacuum-dried after solvent exposure.

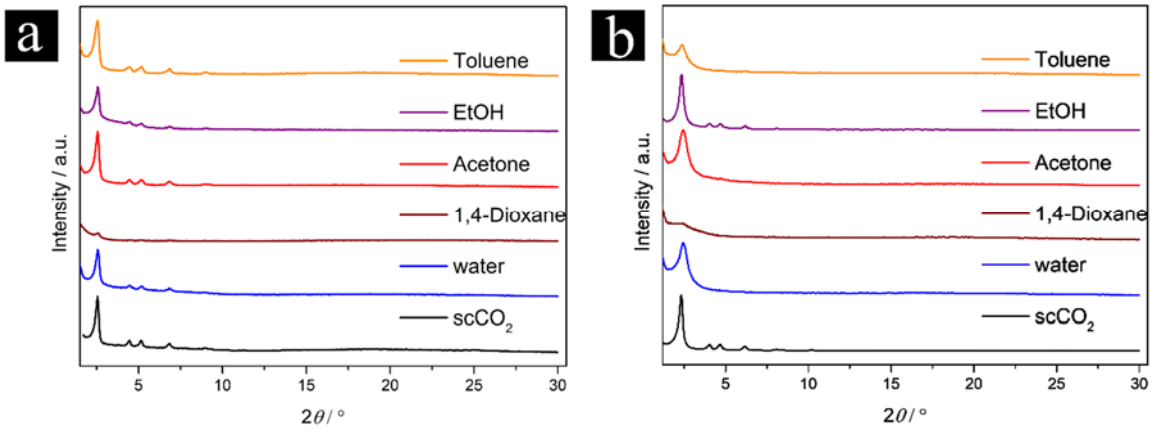


Figure S 6.7: a) PXRDs of $scCO_2$ activated TT TAPB-COF (black) exposed for 24 h to different solvents. b) PXRDs of $scCO_2$ activated BDT TAPB-COF (black) exposed for 24 h to different solvents. The samples were vacuum-dried after solvent exposure.

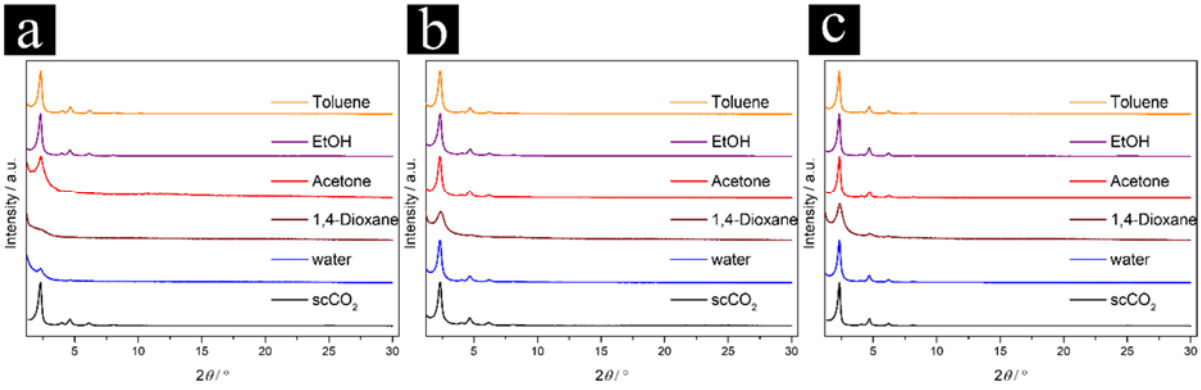


Figure S 6.8: a) PXRDs of $scCO_2$ activated BDT-OMe TAPB-COF (black) exposed for 24 h to different solvents. b) PXRDs of $scCO_2$ activated BDT-OEt TAPB-COFs exposed for 24 h to different solvents. c) PXRDs of $scCO_2$ activated BDT-OPr TAPB-COF (black) exposed for 24 h to different solvents. The samples were vacuum-dried after solvent exposure.

#### 6.5.2.3 Vapor treatment after $scCO_2$ activation

In the following section, we investigated the $scCO_2$ activated COF samples regarding their stability towards vapor treatments. The $scCO_2$ activated COFs were placed in a vial in a bigger vapor chamber without direct contact of solvent to $scCO_2$ activated COF. After vapor exposure for 24 h, the powders were finally dried under vacuum for 30 min.

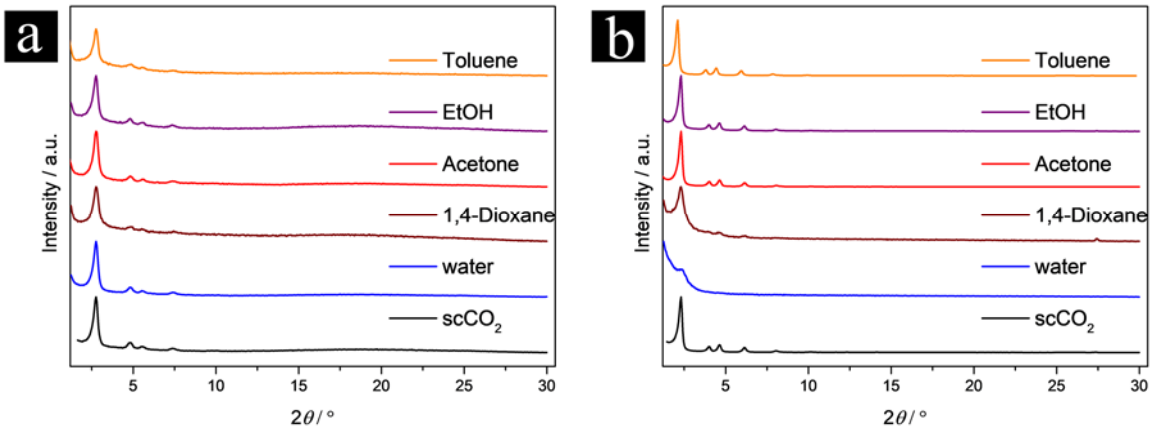


Figure S 6.9: a) PXRDs of $scCO_2$ activated TA TAPB-COF (black) exposed for 24 h to different solvent vapors. b) PXRDs of $scCO_2$ activated Pyrene-2,7 TAPB-COF (black) exposed for 24 h to different solvent vapors. The samples were vacuum-dried after vapor exposure.

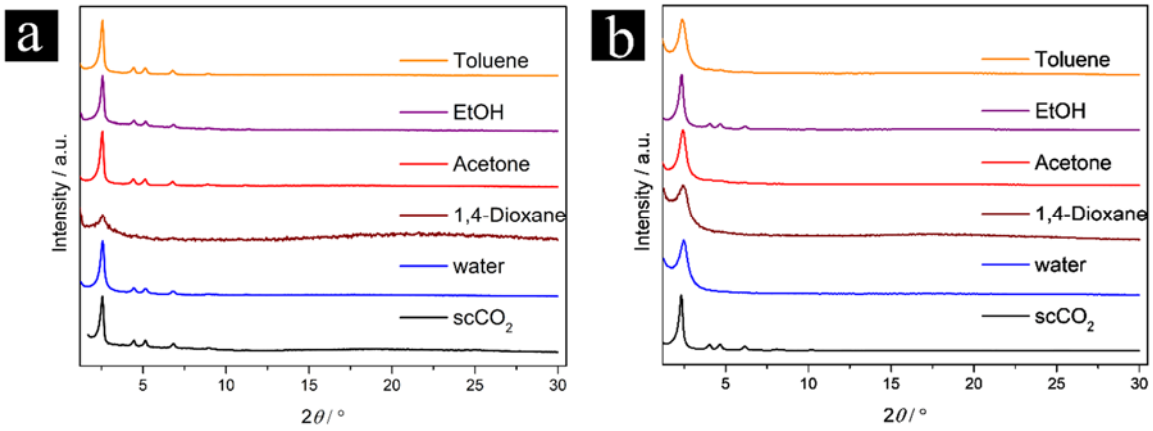


Figure S 6.10: PXRDs of $scCO_2$ activated TT TAPB-COF (black) exposed for 24 h to different solvent vapors. b) PXRDs of $scCO_2$ activated BDT TAPB-COF (black) exposed for 24 h to different solvent vapors. The samples were vacuum-dried after vapor exposure.

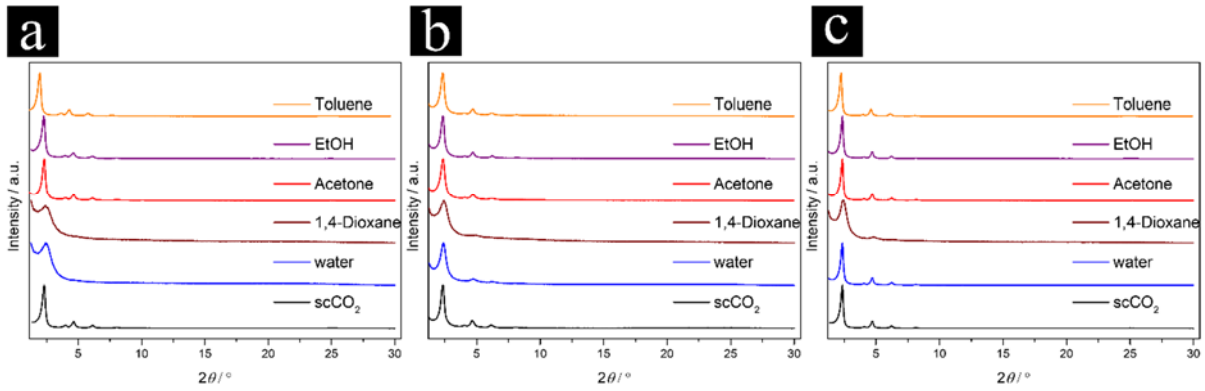


Figure S 6.11: a) PXRDs of $scCO_2$ activated BDT-OMe TAPB-COF (black) exposed for 24 h to different solvent vapors. b) PXRDs of $scCO_2$ activated BDT-OEt TAPB-COFs exposed for 24 h to different solvent vapors. c) PXRDs of $scCO_2$ activated BDT-OPr TAPB-COF (black) exposed for 24 h to different solvent vapors. The samples were vacuum-dried after solvent exposure.

### 6.5.3 SUPERCRITICAL $CO_2$ ACTIVATION

The supercritical $CO_2$ activation (extraction) is well suited for achieving high structural definition and high specific surface areas, which is partially attributed to extracting side products. Even after one day of reaction, highly crystalline COF material was obtained (Figure S 6.12).

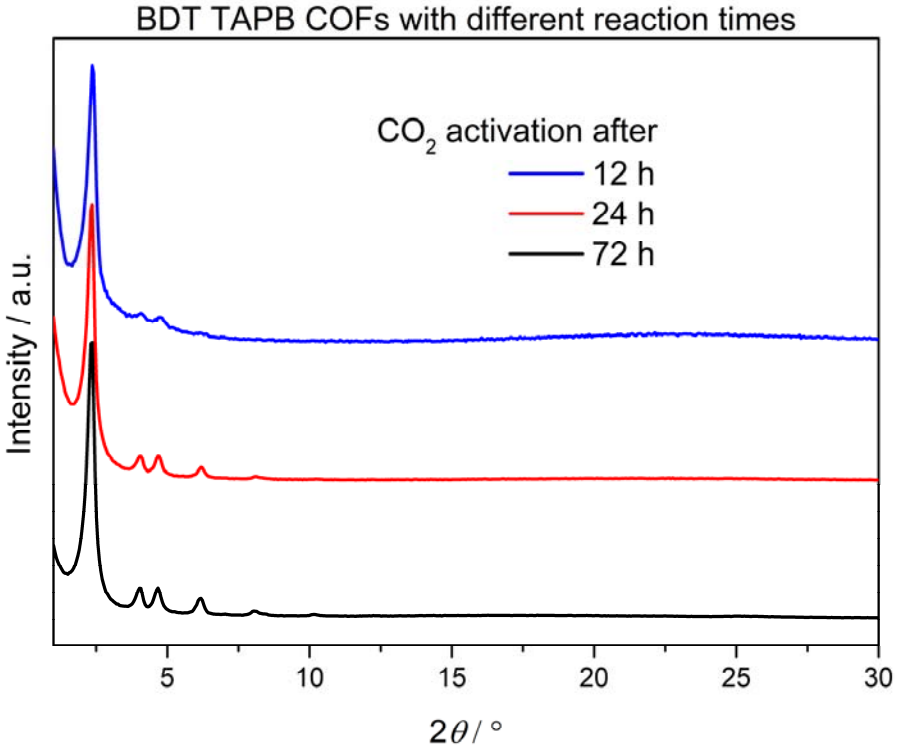


Figure S 6.12: After different times of activation it is already visible that crystalline material is formed. Nevertheless, the crystallinity further increases over the period of time.

As having shown, that there are distinct differences between robust and fragile COFs concerning their stability and tolerance towards different solvents, we investigated whether $scCO_2$ could be a technique to convert amorphous samples into crystalline and porous COF matter. We therefore decided to examine a robust BDT-OMe TAPB-COF network during the steps of $scCO_2$ activation, 1,4-dioxane treatment for amorphization, and finally toluene treatment of the amorphous powder to investigate the ability of toluene to bring back crystallinity as a solvent that was applicable even in Soxhlet extraction resulting in highly crystalline BDT-OMe TAPB-COF directly after synthesis. In Figure S 6.13 the different stages of BDT-OMe TAPB-COF activation, amorphization and reactivation are shown in a bottom-up order. The $scCO_2$ activated BDT-OMe TAPB-COF sample (black) shows high crystallinity, indicated by the sharp, intense reflections. In comparison, after 1,4-dioxane solvent treatment for 24 h and vacuum-drying, the crystallinity is drastically reduced (blue). The sample finally was transferred to a vial filled with toluene for 72 h to allow for reactivation by this tolerated solvent and to bring back crystallinity by reforming the stacked network. As demonstrated with PXRD, the crystallinity is somewhat improved (wine) in comparison to the only 1,4-dioxane treated COF (blue), nevertheless, the crystallinity is still only moderate. This was observed although toluene was an applicable solvent during the BDT-OMe TAPB-COF work-up procedure (Figure S 6.5). To investigate whether $scCO_2$-reactivation can bring back the crystallinity, the sample then was $scCO_2$ activated for 2 h. The crystallinity is indicated by the sharp and distinct reflections (red), showing that even in the case of robust COFs, $scCO_2$ is a unique treatment to recreate crystallinity in the TAPB frameworks.

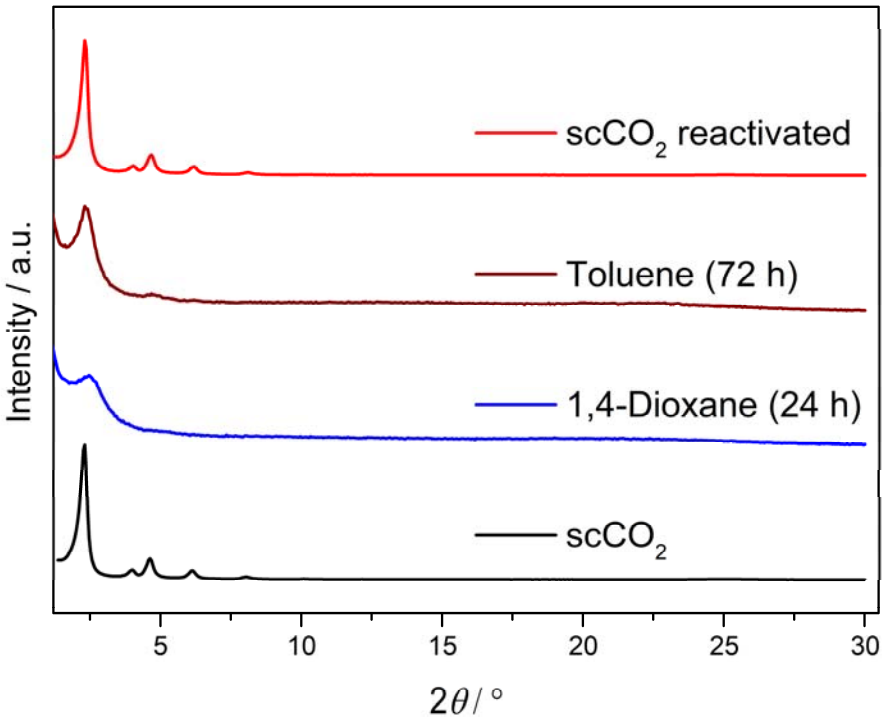


Figure S 6.13: A BDT-OMe TAPB-COF was treated with $scCO_2$ to result in a highly crystalline framework (black). Afterwards, the sample was treated with 1,4-dioxane and vacuum-dried to obtain a mainly amorphous powder with low long-range order (blue). A treatment with toluene for 72 h did not result in bringing back the high crystallinity (wine). The sample finally was $scCO_2$ activated for 2 h to result in a highly crystalline framework again (red).

Besides toluene, EtOH was a suitable washing solvent for the robust TAPB-COFs. In analogy to the toluene reactivation shown in Figure S 6.13, we tried to establish EtOH reactivation, as EtOH is a lower boiling point solvent compared to toluene. The treatment of a $scCO_2$ activated robust BDT-OPr TAPB sample with 1,4-dioxane resulted in the expected amorphization. The amorphous polymer then was immersed in EtOH for 72 h and eventually vacuum-dried prior to PXRD analysis (Figure S 6.14). A reconstitution of the framework's order after immersion in EtOH is well indicated by sharpened reflections. Nevertheless, the peak broadening compared to the $scCO_2$ activated state can be clearly seen as well. Compared to a $scCO_2$ reactivation, solvent reactivation in general appears to be slower and less effective. $ScCO_2$ reactivation can be conducted within a very short period of only 2 h allowing for access to highly crystalline and open porous reactivated TAPB COF frameworks.

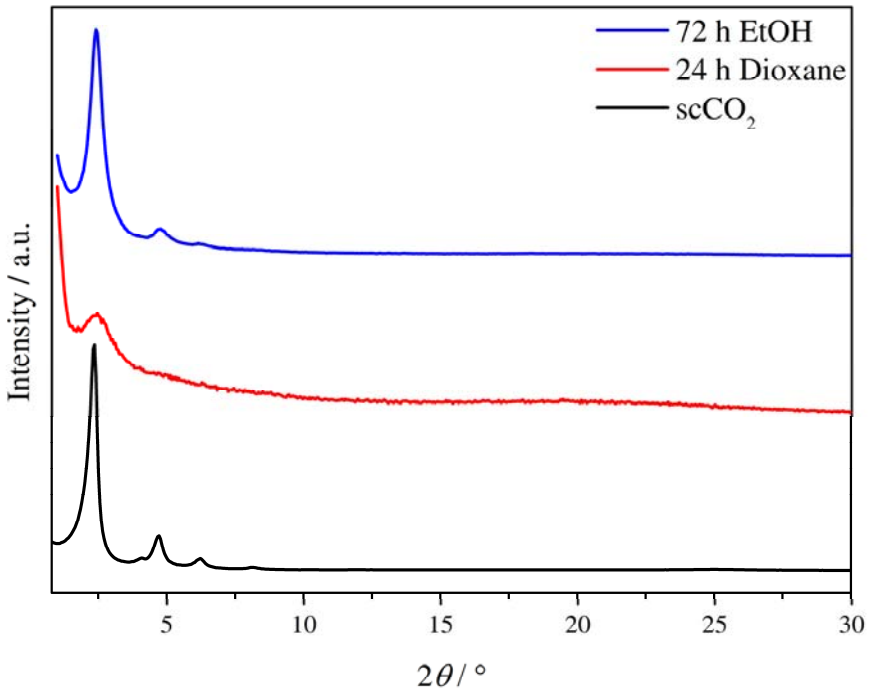


Figure S 6.14: PXRD pattern of a BDT-OPr TAPB-COF after $scCO_2$ activation (black), after a 24 h immersion in 1,4-dioxane and final vacuum drying (red) and a 72 h immersion in EtOH prior to final vacuum drying (blue).

The activation via $scCO_2$ allows for the realization of highly crystalline COFs that were still highly crystalline after one month of storing them under ambient conditions.

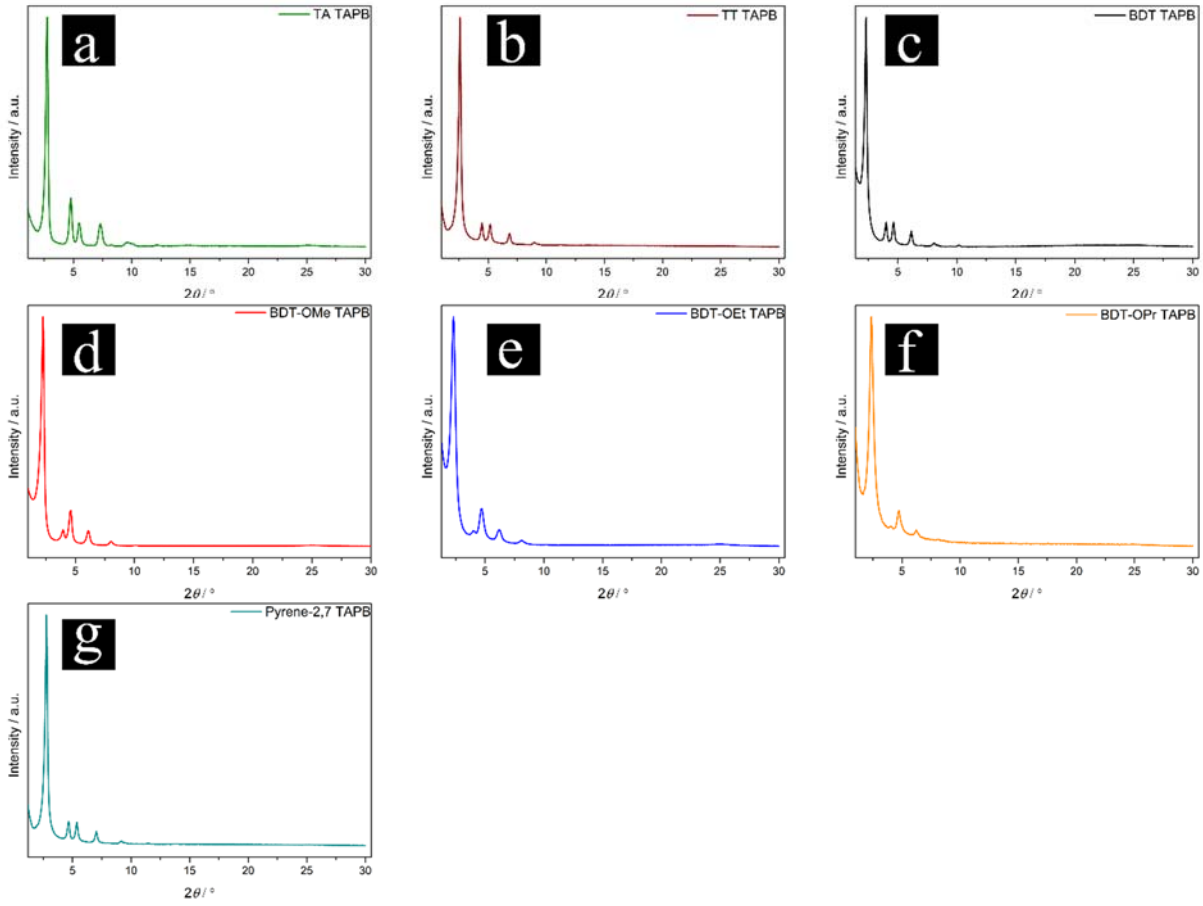


Figure S 6.15: PXRD patterns of $scCO_2$ activated TAPB COFs after storing them for one month at ambient conditions. a) TA TAPB-COF, b) TT TAPB-COF, c) BDT TAPB-COF, d) BDT-OMe TAPB-COF, e) BDT-OEt TAPB-COF, f) BDT-OPr TAPB-COF and g) Pyrene-2,7 TAPB-COF.

During time-dependent PXRD studies of the fragile BDT TAPB-COF and the robust BDT-OMe TAPB-COF being exposed to ethanol or 1,4-dioxane vapors in a plastic bag, the reflection corresponding to the plastic bag for creation of saturated vapors remained stable. On the other hand, the reflection at 25.1 °2θ due to the COFs shifts towards smaller values of °2θ during the exposure. This indicates an expansion of the stacking distance of adjacent layers (Figure S 6.16).

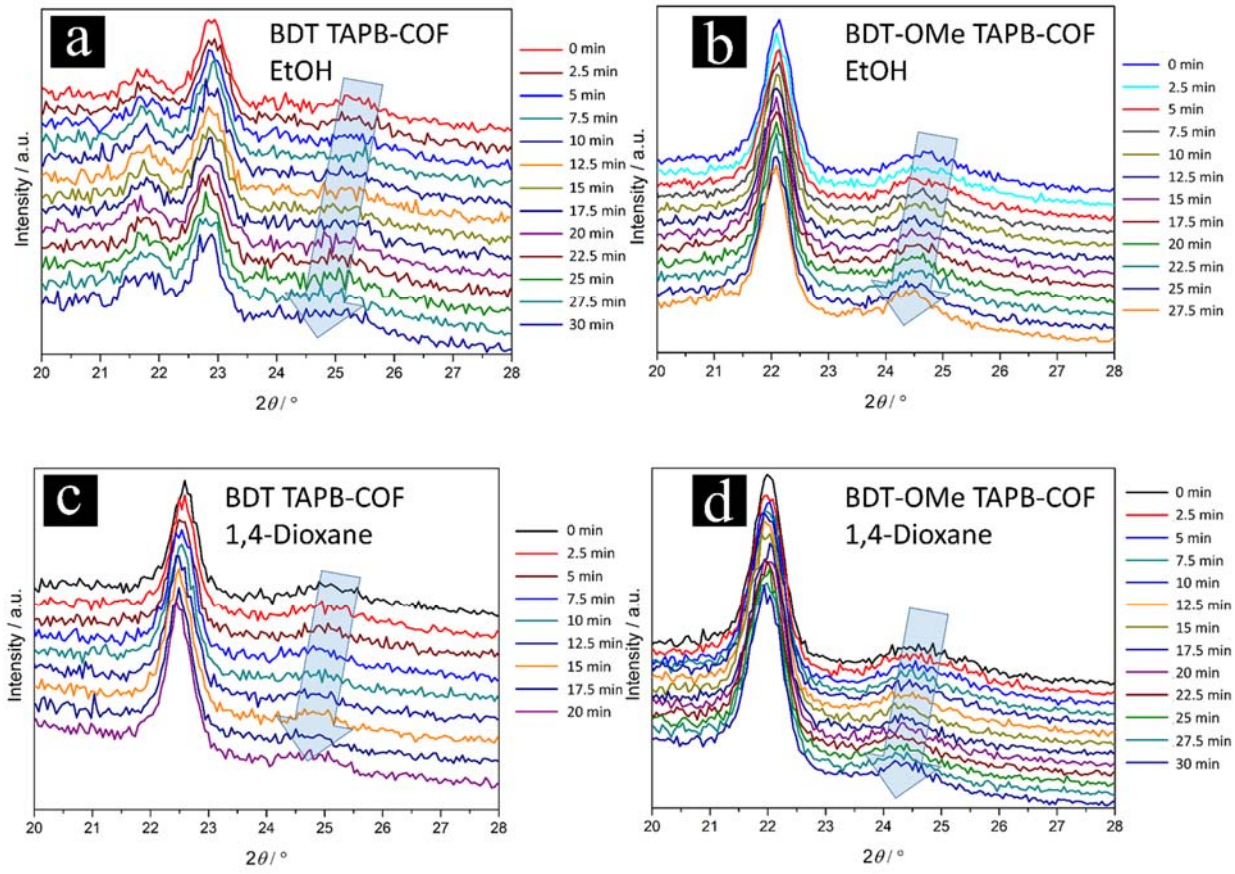


Figure S 6.16: Time-dependent PXRD patterns of COFs in a plastic bag (reflection at 21-23 °2θ) a) BDT TAPB-COF under time dependent PXRD during EtOH-vapor exposure. b). BDT-OMe TAPB-COF under time dependent PXRD during EtOH-vapor exposure. c) BDT TAPB-COF under time dependent PXRD during 1,4-dioxane-vapor exposure and d) BDT-OMe TAPB-COF under time dependent PXRD during 1,4-dioxane-vapor exposure.

To investigate the apparent effects of solvents on the frameworks in more detail, we performed PXRD measurements of $scCO_2$ activated, solvent immersed and $scCO_2$ reactivated COF samples. The solvent molecules enlarge the stacking distance from roughly 3.52 Å (25.3 °2θ) up to 3.91 Å (22.7 °2θ) (Figure S 6.17 – 6.18).

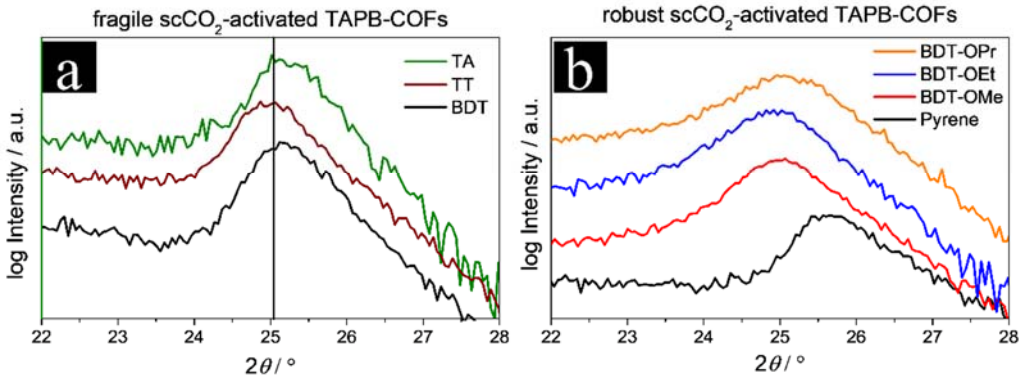


Figure S 6.17: PXRD patterns of the 001 reflections of TAPB-COFs. a) and b) show the influence of the linear dialdehyde part and the TAPB on the π-stacking distance of adjacent TAPB-COF layers. For small linear dialdehydes, the stacking distance is mainly guided by TAPB. Nevertheless, small deviations due to the influence of the linear dialdehyde are visible. Connecting the good aggregator pyrene and TAPB results in a shift of the 001 reflection corresponding to the π-stacking distance of adjacent Pyrene-2,7 TAPB-COF layers. The pyrene dialdehyde induces a closer stacking resulting in a shift of the 001 reflections from 25.1 (preferred distance for TAPB) to 25.7 °2θ.

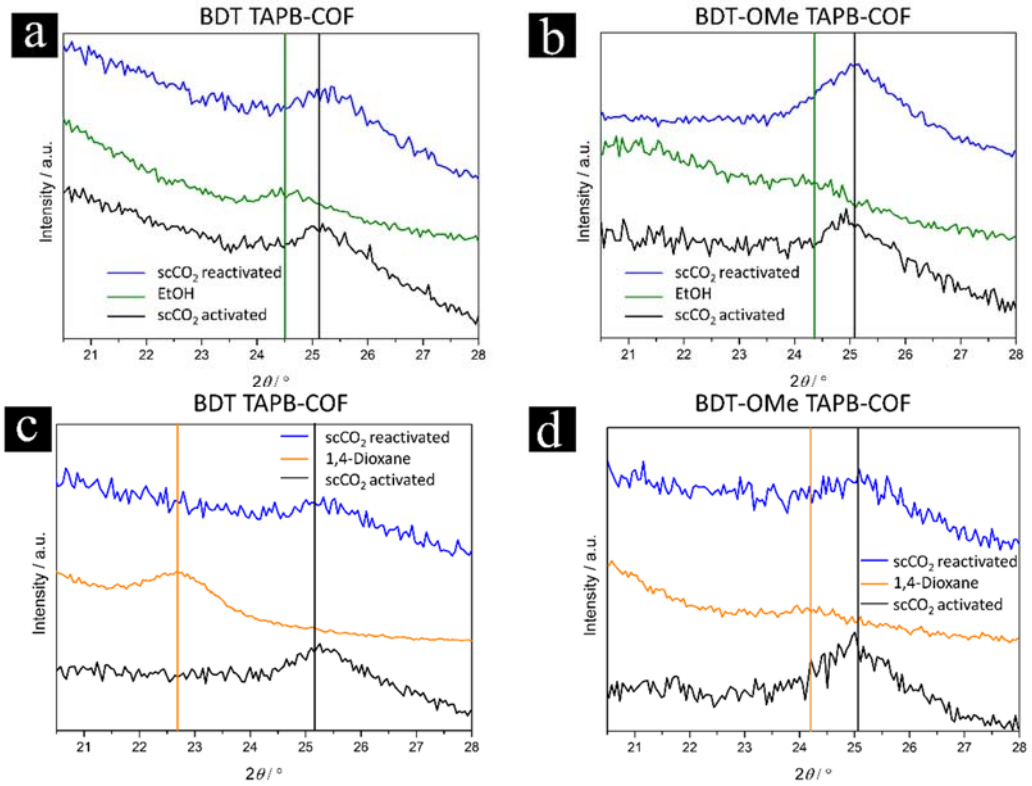


Figure S 6.18: a) to d) show the influence of solvent wetting of the fragile BDT TAPB-COF (a, c) and the robust BDT-OMe TAPB-COF (b, d) on the stacking distance. It is of less importance whether the solvent influence results in an amorphous polymer (BDT TAPB-COF in a)) or allows for regaining high order after vacuum-drying (BDT-OMe TAPB-COF with EtOH); during the wetting, the stacking distance is enlarged (shifting to the left in PXRD). The $scCO_2$ activated COFs show a reflection at 25.1 °2θ representing the stacking distance. Upon solvent wetting with a droplet, the reflection is shifted towards smaller °2θ, indicating an enlarged stacking distance, for ethanol and 1,4-dioxane. After $scCO_2$ reactivation, the original state of 25.1 °2θ is restored.

We also investigated the influence on the stacking distance with the less volatile toluene, towards which the robust BDT-OMe TAPB-COF was highly tolerant. We were able to detect shifted stacking distances (Figure S 6.19).

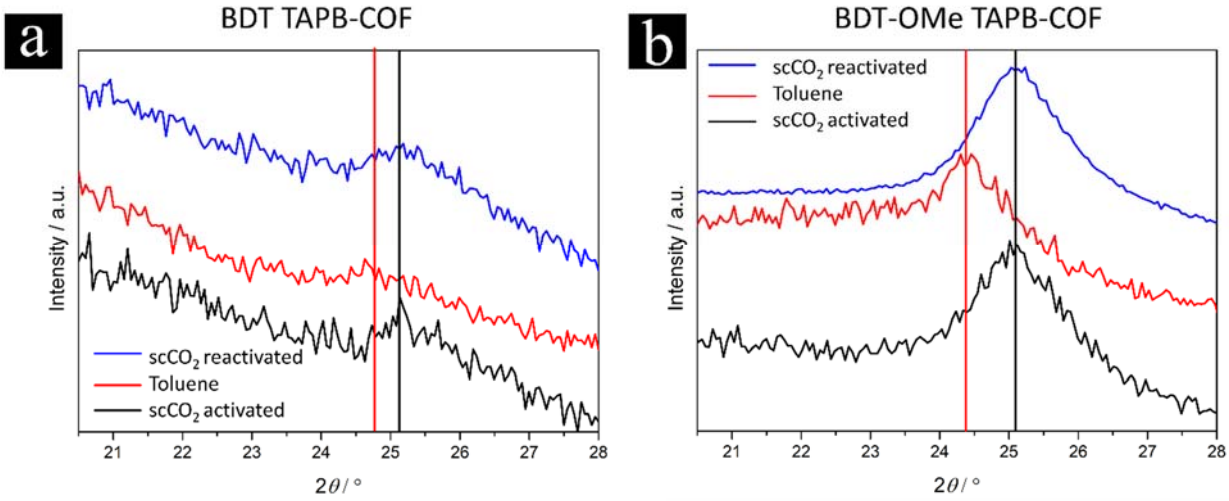


Figure S 6.19: Influence of toluene on the stacking distance in case of the fragile BDT TAPB-COF (a) and the robust BDT-OMe TAPB-COF (b). In both cases, the stacking distance is enlarged, indicated by the shift of the reflection at 25.1 °2θ in the $scCO_2$ activated and -reactivated cases.

To investigate the sensitivity to water and the possibility to even reactivate these samples, we studied the behavior of BDT TAPB-COF. A $scCO_2$ activated BDT TAPB-COF sample (black) was transferred to a vial with water for 24 h. After being vacuum-dried, the sample was investigated by PXRD, revealing the loss of long-range order (red). After rinsing with 1,4-dioxane, the same sample was $scCO_2$-reactivated, showing the recovery of the high crystallinity (blue).

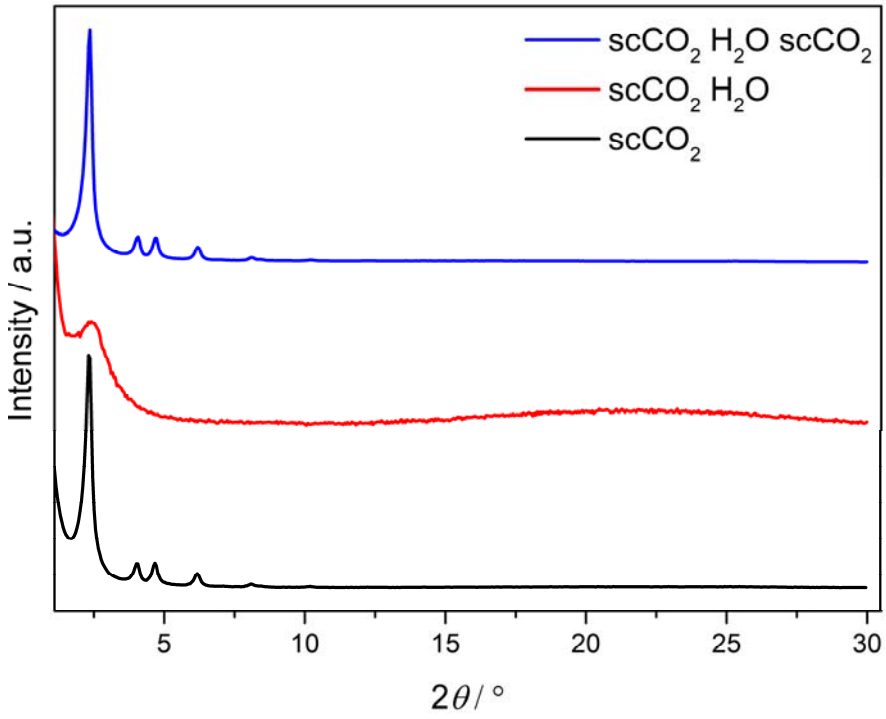


Figure S 6.20: PXRD patterns of BDT TAPB, $scCO_2$ activated (2h, black, crystalline), exposed to water for 24 h and vacuum-dried (red, mostly amorphous) and finally $scCO_2$ reactivated (2h, blue, crystalline).

Investigations on the utility of the $scCO_2$ activation compared to a gaseous system under similar conditions (Ar, 40°C, 85 bar, 2h) revealed that only the supercritical state of $CO_2$ can convert an amorphous TAPB-COF powder, whether fragile or robust, into a highly crystalline state.

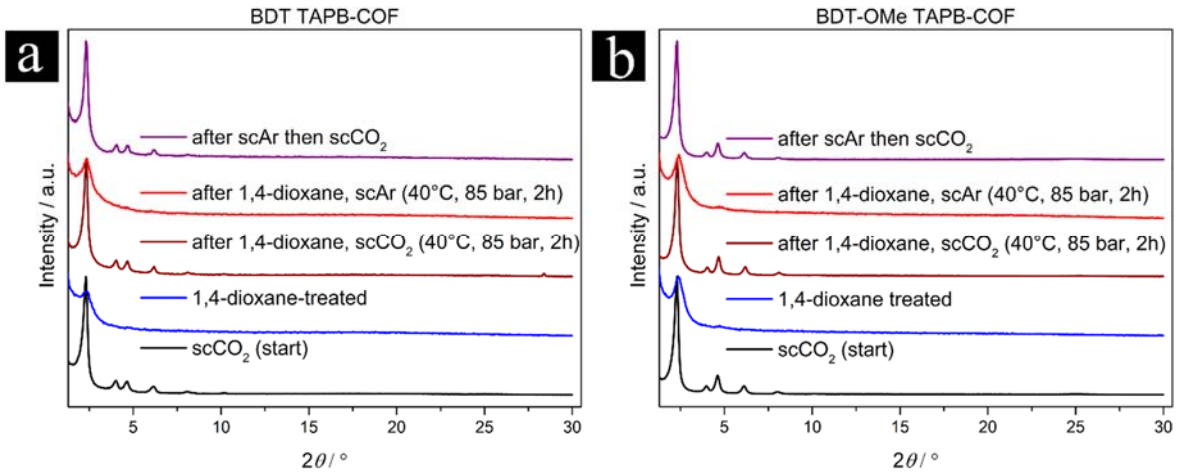


Figure S 6.21: Comparison of the fragile BDT TAPB-COF (a) and the robust BDT-OMe TAPB-COF (b) concerning activation with $scCO_2$ and Argon under the same conditions (40 °C, 85 bar, 2 h). $ScCO_2$ activated samples were transformed into amorphous state by treatment with 1,4-dioxane. The amorphous powders were activated with Ar and $scCO_2$ under the same conditions. While the $scCO_2$ activated samples exhibit high crystallinity, the argon activated samples show no improved crystallinity compared to the 1,4-dioxane treated sample. These samples could be reactivated only by $scCO_2$.

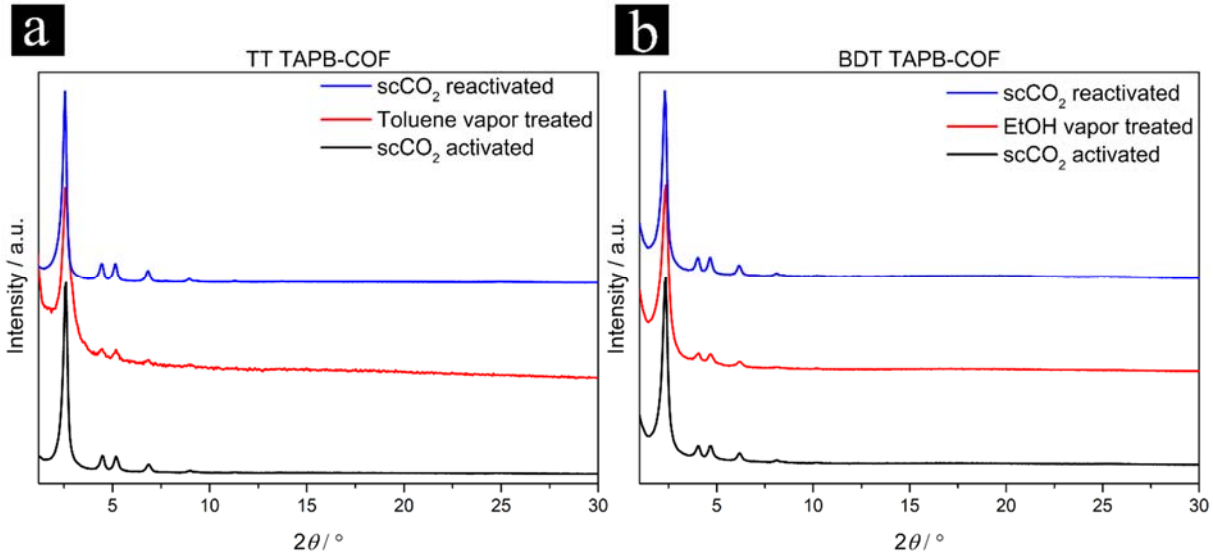


Figure S 6.22: PXRDs of TT TAPB-COF (a) and BDT TAPB-COF (b) after $scCO_2$ activation (black), after exposure to EtOH (a) and toluene (b) vapors for 24 h and final vacuum-drying (red), compared to $scCO_2$ reactivated samples (blue). The crystallinity of the powders is still visible even after vapor exposure, although decreased in both cases.

### 6.5.4 UNIT CELL PARAMETERS AND ATOMIC COORDINATES

a) TA TAPB COF

RWP = 4.65%, Rwp (w/o bck) = 5.79%, RP = 3.66%

| P*6* (168) – hexagonal | | | |
|---|---|---|---|
| a = b = 3.38925(7) nm, c = 0.359 nm | | | |
| α = β = 90°, γ = 120° | | | |
| **Atom** | **x/a** | **y/b** | **z/c** |
| C1 | 0.71006 | 0.35719 | 0.46962 |
| C2 | 0.68591 | 0.37607 | 0.46950 |
| C3 | 0.75594 | 0.38239 | 0.47057 |
| C4 | 0.77637 | 0.42195 | 0.31515 |
| C5 | 0.81918 | 0.44556 | 0.32104 |
| C6 | 0.84272 | 0.43000 | 0.47011 |
| C7 | 0.82279 | 0.39066 | 0.62604 |
| C8 | 0.77995 | 0.36731 | 0.62885 |
| N9 | 0.88655 | 0.45557 | 0.46841 |
| C10 | 0.91285 | 0.44293 | 0.49917 |
| C11 | 0.95737 | 0.47235 | 0.49850 |
| H12 | 0.70076 | 0.40906 | 0.46968 |
| H13 | 0.75960 | 0.43439 | 0.17767 |
| H14 | 0.83441 | 0.47574 | 0.19846 |

| **Atom** | **x/a** | **y/b** | **z/c** |
|---|---|---|---|
| H15 | 0.84005 | 0.37860 | 0.76036 |
| H16 | 0.76584 | 0.33813 | 0.76859 |
| H17 | 0.90268 | 0.41054 | 0.51507 |
| C18 | 0.45771 | 0.47262 | 0.49937 |
| C19 | 0.48512 | 0.45774 | 0.49845 |
| H20 | 0.42506 | 0.45104 | 0.49991 |
| H21 | 0.47323 | 0.42495 | 0.49885 |

b) TT TAPB COF

RWP = 4.94%, Rwp (w/o bck) = 7.44%, RP = 3.80%

| P*6* (168) – hexagonal | | | |
|---|---|---|---|
| a = b = 3.9732(3)(0) nm, c = 0.371 nm | | | |
| α = β = 90°, γ = 120° | | | |
| **Atom** | **x/a** | **y/b** | **z/c** |
| C1 | 0.70717 | 0.35510 | 0.45837 |
| C2 | 0.68514 | 0.37325 | 0.45741 |
| C3 | 0.74998 | 0.37810 | 0.46742 |
| C4 | 0.76981 | 0.41500 | 0.31484 |
| C5 | 0.80975 | 0.43681 | 0.33398 |
| C6 | 0.83094 | 0.42210 | 0.49457 |

| **Atom** | **x/a** | **y/b** | **z/c** |
|---|---|---|---|
| C7 | 0.81156 | 0.38525 | 0.64526 |
| C8 | 0.77157 | 0.36366 | 0.63405 |
| N9 | 0.87178 | 0.44610 | 0.51099 |
| C10 | 0.89649 | 0.43506 | 0.57448 |
| C11 | 0.93763 | 0.46305 | 0.58214 |
| H12 | 0.69989 | 0.40590 | 0.45582 |
| H13 | 0.75294 | 0.42703 | 0.17473 |
| H14 | 0.82542 | 0.46702 | 0.21749 |
| H15 | 0.82847 | 0.37282 | 0.77758 |
| H16 | 0.75595 | 0.33394 | 0.76074 |
| H17 | 0.88621 | 0.40344 | 0.62462 |
| C18 | 0.45155 | 0.48668 | 0.58560 |
| C19 | 0.48354 | 0.48321 | 0.58698 |
| S20 | 0.48793 | 0.44355 | 0.58170 |
| H21 | 0.41972 | 0.46429 | 0.58680 |

c) BDT TAPB COF

RWP = 5.90%, Rwp (w/o bck) = 9.04%, RP = 4.38%

| P*6* (168) – hexagonal | | | |
|---|---|---|---|
| a = b = 4.3675(6) nm, c = 0.367 nm | | | |
| α = β = 90°, γ = 120° | | | |
| **Atom** | **x/a** | **y/b** | **z/c** |
| C1 | 0.70311 | 0.35319 | 0.46869 |
| C2 | 0.68300 | 0.36922 | 0.46838 |
| C3 | 0.74163 | 0.37418 | 0.47151 |
| C4 | 0.75900 | 0.40745 | 0.31764 |
| C5 | 0.79494 | 0.42718 | 0.32720 |
| C6 | 0.81448 | 0.41396 | 0.47816 |
| C7 | 0.79755 | 0.38083 | 0.63150 |
| C8 | 0.76158 | 0.36132 | 0.63098 |
| N9 | 0.85124 | 0.43544 | 0.48153 |
| C10 | 0.87340 | 0.42504 | 0.51848 |
| C11 | 0.91049 | 0.45009 | 0.52117 |
| S12 | 0.92755 | 0.49648 | 0.51906 |
| C13 | 0.96951 | 0.50076 | 0.52462 |
| C14 | 0.96887 | 0.46952 | 0.52612 |
| C15 | 0.93413 | 0.44040 | 0.52557 |

| **Atom** | **x/a** | **y/b** | **z/c** |
|---|---|---|---|
| C16 | 1.00067 | 0.53196 | 0.52550 |
| H17 | 0.69560 | 0.39693 | 0.46883 |
| H18 | 0.74511 | 0.41806 | 0.17930 |
| H19 | 0.80795 | 0.45264 | 0.20696 |
| H20 | 0.81186 | 0.37056 | 0.76670 |
| H21 | 0.74956 | 0.33676 | 0.76943 |
| H22 | 0.86512 | 0.39792 | 0.53676 |
| H23 | 0.92813 | 0.41383 | 0.52697 |
| H24 | 1.00097 | 0.55622 | 0.52463 |

d) BDT-OMe TAPB COF

RWP = 6.71%, Rwp (w/o bck) = 10.70%, RP = 6.65%

| P*6* (168) – hexagonal | | | |
|---|---|---|---|
| a = b = 4.3844(4) nm, c = 0.370 nm | | | |
| α = β = 90°, γ = 120° | | | |
| **Atom** | **x/a** | **y/b** | **z/c** |
| C1 | 0.70178 | 0.35152 | 0.49635 |
| C2 | 0.68253 | 0.36630 | 0.49636 |
| C3 | 0.74032 | 0.37227 | 0.51144 |
| C4 | 0.75830 | 0.40338 | 0.38664 |

| **Atom** | **x/a** | **y/b** | **z/c** |
|---|---|---|---|
| C5 | 0.79218 | 0.42125 | 0.37237 |
| C6 | 0.81263 | 0.41056 | 0.48015 |
| C7 | 0.79523 | 0.37948 | 0.60608 |
| C8 | 0.76100 | 0.36142 | 0.62053 |
| N9 | 0.84842 | 0.43201 | 0.49601 |
| C10 | 0.87381 | 0.42824 | 0.49700 |
| C11 | 0.91119 | 0.45365 | 0.49668 |
| S12 | 0.93219 | 0.49697 | 0.49656 |
| C13 | 0.97183 | 0.50124 | 0.49666 |
| C14 | 0.96914 | 0.47245 | 0.49670 |
| C15 | 0.93466 | 0.44621 | 0.49682 |
| C16 | 1.00240 | 0.52908 | 0.49670 |
| H17 | 0.69423 | 0.39324 | 0.49638 |
| H18 | 0.74375 | 0.41427 | 0.29219 |
| H19 | 0.80462 | 0.44637 | 0.26659 |
| H20 | 0.80812 | 0.36702 | 0.70498 |
| H21 | 0.74856 | 0.33630 | 0.72625 |
| H22 | 0.87059 | 0.40340 | 0.49833 |
| H23 | 0.92848 | 0.42034 | 0.49703 |
| O24 | 0.44263 | 0.00260 | 0.48554 |

| **Atom** | **x/a** | **y/b** | **z/c** |
|---|---|---|---|
| C25 | 0.44564 | 0.03340 | 0.37114 |
| H26 | 0.45538 | 0.03878 | 0.10364 |
| H27 | 0.46248 | 0.05328 | 0.54602 |
| H28 | 0.42135 | 0.03149 | 0.37701 |

e) BDT-OEt TAPB COF

RWP = 4.90%, Rwp (w/o bck) = 7.31%, RP = 3.63%

| P*6* (168) – hexagonal | | | |
|---|---|---|---|
| a = b = 4.3796(5) nm, c = 0.393 nm | | | |
| α = β = 90°, γ = 120° | | | |
| **Atom** | **x/a** | **y/b** | **z/c** |
| C1 | 0.70178 | 0.35152 | 0.49635 |
| C2 | 0.68253 | 0.36630 | 0.49636 |
| C3 | 0.74032 | 0.37227 | 0.51144 |
| C4 | 0.75830 | 0.40338 | 0.38664 |
| C5 | 0.79218 | 0.42125 | 0.37237 |
| C6 | 0.81263 | 0.41056 | 0.48015 |
| C7 | 0.79523 | 0.37948 | 0.60608 |
| C8 | 0.76100 | 0.36142 | 0.62053 |
| N9 | 0.84842 | 0.43201 | 0.49601 |

| **Atom** | **x/a** | **y/b** | **z/c** |
|---|---|---|---|
| C10 | 0.87381 | 0.42824 | 0.49700 |
| C11 | 0.91119 | 0.45365 | 0.49668 |
| S12 | 0.93219 | 0.49697 | 0.49656 |
| C13 | 0.97183 | 0.50124 | 0.49666 |
| C14 | 0.96914 | 0.47245 | 0.49670 |
| C15 | 0.93466 | 0.44621 | 0.49682 |
| C16 | 1.00240 | 0.52908 | 0.49670 |
| H17 | 0.69531 | 0.39573 | 0.49638 |
| H18 | 0.74236 | 0.41497 | 0.28495 |
| H19 | 0.80571 | 0.44839 | 0.25830 |
| H20 | 0.80948 | 0.36627 | 0.71230 |
| H21 | 0.74747 | 0.33428 | 0.73454 |
| H22 | 0.87029 | 0.4011 | 0.49845 |
| H23 | 0.92791 | 0.41795 | 0.49705 |
| O24 | 0.44263 | 0.00260 | 0.48554 |
| C25 | 0.44564 | 0.03340 | 0.37114 |
| C26 | 0.41577 | 0.03512 | 0.35453 |
| H27 | 0.45774 | 0.03894 | 0.10667 |
| H28 | 0.46372 | 0.05541 | 0.54689 |
| H29 | 0.39291 | 0.00937 | 0.43965 |

| **Atom** | **x/a** | **y/b** | **z/c** |
|---|---|---|---|
| H30 | 0.41143 | 0.04076 | 0.08165 |
| H31 | 0.41819 | 0.05668 | 0.52849 |

f) BDT-OPr TAPB COF

RWP = 4.15%, Rwp (w/o bck) = 8.35%, RP = 3.42%

| P*6* (168) – hexagonal | | | |
|---|---|---|---|
| a = b = 4.2493(2) nm, c = 0.394 nm | | | |
| α = β = 90°, γ = 120° | | | |
| **Atom** | **x/a** | **y/b** | **z/c** |
| C1 | 0.70178 | 0.35152 | 0.49635 |
| C2 | 0.68253 | 0.36630 | 0.49636 |
| C3 | 0.74032 | 0.37227 | 0.51144 |
| C4 | 0.7583 | 0.40338 | 0.38664 |
| C5 | 0.79218 | 0.42125 | 0.37237 |
| C6 | 0.81263 | 0.41056 | 0.48015 |
| C7 | 0.79523 | 0.37948 | 0.60608 |
| C8 | 0.76100 | 0.36142 | 0.62053 |
| N9 | 0.84842 | 0.43201 | 0.49601 |
| C10 | 0.87381 | 0.42824 | 0.49700 |
| C11 | 0.91119 | 0.45365 | 0.49668 |
| S12 | 0.93219 | 0.49697 | 0.49656 |

| **Atom** | **x/a** | **y/b** | **z/c** |
|---|---|---|---|
| C13 | 0.97183 | 0.50124 | 0.49666 |
| C14 | 0.96914 | 0.47245 | 0.49670 |
| C15 | 0.93466 | 0.44621 | 0.49682 |
| C16 | 1.00240 | 0.52908 | 0.49670 |
| H17 | 0.69531 | 0.39573 | 0.49638 |
| H18 | 0.74236 | 0.41497 | 0.28495 |
| H19 | 0.80571 | 0.44839 | 0.25830 |
| H20 | 0.80948 | 0.36627 | 0.71230 |
| H21 | 0.74747 | 0.33428 | 0.73454 |
| H22 | 0.87029 | 0.40110 | 0.49845 |
| H23 | 0.92791 | 0.41795 | 0.49705 |
| O24 | 0.44263 | 0.00260 | 0.48554 |
| C25 | 0.44564 | 0.03340 | 0.37114 |
| C26 | 0.41577 | 0.03512 | 0.35453 |
| C27 | 0.45774 | 0.03894 | 0.10667 |
| H28 | 0.46372 | 0.05541 | 0.54689 |
| H29 | 0.41143 | 0.04076 | 0.08165 |
| H30 | 0.41819 | 0.05668 | 0.52849 |
| C31 | 0.62725 | 0.62201 | 0.36724 |
| H32 | 0.63830 | 0.63504 | 0.10801 |

| **Atom** | **x/a** | **y/b** | **z/c** |
|---|---|---|---|
| H33 | 0.64692 | 0.63650 | 0.58034 |
| H34 | 0.60237 | 0.62247 | 0.42280 |

g) Pyrene-2,7 TAPB COF

RWP = 7.50%, Rwp (w/o bck) = 9.78%, RP = 5.67%

| P6 (168) – hexagonal | | | |
|---|---|---|---|
| a = b = 4.4114(0) nm, c = 0.354 nm | | | |
| α = β = 90°, γ = 120° | | | |
| **Atom** | **x/a** | **y/b** | **z/c** |
| C1 | 0.25827 | 0.63099 | 0.38442 |
| C2 | 0.2403 | 0.64663 | 0.53313 |
| C3 | 0.20435 | 0.62962 | 0.527 |
| C4 | 0.18533 | 0.59627 | 0.38578 |
| C5 | 0.20283 | 0.58034 | 0.23712 |
| C6 | 0.2388 | 0.59761 | 0.2332 |
| N7 | 0.14848 | 0.58002 | 0.38793 |
| C8 | 0.12708 | 0.54717 | 0.36186 |
| C9 | 0.08957 | 0.53358 | 0.3625 |
| C10 | 0.07601 | 0.55584 | 0.36352 |

| **Atom** | **x/a** | **y/b** | **z/c** |
|---|---|---|---|
| C11 | 0.04036 | 0.54266 | 0.36288 |
| C12 | 0.01795 | 0.50674 | 0.36232 |
| C13 | 0.0314 | 0.48427 | 0.36162 |
| C14 | 0.06712 | 0.49785 | 0.36091 |
| C15 | 0.02673 | 0.56478 | 0.36259 |
| C16 | 0.00889 | 0.44859 | 0.36167 |
| C17 | 0.29686 | 0.64934 | 0.38513 |
| C18 | 0.31629 | 0.6855 | 0.38525 |
| H19 | 0.25367 | 0.67156 | 0.66601 |
| H20 | 0.19103 | 0.64196 | 0.64373 |
| H21 | 0.18897 | 0.55524 | 0.1089 |
| H22 | 0.25108 | 0.58505 | 0.09773 |
| H23 | 0.1363 | 0.52905 | 0.34963 |
| H24 | 0.09326 | 0.58342 | 0.36381 |
| H25 | 0.0775 | 0.48064 | 0.35998 |
| H26 | 0.04363 | 0.59242 | 0.36286 |
| H27 | 0.01887 | 0.43105 | 0.36121 |
| H28 | 0.30315 | 0.70004 | 0.38517 |

### 6.5.5 MONOMERS

For obtaining more detailed insights into the anticipated/possible stacking behavior of adjacent COF layers, we chose monomer structures containing a mono-functionalized 4-aminophenyl-diphenyl-1,3,5-benzene (MAPB) and the different linear dialdehydes used in this study, respectively. The reactions of the dialdehyde (0.1 mmol) and the MAPB (0.3 mmol) were conducted under argon in 2.5 mL of a mixture of $CHCl_3$ and 1,4-dioxane (v:v 4:1). As a reaction vessel, a 6 mL tube was sealed and placed in an oven at 100 °C for 16 h with four molecular sieve beads (2 mm, 10 mesh, 0.3 nm), respectively. The mixture was filtered and washed with anhydrous EtOH to yield amorphous powders. Finally, 5 mg of the powders was dissolved in anhydrous DMF (0.5 mL) to result in a saturated mixture. 1.0 mL of $CHCl_3$ was allowed to enter the mixture through the vapor phase. The resulting crystals were picked, measured and their structure determined under consideration of co-crystallized solvent molecules.

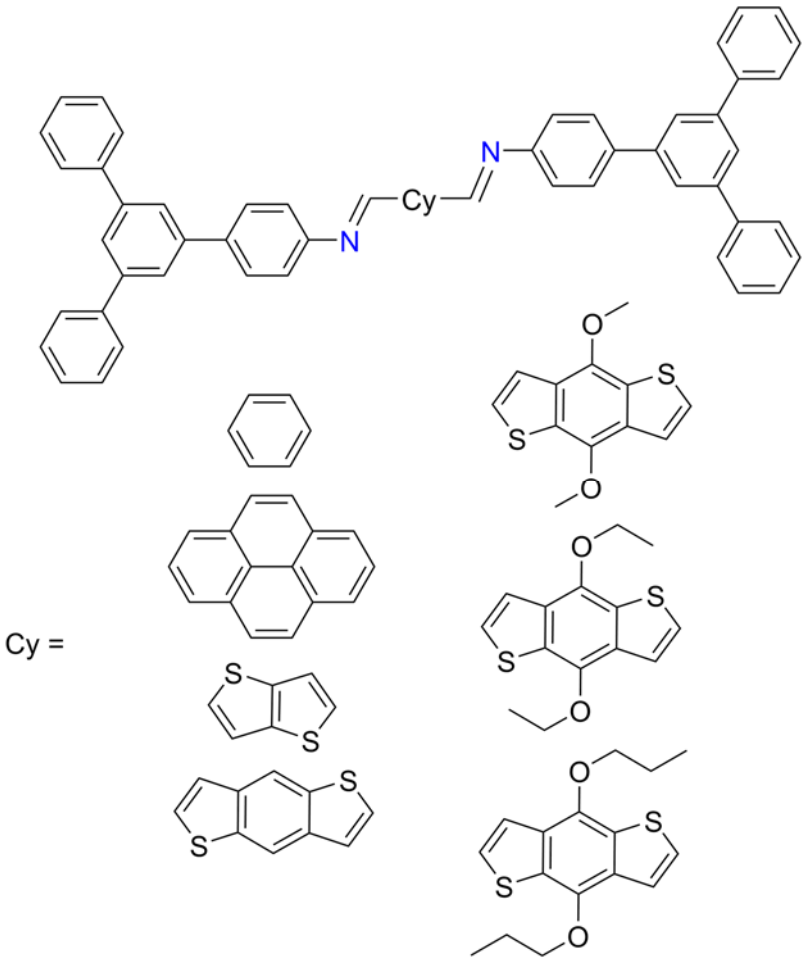


Figure S 6.23: Structures that were synthesized as monomers and grown as single crystals to obtain more insights into stacking behavior.

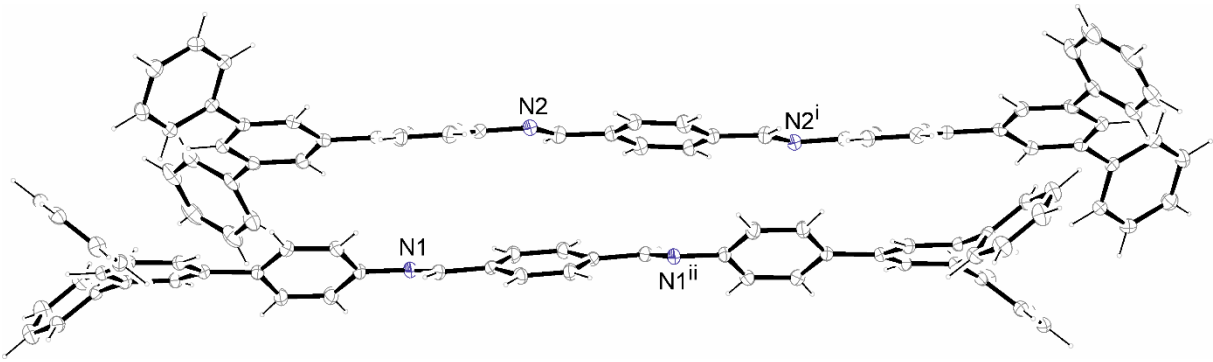


Figure S 6.24: Single crystal structure of TA MAPB.

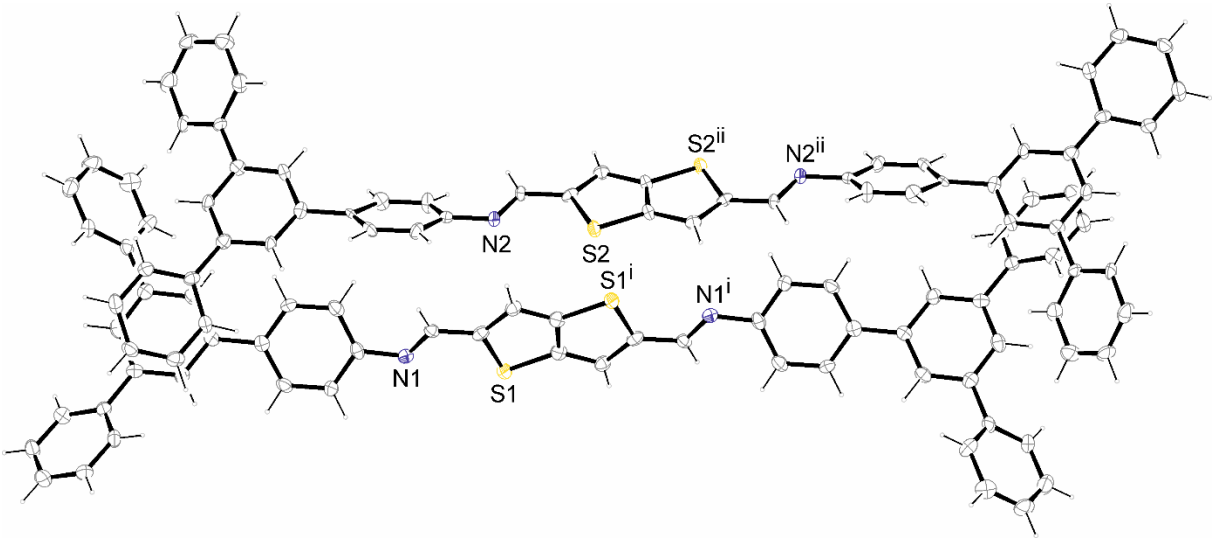


Figure S 6.25: Single crystal structure of TT MAPB.

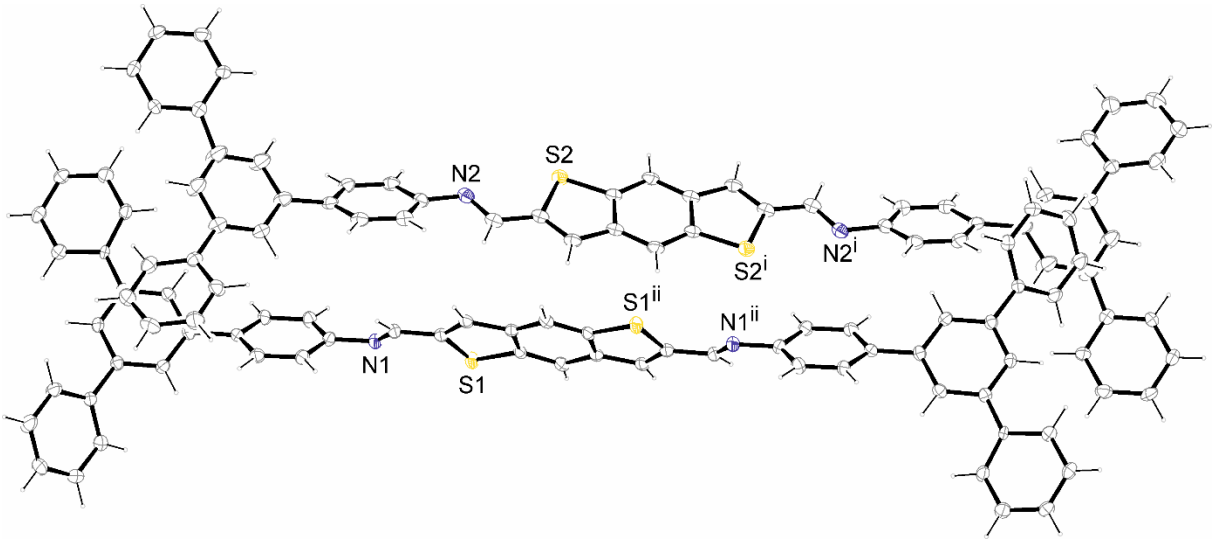


Figure S 6.26: Single crystal structure of BDT MAPB.

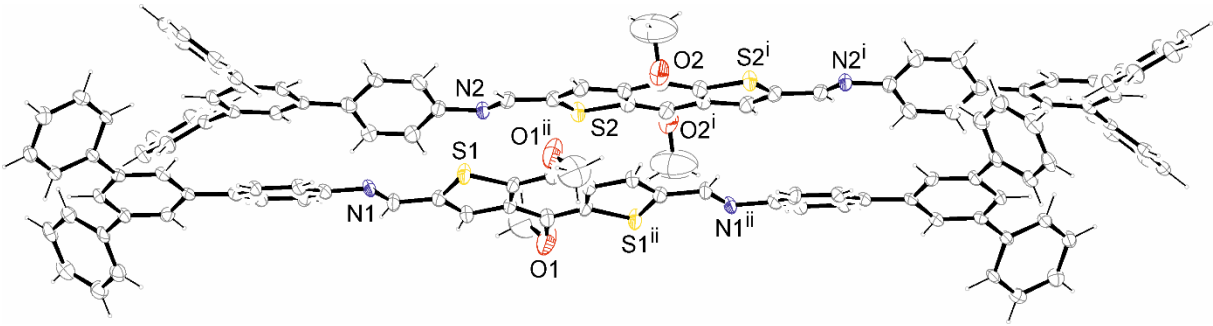


Figure S 6.27: Single crystal structure of BDT-OMe MAPB.

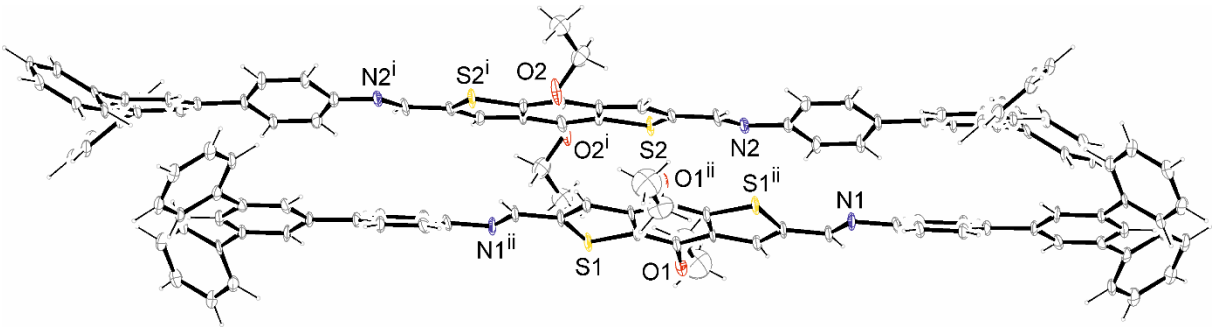


Figure S 6.28: Single crystal structure of BDT-OEt MAPB.

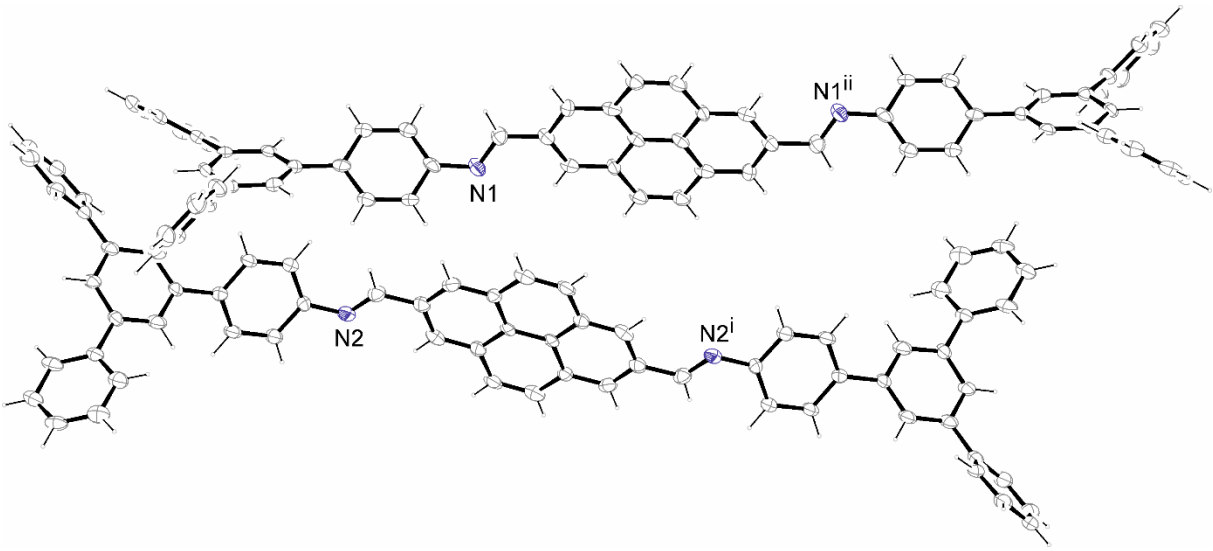


Figure S 6.29: Single crystal structure of Pyrene-2,7 MAPB.

Unfortunately, BDT-OPr MAPB did not result in single crystals that could be investigated.

The corresponding parameters are summarized in Table 6.1.

Table 6.1: Summary of the obtained single crystal data of the MAPB capped linear dialdehydes.

| | **BDT MAPB** | **BDT-OMe MAPB** | **BDT-OEt MAPB** | **Pyrene-2,7 MAPB** | **TA MAPB** | **TT MAPB** |
|---|---|---|---|---|---|---|
| **net formula** | $C_{63}H_{47}N_3OS_2$ | $C_{62}H_{44}N_2O_2S_2$ | $C_{71}H_{63}Cl_3N_4O_4S_2$ | $C_{66}H_{44}N_2$ | $C_{66.50}H_{52}N_2$ | $C_{64}H_{54}N_2O_4S_2$ |
| $M_r$**/g mol$^{-1}$** | 926.15 | 913.11 | 1206.72 | 865.03 | 879.10 | 979.21 |
| **crystal size/mm** | 0.10 × 0.03 × 0.02 | 0.10 × 0.03 × 0.03 | 0.10 × 0.02 × 0.01 | 0.100×0.020×0.010 | 0.10 × 0.04 × 0.04 | 0.10 × 0.07 × 0.05 |
| **crystal system** | triclinic | triclinic | triclinic | monoclinic | triclinic | triclinic |
| **space group** | 'P -1' | 'P -1' | 'P -1' | 'P 1 21/c 1' | 'P -1' | 'P -1' |
| ***a*/Å** | 9.4004(4) | 10.0992(5) | 10.0629(19) | 9.2607(9) | 9.9620(4) | 11.18(2) |
| ***b*/Å** | 11.0528(5) | 12.3535(6) | 12.379(3) | 55.196(5) | 13.7057(5) | 13.88(2) |
| ***c*/Å** | 24.8340(10) | 25.0363(9) | 25.104(5) | 9.7148(9) | 18.6233(7) | 16.93(3) |
| **α/°** | 85.538(2) | 85.671(2) | 86.773(7) | 90 | 89.0380(10) | 74.23(4) |
| **β/°** | 84.1100(10) | 80.923(2) | 81.159(7) | 115.707(3) | 78.2490(10) | 85.68(3) |
| **γ/°** | 65.6660(10) | 78.079(2) | 78.540(7) | 90 | 74.177(2) | 87.32(4) |
| ***V*/Å$^3$** | 2336.83(17) | 3014.9(2) | 3027.3(11) | 4474.3(7) | 2393.11(16) | 2520.(8) |
| ***Z*** | 2 | 2 | 2 | 4 | 2 | 2 |
| **calc. density/g cm$^{-3}$** | 1.316 | 1.006 | 1.324 | 1.284 | 1.220 | 1.291 |

| | | | | | | |
|---|---|---|---|---|---|---|
| **μ/mm$^{-1}$** | 0.163 | 0.127 | 0.275 | 0.074 | 0.070 | 0.159 |
| **refls. measured** | 25569 | 10869 | 33091 | 25001 | 24704 | 6655 |
| **$R_{int}$** | 0.0626 | 0.0689 | 0.1117 | 0.1366 | 0.0393 | 0.0000 |
| **mean σ($I$)/$I$** | 0.0710 | 0.1059 | 0.1296 | 0.2140 | 0.0534 | 0.0843 |
| **θ range** | 3.136–25.350 | 3.170–25.349 | 3.191–25.027 | 3.139–25.028 | 3.245–26.372 | 3.262–26.368 |
| **observed refls.** | 6017 | 6186 | 5985 | 3603 | 7128 | 5248 |
| ***x*, *y* (weight. scheme)** | 0.0492, 1.4248 | 0.1347, 0.0 | 0.1248, 1.7749 | 0.0158, 7.4624 | 0.0776, 2.5018 | 0.0072, 8.5537 |
| **refls in refinement** | 8521 | 10869 | 10528 | 7266 | 9714 | 6655 |
| **parameters** | 734 | 615 | 766 | 613 | 639 | 681 |
| **restraints** | 78 | 0 | 42 | 0 | 87 | 0 |
| **$R(F_{obs})$** | 0.0517 | 0.0739 | 0.0843 | 0.1065 | 0.0664 | 0.0777 |
| **$R_w(F^2)$** | 0.1275 | 0.2268 | 0.2439 | 0.2143 | 0.1816 | 0.1678 |
| ***S*** | 1.013 | 0.971 | 1.035 | 1.066 | 1.033 | 1.152 |
| **shift/error$_{max}$** | 0.001 | 0.001 | 0.001 | 0.001 | 0.001 | 0.001 |
| **max el. dens./e Å$^{-3}$** | 0.502 | 0.413 | 0.805 | 0.260 | 1.028 | 0.426 |
| **min el. dens./e Å$^{-3}$** | −0.324 | −0.435 | −0.729 | −0.264 | −0.601 | −0.391 |

As BDT TAPB-COF and the alkoxy-functionalized BDT TAPB-COF analogs (BDT-OMe TAPB-COF and BDT-OEt TAPB-COF) showed very different tolerance towards external stimuli, in collaboration with the group of Tim Clark, we calculated the dimerization energies of the different BDT cores only. Any other potential interactions, i.e. with solvents, were not considered for these measurements. The obtained data show, that the dimerization energies of the alkoxy-functionalized BDT-cores lie in general below those of the BDT-only core. As a result, the dimerization of BDT-alkoxy functionalized linkers might result in a stronger interaction between adjacent COF layers as well. In the case of BDT cores, it is possible that the molecules dimerize with the sulfur atoms sitting directly on top of each other or preventing a close proximity by a 180 ° flip. Our results predict, that the sulfur atoms prefer to sit directly on top of each other, which led us to the conclusion that this arrangement is possible in a stacked COF as well.

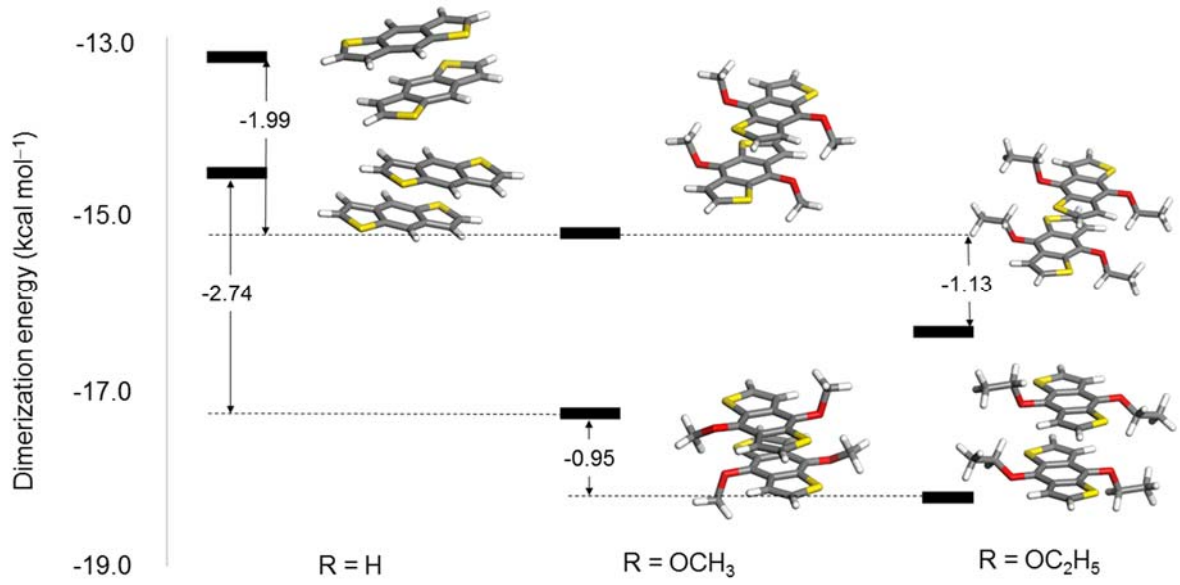


Figure S 6.30: Dimerization energies of BDT (R=H), BDT-OMe (R=$OCH_3$) and BDT-OEt (R=$OC_2H_5$). The incorporation of alkoxy side chains clearly results in a more favorable stacking.

### 6.5.6 FTIR

For infrared spectroscopy, an ATR-FTIR instrument (attenuated total reflection – Fourier transform infrared spectroscopy) was used.

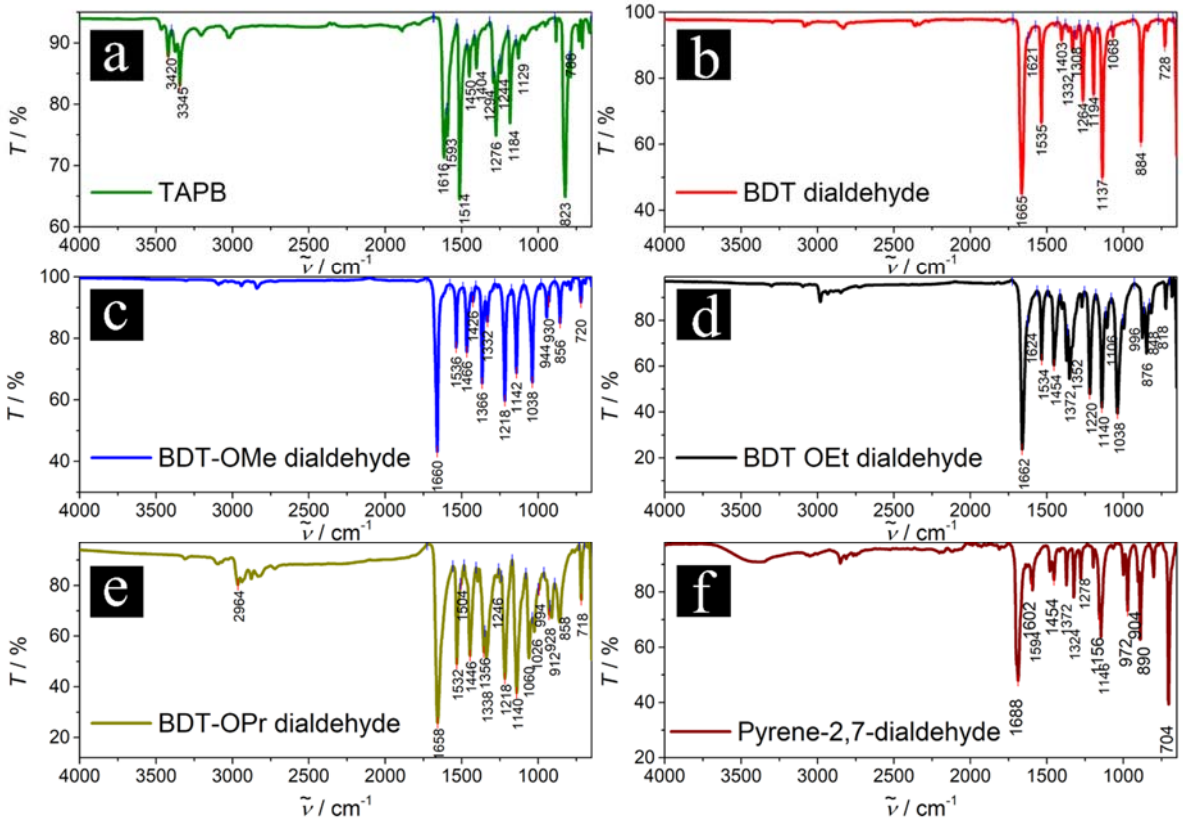


Figure S 6.31: Infrared spectra of TAPB and the synthesized starting materials for the COF reactions. a) TAPB, b) BDT dialdehyde, c) BDT-OMe dialdehyde, d) BDT-OEt dialdehyde, e) BDT-OPr dialdehyde, f) Pyrene-2,7-dialdehyde.

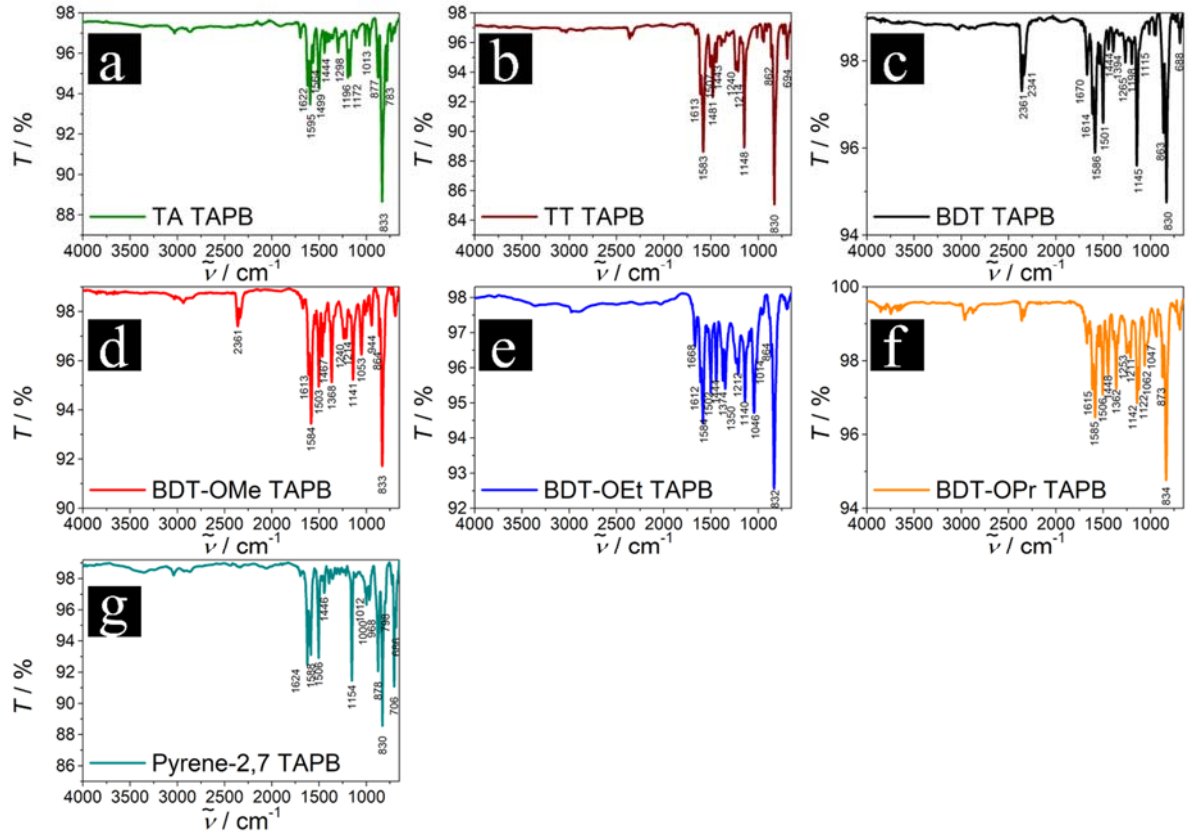


Figure S 6.32: Infrared spectra of all synthesized COF structures. a) TA TAPB-COF, b) TT TAPB-COF, c) BDT TAPB-COF, d) BDT-OMe TAPB-COF, e) BDT-OEt TAPB-COF, f) BDT-OPr TAPB-COF, g) Pyrene-2,7 TAPB-COF.

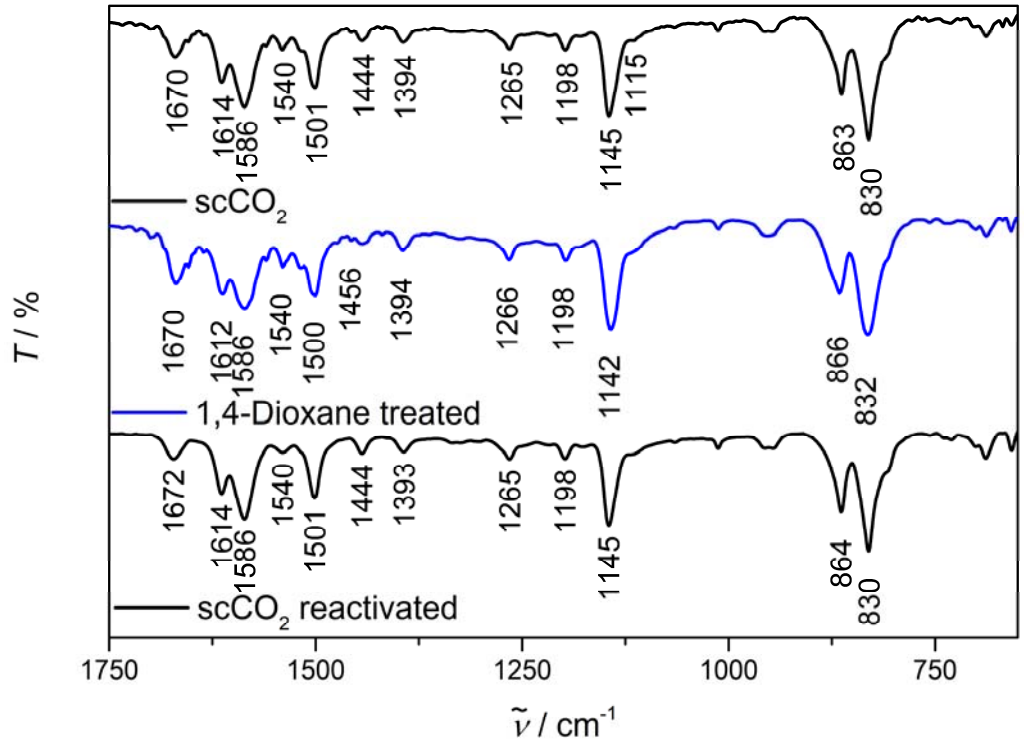


Figure S 6.33: Infrared spectra (selected region) of BDT TAPB COF, $scCO_2$ (re-)activated (crystalline, black) and 1,4-dioxane treated (amorphous, blue). There are no distinct difference between the IR spectra.

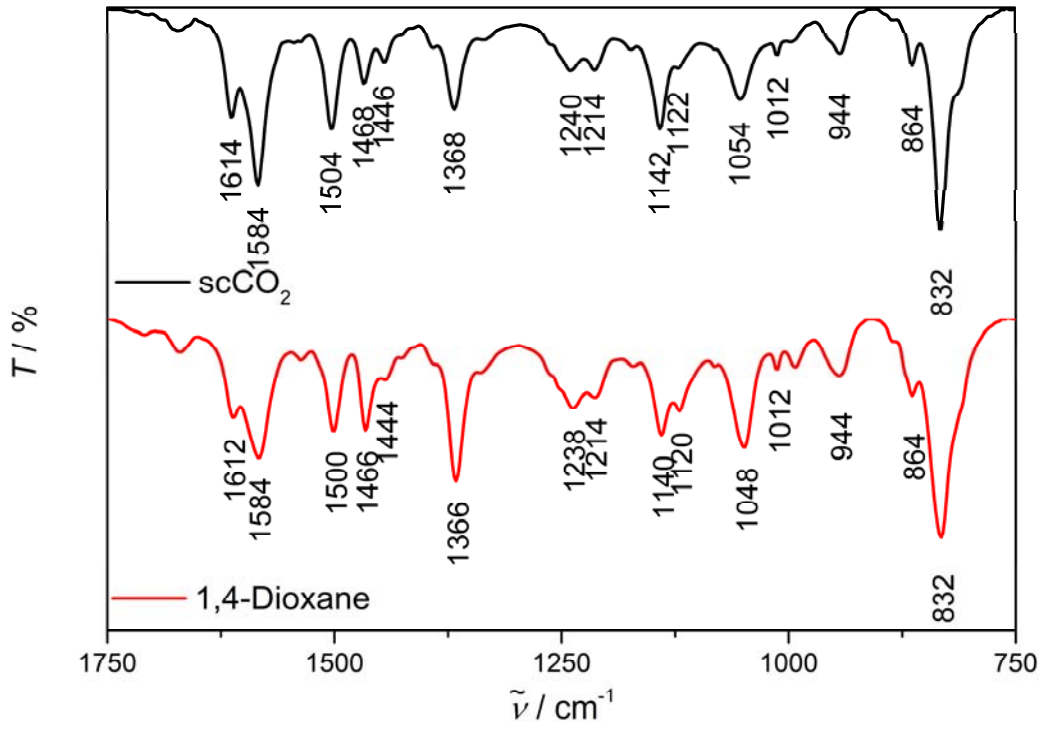


Figure S 6.34: Infrared spectra (selected region) of BDT-OMe TAPB-COFs, $scCO_2$ activated (crystalline, black) and 1,4-dioxane treated (amorphous, red). No distinct differences can be observed.

## 6.5.7 MORPHOLOGY

### 6.5.7.1 SEM

The SEM images reveal, that the frameworks consist of mixtures of spherical and rod-like structures (Figure S 6.35 and Figure S 6.36). An exception is presented by TT TAPB-COF, synthesized either in a 1,4-dioxane/mesitylene or an anisole/EtOH mixture, which consists of monodisperse, spherical particles of about 5 µm and 2 µm in size, respectively. Finally, these particles assemble/condense in superstructures (Figure S 6.35c and Figure S 6.37).

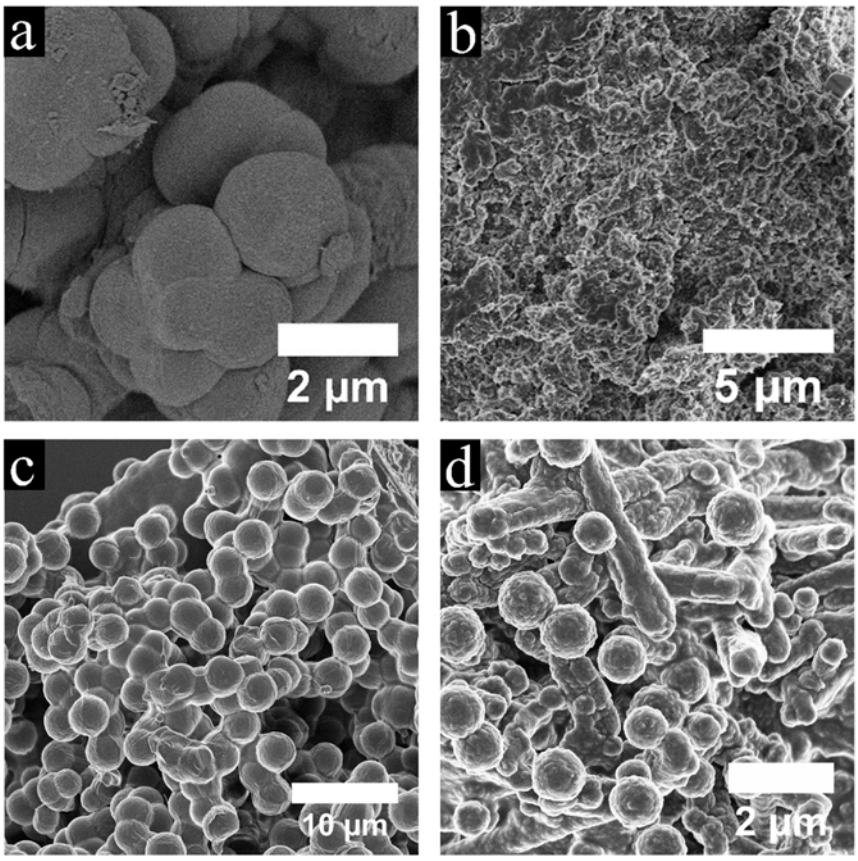


Figure S 6.35: SEM images of $scCO_2$ activated a) TA TAPB-COF, b) Pyrene-2,7 TAPB-COF, c) TT TAPB-COF and d) BDT TAPB-COF.

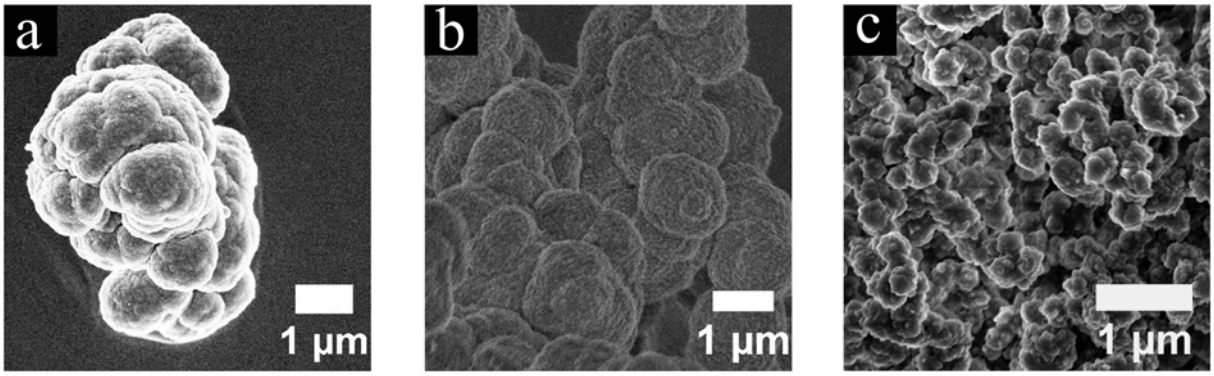


Figure S 6.36: SEM images of a) BDT-OMe TAPB-COF, b) BDT-OEt TAPB-COF and c) BDT-OPr TAPB-COF

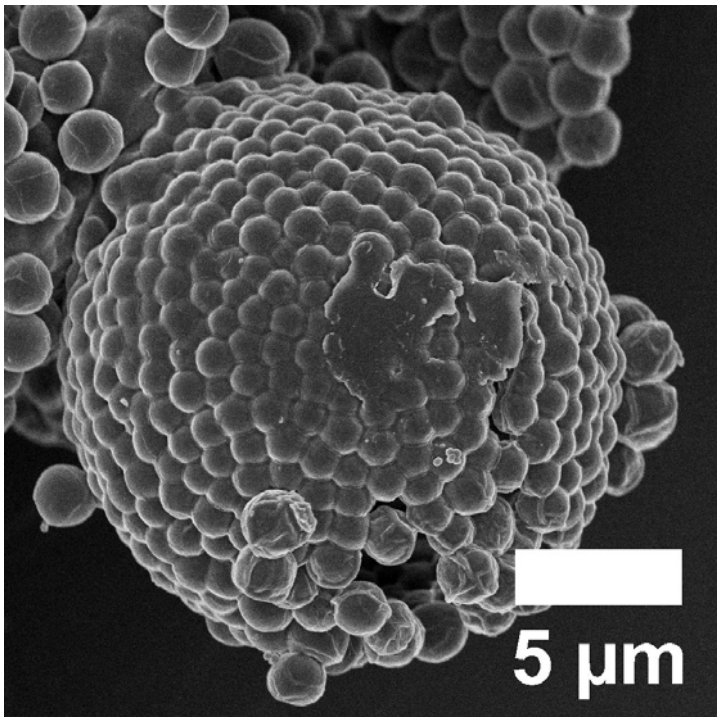


Figure S 6.37: SEM of TT TAPB-COF synthesized with a reaction mixture of anisole/EtOH from a previous report.[37] The almost monodisperse particles of 2 µm in size self-assembled to superstructures.

#### 6.5.7.2 TEM

The TEM images in Figure S 6.38 reveal highly crystalline TAPB-COFs with domain sizes ranging from about 20 to 200 nm.

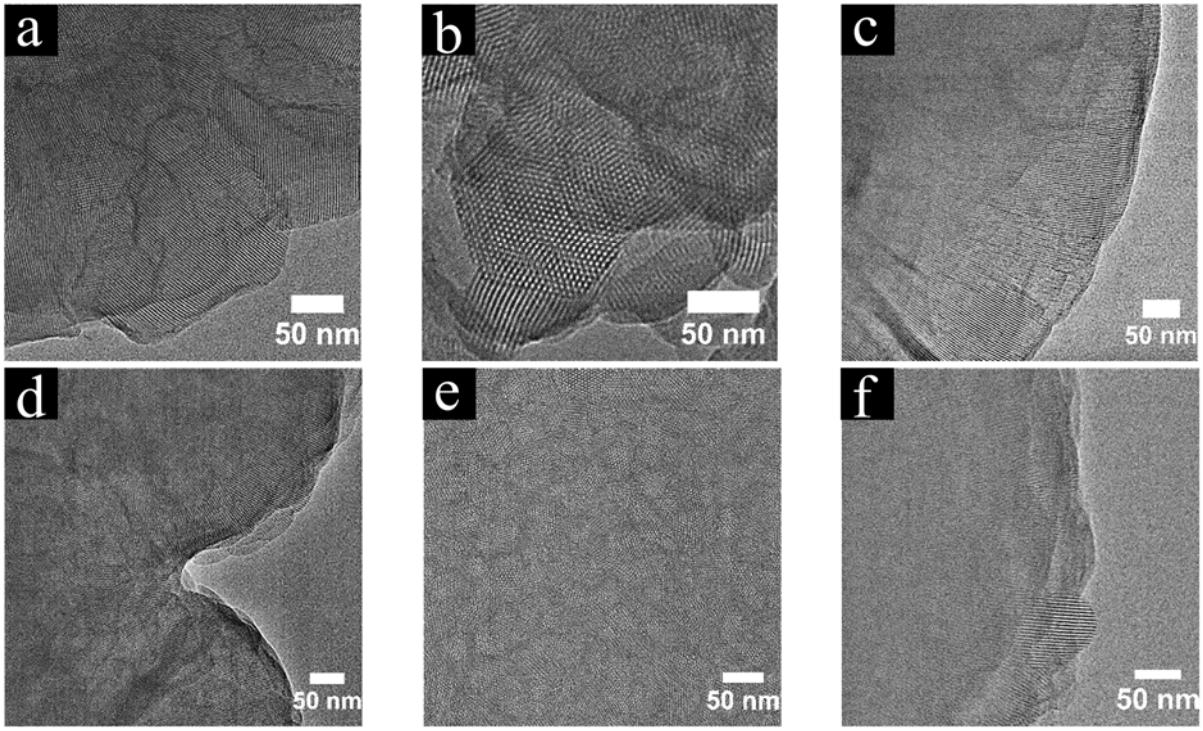


Figure S 6.38: TEM images of $scCO_2$ activated COFs a) TA TAPB, b) Pyrene-2,7 TAPB, c) TT TAPB, d) BDT TAPB, e) BDT-OMe TAPB and f) BDT-OEt TAPB.

Taking images of BDT-OPr TAPB was unfortunately not possible due to charging and detachment of sample from the grid within the TEM.

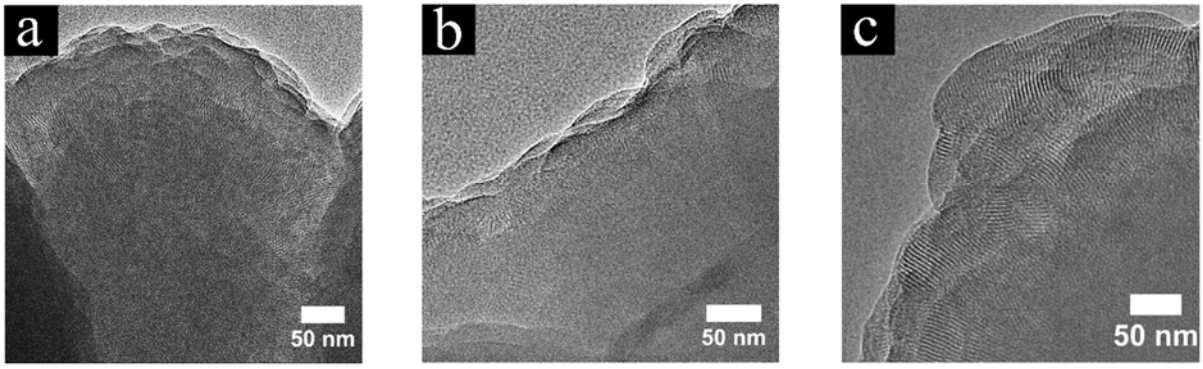


Figure S 6.39: TEM images of BDT TAPB-COF fractions after different work-up treatments, namely vacuum-drying (a), 1,4-dioxane immersion (24 h, b), and $scCO_2$ activation (c). While a) and b) only exhibit moderately crystalline and small domain sizes, the $scCO_2$ activated fraction comprises big domain sizes of up to 100 nm.

### 6.5.8 SORPTION

The nitrogen physisorption measurements reveal type IVa isotherms corresponding to mesoporous materials (Figure S 6.40 – 6.43). The pore size distributions show pore sizes between 2.6 and 5.1 nm (extreme values), depending on the length of the linear linkers. For analyzing the pore size distributions, we used a carbon QSDFT kernel for a cylindrical pore. The resulting pore size distributions show well-defined mesoporosity with a narrow distribution and a small additional micropore feature. The latter might be a result of local structure defects (Figure S 6.40).

BET surface areas, pore volumes and maxima of pore size distributions are summarized in Table 6.2.

Table 6.2: BET surface areas, pore volumes and maxima of pore size distributions of the synthesized TAPB-based COFs.

| TAPB-COF | BET surface are / $m^2g^{-1}$ | Pore volume / $cm^3g^{-1}$ | pore size maxima / nm |
|---|---|---|---|
| TA | 1070 | 0.799 | 3.32 |
| Py | 1210 | 0.808 | 4.08 |
| TT | 1860 | 0.980 | 3.68 |
| BDT | 1530 | 0.850 | 4.08 |
| BDT-OMe | 2080 | 0.979 | 3.94 |
| BDT-OEt | 1580 | 0.926 | 3.81 |
| BDT-OPr | 1290 | 0.875 | 3.68 |

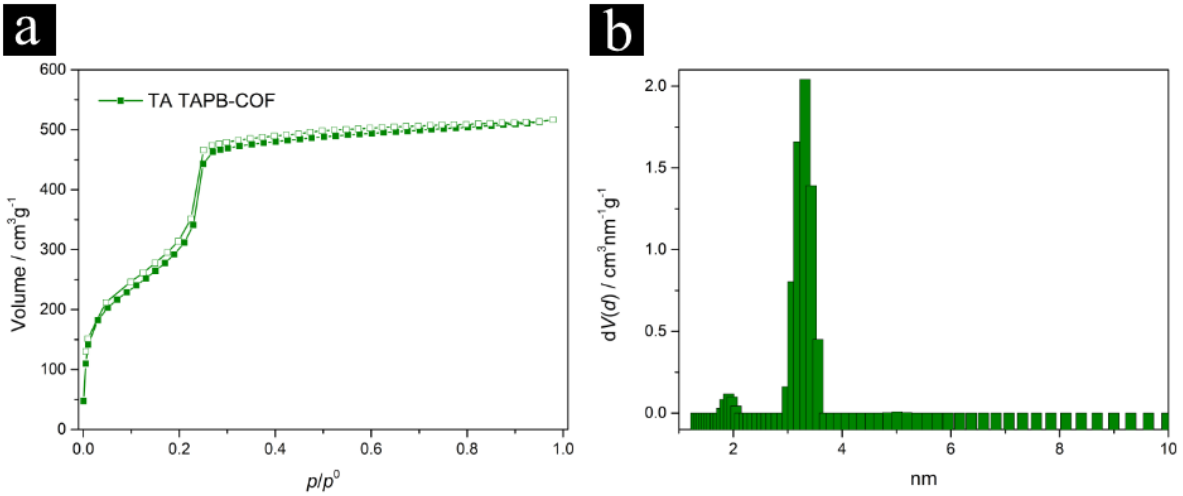


Figure S 6.40: a) Nitrogen physisorption isotherm of $scCO_2$ activated TA TAPB COF. b) Pore size distributions (PSD) of the corresponding nitrogen physisorption isotherm with a QSDFT kernel for carbon results in a narrow mesoporous PSD with a small share of microporosity.

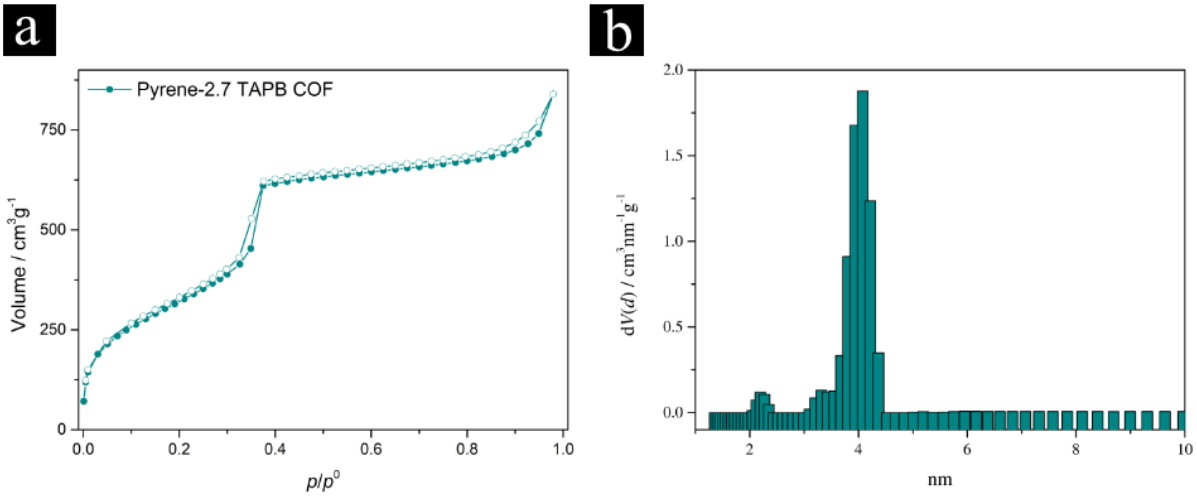


Figure S 6.41: a) Nitrogen physisorption isotherm of $scCO_2$ activated Pyrene-2,7 TAPB COF. b) Pore size distributions (PSD) of the corresponding nitrogen physisorption isotherm with a QSDFT, carbon kernel for nitrogen and a hexagonal pore arrangement.

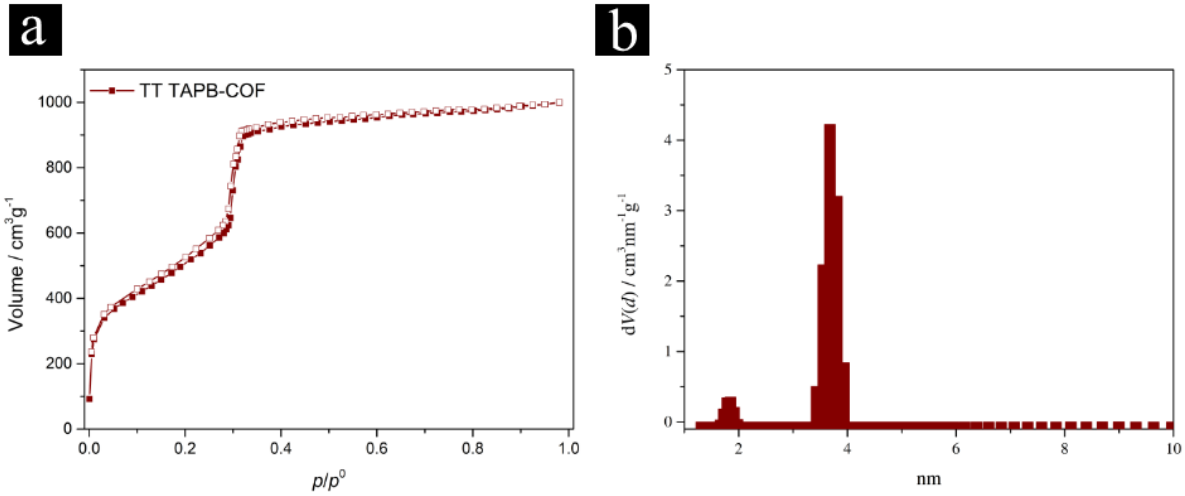


Figure S 6.42: a) Nitrogen physisorption isotherm of $scCO_2$ activated TT TAPB COF. b) Pore size distributions (PSD) of the corresponding nitrogen physisorption isotherm with a QSDFT, carbon kernel for nitrogen and a hexagonal pore arrangement.

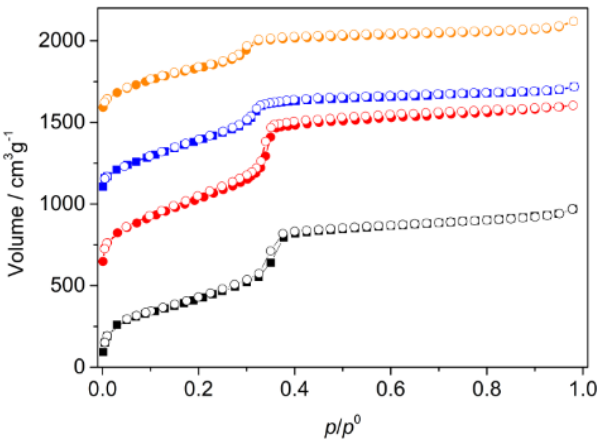


Figure S 6.43: Nitrogen physisorption isotherms of BDT-containing TAPB COFs of different side-chain length. BDT (black), BDT-OMe (red, y+500), BDT-OEt (blue, y+1000) and BDT-OPr (orange, +1500) TAPB COFs. A shift in the steep uptake for $p/p^0$ between 0.3 and 0.4 to lower relative pressures is visible and consistent with the increasing lengths of the sidechains reducing the available pore space.

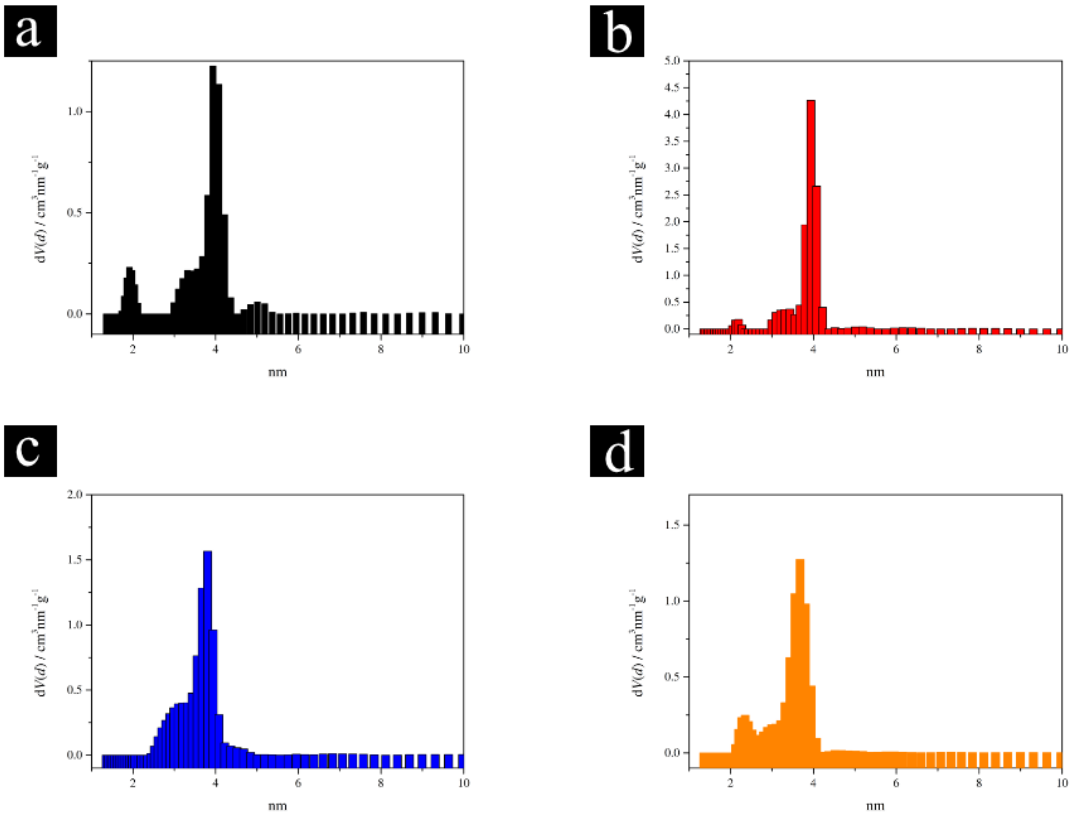


Figure S 6.44: Pore size distributions (PSD) of BDT TAPB-COF (a), BDT-OMe TAPB-COF (b), BDT-OEt TAPB-COF (c) and BDT-OPr TAPB-COF (d) for the corresponding nitrogen physisorption isotherms with a QSDFT carbon kernel for a hexagonal pore arrangement. The main pore size is reduced from BDT TAPB-COF to BDT-OPr TAPB-COF due to the into the pore pointing alkoxy groups of different lengths.

The treatment of TT TAPB-COF with toluene and of BDT TAPB-COF with ethanol resulted - after vacuum-drying - in powders of moderate crystallinity (Figure S 6.7). Nevertheless, the TT TAPB-COF was only moderately porous (BET surface area ~60 $m^2g^{-1}$), while the BDT TAPB-COF exhibited reduced porosity of 600 $m^2g^{-1}$ (calculated theoretical Connolly surface area of BDT TAPB-COF: 2448 $m^2g^{-1}$).

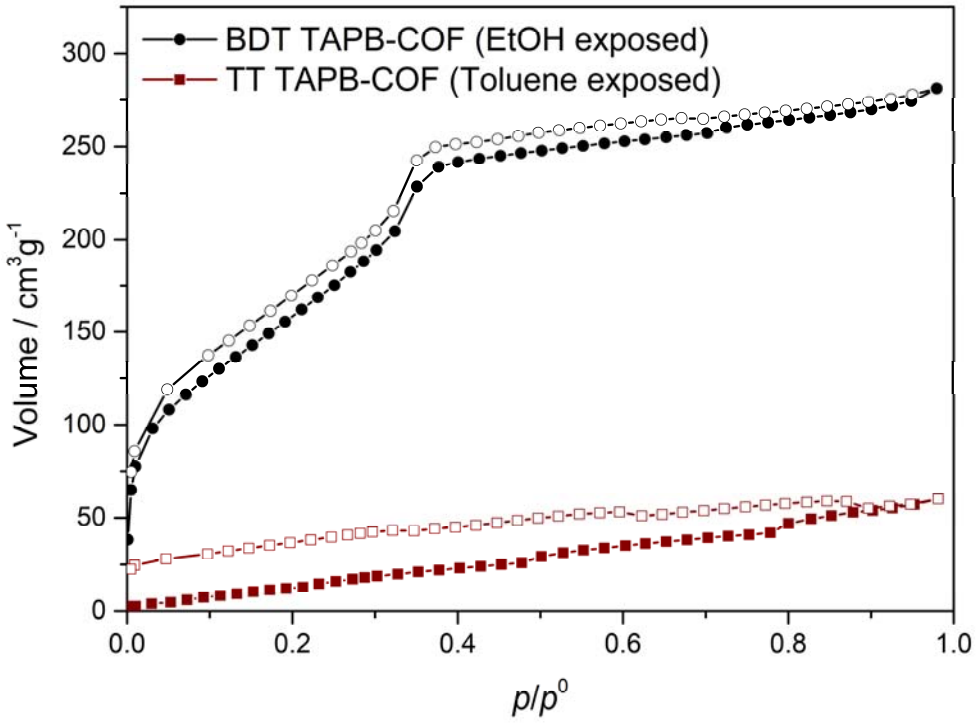


Figure S 6.45: Isotherms of $scCO_2$ activated BDT TAPB-COF and TT TAPB-COF being exposed to EtOH and toluene vapor for 24 h, respectively.

After reactivation by $scCO_2$ the BET surface areas for TT TAPB-COF and BDT TAPB-COF were 1230 $m^2g^{-1}$ and 1460 $m^2g^{-1}$, respectively.

For all COFs we were able to regain the desired state of open porosity after $scCO_2$ activation or reactivation. For the fragile COFs, a treatment with toluene resulted in non-porous polymers, while the robust COFs retained their open porosity. All TAPB-COFs lost their structural order upon treatment with 1,4-dioxane. In Table 6.3, an overview about the stage of treatment and corresponding BET surface areas of all TAPB-COFs is given.

Table 6.3: Overview of TAPB-based COFs, their treatment and the resulting BET surface areas.

| **Treatment** / **TAPB-COF** | **$scCO_2$** | **Toluene** | **1,4-Dioxane** | **$scCO_2$ reactivation** |
|---|---|---|---|---|
| | **BET surface area /$m^2g^{-1}$** | | | |
| **TA TAPB-COF** | 1070 | Non-porous | Non-porous | 1300 |
| **TT TAPB-COF** | 1410 | Non-porous | Non-porous | 1340 |
| **BDT TAPB-COF** | 1120 | Non-porous | Non-porous | 1200 |
| **BDT-OMe TAPB-COF** | 1440 | 2080 | Non-porous | 1850 |
| **BDT-OET TAPB-COF** | 1590 | 1860 | Non-porous | 1910 |
| **BDT-OPr TAPB-COF** | 1660 | 1290 | Non-porous | 1500 |
| **Pyrene-2,7 TAPB-COF** | 1180 | 1210 | Non-porous | 1280 |

### 6.5.9 IDEAL ADSORBED SOLUTION THEORY (IAST)

The IAST was calculated in collaboration with Quantachrome. IAST allows for the adsorption behavior of a binary gas mixture from (ideal) adsorption isotherms of the pure gases. The selectivity can finally be estimated without need of measuring the binary mixtures themselves. We measured isotherms of $N_2$ and $CO_2$ on a crystalline as well as on an amorphous sample of BDT TAPB-COF. The calculation of the selectivity between $N_2$ and $CO_2$ towards $CO_2$, which were conducted by Quantachrome for high pressure and low pressure adsorption, revealed, that in the amorphous case, the selectivity is about 2.7 times higher (Figure S 6.46).

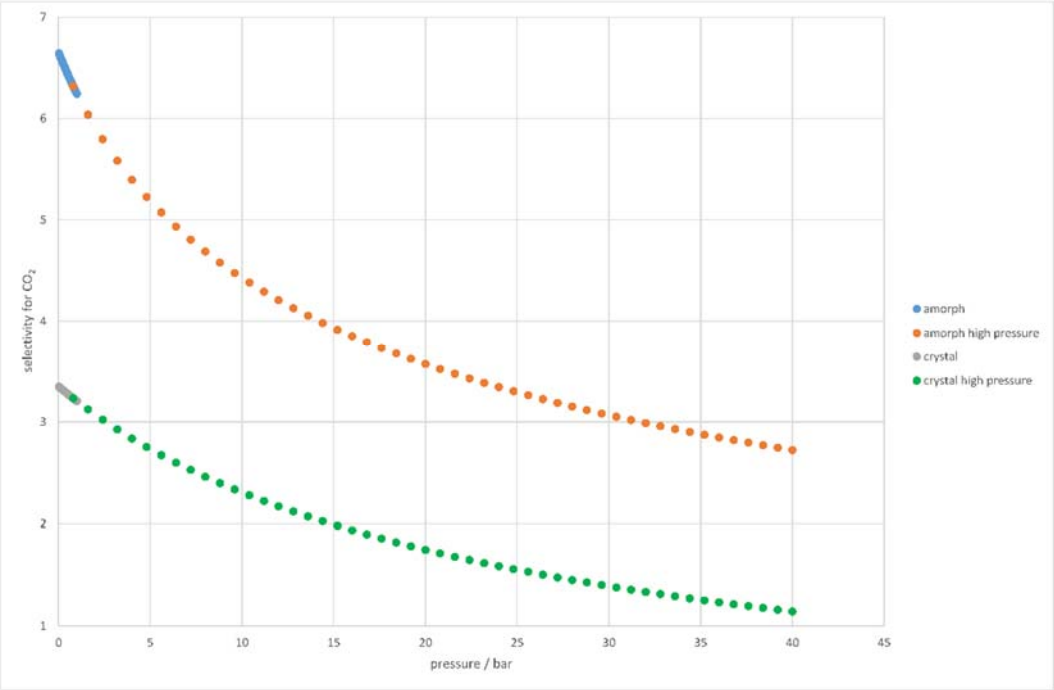


Figure S 6.46: IAST model on amorphous and crystalline BDT TAPB-COF regarding the selectivity of a gas mixture of $N_2$ and $CO_2$. The selectivity for $CO_2$ in the case of amorphous BDT TAPB-COF is 2.7 times higher than in the case of crystalline BDT TAPB-COF.

### 6.5.10 TGA

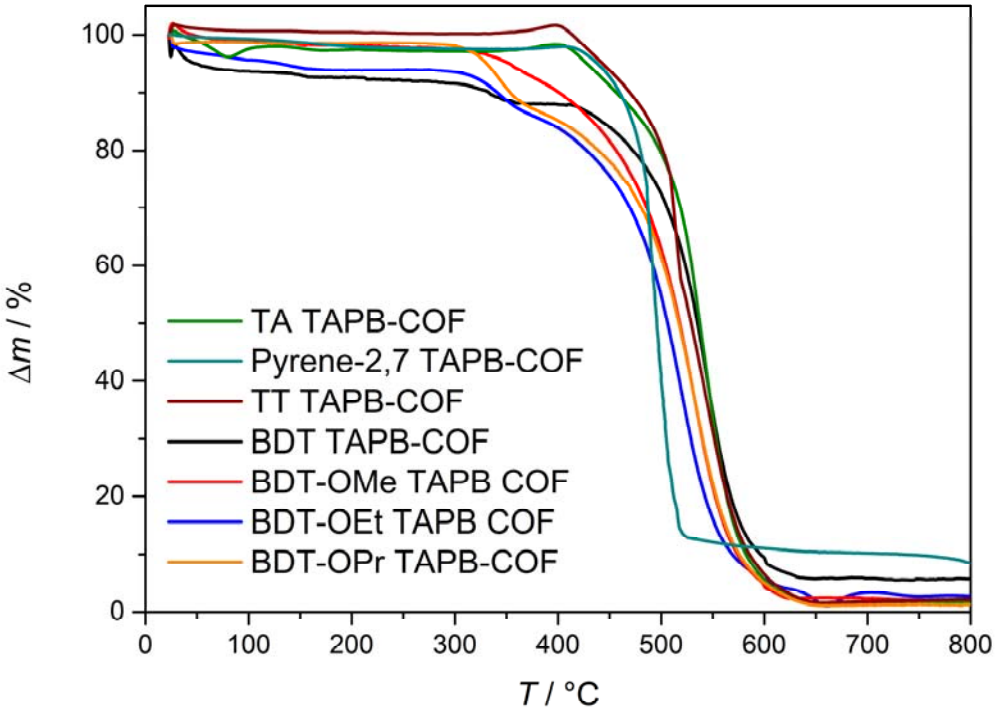


Figure S 6.47: TGA results of $scCO_2$ activated TAPB-COFs. All COFs are stable up to 300 °C under synthetic air (79.5 vol% nitrogen, 20.5 vol% oxygen). Slight variations in combustion behavior can be attributed to the chemical variation in the linear linkers.

## 6.5.11 UV-VIS SPECTROSCOPY

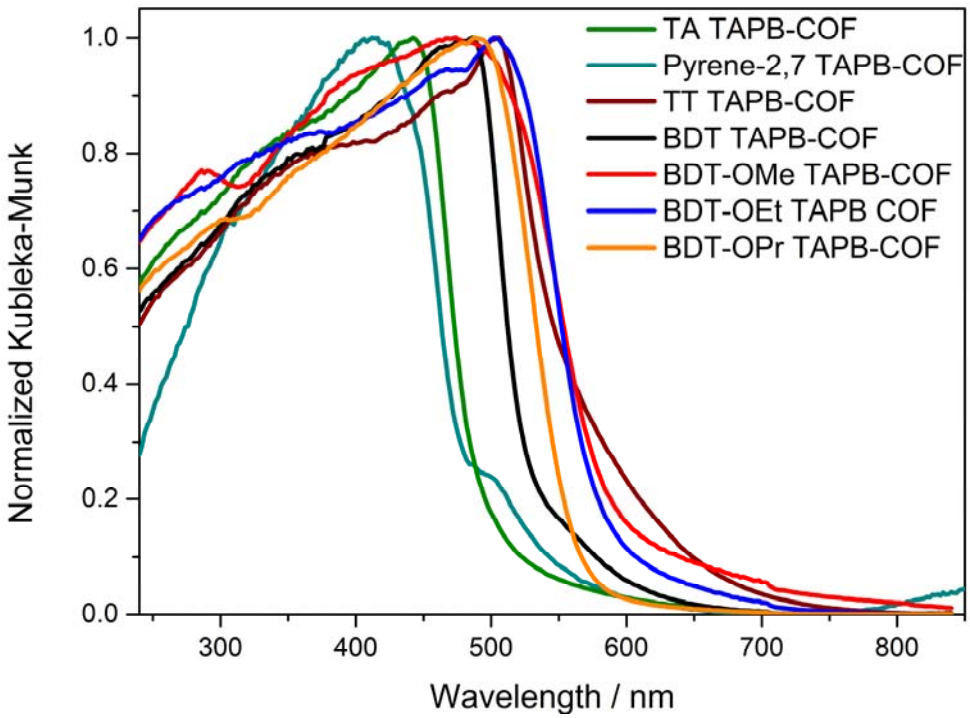


Figure S 6.48: UV-Vis absorption of the $scCO_2$ activated TAPB-COF powders in a normalized Kubelka-Munk plot shows different absorption onsets depending on the linear linker. All COFs have their absorption maximum in the visible range.

## 6.5.12 STRUCTURAL CHARACTERIZATION

$^1$H NMR spectra were recorded on Bruker AV 400 and AV 400 TR spectrometers. Proton chemical shifts are expressed in parts per million ($\delta$ scale) and are calibrated using residual undeuterated solvent peaks as an internal reference (e.g. DMSO-$d_6$: 2.50). Ultraviolet–Vis–infrared diffuse reflectance spectra (Kubelka-Munk spectrum) were recorded on a Perkin-Elmer Lambda 1050 spectrometer equipped with a 150 mm integrating sphere. Diffuse reflectance measurements of COF powders were performed with a Harrick Praying Mantis accessory and referenced to $BaSO_4$. Scanning electron microscopy (SEM) images were recorded with a Helios NanoLab G3 UC scanning electron microscope equipped with a field emission gun operated at 3-5 kV. Transmission electron microscopy (TEM) was performed on an FEI Titan Themis equipped with a field emission gun operated at 300 kV. X-ray diffraction (XRD) measurements were performed using a Bruker D8 Discover with Ni-filtered Cu K$\alpha$ radiation and a LynxEye position-sensitive detector. Experimental XRD data were analyzed with Pawley refinement to optimize the hypothetical structure. The initial structure models of the COFs were built using the Forcite module of the Accelrys Materials Studio software package. We applied the space

group with the highest possible symmetry, i.e. *P*6, considering the propeller-like conformation of the central building blocks. Using this coarse model, we determined the unit cell parameters via Pawley refinement of our PXRD data. Nitrogen sorption isotherms were recorded on a Quantachrome Autosorb 1 at 77 K within a pressure range from $p/p^0$ = 0.001 to 0.98. Prior to the measurement of the sorption isotherms the samples were heated for 24 h at 120 °C under turbo-pumped vacuum. For the evaluation of the surface area the BET model was applied between 0.05 and 0.2 $p/p^0$. Pore size distributions were calculated using the QSDFT equilibrium model with a carbon kernel for cylindrical pores. Thermogravimetric analysis (TGA) measurements were performed on a Netzsch Jupiter ST 449 C instrument equipped with a Netzsch TASC 414/4 controller. The samples were heated from room temperature to 900 °C under a synthetic air flow (25 mL $min^{-1}$) at a heating rate of 10 K/min.

### 6.5.13 NMR

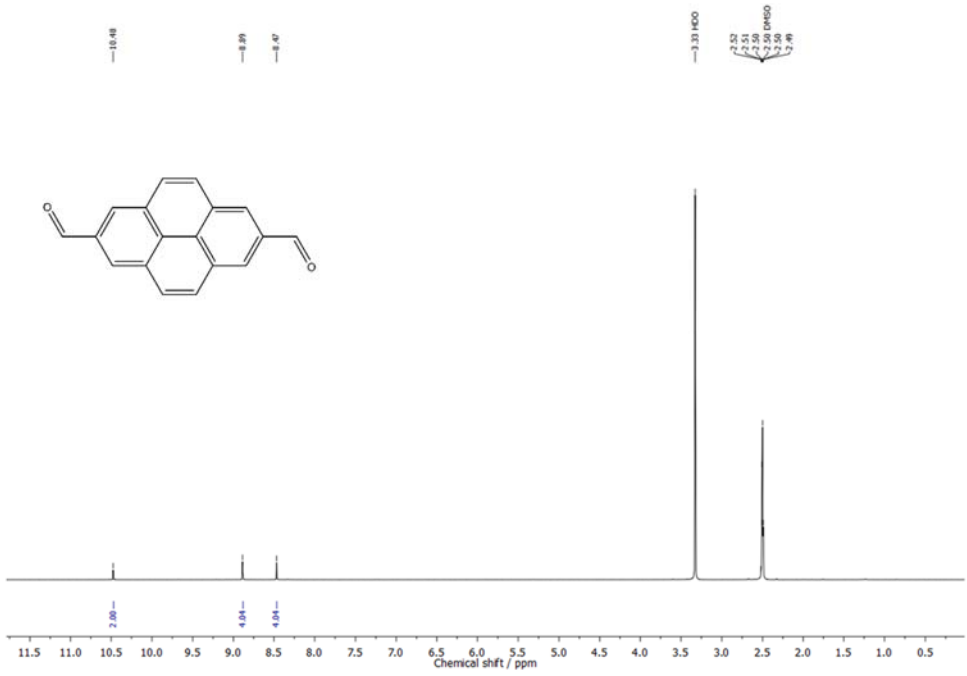


Figure S 6.49: $^1$H NMR of pyrene-2,7 dialdehyde in DMSO-d6. $^1$H NMR (DMSO-d6): 10.5 (s, 2H, SCH), 8.9 (s,4H, CH), 8.5 (s, 4H, CH).

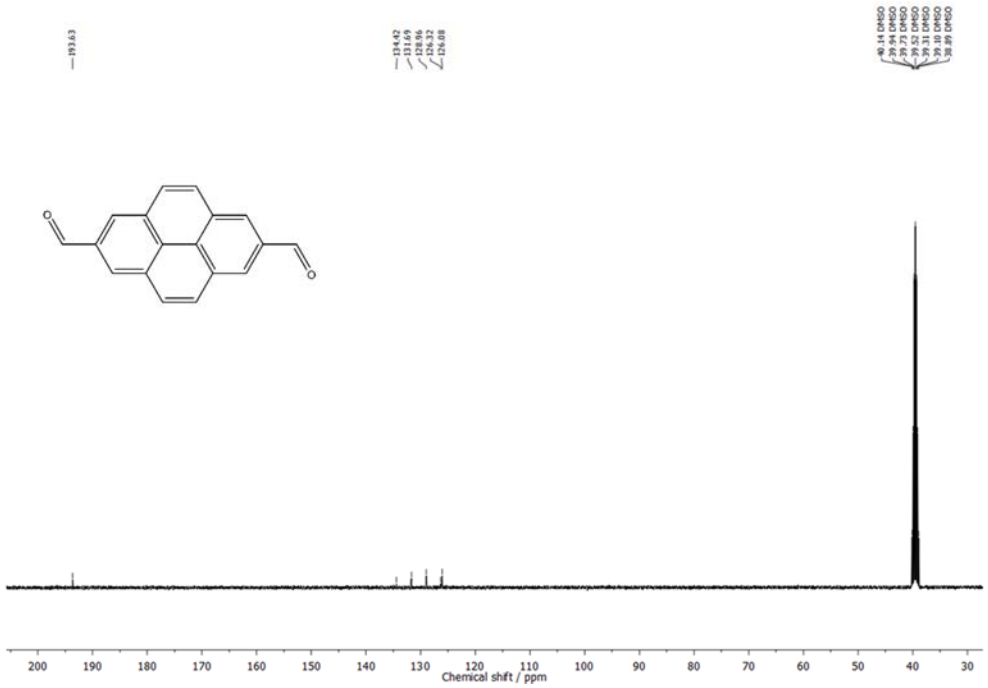


Figure S 6.50: $^{13}C$ NMR of pyrene-2,7 dialdehyde in DMSO-d6. $^{13}C$ NMR (DMSO-d6): 193.6, 134.4, 131.7, 129.0, 126.3, 126.1.

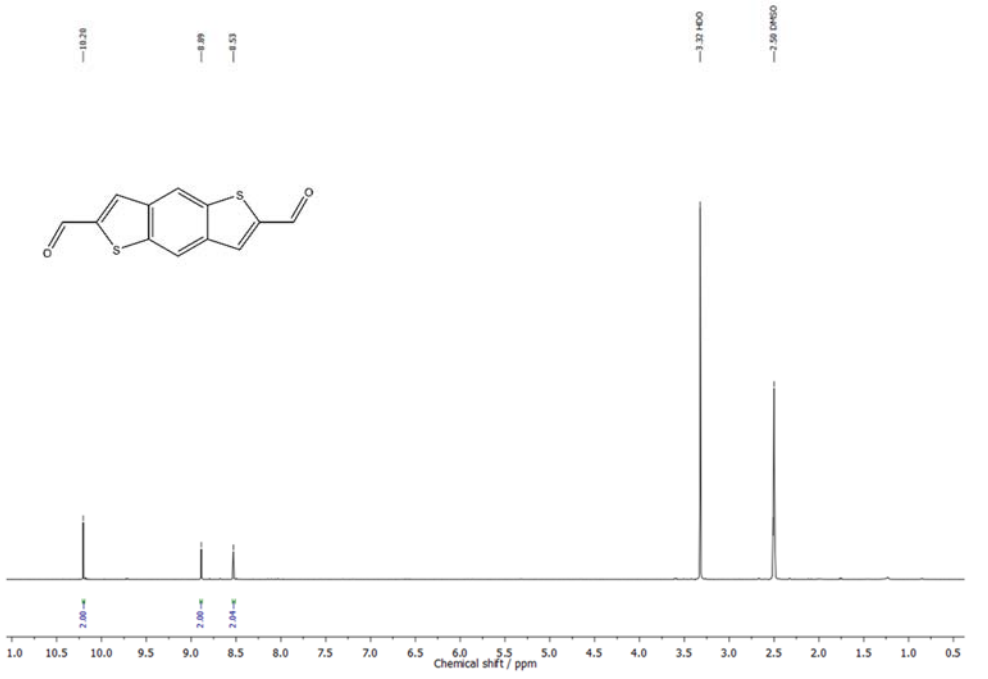


Figure S 6.51: $^{1}H$ NMR of BDT dialdehyde in DMSO-d6. $^{1}H$ NMR (DMSO-d6): 10.20 (s, 5.5 Hz 2H, SCH), 7.58 (d, 5.5 Hz 2H, CH), 4.07 (s, 6H, $OCH_3$).

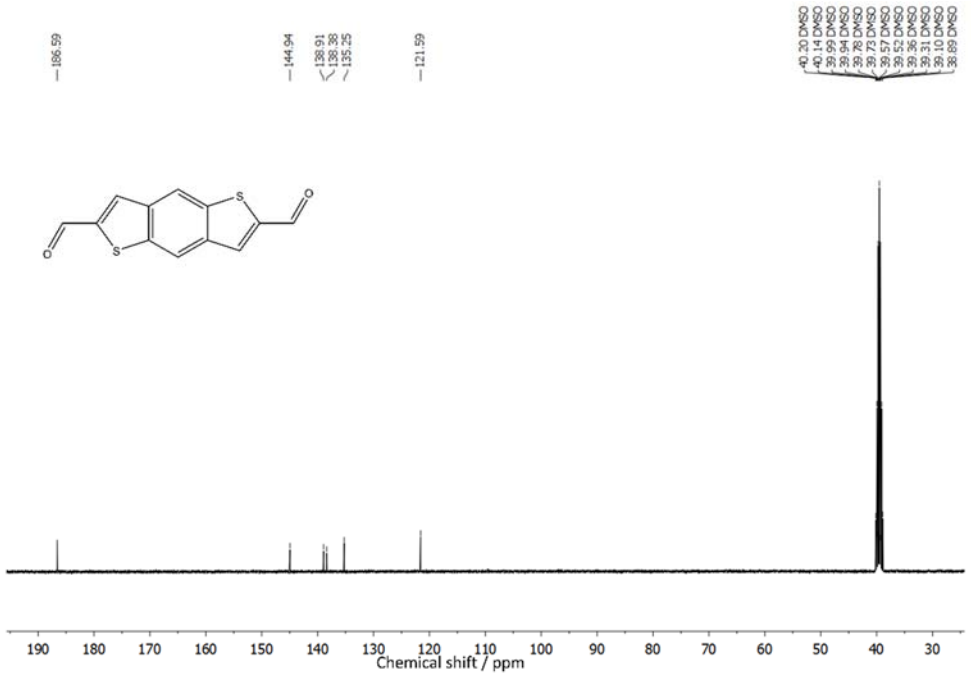


Figure S 6.52: $^{13}$C NMR of BDT dialdehyde in DMSO-d6. $^{13}$C NMR (DMSO-d6): 186.6, 144.9, 138.9, 138.4, 135.3, 121.6.

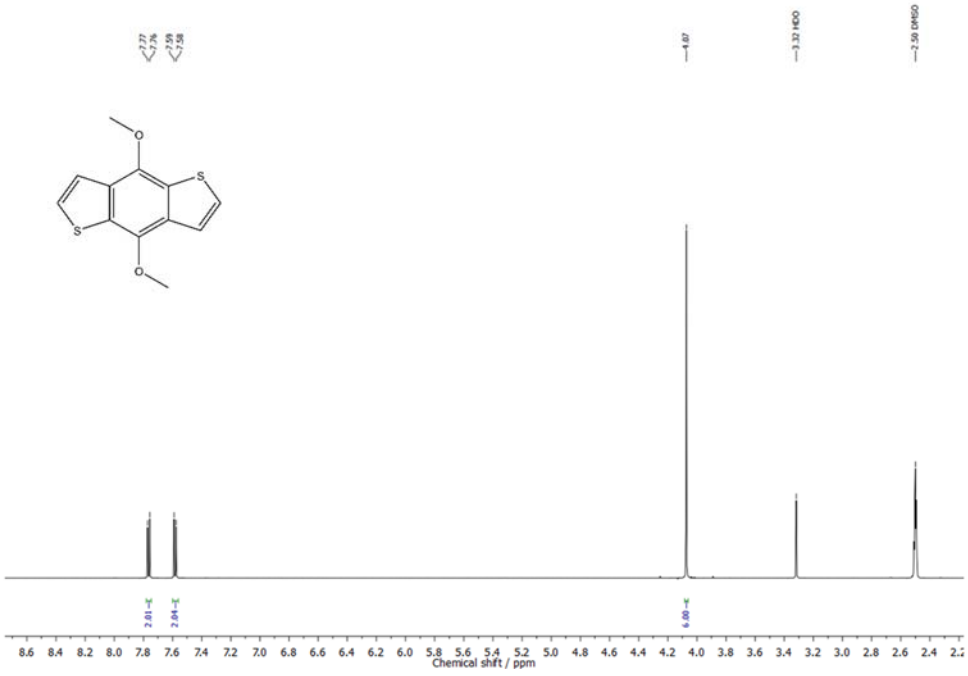


Figure S 6.53: $^{1}$H NMR of BDT-OMe in DMSO-d6. $^{1}$H NMR (DMSO-d6): 7.76 (d, 5.5 Hz 2H, SCH), 7.58 (d, 5.5 Hz 2H, CH), 4.07 (s, 6H, $OCH_3$).

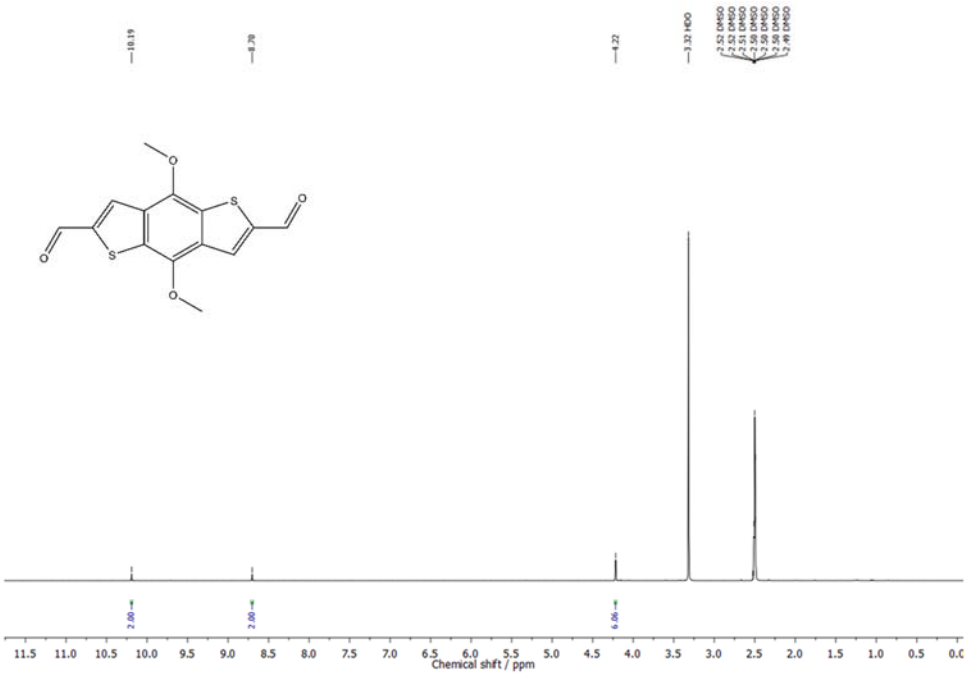


Figure S 6.54: [1]HNMR of BDT-OMe dialdehyde monomer in DMSO-d6. [1]H NMR (DMSO-d6): 10.19 (s, 2H, CHO), 8.70 (s, 2H, CH), 4.22 (s, 6H, OCH3).

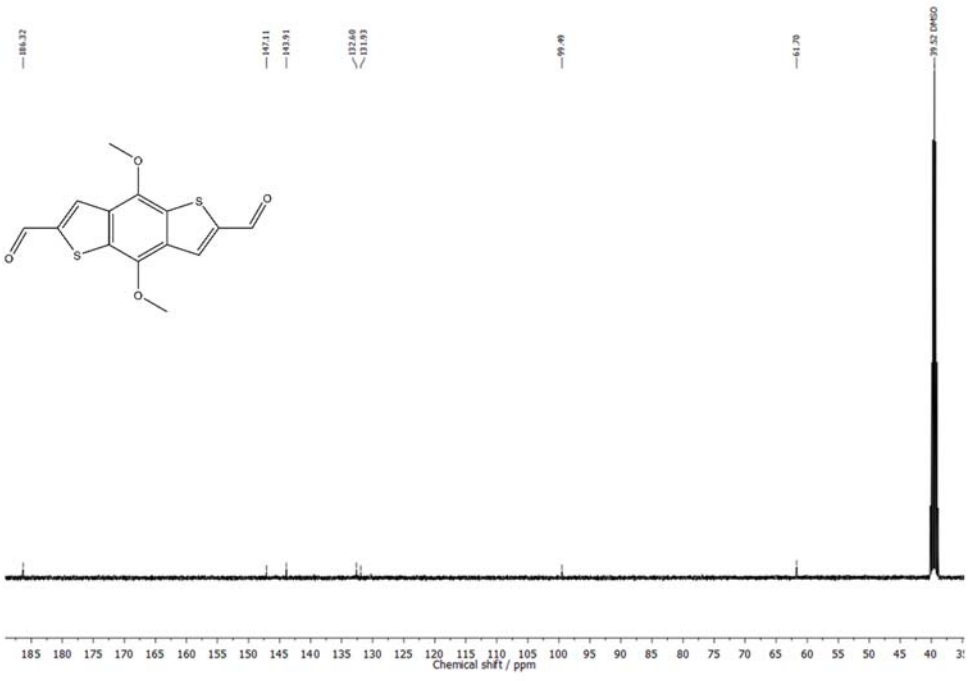


Figure S 6.55: [13]C NMR of BDT-OMe dialdehyde monomer in DMSO-d6. [13]C NMR (DMSO-d6): 186.3, 147.1, 143.9, 132.6, 131.9, 99.5, 61.7.

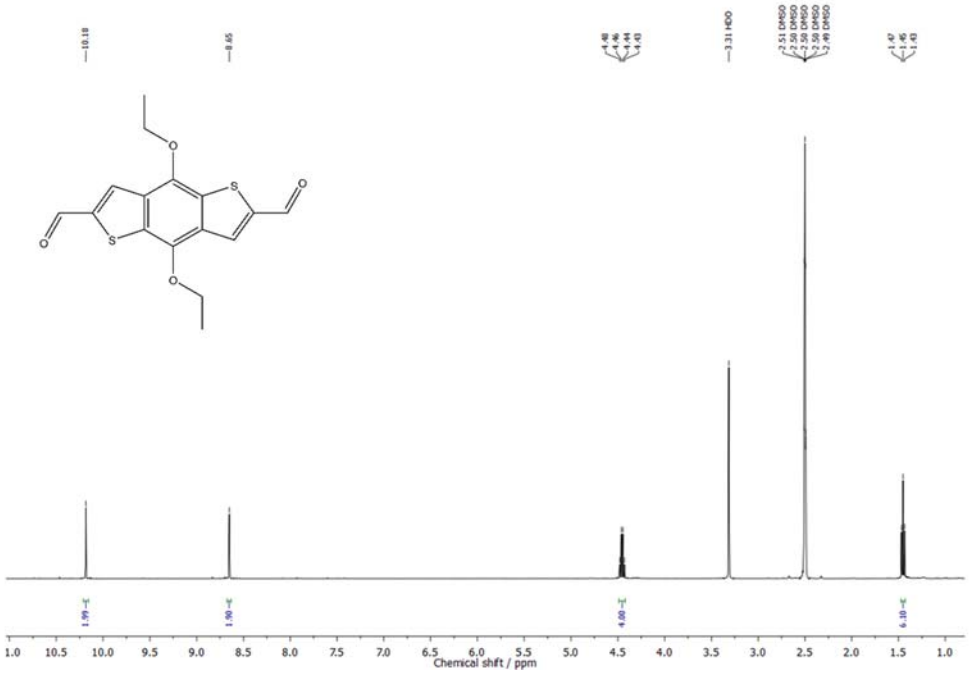


Figure S 6.56: $^{1}$HNMR of BDT-OEt dialdehyde monomer in DMSO-d6. $^{1}$H NMR (DMSO-d6): 10.18 (s, 2H, CHO), 8.65 (s, 2H, CH), 4.45 (q, J = 7.0 Hz, 4H, $OCH_2$), 1.45 (t, J = 7.0 Hz, 6H, $CH_3$).

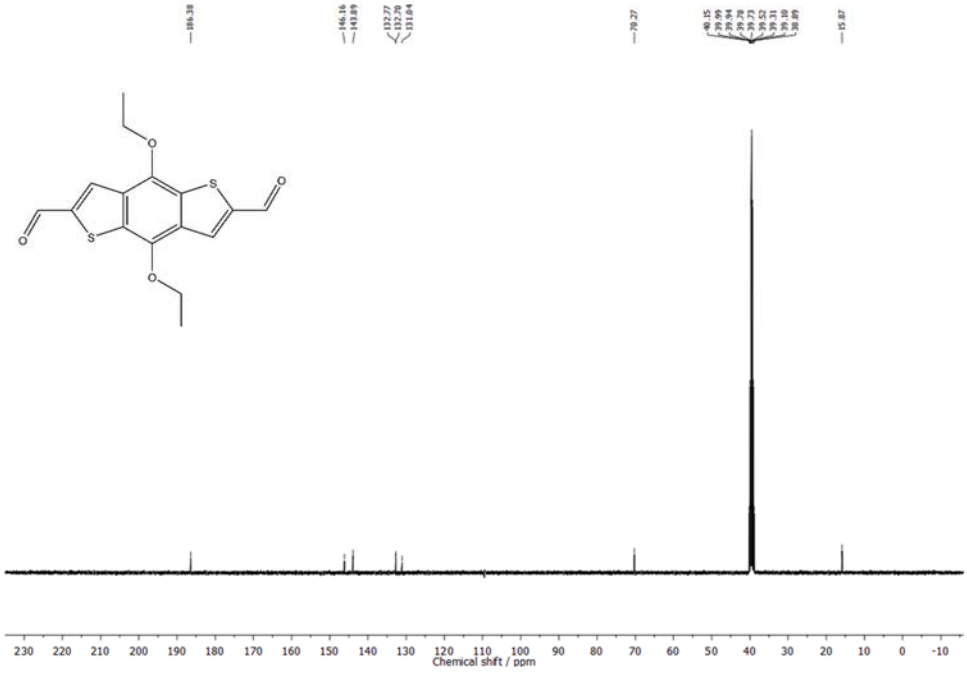


Figure S 6.57: $^{13}$C NMR of BDT-OEt dialdehyde monomer in DMSO-d6. $^{13}$C NMR (DMSO-d6): 186.4, 146.2, 143.9, 132.8, 132.7, 131.0, 70.3, 15.9.

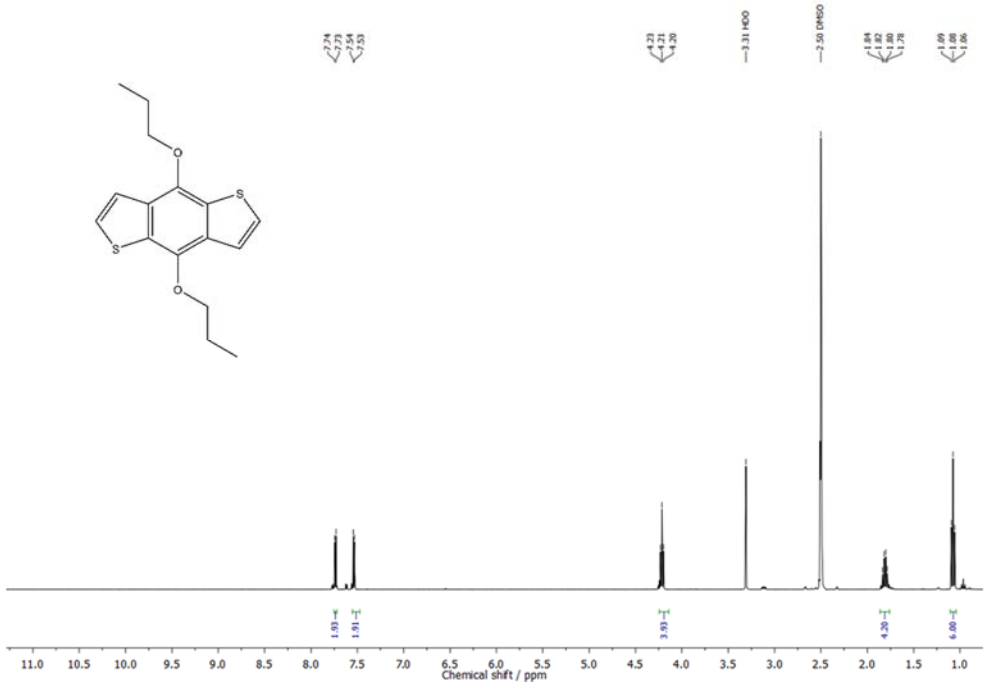


Figure S 6.58: $^{1}$H NMR of BDT-OPr in DMSO-d6. $^{1}$H NMR (400 MHz, DMSO-d6):δ [ppm] 7.74 (d, J = 5.5 Hz, 2H, SCH), 7.54 (d, J = 5.5 Hz, 2H, CH), 4.21 (t, J = 6.4 Hz, 4H, $OCH_2$), 1.86-1.78 (m, 4H, $CH_2$), 1.08 (t, 7.4 Hz, 6H, $CH_3$).

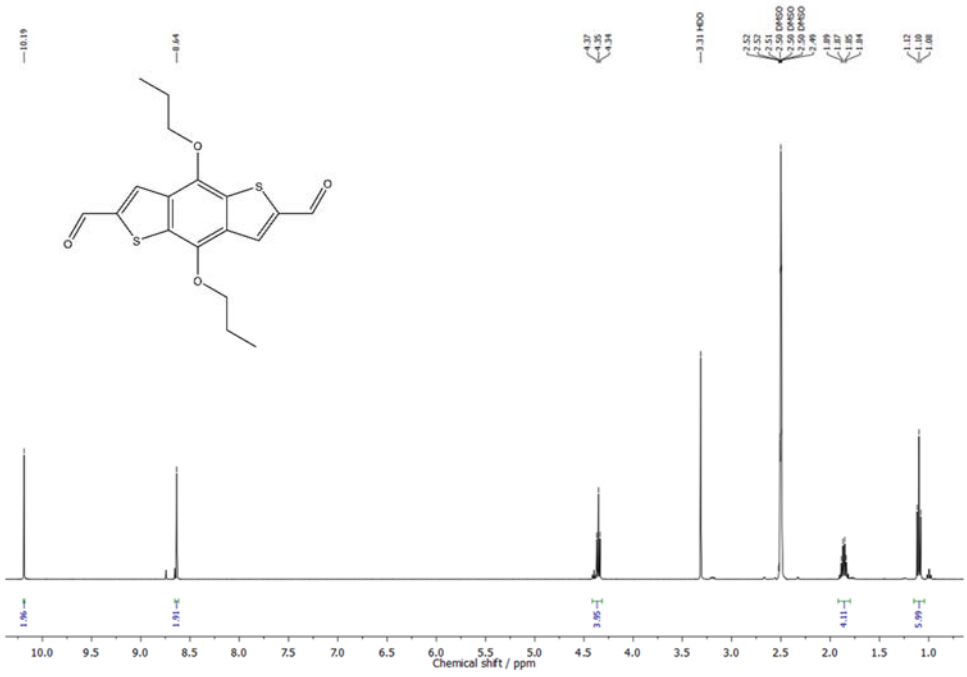


Figure S 6.59: $^{1}$HNMR of BDT-OPr dialdehyde monomer in DMSO-d6. $^{1}$H NMR (DMSO-d6): 10.19 (s, 2H, CHO), 8.64 (s, 2H, CH), 4.35 (t, *J* = 7.0 Hz, 4H, $OCH_2$), 1.86, (m, 4H, $CH_2$), 1.10 (t, *J* = 7.0 Hz, 6H, $CH_3$).

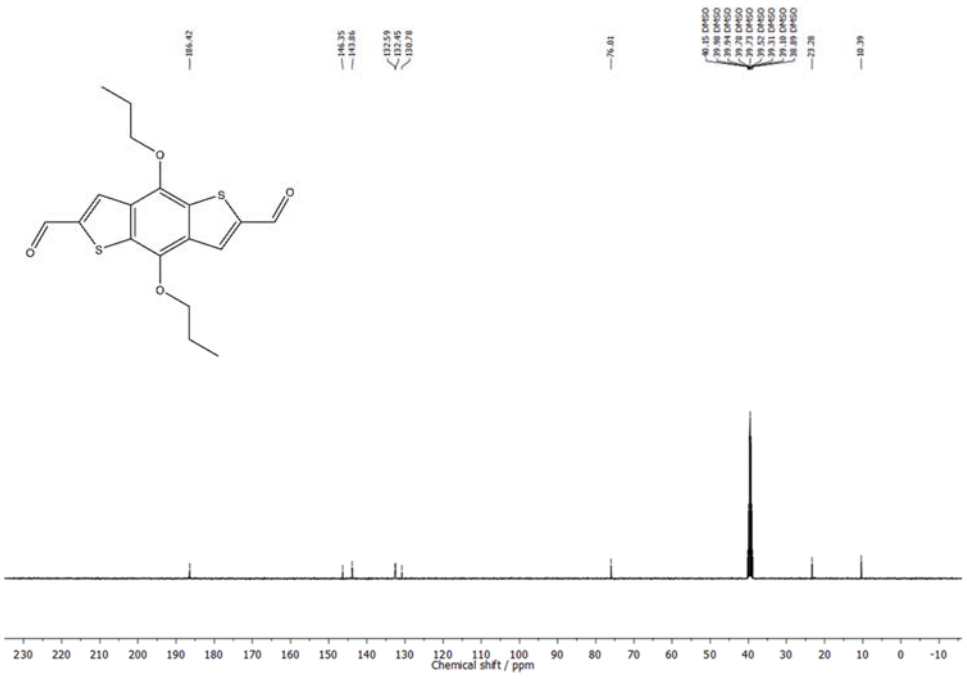


Figure S 6.60: $^{13}$C NMR of BDT-OPr dialdehyde monomer in DMSO-d6. $^{13}$C NMR (DMSO-d6): 186.4, 146.4, 143.9, 132.6, 132.5, 130.8, 76.0, 23.3, 10.4.

# 6.6 REFERENCES

(1) Cote, A. P.; Benin, A. I.; Ockwig, N. W.; O'Keeffe, M.; Matzger, A. J.; Yaghi, O. M., *Science* **2005**, *310*, 1166-1170.

(2) Yang, S.-T.; Kim, J.; Cho, H.-Y.; Kim, S.; Ahn, W.-S., *RSC Adv.* **2012**, *2*, 10179.

(3) Cote, A. P.; El-Kaderi, H. M.; Furukawa, H.; Hunt, J. R.; Yaghi, O. M., *J. Am. Chem. Soc.* **2007**, *129*, 12914-12915.

(4) Han, S. S.; Furukawa, H.; Yaghi, O. M.; Goddard, W. A., 3rd, *J. Am. Chem. Soc.* **2008**, *130*, 11580-11581.

(5) Furukawa, H.; Yaghi, O. M., *J. Am. Chem. Soc.* **2009**, *131*, 8875-8883.

(6) Dogru, M.; Sonnauer, A.; Gavryushin, A.; Knochel, P.; Bein, T., *Chem Commun (Camb)* **2011**, *47*, 1707-1709.

(7) Medina, D. D.; Sick, T.; Bein, T., *Advanced Energy Materials* **2017**, *7*, 1700387.

(8) Calik, M.; Auras, F.; Salonen, L. M.; Bader, K.; Grill, I.; Handloser, M.; Medina, D. D.; Dogru, M.; Lobermann, F.; Trauner, D.; Hartschuh, A.; Bein, T., *J. Am. Chem. Soc.* **2014**, *136*, 17802-17807.

(9) Dalapati, S.; Jin, E.; Addicoat, M.; Heine, T.; Jiang, D, *J. Am. Chem. Soc.* **2016**, *138* , 5797-5800.

(10) Uribe-Romo, F. J.; Hunt, J. R.; Furukawa, H.; Klock, C.; O'Keeffe, M.; Yaghi, O. M., *Am. Chem. Soc.* **2009**, *131*, 4570-4571.

(11) Dalapati, S.; Addicoat, M.; Jin, S.; Sakurai, T.; Gao, J.; Xu, H.; Irle, S.; Seki, S.; Jiang, D., *Nat. Commun.* **2015**, *6*, 7786-7793.

(12) Bessinger, D.; Ascherl, L.; Auras, F.; Bein, T., *J. Am. Chem. Soc.* **2017**, *139*, 12035-12042.

(13) Keller, N.; Bessinger, D.; Reuter, S.; Calik, M.; Ascherl, L.; Hanusch, F. C.; Auras, F.; Bein, T., *J. Am. Chem. Soc.* **2017**, *139*, 8194-8199.

(14) Dalapati, S.; Jin, S.; Gao, J.; Xu, Y.; Nagai, A.; Jiang, D., *J. Am. Chem. Soc.* **2013**, *135*, 17310-17313.

(15) Vyas, V. S.; Haase, F.; Stegbauer, L.; Savasci, G.; Podjaski, F.; Ochsenfeld, C.; Lotsch, B. V., *Nat. Commun.* **2015**, *6*, 8508-8516.

(16) Fang, Q.; Zhuang, Z.; Gu, S.; Kaspar, R. B.; Zheng, J.; Wang, J.; Qiu, S.; Yan, Y., *Commun* **2014**, *5*, 4503-4510.

(17) Fang, Q.; Wang, J.; Gu, S.; Kaspar, R. B.; Zhuang, Z.; Zheng, J.; Guo, H.; Qiu, S.; Yan, Y., *J. Am. Chem. Soc.* **2015**, *137*, 8352-8355.

(18) Uribe-Romo, F. J.; Doonan, C. J.; Furukawa, H.; Oisaki, K.; Yaghi, O. M., *J. Am. Chem. Soc.* **2011**, *133*, 11478-114781.

(19) Bunck, D. N.; Dichtel, W. R., *J. Am. Chem. Soc.* **2013**, *135*, 14952-14955.

(20) Stegbauer, L.; Schwinghammer, K.; Lotsch, B. V., *Chem. Sci.* **2014**, *5*, 2789-2793.

(21) Kuhn, P.; Antonietti, M.; Thomas, A., *Chem. Int. Ed. Engl.* **2008**, *47*, 3450-3453.

(22) Schwinghammer, K.; Tuffy, B.; Mesch, M. B.; Wirnhier, E.; Martineau, C.; Taulelle, F.; Schnick, W.; Senker, J.; Lotsch, B. V., *Chem. Int. Ed. Engl.* **2013**, *52*, 2435-2439.

(23) Schwinghammer, K.; Hug, S.; Mesch, M. B.; Senker, J.; Lotsch, B. V., *Energy Environ. Sci.* **2015**, *8*, 3345-3353.

(24) Kuecken, S.; Acharjya, A.; Zhi, L.; Schwarze, M.; Schomacker, R.; Thomas, A., *Chem Commun (Camb)* **2017**, *53*, 5854-5857.

(25) Huang, N.; Wang, P.; Jiang, D., *Nat. Rev. Mater.* **2016**, *1*, 16068-16094.

(26) Waller, P. J.; Lyle, S. J.; Osborn Popp, T. M.; Diercks, C. S.; Reimer, J. A.; Yaghi, O. M., *J. Am. Chem. Soc.* **2016**, *138*, 15519-15522.

(27) Campbell, N. L.; Clowes, R.; Ritchie, L. K.; Cooper, A. I., *Chem. Mater.* **2009**, *21*, 204-206.

(28) Smith, B. J.; Hwang, N.; Chavez, A. D.; Novotney, J. L.; Dichtel, W. R., *Chem Commun (Camb)* **2015**, *51*, 7532-7535.

(29) Pachfule, P.; Acharjya, A.; Roeser, J.; Langenhahn, T.; Schwarze, M.; Schomacker, R.; Thomas, A.; Schmidt, J., *J. Am. Chem. Soc.* **2018**, *140*, 1423-1427.

(30) Peng, Y.; Huang, Y.; Zhu, Y.; Chen, B.; Wang, L.; Lai, Z.; Zhang, Z.; Zhao, M.; Tan, C.; Yang, N.; Shao, F.; Han, Y.; Zhang, H., *J. Am. Chem. Soc.* **2017**, *139*, 8698-8704.

(31) Li, G.; Zhang, K.; Tsuru, T., *ACS Appl Mater Interfaces* **2017**, *9*, 8433-8436.

(32) Das, G.; Biswal, B. P.; Kandambeth, S.; Venkatesh, V.; Kaur, G.; Addicoat, M.; Heine, T.; Verma, S.; Banerjee, R., *Chem Sci* **2015**, *6*, 3931-3939.

(33) Wang, S.; Wang, Q.; Shao, P.; Han, Y.; Gao, X.; Ma, L.; Yuan, S.; Ma, X.; Zhou, J.; Feng, X.; Wang, B., *J. Am. Chem. Soc.* **2017**, *139*, 4258-4261.

(34) Chandra, S.; Kandambeth, S.; Biswal, B. P.; Lukose, B.; Kunjir, S. M.; Chaudhary, M.; Babarao, R.; Heine, T.; Banerjee, R., *J. Am. Chem. Soc.* **2013**, *135*, 17853-17861.

(35) Shinde, D. B.; Aiyappa, H. B.; Bhadra, M.; Biswal, B. P.; Wadge, P.; Kandambeth, S.; Garai, B.; Kundu, T.; Kurungot, S.; Banerjee, R., *J. Mater. Chem. A* **2016**, *4*, 2682-2690.

(36) Feldblyum, J. I.; McCreery, C. H.; Andrews, S. C.; Kurosawa, T.; Santos, E. J.; Duong, V.; Fang, L.; Ayzner, A. L.; Bao, Z., *Chem Commun (Camb)* **2015**, *51*, 13894-13897.

(37) Ascherl, L.; Sick, T.; Margraf, J. T.; Lapidus, S. H.; Calik, M.; Hettstedt, C.; Karaghiosoff, K.; Döblinger, M.; Clark, T.; Chapman, K. W.; Auras, F.; Bein, T., *Nat. Chem.* **2016**, *8*, 310-316.

(38) Auras, F.; Ascherl, L.; Hakimioun, A. H.; Margraf, J. T.; Hanusch, F. C.; Reuter, S.; Bessinger, D.; Doblinger, M.; Hettstedt, C.; Karaghiosoff, K.; Herbert, S.; Knochel, P.; Clark, T.; Bein, T., *J. Am. Chem. Soc.* **2016**, *138*, 16703-16710.

(39) Xu, H.; Gao, J.; Jiang, D., *Nat. Chem.* **2015**, *7*, 905-912.

(40) Calik, M.; Sick, T.; Dogru, M.; Doblinger, M.; Datz, S.; Budde, H.; Hartschuh, A.; Auras, F.; Bein, T., *J. Am. Chem. Soc.* **2016**, *138*, 1234-1239.

(41) Chen, X.; Addicoat, M.; Irle, S.; Nagai, A.; Jiang, D., *Am. Chem. Soc.* **2013**, *135*, 546-549.

(42) Smith, B. J.; Overholts, A. C.; Hwang, N.; Dichtel, W. R., *Chem Commun (Camb)* **2016**, *52*, 3690-3693.

(43) Romero, J.; Rodriguez-San-Miguel, D.; Ribera, A.; Mas-Ballesté, R.; Otero, T. F.; Manet, I.; Licio, F.; Abellán, G.; Zamora, F.; Coronado, E., *J. Mater. Chem. A* **2017**, *5*, 4343-4351.

(44) Rodriguez-San-Miguel, D.; Abrishamkar, A.; Navarro, J. A.; Rodriguez-Trujillo, R.; Amabilino, D. B.; Mas-Balleste, R.; Zamora, F.; Puigmarti-Luis, J., *Chem Commun (Camb)* **2016**, *52*, 9212-9215.

(45) Zhai, L.; Huang, N.; Xu, H.; Chen, Q.; Jiang, D., *Chem Commun (Camb)* **2017**, *53*, 4242-4245.

(46) Matsumoto, M.; Dasari, R. R.; Ji, W.; Feriante, C. H.; Parker, T. C.; Marder, S. R.; Dichtel, W. R., *J. Am. Chem. Soc.* **2017**, *139*, 4999-5002.

(47) Kandambeth, S.; Venkatesh, V.; Shinde, D. B.; Kumari, S.; Halder, A.; Verma, S.; Banerjee, R., *Nat. Commun.* **2015**, *6*, 6786-6795.

(48) Xu, H.; Tao, S.; Jiang, D., *Nat. Mater.* **2016**, *15*, 722-726.

(49) Shi, X.; Yao, Y.; Xu, Y.; Liu, K.; Zhu, G.; Chi, L.; Lu, G., *ACS Appl Mater Interfaces* **2017**, *9*, 7481-7488.

(50) Huang, N.; Zhai, L.; Xu, H.; Jiang, D., *J. Am. Chem. Soc.* **2017**, *139*, 2428-2434.

(51) Halder, A.; Kandambeth, S.; Biswal, B. P.; Kaur, G.; Roy, N. C.; Addicoat, M.; Salunke, J. K.; Banerjee, S.; Vanka, K.; Heine, T.; Verma, S.; Banerjee, R., *Angew. Chem. Int. Ed. Engl.* **2016**, *55*, 7806-7810.

(52) Hughes, B. K.; Braunecker, W. A.; Bobela, D. C.; Nanayakkara, S. U.; Reid, O. G.; Johnson, J. C., *J Phys Chem Lett* **2016**, *7*, 3660-3665.

(53) Cooper, A. I., *J. Mater. Chem.* **2000**, *10*, 207-234.

(54) Cooper, A. I., *Adv. Mater.* **2003**, *15*, 1049-1059.

(55) Lubguban, J. A.; Gangopadhyay, S.; Lahlouh, B.; Rajagopalan, T.; Biswas, N.; Sun, J.; Huang, D. H.; Simon, S. L.; Mallikarjunan, A.; Kim, H. C.; Hedstrom, J.; Volksen, W.; Miller, R. D.; Toney, M. F., *J. Mater. Res.* **2011**, *19*, 3224-3233.

(56) Nelson, A. P.; Farha, O. K.; Mulfort, K. L.; Hupp, J. T., *J. Am. Chem. Soc.* **2009**, *131*, 458-460.

(57) Lohe, M. R.; Rose, M.; Kaskel, S., *Chem Commun (Camb)* **2009**, 6056-6058.

(58) Lin, S.; Diercks, C. S.; Zhang, Y. B.; Kornienko, N.; Nichols, E. M.; Zhao, Y.; Paris, A. R.; Kim, D.; Yang, P.; Yaghi, O. M.; Chang, C. J., *Science* **2015**, *349*, 1208-1213.

(59) Matsuyama, K.; Tanaka, S.; Kato, T.; Okuyama, T., Muto, H.; Miyamoto, R.; Bai, H.; *J. of Supercritical Fluids*, **2017**, *130*, 140-146.

(60) Thommes, M.; Kaneko, K.; Neimark, A. V.; Olivier, J. P.; Rodriguez-Reinoso, F.; Rouquerol, J.; Sing, K. S. W., *Pure Appl. Chem.* **2015**, *87*, 929-1069.

(61) Lohse, M. S.; Rotter, J. M.; Margraf, J. T.; Werner, V.; Becker, M.; Herbert, S.; Knochel, P.; Clark, T.; Bein, T.; Medina, D. D., *CrystEngComm* **2016**, *18*, 4295-4302.

# 7. STABLE AND PHOTOACTIVE CHRYSENE-BASED DUAL PORE COVALENT ORGANIC FRAMEWORKS–CLOSING THE GAP TOWARDS PLANAR AND CONJUGATED STRUCTURES

Torben Sick, Niklas Keller, Nicolai N. Bach, Andreas Koszalkowski, Julian M. Rotter, Markus Döblinger, Dana D. Medina and Thomas Bein*

Department of Chemistry and Center for NanoScience (CeNS), University of Munich (LMU), Butenandtstraße 5-13, 81377 Munich, Germany

## 7.1 ABSTRACT

Covalent organic frameworks (COFs), consisting of covalently connected organic building units, combine attractive features such as crystallinity, open porosity and widely tunable physical properties. For potential optoelectronic applications, the incorporation of heteroatoms into a 2D COF can result in the desired optoelectronic properties, but can also lead to lateral offsets of adjacent layers. Lateral offsets directly affect and reduce the desired high degree of order and the accessibility of pores. Here we introduce dibenzo[*g*,*p*]chrysene (DBC) as a novel building block for the synthesis of 2D dual-pore COFs showing interesting properties for optoelectronic applications. The newly synthesized terephthalaldehyde (TA), biphenyl (Biph), and thienothiophene (TT) DBC-COFs combine full conjugation in the a,b-plane with a very close π-stacking of adjacent layers guided through a molecular docking site. The resulting DBC-COFs exhibit a hexagonal dual-pore kagome geometry, which is comparable to COFs containing another molecular docking site, namely 4,4′,4″,4‴-(ethylene-1,1,2,2-tetrayl)-tetraaniline (ETTA). But the respective interlayer distances decreases from about 4.60 Å in ETTA-COFs to about 3.65 Å in DBC-COFs. Furthermore, the growth of oriented, thin films of TT DBC-COF was successful on different substrates like quartz or transparent conducting oxides.

## 7.2 INTRODUCTION

Covalent organic frameworks (COF) are crystalline polymers formed by crosslinking relatively rigid and geometrically defined organic building blocks. Usually, the crosslinking is achieved through slightly reversible condensation reactions yielding linkages such as boronic esters[1] boroxines[2], imines[3], imides[4] or others.[5-7] Their high porosity and great structural tunability make them attractive candidates for applications in energy storage,[8-9] gas storage,[10-12] proton conduction,[13-15] and molecular separation.[16-17] While in 3D COFs the frameworks are covalently connected in all dimensions, in 2D COFs individual polymer layers stack in a defined manner to form molecular columns and 1D pores. This mode of layer assembly is governed by weak dispersive π-stacking interactions between adjacent layers. These crystalline and porous materials offer numerous options regarding structural design, as tailoring of the pore size, shape and molecular interface is mainly governed by the selection of the organic building units. In the context of optoelectronics, this involves the potential ability to precisely manipulate the COFs' electronic properties such as the optical absorption, charge carrier mobility[18-21] or photoluminescence.[2, 7, 22-23] The incorporation of heteroatoms within the structures enables the chemical linkage of different building blocks *via* strong chemical bonds, for example boron atoms in the case of boronic esters and boroxines or nitrogen atoms in the case of imines, imides or others. However, heteroatoms exhibit electrostatic repulsion in an eclipsed stacking of adjacent layers, which results in slight lateral offsets.[24] Especially large and polarizable heteroatoms within adjacent COF layers prefer a stacking with lateral offsets with respect to one another.[25-26] This phenomenon can result in a weak and broadened 001 reflection indicating the stacking distance of adjacent layers. Furthermore the polarization of certain chemical bonds may affect the stability of the frameworks.[27] Strategies aimed at controlling stacking interactions include the implementation of sterically demanding pyrene building units (enforcing predefined offset stacking angles)[28] or the usage of propeller- and screw-like building blocks in imine-based frameworks.[29] In the latter case, the screw-like building blocks enable molecular docking sites for adjacent molecular sheets and predefine a perfectly eclipsed stacking of adjacent layers. However, due to the steric demands of molecular docking sites such as 4,4′,4″,4‴-(ethylene-1,1,2,2-tetrayl)-tetraaniline (ETTA)[30], the stacking distance of adjacent layers of the resulting dual-pore kagome COF structure is comparably large. The enlarged stacking distance in combination with rotated building blocks acting as molecular docking sites may have an influence on the π–overlap of adjacent COF layers and on the conjugation within each layer.

Herein, we investigate the possibility to adopt the ETTA-enforced COF structure with high crystal quality while using a more rigid molecular node intended to induce closer π-stacking distances. A promising candidate for this strategy is dibenzo[*g*,*p*]chrysene DBC, as the central naphthyl unit does not allow for significant rotation of the attached phenyl rings. For this purpose, we synthesized a series of DBC-containing imine COFs with linear dialdehydes, namely terephthalaldehyde (TA), 4,4'-biphenyldicarbaldehyde (Biph) and thieno[3,2-*b*]thiophene-2,5-dicarboxaldehyde (TT).

One of the intriguing possible applications of suitable COFs is their incorporation into organic photovoltaic (OPV) devices. A first OPV device with a boronic ester-based COF serving as photo-absorbing material was reported by our group in 2013.[31] A further study on boronic ester COFs provided insights regarding the charge carrier generation and charge extraction.[32] In the latter study, oriented thin films of a triphenylene-porphyrin based COF featuring inherently integrated and aligned donor-acceptor units allowed for broad-range absorption of visible light. The COF integrated heterojunction could promote charge separation upon photoexcitation. Medina *et al.* realized hole-only devices with benzo[1,2-*b*:4,5-*b′*]dithiophene-containing boronic esters.[18] Guo *et al*. were able to demonstrate solar cells with a spin-coated phenazine-based COF.[33] Bessinger *et al.* introduced an isoindigo-based electron-deficient building block that could be modified to result in intramolecular donor-acceptor units.[34] After incorporation into an oriented COF film and infiltration with a soluble fullerene derivative, a strongly light absorbing material was realized (up to the near-infrared) with an interpenetrated heterojunction. Nevertheless COF-based optoelectronic devices are still rare[35] and further breakthroughs are anticipated in the near future.

## 7.3 RESULTS AND DISCUSSION

The DBC-based COF series was synthesized by the (slightly) reversible reaction of DBC with the respective linear dialdehydes TA, Biph, and TT to form imine-based kagome COFs. Briefly, 30 µmol of the linear dialdehyde and 15 µmol of the fourfold amine functionalized DBC (DBCA) were suspended in a mixture of benzyl alcohol and mesitylene (500 µL) in a culture tube. After the addition of 50 µL of acetic acid (6 M), the sealed tubes were kept in an oven at 120 °C for 72 h. The resulting precipitate was isolated by filtration, rinsed and finally Soxhlet extracted with anhydrous THF for 2 h. After vacuum-drying, the COF powders were examined concerning crystallinity, porosity and optoelectronic properties.

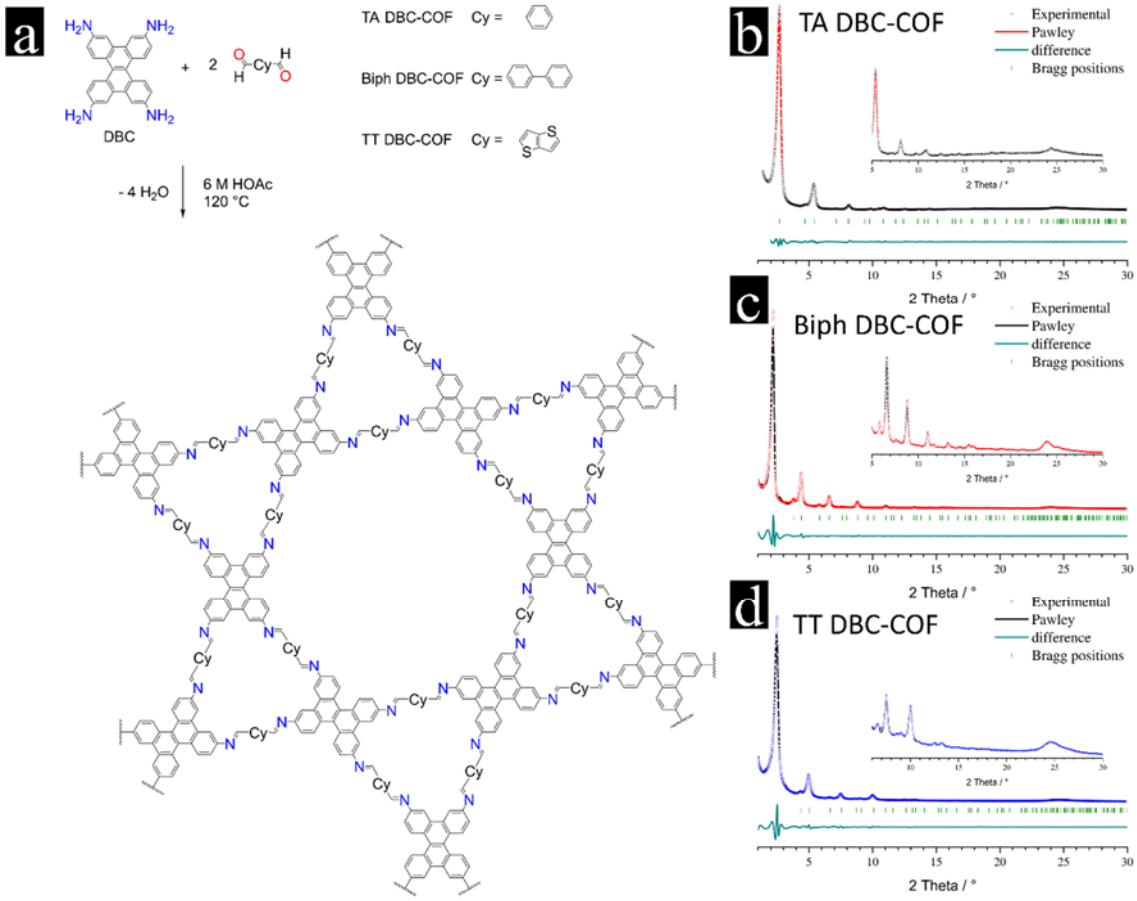


Figure 7.1: a) Structure of the DBC-containing covalent organic frameworks (schematic). b-d) PXRD patterns of the TA, Biph, and TT DBC-COFs with Pawley-refined simulations. The insets show the higher order reflections in magnification.

The investigation of the COF powders in PXRD revealed their high degree of order. Intense 100 reflections and further reflections corresponding to *hkl* 110, 200, 210, 120, 300, 220, 310, 400 and 500 (indexed in space group *P*6) indicate the excellent crystallinity (Figure 7.1). The

001 reflections at around 23.9 °2θ (*d*-spacing of about 4.65 Å) correspond to the distance of adjacent layers which directly indicates the $\pi$-stacking distance.

Nitrogen physisorption isotherms of the COFs exhibit a mixture of type I and type IVb isotherm shapes, being indicative of the expected hierarchically nanoporous systems featuring micro- and small mesopores (< 5 nm).[36] Pore size distributions based on carbon with a QSDFT kernel for cylindrical pores show excellent agreement with the structurally modelled pore sizes (Figure S 7.6 – 7.8). For DFT-calculated pore sizes were 1.50 nm and 2.89 nm (simulated 1.5 nm and 2.9 nm), 1.73 nm and 3.68 nm (simulated 1.7 nm and 3.7 nm) and 1.45 nm and 3.10 nm (simulated 1.5 nm and 3.1 nm) for TA DBC-COF, Biph DBC-COF, and TT DBC-COF, respectively. The BET surface areas and pore volumes of 2050 $m^2g^{-1}$ and 1.23 $cm^3g^{-1}$ (TA DBC-COF), 2170 $m^2g^{-1}$ and 1.39 $cm^3g^{-1}$ (Biph DBC-COF) as well as 1230 $m^2g^{-1}$ and 0.67 $cm^3g^{-1}$ (TT DBC-COF) can be compared to predicted accessible Connolly surface areas and pore volumes of 2090 $m^2g^{-1}$ and 0.90 $cm^3g^{-1}$ (TA DBC-COF), 2490 $m^2g^{-1}$ and 1.31 $cm^3g^{-1}$ (Biph DBC-COF) and 2260 $m^2g^{-1}$ and 1.12 $cm^3g^{-1}$ (TT DBC-COF). The accessible BET surface areas and pore volumes might be enlarged by further extraction, i.e. other solvents or supercritical fluids.

In comparison to our previously reported ETTA systems with the same linear dialdehydes, namely TA, Biph, and TT, the layer stacking distances derived from PXRD data are shifted from about 19.5 °2θ to 23.9 °2θ, corresponding to stacking distances of about 4.60 Å (for TA ETTA-COF, Biph ETTA-COF, and TT ETTA-COF)[29] to much decreased values of 3.65 Å (TA DBC-COF), 3.70 Å (Biph DBC-COF) and 3.60 Å (TT DBC-COF). This drastically decreased stacking distance (by almost 1.0 Å!) for each DBC-containing COF in comparison to ETTA-analogs is attributed to the more planar structure of the chrysene building block compared to the more sterically demanding ETTA. The influence of the linear dialdehyde on the stacking distance is apparently less dominant, though being still detectable.

Single crystal structures of the core elements of the different 4-connected COF building blocks, i.e., 1,1',2,2'-tetraphenylethylene and DBC, clearly indicate the influence on the angles and steric hindrances of the differently linked aromatic groups (Figure S 7.9). By using DBC motifs, the ETTA topology and connectivity in the COF is maintained, but the incorporation of a central naphthyl unit compared to an ethylene unit in ETTA strongly reduces the torsion/rotation of the attached aromatic groups. As a result, in 1,1',2,2'-tetraphenylethylene, an average dihedral angle of 47.3°[37] can be detected, while in DBC the average angle reduces to 24.7°[38]. The angles were calculated for the central double bond regarding the trans-arranged carbon atoms within

the aromatic group carrying a hydrogen atom (Figure S 7.9). Thereby, the resulting π-stacking distance between adjacent COF layers will be reduced, enabling potentially larger π-π-interactions.

Morphological investigations of the three new DBC COFs using scanning and transmission electron microscopy (SEM and TEM) revealed hexagonally shaped crystallites of different sizes, ranging from 10 to 150 nm (Figure S 7.1 and Figure S 7.2).

The optoelectronic properties of the new DBC COFs were investigated with UV-Vis, photoluminescence (PL) and time correlated single photon counting (TCSPC) spectroscopies. The influence of the respective linear building block on the optical absorption can be clearly seen in the Kubelka-Munk plots (Figure S 7.13). While the phenyl-based linear linkers TA and Biph exhibit comparable absorption features and comparable absorption onsets at around 550 to 580 nm, the incorporation of the thiophene-based TT shifts the steep onset to longer wavelengths at around 650 nm. Consequently, the TT DBC-COF exhibits a comparably small band gap, which was calculated from the Tauc plot. For our material we expect a direct optical band gap, which was calculated from the Tauc plot of the corresponding Kubelka-Munk plot to be 2.05 eV. In comparison, the direct optical band gaps of TA DBC-COF and Biph DBC-COF were calculated to be 2.29 eV and 2.38 eV (Figure S 7.13), respectively.

To use TT DBC-COF in optoelectronic devices, the COF must be grown as uniformly thick and oriented film. Successful film growth is essential for different applications such as photovoltaic or photoabsorbing electrodes.[39] Therefore, first attempts regarding the growth of oriented films of TT DBC-COF were realized with different substrates. It was possible to grow TT DBC-COF as oriented films, not only on quartz but also on conductive and transparent indium tin oxide (ITO) substrates. The growth as highly oriented films was indicated by GIWAXS measurements in Figure 7.2a, where reflections in z-direction indicate parallel assembly towards the surface, while reflection marks in stacking direction are indicated by reflections in y-direction. Non-oriented but crystalline material would result in closed semicircular patterns. Not only the first 100 reflection is clearly visible, but higher order reflections can also be distinguished. The absorbance of the TT DBC-COF film (measured in transmission) is in good agreement with the UV-Vis absorption of the corresponding powder (Figure 7.2b and Figure S 7.13). SEM cross sectional and top view images reveal a film thickness of about 350 nm, a well adhered film and a smooth top (Figure 7.2c and d).

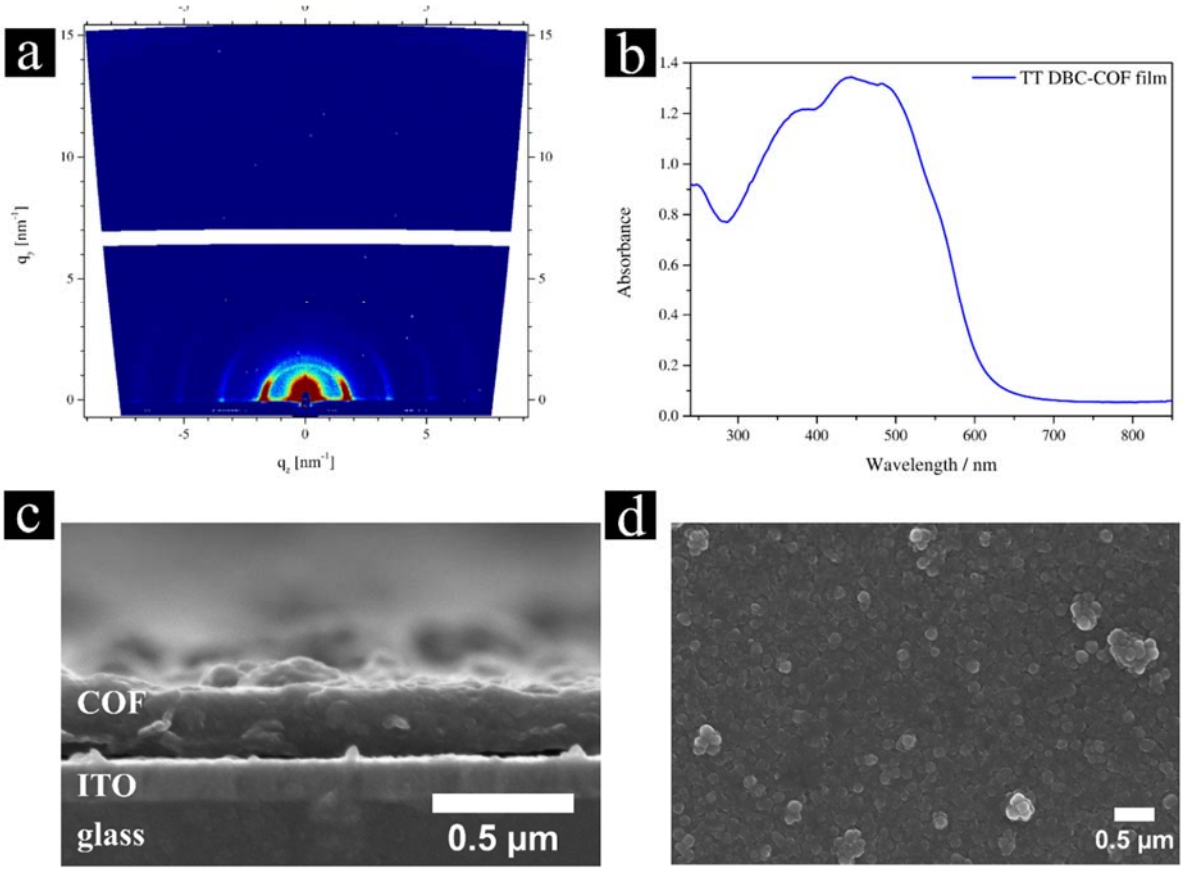


Figure 7.2: a) GIWAXS data of TT DBC-COF film. Reflections in z-direction indicate parallel arrangement with respect to the surface, while reflections in y-direction indicate a perpendicular assembly. b) Absorbance of the corresponding film with a steep onset at about 620 nm. c) Cross-sectional SEM image of the film, with clearly distinguishable substrate (ITO and glass) and COF, which is roughly 350 nm thick. d) SEM top view of the film. The film is smooth in large areas with some additional particles on top.

The time-correlated single photon counting data (TCSPC, Figure S 7.17 - 7.19) of the DBC-COFs revealed the lifetimes of the excited states. For TT DBC-COF lifetimes between 3.3 ns and 0.2 ns were detected. Notably, for Biph DBC-COF (Figure S 7.18) we observed a 19.6% share of a long-lived excited state with a lifetime of 7.85 ns. Long-lived excited states are attractive with a view on efficient charge carrier separation, as electron and holes live long enough to diffuse and to be separated in the respective device. On the other hand, if the excited states live too long, the efficiency of solar cells can decrease as well, as not every incident photon can be photo-absorbed and used for charge carrier generation. We conclude that TT DBC-COF films are promising candidates for applications in photovoltaics or as a photoabsorber in other optoelectronic applications.

## 7.4 CONCLUSION

We have successfully evolved the highly crystalline screw-containing COF motif based on the ETTA building block to create a flattened structural analog with extraordinarily high crystallinity, porosity, and structural precision. Following this strategy, COFs based on dibenzo[*g*,*p*]chrysene were synthesized with different linear linkers to not only vary the pore sizes but more importantly the optoelectronic properties. Strikingly, in comparison with ETTA analogs the stacking distance of adjacent layers was drastically reduced by 1 Å, from about 4.6 Å in ETTA-COFs to about 3.6 Å in DBC-COFs. Among the newly synthesized, tightly π-stacked DBC-COFs, TT DBC-COF is viewed to be a promising candidate for photovoltaic applications, as it combines a relatively small band gap and a steep absorption onset with a broad optical absorption ranging from the UV deep into the visible. Further mechanistic investigations in our laboratories regarding the charge carrier dynamics in these intriguing molecular frameworks are expected to shed light on the impact of the building blocks and the nature of the layer stacking on the optoelectronic properties. In view of the above results, dibenzochrysene-based COFs represent a promising platform of tunable framework materials with bright prospects for optoelectronic applications.

# 7.5 SUPPORTING INFORMATION

## 7.5.1 MATERIALS AND METHODS

All reagents and solvents were obtained from commercial suppliers and used as received. Terephthalaldehyde (TA, 99%, Sigma-Aldrich), 4,4'-biphenyldicarboxaldehyde (Biph, >98%, TCI), benzyl alcohol (BnOH, anhydrous, Sigma-Aldrich), dibenzo[*g*,*p*]chrysene (DBC, >98%, TCI), mesitylene (anhydrous, Sigma-Aldrich), tetrahydrofuran (THF, extra dry, stabilized, Acros Organics), ITO glass substrates (Visiontek, 12 Ω/sq), quartz substrates (SQ2, hellma-optics). Thieno[3,2-*b*]thiophene-2,5-dicarboxaldehyde (TT, >93%, TCI) was recrystallized from N,N-dimethylformamide (DMF, anhydrous, 99.8%, Sigma-Aldrich).

**Nuclear magnetic resonance (NMR) spectra** were recorded on Bruker AV 400 and AV 400 TR spectrometers. Proton chemical shifts are expressed in parts per million ($\delta$ scale) and are calibrated using residual non-deuterated solvent peaks as internal reference (e.g. DMSO-$d_6$: 2.50 ppm).

**Infrared (IR) spectra** were recorded on a Perkin Elmer Spectrum BX II FT-IR system and a Thermo Scientific Nicolet™ 6700 FT-IR spectrometer in transmission mode. IR data are reported in wavenumbers ($cm^{-1}$).

**UV-Vis** spectra were recorded using a Perkin-Elmer Lambda 1050 spectrometer equipped with a 150 mm integrating sphere. The reflectance-corrected absorbance $A_{corr}$ was calculated according to Equation 7.1, where $T_{sample}$, $T_{substrate}$, $R_{sample}$ and $R_{substrate}$ denote the transmittance and reflectance of the sample (substrate with COF film) and bare substrate, respectively.[40]

$$A_{corr} = -\log_{10}\left(\frac{\frac{T_{sample}}{T_{substrate}}}{1-\frac{R_{sample}-R_{substrate}}{T^2_{substrate}}}\right) \tag{7.1}$$

**Nitrogen sorption isotherms** were recorded on a Quantachrome Autosorb 1 at 77 K within a pressure range of $p/p^0$ = 0.001 to 0.98. Prior to the measurement of the sorption isotherms the samples were heated for 24 h at 120 °C under turbo-pumped vacuum. For the evaluation of the surface area the BET model was applied between 0.05 and 0.3 $p/p^0$. Pore size distributions were calculated using the QSDFT equilibrium model (desorption branch) with a carbon kernel for cylindrical pores. Connolly surfaces were generated using an $N_2$-sized probe (r = 0.184 nm) at a 0.025 nm grid interval.

**Thermogravimetric analysis** (TGA) measurements were performed on a Netzsch Jupiter ST 449 C instrument equipped with a Netzsch TASC 414/4 controller. The samples were heated from room temperature to 900 °C under a synthetic air flow (25 mL $min^{-1}$) at a heating rate of 10 K $min^{-1}$.

**Powder X-ray diffraction** (PXRD) measurements were performed using a Bruker D8 Discover with Ni-filtered Cu-K$\alpha$ radiation and a LynxEye position-sensitive detector (scan speed of 4 s per 0.01 degree 2θ). Experimental XRD data were used for Pawley refinement to optimize the hypothetical structure.

The initial **structure models of the COFs** were built using the Forcite module of the Accelrys Materials Studio software package. We applied the space group with the highest possible symmetry, i.e. *P*6, considering the propeller-like conformation of the central building blocks. Using this coarse model, we determined the unit cell parameters via Pawley refinement of our PXRD data.

**Transmission electron microscopy (TEM)** was performed on an FEI Titan Themis equipped with a field emission gun operated at 300 kV.

**Scanning electron microscopy (SEM)** images were recorded with a JEOL 6500F and an FEI Helios NanoLab G3 UC scanning electron microscope equipped with a field emission gun operated at 3-5 kV.

**Photoluminescence (PL)** and **time-correlated single photon counting (TCSPC)** data were processed with a FluoTime 300 from PicoQuant GmbH. The samples were photo-excited using lasers with suitable wavelengths according to the sample absorption, i.e. 378 nm, 403 nm or 507 nm wavelength (LDH-P-C-375, LDH-P-C-405, and LDH-P-C-510, respectively, all from PicoQuant GmbH) pulsed at 500 kHz, with a pulse duration of ~100 ps and fluence of ~ 300 nJ $cm^{-2}$/pulse. The samples were exposed to the pulsed light source set at 3 μJ $cm^{-2}$/pulse fluence for ~10 minutes prior to measurement to ensure stable sample emission. The PL was collected using a high-resolution monochromator and photomultiplier detector assembly (PMA-C 192-N-M, PicoQuant GmbH).

## 7.5.2 SYNTHETIC PROCEDURES

### 7.5.2.1 Tetranitro-DBC

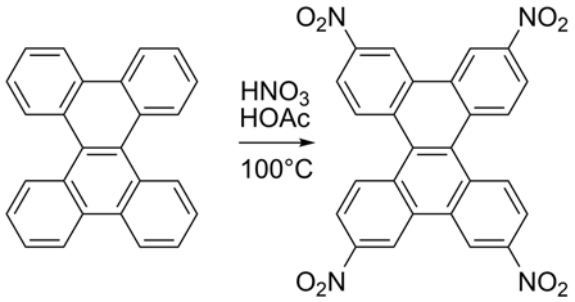


DBC (1.0 g, 3.0 mmol) was slowly added with stirring at 0 °C to a mixture of 10 mL nitric acid (≥ 99%) and 10 mL glacial acetic acid. After 10 min at 0 °C the solution was stirred at 100 °C for 2 h. The solution was poured into an ice-water mixture. The resulting precipitate was filtered, washed with 1,4-dioxane and recrystallized from nitrobenzene. After filtration and extensive washing with ethanol, 1.1 g of a yellow solid of tetranitro-DBC with 69% yield were obtained. MS-EI: calculated (m/z): 508.066, measured (m/z): 508.065.

### 7.5.2.2 Tetraamino-DBC (adapted from Lu *et al.*[41])

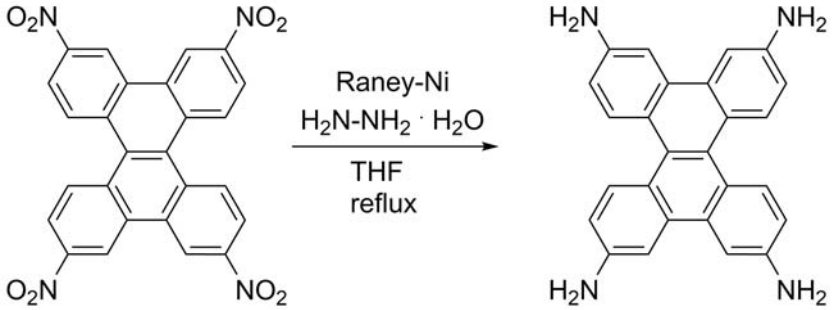


Under argon, tetranitro-DBC (500 mg, 0.98 mmol) was dissolved in 80 mL of anhydrous THF in a flame-dried 500 mL flask. Approximately 2.3 g of Raney-nickel catalyst slurry was added to the mixture with stirring. Hydrazine monohydrate (0.67 mL, 8.8 mmol) was added dropwise to the stirred mixture. The resulting solution was heated to reflux for two hours. The solution was allowed to cool to room temperature and filtered. The filtrate was dried under reduced pressure, giving 320 mg of a yellowish-greenish solid with 84% yield. $^{1}$H NMR (400 MHz, DMSO-$d_6$) δ (ppm): 8.15 (d, $J$ = 8.8 Hz, 4H, CH), 7.56 (d, $J$ = 2.3 Hz, 4H, CH), 6.90 (dd, $J$ = 8.8, 2.3 Hz, 4H, CH), 5.39 (s, 8H, $NH_2$). MS-EI: calculated (m/z): 388.169, measured (m/z): 388.168.

#### 7.5.2.3 Synthesis of TA DBC-COF

In a 6 mL culture tube, terephthalaldehyde (4.02 mg, 30.0 µmol) and DBCA (5.83 mg, 15.0 µmol) were suspended in a mixture of BnOH and mesitylene (500 µL, v:v 9:1). After adding 50 µL of acetic acid (aqueous, 6 M) the tube was sealed and heated at 120 °C for 72 h. The resulting precipitate was filtered and rinsed with anhydrous THF before Soxhlet extraction with anhydrous THF for 12 h. The final product was vacuum-dried, to yield 5.07 mg (58%) as a light brown powder.

#### 7.5.2.4 Synthesis of Biph DBC-COF

In a 6 mL culture tube, 4,4'-biphenyldicarboxaldehyde (6.31 mg, 30.0 µmol) and DBCA (5.83 mg, 15.0 µmol) were suspended in a mixture of BnOH and mesitylene (500 µL, v:v 1:1). After adding 50 µL of acetic acid (aqueous, 6 M) the culture tube was sealed and heated at 120 °C for 72 h. The resulting precipitate was filtered and rinsed with anhydrous THF before Soxhlet extraction with anhydrous THF for 12 h. The final product was vacuum-dried, to yield 5.47 mg (50%) as a brown powder.

#### 7.5.2.5 Synthesis of TT DBC-COF

In a 6 mL culture tube, thieno[3,2-*b*]thiophene-2,5-dicarboxaldehyde (5.89 mg, 30.0 µmol) and DBCA (5.83 mg, 15.0 µmol) were suspended in a mixture of BnOH and mesitylene (500 µL, v:v 9:1). After adding 50 µL of acetic acid (aqueous, 6 M) the tube was sealed and heated at 120 °C for 72 h. The resulting precipitate was filtered and rinsed with anhydrous THF before Soxhlet extraction with anhydrous THF for 12 h. The final product was vacuum-dried, to yield 5.87 mg (55%) as a red powder.

#### 7.5.2.6 Synthesis of TT DBC-COF films

In an autoclave TT (6.28 mg, 32.0 µmol) and DBCA (6.22 mg, 16.0 µmol) were suspended in a mixture of BnOH and mesitylene (2000 µL, v:v 9:1). After adding 200 µL of acetic acid (aqueous, 6 M), a glass slide holder was introduced to the autoclave, which finally was sealed and heated at 120 °C for 72 h. The slide was rinsed with anhydrous THF and the side facing up was cleared from precipitate with a cotton swab. Finally, the film was dried under vacuum prior to further investigations.

### 7.5.3 SEM

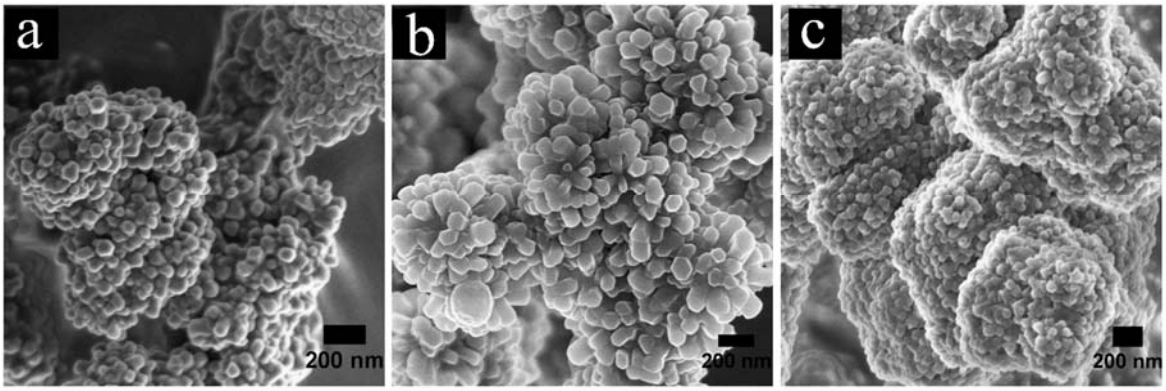


Figure S 7.1: SEM images of TA DBC-COF (a), Biph DBC-COF (b) and TT DBC-COF (c). A hexagonal morphology is visible for many of the crystallites.

### 7.5.4 TEM

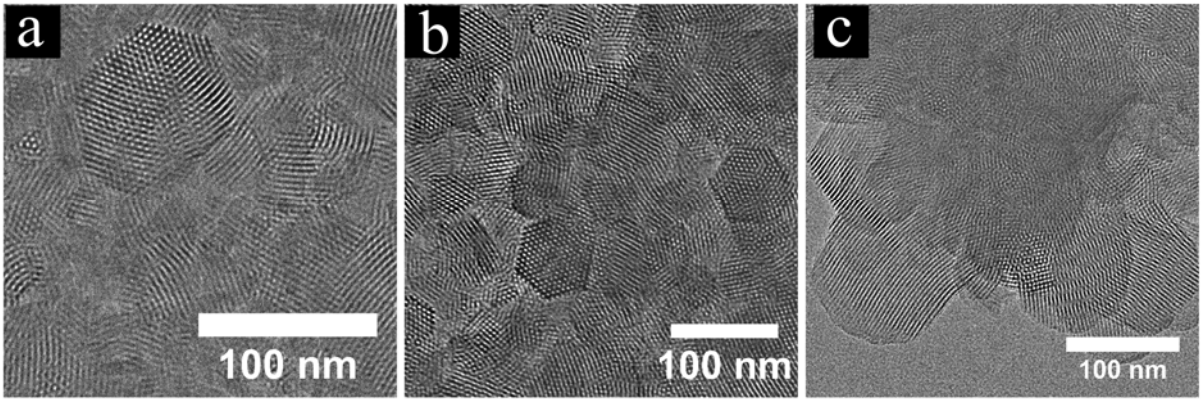


Figure S 7.2: TEM images of TA DBC-COF (a), Biph DBC-COF (b) and TT DBC-COF (c). The long-range order of the hexagonal crystallites is apparent from the large domains of about 50 to 100 nm.

X-RAY DIFFRACTION ANALYSIS

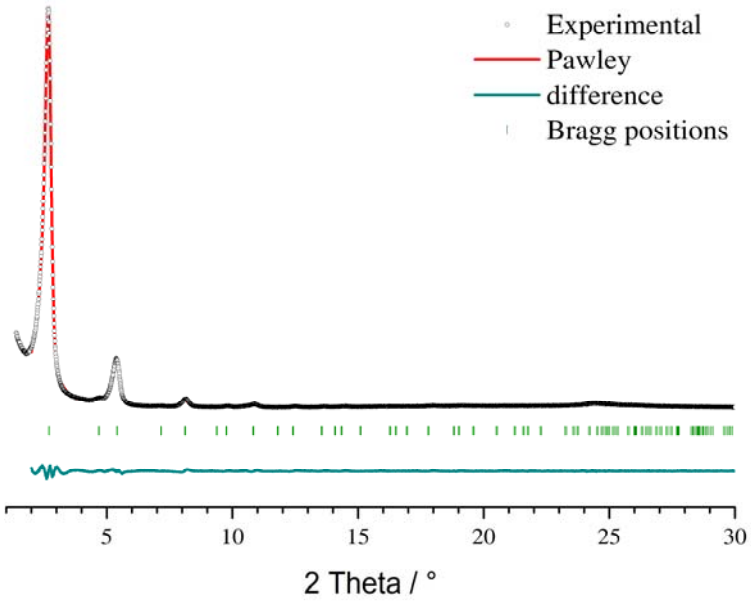


Figure S 7.3: Pawley refinement of TA DBC-COF. Experimental (black), Pawley refined simulation (red), difference (navy) and Bragg positions (olive) show good agreement of experimental and simulated PXRD patterns.

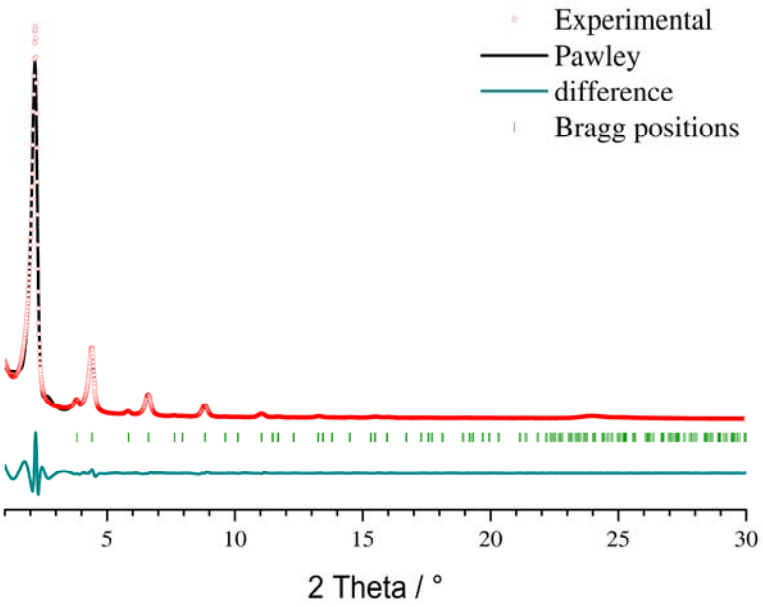


Figure S 7.4: Pawley refinement of Biph DBC-COF. Experimental (red), Pawley refined simulation (black), difference (navy) and Bragg positions (olive) show good agreement of experimental and simulated PXRD patterns.

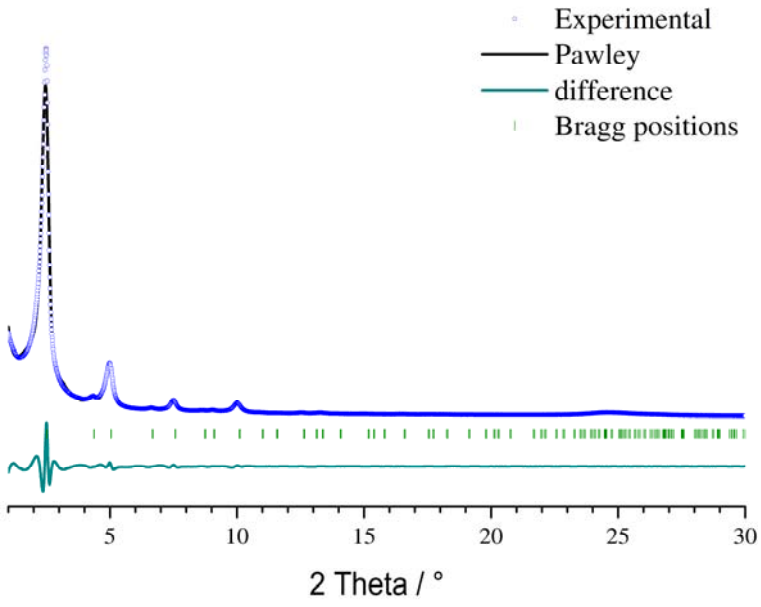


Figure S 7.5: Pawley refinement of TT DBC-COF. Experimental (blue), Pawley refined simulation (black), difference (navy) and Bragg positions (olive) show good agreement of experimental and simulated PXRD patterns.

### 7.5.5 SORPTION

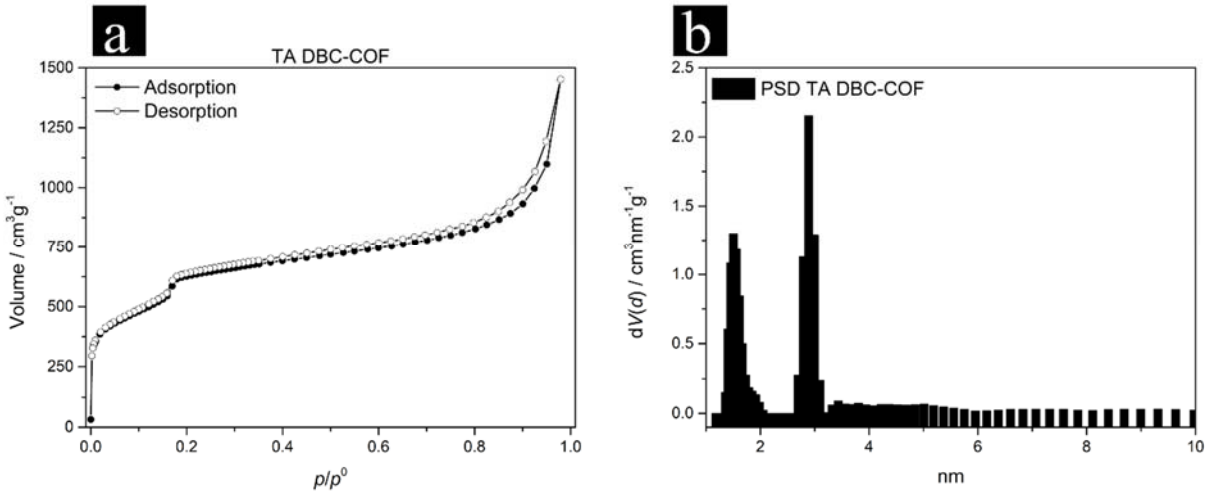


Figure S 7.6: Nitrogen physisorption isotherm of TA DBC-COF (a) and the corresponding PSD with a QSDFT carbon equilibrium kernel for cylindrical pores reveal the dual-pore COF-structure (b).

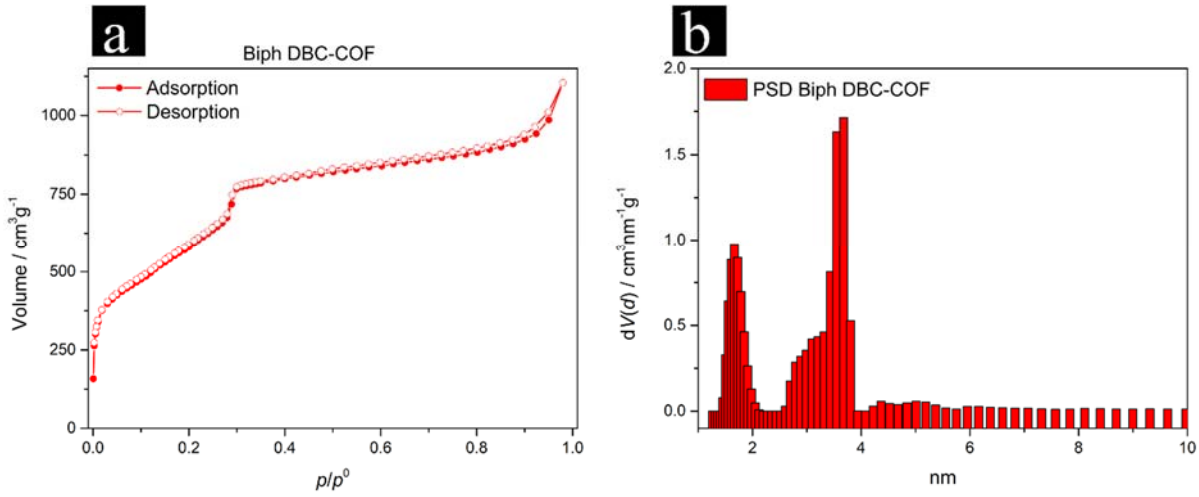


Figure S 7.7: Nitrogen physisorption isotherm of Biph DBC-COF (a) and the corresponding PSD with a QSDFT carbon equilibrium kernel for cylindrical pores reveal the dual-pore COF-structure (b).

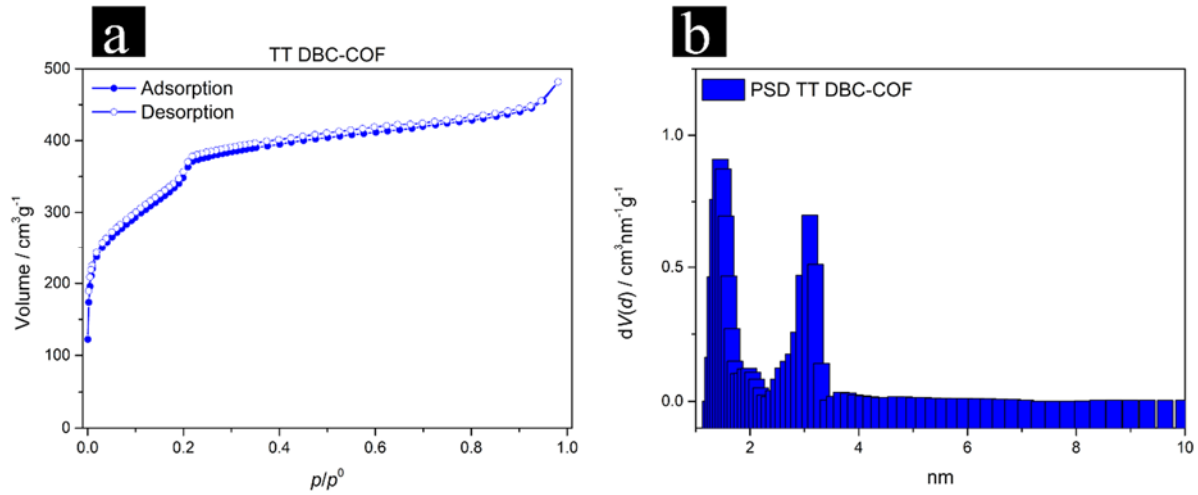


Figure S 7.8: Nitrogen physisorption isotherm of TT DBC-COF (a) and the corresponding PSD with a QSDFT carbon kernel for cylindrical pores reveal the dual-pore COF-structure (b).

The first steep uptakes at very low $p/p^0$ in Figure S 7.6 – 7.8 indicate the micropore filling, while the second one ($p/p^0$ = 0.15 to 0.35) represents the capillary condensation within the mesopores, respectively. Due to the comparably small size of the mesopores (≤ 4 nm), a type IVb physisorption isotherm without a hysteresis loop is obtained.[36] The pore size distribution was calculated from the equilibrium branch (desorption) with QSDFT with a carbon kernel for cylindrical pore geometry, respectively.

### 7.5.6 STRUCTURAL SIMULATIONS OF DBC-COFS

Space group: P*6* with an AA-hexagonal eclipsed stacking (AA-H).

Table 7.1: Fractional atomic coordinates for the unit cell of AA-H calculated with Materials Studio v7.0 modeling program for TA DBC-COF.

| P*6* (168) – hexagonal | | | |
|---|---|---|---|
| a = b = 347762(9) nm, c = 0.3611(6) nm | | | |
| α = β = 90°, γ = 120° | | | |
| **Atom** | **x/a** | **y/b** | **z/c** |
| C1 | 0.48191 | 0.48325 | 0.48052 |
| C2 | 0.55441 | 0.51297 | 0.42694 |
| C3 | 0.52066 | 0.55641 | 0.54156 |
| C4 | 0.59020 | 0.54403 | 0.29244 |
| C5 | 0.62475 | 0.54203 | 0.29230 |
| C6 | 0.62425 | 0.50820 | 0.42101 |
| C7 | 0.58821 | 0.47561 | 0.51286 |
| C8 | 0.55272 | 0.47667 | 0.48965 |
| C9 | 0.44374 | 0.40906 | 0.63294 |
| C10 | 0.44115 | 0.37230 | 0.64931 |
| C11 | 0.47408 | 0.36870 | 0.58695 |
| C12 | 0.51035 | 0.40275 | 0.52521 |
| C13 | 0.51377 | 0.44046 | 0.52582 |
| N14 | 0.65911 | 0.50510 | 0.45965 |
| N15 | 0.46921 | 0.32992 | 0.56729 |
| C16 | 0.49663 | 0.32108 | 0.62398 |
| C17 | 0.69535 | 0.53248 | 0.40083 |
| H18 | 0.59210 | 0.57034 | 0.18775 |
| H19 | 0.65141 | 0.56709 | 0.19352 |
| H20 | 0.58881 | 0.44988 | 0.60748 |
| H21 | 0.41715 | 0.40928 | 0.69160 |
| H22 | 0.41317 | 0.34619 | 0.70662 |
| H23 | 0.53515 | 0.39927 | 0.45855 |
| H24 | 0.70243 | 0.56149 | 0.31031 |

| Atom | x/a | y/b | z/c |
|---|---|---|---|
| C25 | 0.72818 | 0.52481 | 0.46130 |
| C26 | 0.76693 | 0.55452 | 0.38691 |
| C27 | 0.79842 | 0.54785 | 0.44169 |
| C28 | 0.79169 | 0.51129 | 0.57228 |
| C29 | 0.75295 | 0.48161 | 0.64787 |
| C30 | 0.72145 | 0.48829 | 0.59315 |
| H31 | 0.77280 | 0.58279 | 0.28273 |
| H32 | 0.82803 | 0.57105 | 0.37785 |
| H33 | 0.74708 | 0.45329 | 0.75074 |
| H34 | 0.69183 | 0.46504 | 0.65574 |
| H35 | 0.47430 | 0.65667 | 0.71292 |

Table 7.2: Fractional atomic coordinates for the unit cell of AA-H calculated with Materials Studio v7.0 modeling program for Biph DBC-COF.

| P*6* (168) – hexagonal | | | |
|---|---|---|---|
| a = b = 4.6299(9) nm, c = 0.4017(6) nm | | | |
| α = β = 90°, γ = 120° | | | |
| **Atom** | **x/a** | **y/b** | **z/c** |
| C1 | 0.48657 | 0.48523 | 0.40595 |
| C2 | 0.54747 | 0.51934 | 0.47987 |
| C3 | 0.51209 | 0.54571 | 0.33928 |
| C4 | 0.57621 | 0.54952 | 0.58548 |
| C5 | 0.60724 | 0.55217 | 0.64763 |
| C6 | 0.61072 | 0.52399 | 0.61072 |
| C7 | 0.58252 | 0.49341 | 0.52786 |
| C8 | 0.55050 | 0.48998 | 0.47046 |
| C9 | 0.46428 | 0.42667 | 0.20464 |
| C10 | 0.46592 | 0.39731 | 0.18524 |
| C11 | 0.49474 | 0.39752 | 0.29305 |
| C12 | 0.52262 | 0.42804 | 0.38814 |
| C13 | 0.52182 | 0.45850 | 0.39736 |
| N14 | 0.63973 | 0.52397 | 0.64491 |

| **Atom** | **x/a** | **y/b** | **z/c** |
|---|---|---|---|
| N15 | 0.49293 | 0.36755 | 0.31443 |
| C16 | 0.51695 | 0.35928 | 0.35322 |
| C17 | 0.67165 | 0.54914 | 0.67079 |
| C18 | 0.69733 | 0.54129 | 0.67394 |
| C19 | 0.72920 | 0.56440 | 0.54611 |
| C20 | 0.75392 | 0.55532 | 0.51221 |
| C21 | 0.74763 | 0.52321 | 0.61062 |
| C22 | 0.71632 | 0.50088 | 0.75625 |
| C23 | 0.69152 | 0.50981 | 0.78764 |
| C24 | 0.77174 | 0.51343 | 0.55738 |
| C25 | 0.76261 | 0.48184 | 0.41627 |
| C26 | 0.78678 | 0.47255 | 0.35085 |
| C27 | 0.82080 | 0.49480 | 0.42288 |
| C28 | 0.82988 | 0.52607 | 0.57053 |
| C29 | 0.80569 | 0.53521 | 0.63833 |
| H30 | 0.57550 | 0.57078 | 0.62568 |
| H31 | 0.62702 | 0.57457 | 0.71974 |
| H32 | 0.58659 | 0.47382 | 0.50670 |
| H33 | 0.44290 | 0.42517 | 0.12112 |
| H34 | 0.44592 | 0.37570 | 0.09814 |
| H35 | 0.54311 | 0.42699 | 0.45890 |
| H36 | 0.67735 | 0.57358 | 0.66739 |
| H37 | 0.73437 | 0.58762 | 0.46757 |
| H38 | 0.77636 | 0.57219 | 0.40737 |
| H39 | 0.71121 | 0.47784 | 0.83934 |
| H40 | 0.66899 | 0.49303 | 0.89182 |
| H41 | 0.73825 | 0.46540 | 0.35523 |
| H42 | 0.77938 | 0.44963 | 0.24633 |
| H43 | 0.85426 | 0.54239 | 0.63296 |
| H44 | 0.81311 | 0.55787 | 0.74889 |
| H45 | 0.83795 | 0.46094 | 0.33347 |

Table 7.3: Fractional atomic coordinates for the unit cell of AA-H calculated with Materials Studio v7.0 modeling program for TT DBC-COF.

| P*6* (168) – hexagonal | | | |
|---|---|---|---|
| a = b = 4.0444(2) nm, c = 0.3782(7) nm | | | |
| α = β = 90°, γ = 120° | | | |
| **Atom** | **x/a** | **y/b** | **z/c** |
| C1 | 0.0338 | 0.48331 | 0.55114 |
| C2 | 0.03593 | 0.45208 | 0.66021 |
| C3 | 0.06869 | 0.45123 | 0.67445 |
| C4 | 0.10173 | 0.48243 | 0.58930 |
| C5 | 0.10105 | 0.51468 | 0.51320 |
| C6 | 0.06812 | 0.51646 | 0.51685 |
| N7 | 0.13190 | 0.47895 | 0.58251 |
| C8 | 0.16786 | 0.50433 | 0.56654 |
| C9 | 0.19472 | 0.49415 | 0.53650 |
| S10 | 0.18458 | 0.44890 | 0.46926 |
| C11 | 0.23115 | 0.46555 | 0.45473 |
| C12 | 0.25258 | 0.50249 | 0.50360 |
| C13 | 0.23222 | 0.51956 | 0.55076 |
| C14 | 0.25154 | 0.44857 | 0.40208 |
| C15 | 0.28904 | 0.47401 | 0.41620 |
| S16 | 0.29915 | 0.51912 | 0.49306 |
| C17 | 0.31599 | 0.46407 | 0.37540 |
| C18 | 0.48282 | 0.48310 | 0.49344 |
| N19 | 0.44993 | 0.48486 | 0.43522 |
| C20 | 0.44981 | 0.51846 | 0.47705 |
| C21 | 0.41555 | 0.51758 | 0.48434 |
| C22 | 0.38229 | 0.48620 | 0.40126 |
| C23 | 0.38319 | 0.45469 | 0.30274 |
| C24 | 0.41632 | 0.45455 | 0.31703 |
| N25 | 0.35176 | 0.48897 | 0.42046 |
| H26 | 0.06849 | 0.42769 | 0.74564 |

| **Atom** | **x/a** | **y/b** | **z/c** |
|---|---|---|---|
| H27 | 0.12536 | 0.53671 | 0.44594 |
| H28 | 0.17600 | 0.53155 | 0.57639 |
| H29 | 0.24348 | 0.54707 | 0.58927 |
| H30 | 0.24031 | 0.42112 | 0.35984 |
| H31 | 0.30814 | 0.43753 | 0.31501 |
| H32 | 0.41364 | 0.53983 | 0.55603 |
| H33 | 0.35995 | 0.43173 | 0.22183 |
| H34 | 0.41493 | 0.43116 | 0.23370 |
| H35 | 0.01350 | 0.42866 | 0.73592 |

## 7.5.7 CRYSTALLOGRAPHIC DATA

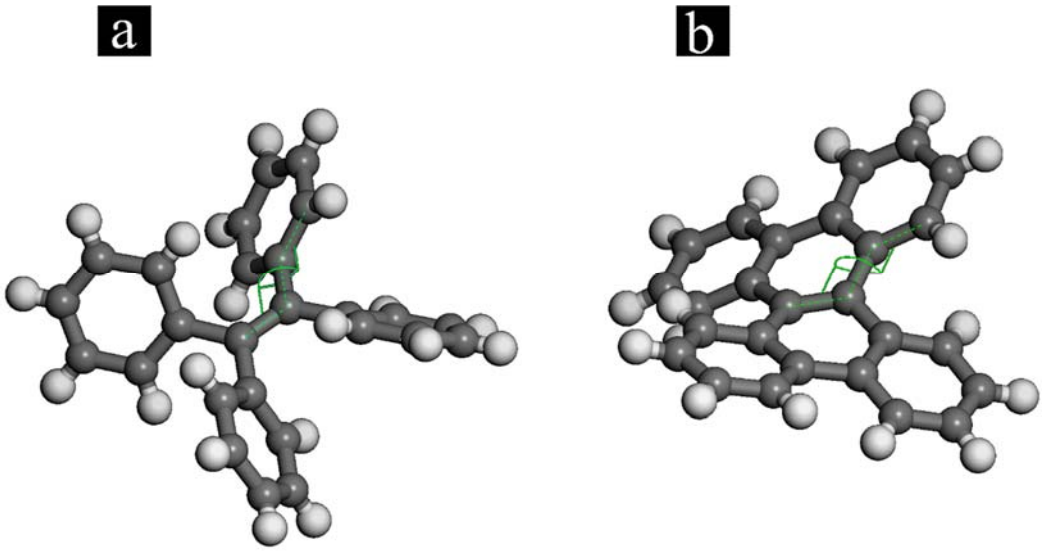


Figure S 7.9: Crystallographic data of the molecular cores of the respective amine-functionalized building blocks. The dihedral angle (green) of the core of ETTA (a) is much bigger (47.3°) due to steric hindrances. In the case of the DBC core (b), the additional bonds force the system to stay more planar (dihedral angle of 24.7°).

## 7.5.8 IR SPECTROSCOPY

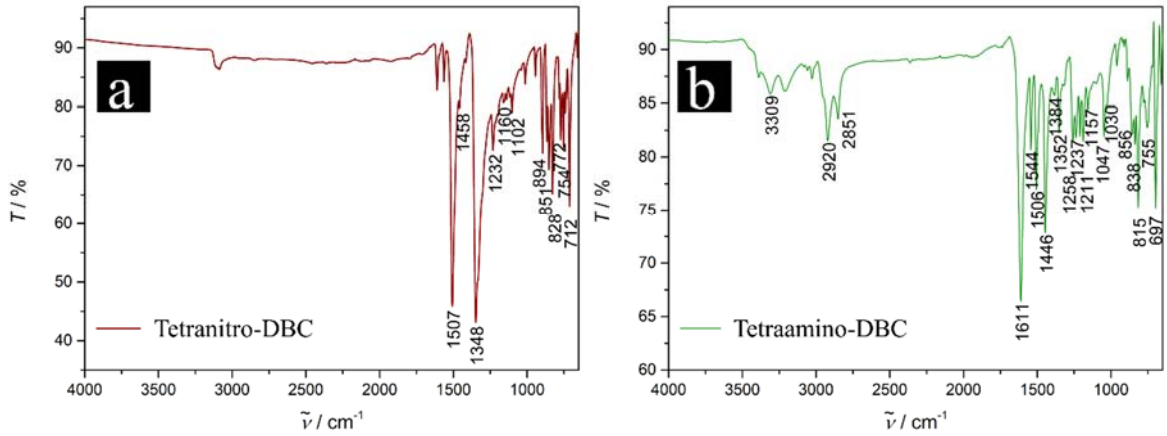


Figure S 7.10: IR spectra of tetranitro- (a) and tetraamino-DBC (DBCA) (b).

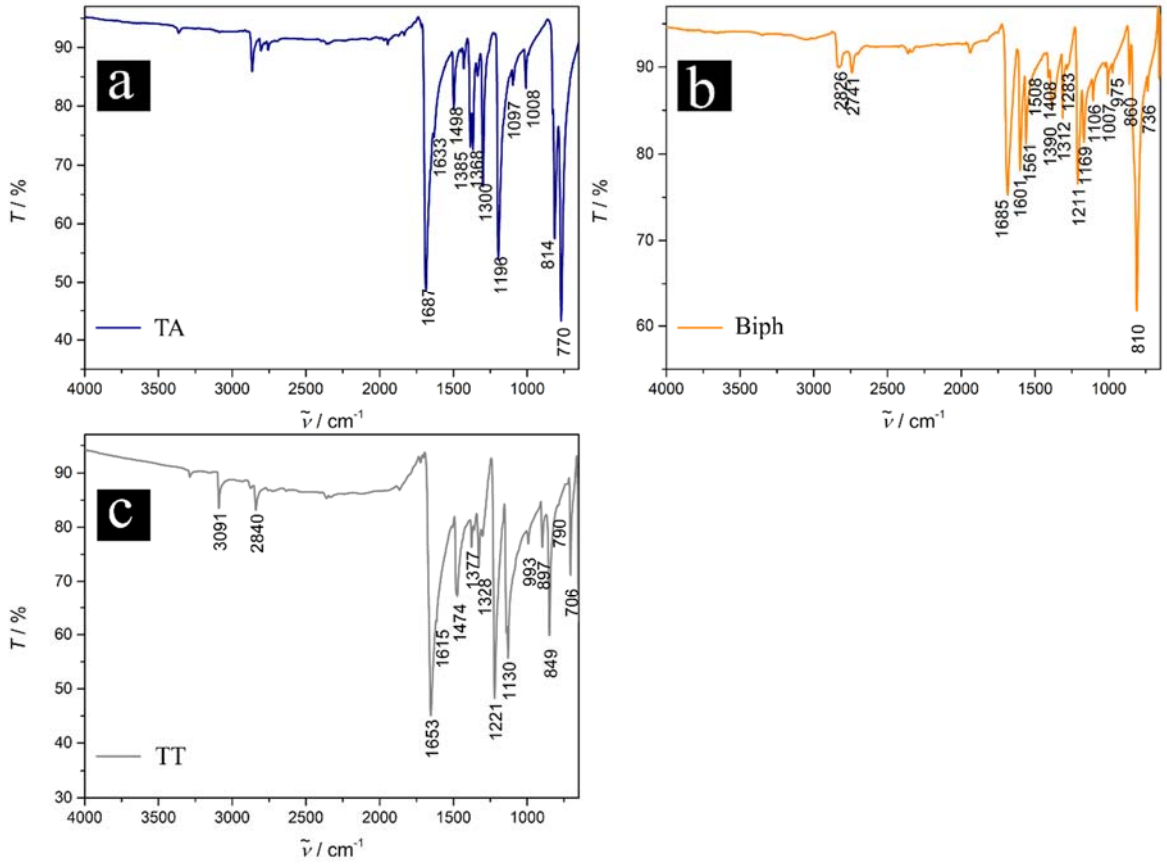


Figure S 7.11: IR spectra of TA (a), Biph (b) and TT (c) precursors.

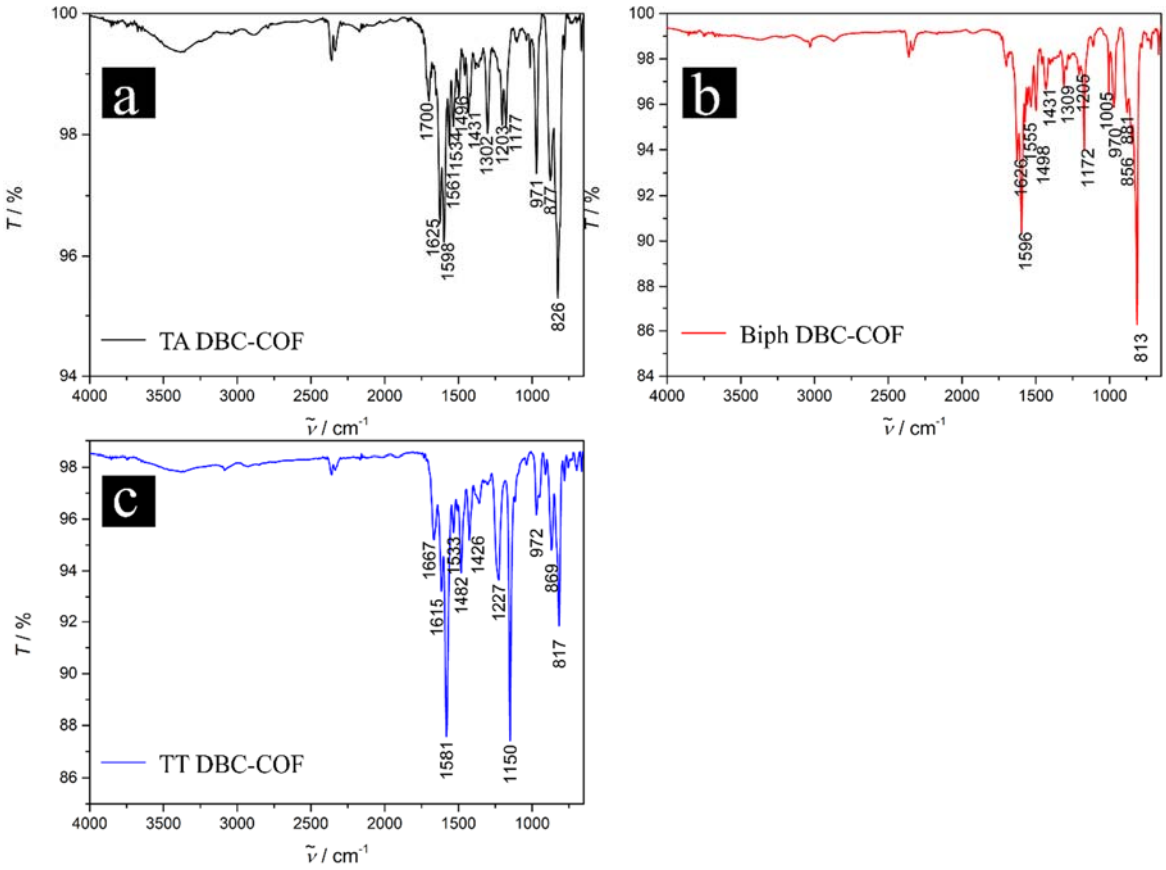


Figure S 7.12: IR spectra of the synthesized DBC-COFs, namely TA DBC-COF (a), Biph DBC-COF (b) and TT DBC-COF (c).

### 7.5.9 UV-VIS SPECTROSCOPY

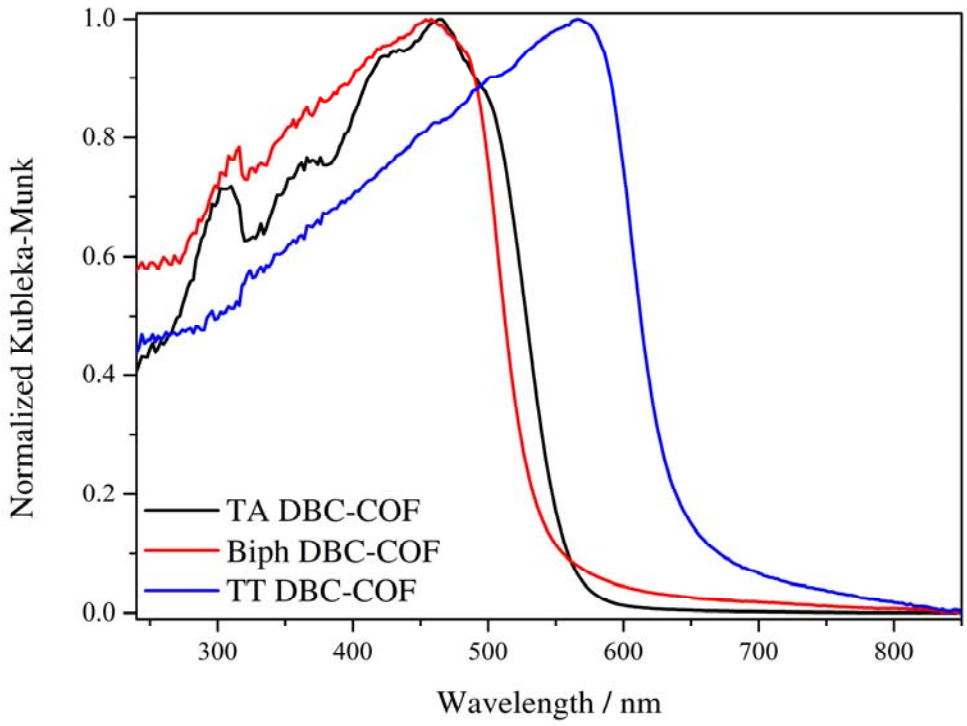


Figure S 7.13: UV-Vis diffuse reflectance spectra of the DBC-COFs. The data are expressed in Kubelka-Munk units and normalized to the strongest absorption.

## 7.5.10 PHOTOLUMINESCENCE (SSPL AND TCSPC)

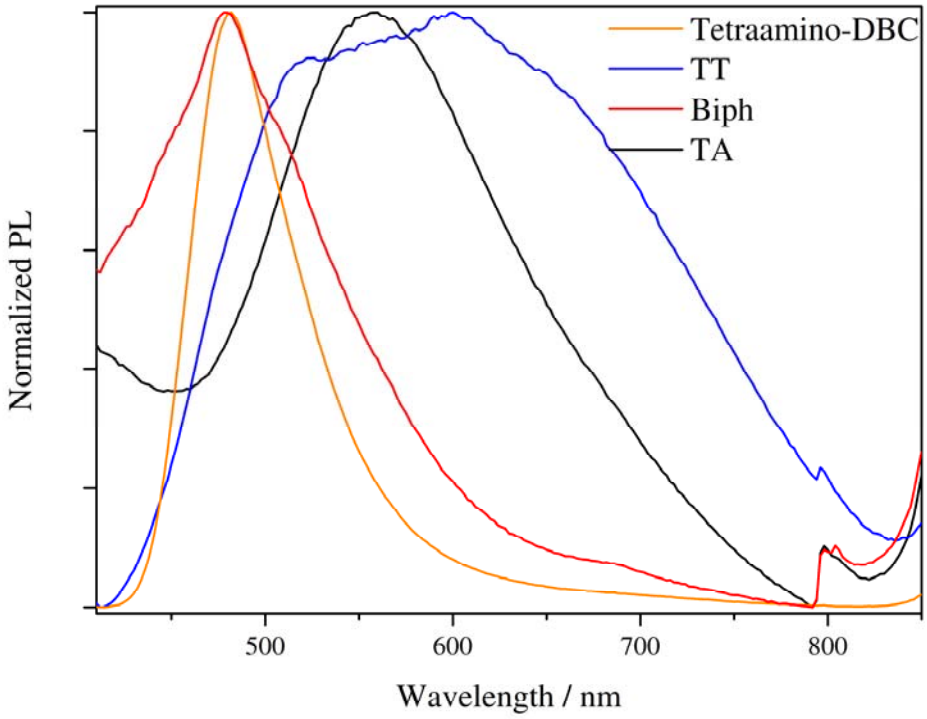


Figure S 7.14: Normalized PL of the solid precursors tetraamino-DBC (DBCA, orange), TT (blue), Biph (red) and TA (black) obtained with 375 nm excitation. By far the highest emission intensity resulted from excitation of DBCA.

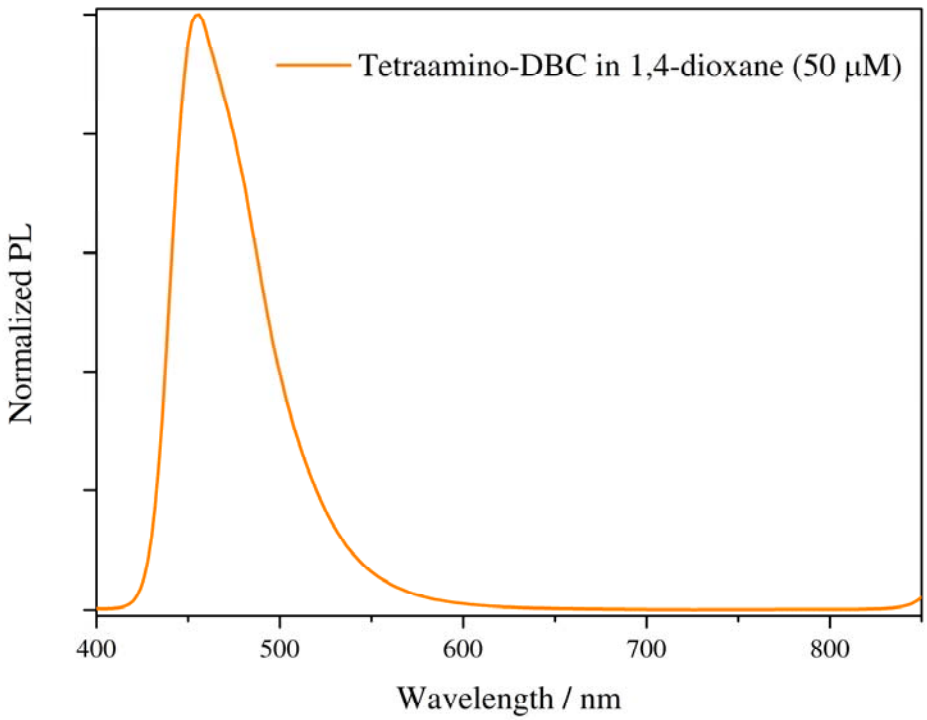


Figure S 7.15: Normalized PL spectrum of DBCA measured as solution in 1,4-dioxane (50 µM) and excited by a 375 nm laser. A strong emission could be detected at 480 nm.

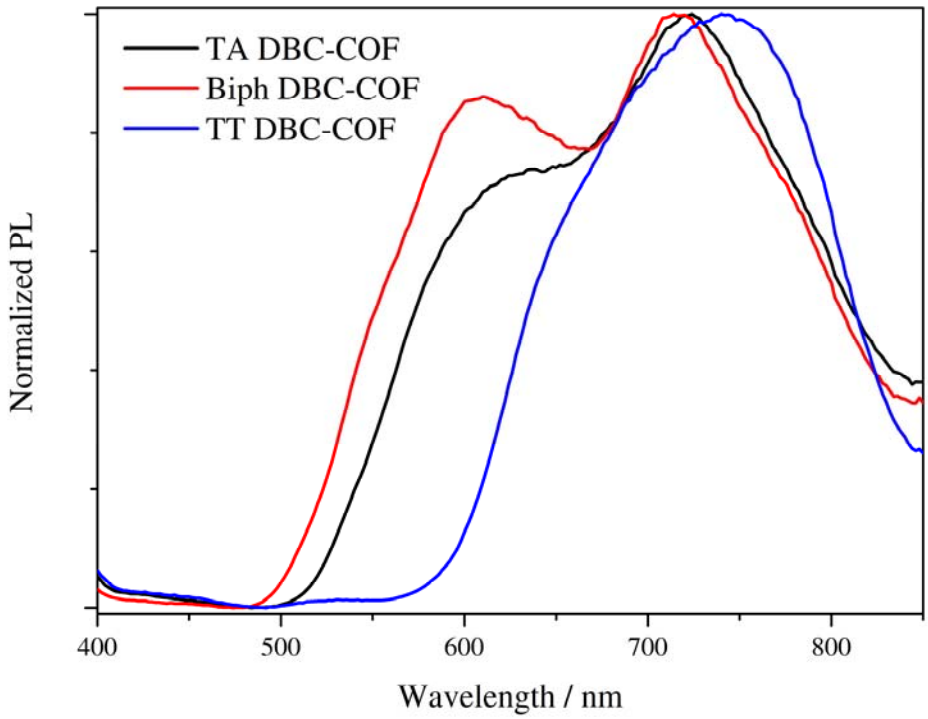


Figure S 7.16: PL spectra of TA, Biph and TT DBC-COF. The emission of TT DBC-COF is red-shifted in comparison to the spectra of the phenyl-based TA and Biph DBC-COFs.

## 7.5.11 TCSPC DATA OF DBC-COFS

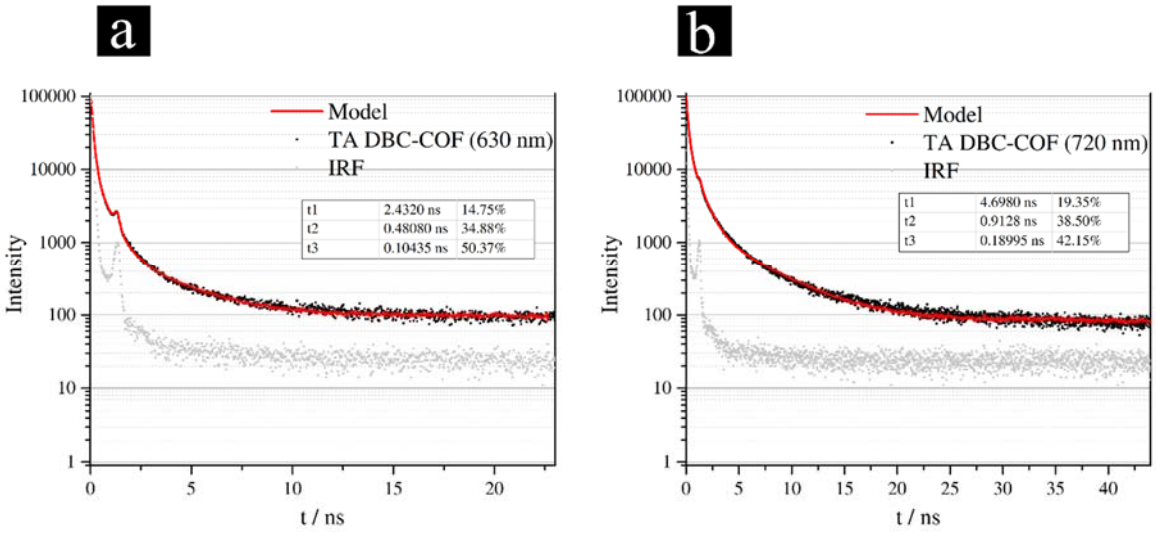


Figure S 7.17: Results of the TCSPC investigations of TA DBC-COF powder under argon. The powder was excited with a 375 nm pulsed laser and the life times were detected for the emissions at the PL maxima at 630 (a) and 720 nm (b). The instrument response function is shown in grey.

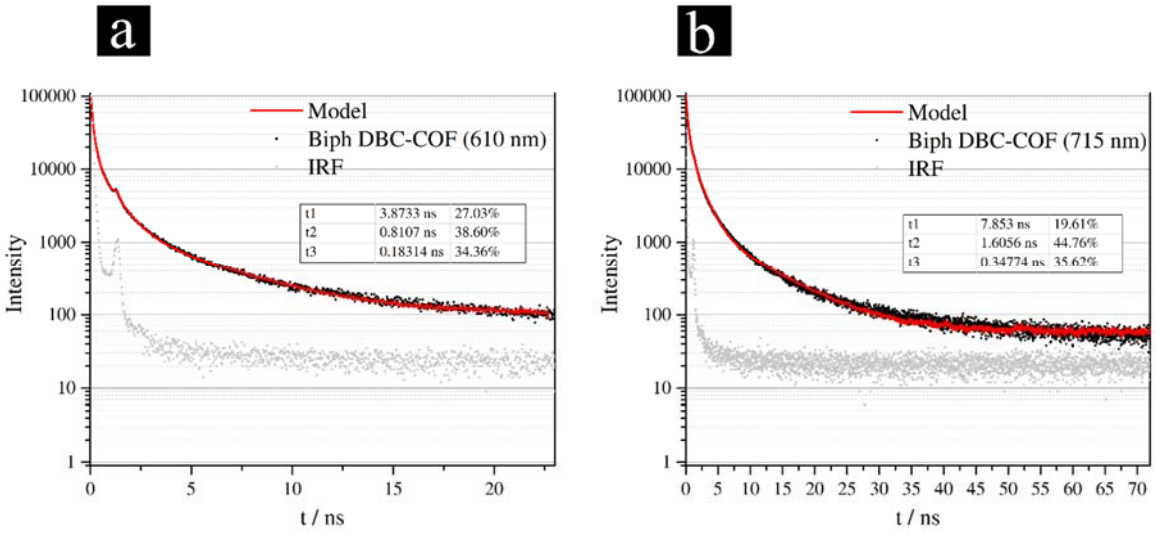


Figure S 7.18: Results of the TCSPC investigations of Biph DBC-COF powder under argon. The powder was excited with a 375 nm pulsed laser and the lifetimes were detected for the emissions at the PL maxima at 610 and 715 nm. The instrument response function is shown in grey.

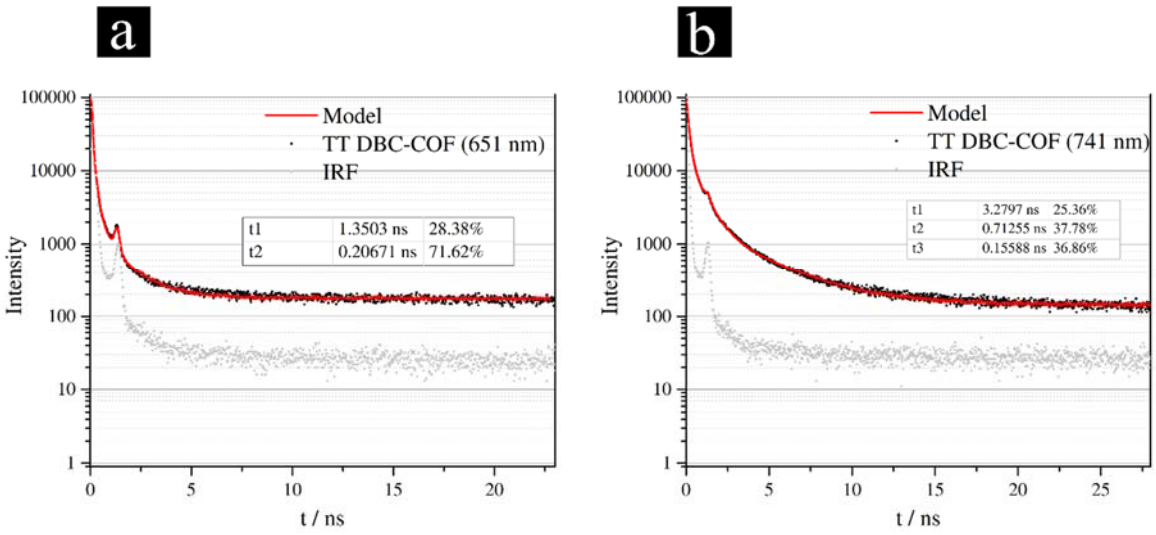


Figure S 7.19: Results of the TCSPC investigations of TT DBC-COF powder under argon. The powder was excited with a 375 nm pulsed laser and the lifetimes were detected for the emissions at the PL maxima at 651 and 741 nm. The instrument response function is shown in grey.

## 7.5.12 THERMOGRAVIMETRIC ANALYSIS

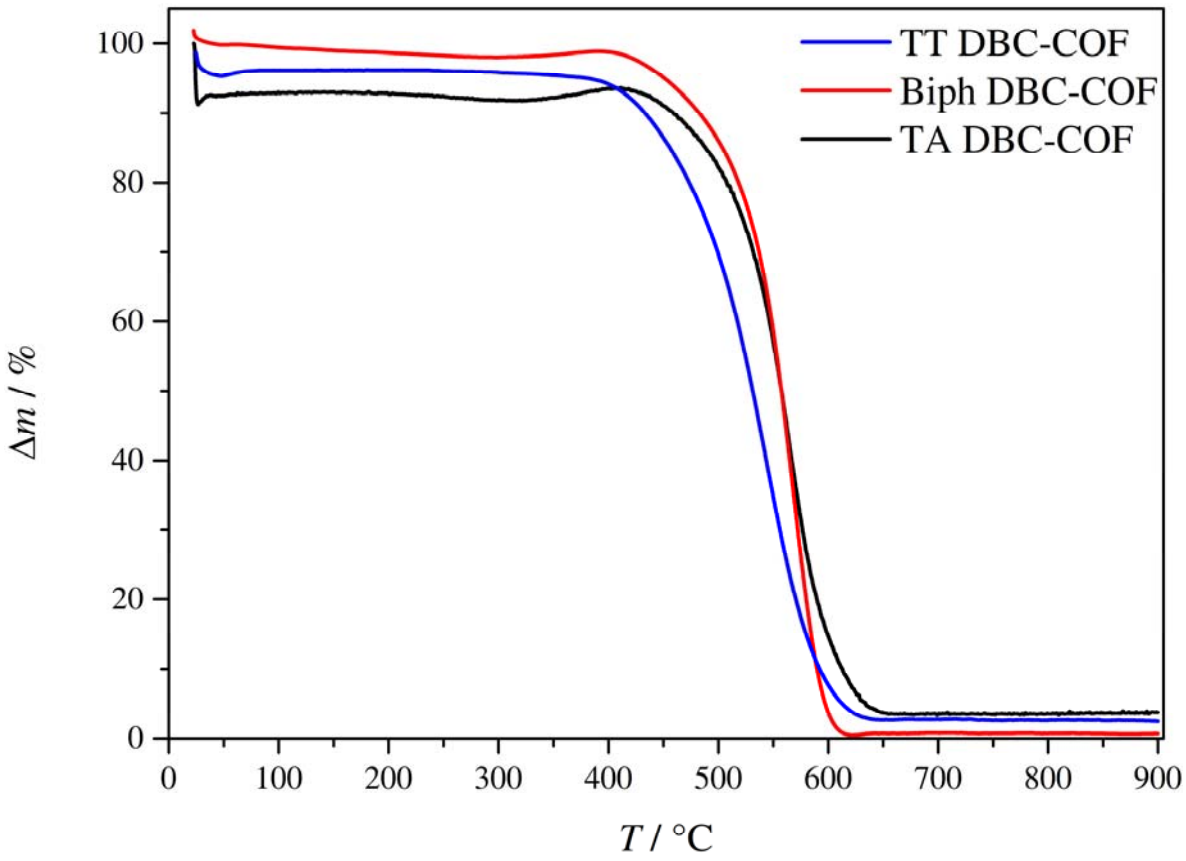


Figure S 7.20: Thermogravimetric analysis of DBC COFs. TA DBC-COF (black), Biph DBC-COF (red) and TT DBC-COF (blue) are all stable until 350 °C under a heating rate of 10°C/min and under synthetic air ($N_2/O_2$ V/V 79.5/20.5, 25 mL $min^{-1}$).

### 7.5.13 ELEMENTAL ANALYSIS

Table 7.4: Elemental analysis of TA DBC-COF bulk material compared with the calculated mass percentages.

| Element | TA DBC-COF | |
|---|---|---|
| | Theoretical percentage | Measured percentage |
| **N** | 9.58 | 8.49 |
| **C** | 86.28 | 77.68 |
| **H** | 4.14 | 4.70 |

Table 7.5: Elemental analysis of Biph DBC-COF bulk material compared with the calculated mass percentages.

| Element | Biph DBC-COF | |
|---|---|---|
| | Theoretical percentage | Measured percentage |
| **N** | 7.60 | 7.63 |
| **C** | 88.02 | 83.35 |
| **H** | 4.38 | 4.59 |

Table 7.6: Elemental analysis of TT DBC-COF bulk material compared with the calculated mass percentages.

| Element | TT DBC-COF | |
|---|---|---|
| | Theoretical percentage | Measured percentage |
| **N** | 7.90 | 7.01 |
| **C** | 71.16 | 65.73 |
| **H** | 2.84 | 3.19 |
| **S** | 18.09 | 16.64 |

The differences between theoretical and measured atomic percentages are tentatively attributed to COF structures having a certain number of defects (missing building blocks).

### 7.5.14 NMR

$^1$H, 400 MHz, DMSO-$d_6$

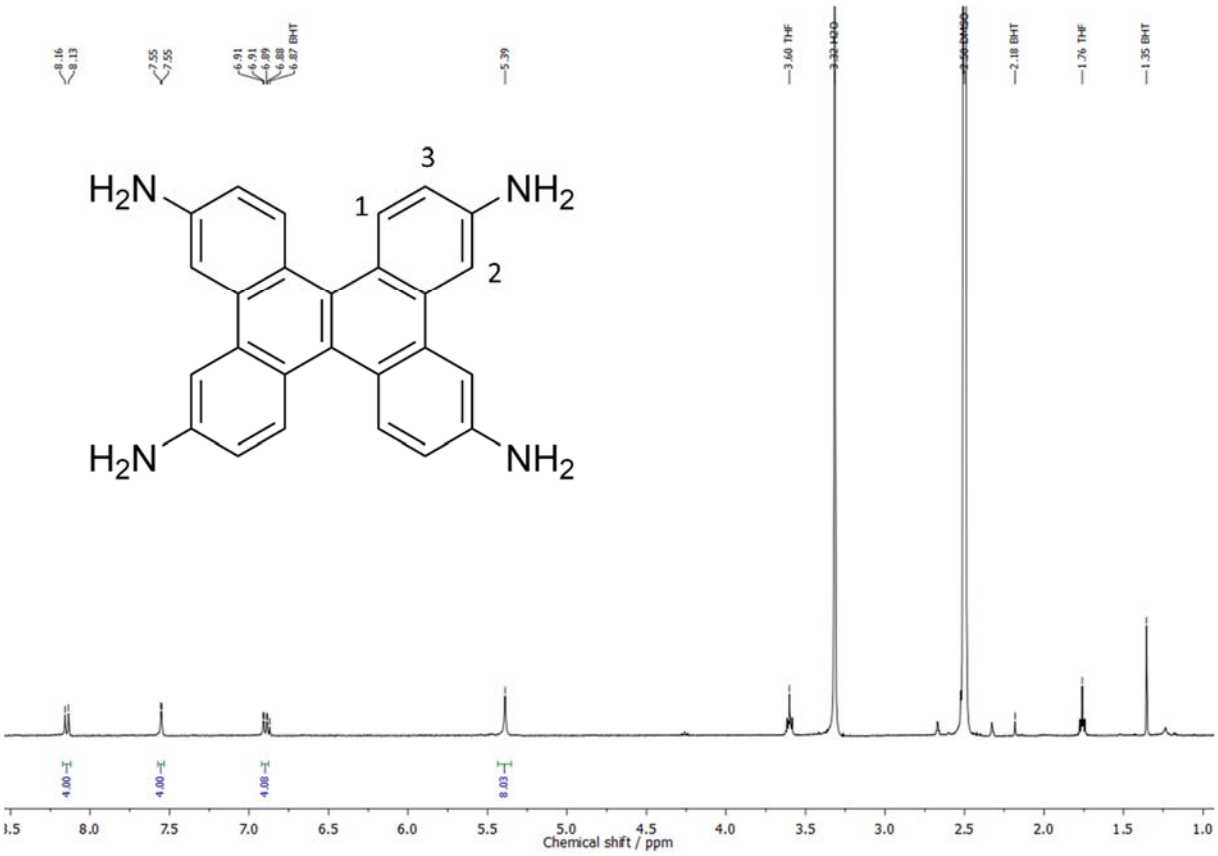


Figure S 7.21: $^1$H NMR spectrum of DBCA: $^1$H NMR (400 MHz, DMSO-$d_6$) δ (ppm): 8.15 (d, $J$ = 8.8 Hz, 4H, C(1)H), 7.55 (d, $J$ = 2.3 Hz, 4H, C(2)H), 6.9 (dd, $J$ = 8.8, 2.3 Hz, 4H, C(3)H), 5.39 (s, 8H, $NH_2$).

**Tetraamino-DBC**

$^{13}$C, 100 MHz, DMSO-$d_6$

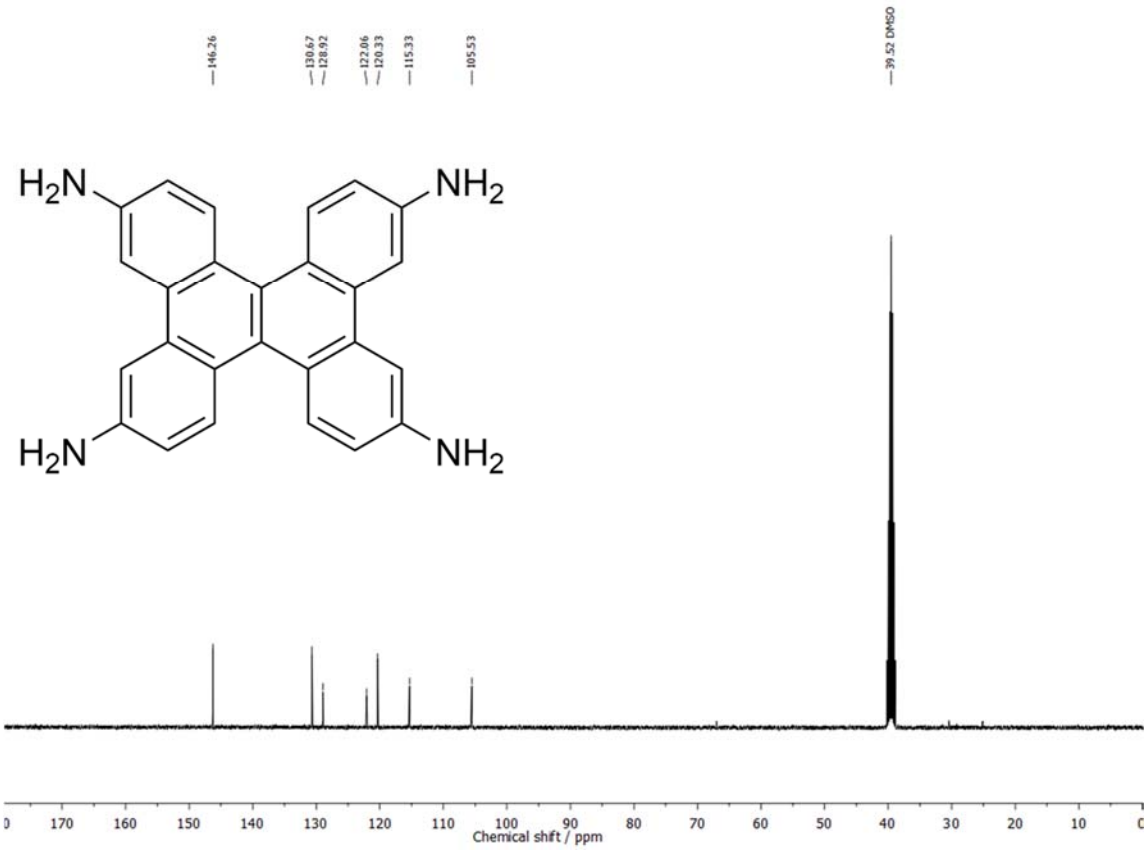


Figure S 7.22: $^{13}$C NMR spectrum of DBCA. $^{13}$C NMR (100 MHz, DMSO-$d_6$) δ (ppm): 146.3, 130.7, 128.9, 122.1, 120.3, 115.3, 105.5.

# 7.6 REFERENCES

(1) Cote, A. P.; Benin, A. I.; Ockwig, N. W.; O'Keeffe, M.; Matzger, A. J.; Yaghi, O. M., *Science* **2005**, *310*, 1166-1170.

(2) Wan, S.; Guo, J.; Kim, J.; Ihee, H.; Jiang, D., *Angew. Chem. Int. Ed. Engl.* **2009**, *48*, 5439-5442.

(3) Uribe-Romo, F. J.; Hunt, J. R.; Furukawa, H.; Klock, C.; O'Keeffe, M.; Yaghi, O. M., *J. Am. Chem. Soc.* **2009**, *131*, 4570-4571.

(4) Fang, Q.; Zhuang, Z.; Gu, S.; Kaspar, R. B.; Zheng, J.; Wang, J.; Qiu, S.; Yan, Y., *Nat. Commun.* **2014**, *5*, 4503.

(5) Uribe-Romo, F. J.; Doonan, C. J.; Furukawa, H.; Oisaki, K.; Yaghi, O. M., *J. Am. Chem. Soc.* **2011**, *133*, 11478-11481.

(6) Kuhn, P.; Antonietti, M.; Thomas, A., *Angew. Chem. Int. Ed. Engl.* **2008**, *47*, 3450-3453.

(7) Dalapati, S.; Jin, S.; Gao, J.; Xu, Y.; Nagai, A.; Jiang, D., *J. Am. Chem. Soc.* **2013**, *135*, 17310-17313.

(8) Yang, H.; Zhang, S.; Han, L.; Zhang, Z.; Xue, Z.; Gao, J.; Li, Y.; Huang, C.; Yi, Y.; Liu, H.; Li, Y., *ACS Appl Mater Interfaces* **2016**, *8*, 5366-5375.

(9) DeBlase, C. R.; Hernandez-Burgos, K.; Silberstein, K. E.; Rodriguez-Calero, G. G.; Bisbey, R. P.; Abruna, H. D.; Dichtel, W. R., *ACS Nano* **2015**, *9*, 3178-3183.

(10) Lee, G. Y.; Lee, J.; Vo, H. T.; Kim, S.; Lee, H.; Park, T., *Sci Rep* **2017**, *7*, 557.

(11) Ding, S. Y.; Wang, W., *Chem. Soc. Rev.* **2013**, *42*, 548-568.

(12) Furukawa, H.; Yaghi, O. M., *J. Am. Chem. Soc.* **2009**, *131*, 8875-8883.

(13) Shinde, D. B.; Aiyappa, H. B.; Bhadra, M.; Biswal, B. P.; Wadge, P.; Kandambeth, S.; Garai, B.; Kundu, T.; Kurungot, S.; Banerjee, R., *J. Mater. Chem. A* **2016**, *4*, 2682-2690.

(14) Xu, H.; Tao, S.; Jiang, D., *Nat. Mater.* **2016**, *15*, 722-726.

(15) Chandra, S.; Kundu, T.; Kandambeth, S.; Babarao, R.; Marathe, Y.; Kunjir, S. M.; Banerjee, R., *J. Am. Chem. Soc.* **2014**, *136*, 6570-6573.

(16) Han, X.; Huang, J.; Yuan, C.; Liu, Y.; Cui, Y., *J. Am. Chem. Soc.* **2018**, *140*, 892-895.

(17) Liu, L. H.; Yang, C. X.; Yan, X. P., *J. Chromatogr. A* **2017**, *1479*, 137-144.

(18) Medina, D. D.; Petrus, M. L.; Jumabekov, A. N.; Margraf, J. T.; Weinberger, S.; Rotter, J. M.; Clark, T.; Bein, T., *ACS Nano* **2017**, *11*, 2706-2713.

(19) Cai, S.-L.; Zhang, Y.-B.; Pun, A. B.; He, B.; Yang, J.; Toma, F. M.; Sharp, I. D.; Yaghi, O. M.; Fan, J.; Zheng, S.-R.; Zhang, W.-G.; Liu, Y., *Chem. Sci.* **2014**, *5*, 4693-4700.

(20) Patwardhan, S.; Kocherzhenko, A. A.; Grozema, F. C.; Siebbeles, L. D. A., *J. Phys. Chem. C* **2011**, *115*, 11768-11772.

(21) Wan, S.; Gándara, F.; Asano, A.; Furukawa, H.; Saeki, A.; Dey, S. K.; Liao, L.; Ambrogio, M. W.; Botros, Y. Y.; Duan, X.; Seki, S.; Stoddart, J. F.; Yaghi, O. M., *Chem. Mater.* **2011**, *23*, 4094-4097.

(22) Dalapati, S.; Jin, E.; Addicoat, M.; Heine, T.; Jiang, D., *J. Am. Chem. Soc.* **2016**, *138*, 5797-5800.

(23) Wan, S.; Guo, J.; Kim, J.; Ihee, H.; Jiang, D., *Angew. Chem. Int. Ed. Engl.* **2008**, *47*, 8826-8830.

(24) Lukose, B.; Kuc, A.; Frenzel, J.; Heine, T., *Beilstein J Nanotechnol* **2010**, *1*, 60-70.

(25) Haase, F.; Gottschling, K.; Stegbauer, L.; Germann, L. S.; Gutzler, R.; Duppel, V.; Vyas, V. S.; Kern, K.; Dinnebier, R. E.; Lotsch, B. V., *Materials Chemistry Frontiers* **2017**, *1*, 1354-1361.

(26) Lukose, B.; Kuc, A.; Heine, T., *Chemistry* **2011**, *17*, 2388-2392.

(27) Xu, H.; Gao, J.; Jiang, D., *Nat. Chem.* **2015**, *7*, 905-912.

(28) Auras, F.; Ascherl, L.; Hakimioun, A. H.; Margraf, J. T.; Hanusch, F. C.; Reuter, S.; Bessinger, D.; Doblinger, M.; Hettstedt, C.; Karaghiosoff, K.; Herbert, S.; Knochel, P.; Clark, T.; Bein, T., *J. Am. Chem. Soc.* **2016**, *138*, 16703-16710.

(29) Ascherl, L.; Sick, T.; Margraf, J. T.; Lapidus, S. H.; Calik, M.; Hettstedt, C.; Karaghiosoff, K.; Döblinger, M.; Clark, T.; Chapman, K. W.; Auras, F.; Bein, T., *Nat. Chem.* **2016**, *8*, 310-316.

(30) Zhou, T. Y.; Xu, S. Q.; Wen, Q.; Pang, Z. F.; Zhao, X., *J. Am. Chem. Soc.* **2014**, *136*, 15885-15888.

(31) Dogru, M.; Handloser, M.; Auras, F.; Kunz, T.; Medina, D.; Hartschuh, A.; Knochel, P.; Bein, T., *Angew. Chem. Int. Ed. Engl.* **2013**, *52*, 2920-2924.

(32) Calik, M.; Auras, F.; Salonen, L. M.; Bader, K.; Grill, I.; Handloser, M.; Medina, D. D.; Dogru, M.; Lobermann, F.; Trauner, D.; Hartschuh, A.; Bein, T., *J. Am. Chem. Soc.* **2014**, *136*, 17802-17807.

(33) Guo, J.; Xu, Y.; Jin, S.; Chen, L.; Kaji, T.; Honsho, Y.; Addicoat, M. A.; Kim, J.; Saeki, A.; Ihee, H.; Seki, S.; Irle, S.; Hiramoto, M.; Gao, J.; Jiang, D., *Nat. Commun.* **2013**, *4*, 2736.

(34) Bessinger, D.; Ascherl, L.; Auras, F.; Bein, T., *J. Am. Chem. Soc.* **2017**, *139*, 12035-12042.

(35) Medina, D. D.; Sick, T.; Bein, T., *Advanced Energy Materials* **2017**, *7*, 1700387.

(36) Thommes, M.; Kaneko, K.; Neimark, A. V.; Olivier, J. P.; Rodriguez-Reinoso, F.; Rouquerol, J.; Sing, K. S. W., *Pure Appl. Chem.* **2015**, *87*, 929-1069.

(37) Zhang, G. F.; Chen, Z. Q.; Aldred, M. P.; Hu, Z.; Chen, T.; Huang, Z.; Meng, X.; Zhu, M. Q., *Chem Commun (Camb)* **2014**, *50*, 12058-12060.

(38) Hatakeyama, T.; Hashimoto, S.; Seki, S.; Nakamura, M., *J. Am. Chem. Soc.* **2011**, *133*, 18614-18617.

(39) Sick, T.; Hufnagel, A. G.; Kampmann, J.; Kondofersky, I.; Calik, M.; Rotter, J. M.; Evans, A.; Doblinger, M.; Herbert, S.; Peters, K.; Bohm, D.; Knochel, P.; Medina, D. D.; Fattakhova-Rohlfing, D.; Bein, T., *J. Am. Chem. Soc.* **2018**, *140*, 2085-2092.

(40) Klahr, B. M.; Martinson, A. B.; Hamann, T. W., *Langmuir* **2011**, *27*, 461-468.

(41) Lu, J.; Zhang, J., *J. Mater. Chem. A* **2014**, *2*, 13831-13834.

# 8. CONCLUSION AND OUTLOOK

This work is focused on developing novel methodologies for the synthesis of highly crystalline and open porous covalent organic frameworks (COFs) and their final usage in optoelectronic applications.

In chapter three, we describe a modulation strategy for the synthesis of highly crystalline COF-5, consisting of a linear diboronic acid (BDBA) and a triphenylene unit (HHTP) with three identical connecting sites. Through the modulation strategy, COF-5 crystals with large domain sizes and unprecedented high surface areas are obtained. The synthesis pathways are based on including mono-functional competing reactants in the reaction mixture to slow down the reaction kinetics and thereby the growth of the COF fragments. As a direct result, a material with enlarged effective COF domain sizes reaching up to several hundreds of nanometers is obtained. Nitrogen sorption experiments revealed BET surface areas of about 2000 $m^2g^{-1}$, which is in the range of the predicted value for the COF-5 framework. In combination with a narrow pore size distribution and large pore volumes we conclude that a highly ordered and open porous framework was realized. Further mechanistic investigations on the chemical composition of the modulated COF *via* NMR showed that COF-5 forms over a broad range of boronic acid compositions, ranging from fully saturated in the non-modulated case consisting of solely BDBA building blocks to 60% deficiency of BDBA in modulated COF syntheses. Furthermore, the addition of a monofunctional modulator (-SH and –COOH) allows for incorporation of additional functional groups that are available for post-synthetic functionalization at the outer surface of the COF-5 crystallites. A subsequent covalent attachment to these accessible functionalities was proven by reactive polymers and molecules, varying the properties of the resulting composite regarding chemical, physical or electronic properties. Additionally, a higher stability towards ethanol treatments was shown for a PEG-modified COF-5. Furthermore, fluorescent labels were successfully attached to the outer COF surface. Being able to precisely vary the outer surface can play a pivotal role in systematically varying attachments and investigating their influence on potential applications like gas storage, catalysis or charge carrier diffusion and conductivity. Enhancing the degree of crystallinity and gaining control of the outer surface in only one step might be useful for many different applications.

In chapter four the influence and the importance of propeller and screw-like building blocks was investigated in detail. The stacking of adjacent layers in totally planar systems like COF-5

is not perfectly eclipsed but influenced by electrostatic forces of repulsion or solvent intercalation. By the incorporation of building blocks that pivot due to steric hindrances, adjacent layers have energetically predefined points of docking (ETTA; TAPB; TAPA). Especially in the case of ETTA COFs, the transfer of the orientation of the rotated/pivoted groups through linear building blocks with C2 symmetry allows for the growth of COFs with highly extended domain sizes, extraordinary long-range order and open porosity. This minimization of occurring dislocations and stacking faults enabled the precise structural investigation *via* pair distribution function (PDF) at a synchrotron. The generality of the concept was shown for several different ETTA-based structures.

As a platform for a new field of application, BDT-ETTA-based, oriented COF thin films of 100 nm were found to be active as photocathodes in light-driven water-splitting as described in chapter five. A favorable bandgap of 2.47 eV which is suitable for the water-splitting application was evaluated for the BDT-ETTA COF. These bare COF films without any noble metal co-catalyst or sacrificial agents showed considerable activity. The light-to-current conversion efficiency was measured to be 0.38% at 355 nm. The film's general photoabsorbing stability was proven by chronoamperometric measurements under chopped illumination at different potentials. At 0.4 V, the BDT-ETTA COF film showed structural stability and good photoactivity. To detect hydrogen, a four-electrode setup with a platinum indicator electrode monitoring evolving hydrogen was built. To confirm the hydrogen detection, a hydrogen microsensor with a hydrogen selective silicone membrane was incorporated into the setup. The detection of hydrogen proved the successful light-driven water-splitting process by the COF film. To further increase the obtained photocurrent for the BDT-ETTA system (current density of 0.9 μA $cm^{-2}$ at 0.4 V vs. RHE), platinum co-catalyst nanoparticles were deposited on top of the electrodes. With this approach a fourfold increase of the obtained photocurrents could be realized. The films retained their stability and preferred crystallite orientation during the water-splitting process under applied bias, which was proven by GIWAXS measurements prior and after the usage of the COF photocathode for the water-splitting process.

Additionally, ETTA-COFs proved to be highly stable towards many organic and aqueous solution treatments, being beneficial for numerous fields of application. Nevertheless, the usage of ETTA-based COFs involves challenges. The π-stacking distance in ETTA-based COFs is significantly larger compared to COFs containing planar building blocks. This is attributed to the sterically-demanding pivoted ETTA configuration, acting as a rigid propeller-like building block. This increase in stacking distances can act as a barrier for charge carrier diffusion along

the molecular stacks. To counteract the increased π-stacking distance in the case of propeller building blocks, we further investigated in detail the structural properties of TAPB-based COFs in chapter six. Overall, TAPB is a more flexible propeller-like building block compared to ETTA. This is indicated by DFT-calculated dihedral angles of 30° in the case of TAPB versus 44° in case of ETTA. On this basis, in the fourth project in the thesis, we investigated the structural stability of TAPB-COFs with respect to their crystallinity and porosity. The detailed investigation of the role of the linear building block counterpart to the TAPB revealed a strong impact on the COFs' structural stability. While small, non-functionalized linear building blocks resulted in solvent and vapor sensitive TAPB-COFs (fragile), alkoxy-modified and π-extended linear building blocks allowed for the synthesis of highly solvent-resistant frameworks (robust). To access high crystallinity and porosity in each TAPB-based COF, an activation procedure *via* supercritical carbon dioxide ($scCO_2$) extraction was developed as a highly efficient and fast protocol to access high quality TAPB-COFs. The sensitivity of the frameworks, especially towards 1,4-dioxane, was found to be reversible. The successful reactivation/switching of amorphous, non-porous polymers back to highly crystalline, open porous frameworks (with surface areas of up to 2000 $m^2g^{-1}$) underlines the drastic changes and the tunable properties. This reversible process might be useful in sensing applications or in the selective separation of gases through TAPB-COF-membranes.

In the final chapter seven, we targeted a relative of the ETTA building block featuring a more planar configuration, namely a dibenzo[*g*,*p*]chrysene-based tetraamine (DBCA). DBC-based COFs with a similar linear linkers as the ETTA-based COFs yielded similar pore size and topology however with significantly closer stacking distances between adjacent layers. In general, the ETTA-based COFs exhibit a stacking distance of about 0.46 nm, while the DBC analogs feature stacking distances of about 0.37 nm. Furthermore, extending the π-overlapped system by the enforced planarization of the DBC molecule, the charge carrier transport within the COF layer is expected to be positively affected as well. Oriented thin films of TT DBC-COF were successfully grown on different substrates such as quartz and ITO. The photo-physical properties of thienothiophene-based chrysene COF films namely UV-Vis, ssPL, and TCSPC data revealed potential for OPV applications. A comparably small direct band gap of 2.05 eV was evaluated for the COF reflecting its broad absorption in the visible part of the spectrum. In addition, the long lifetimes of the DBC powders and films shown in the TCSPC investigations and their high contribution to the overall intensity are promising features for potential optoelectronic applications. Especially in the case of Biph DBC-COF, a 19.6%

contribution of a long-lived state of 7.85 ns is noteworthy. In combination with the enlarged π-system, we expect an improved conductivity and mobility of excited charge carriers in all three dimensions, which is currently under investigation.

Future developments could aim at the incorporation of enlarged π-systems to benefit from the great possibilities in COF design. A good combination of photoabsorbing and conduction properties could pave the way towards more efficient OPVs based on COFs. Furthermore, this class of materials already shows rising potential in water-splitting applications and energy storage. Especially the synthesis of high quality and oriented COF films is expected to play a key role in the near future. Optoelectronic applications require pure materials comprising a low number of structural defects mainly when deposited on surfaces. Aiming at COF films with enlarged domains and a low density of grain boundaries in combination with fast and efficient film deposition or film growth processes would allow for the incorporation in photovoltaics or field effect transistors. The incorporation of new functionalities or the design of new COFs with charged back bones or side groups could allow for the introduction of new applications such as selective adsorption of pollutants and removal of green house gases.

# 9.APPENDIX

LIST OF ABBREVIATIONS

| | |
|---|---|
| 2θ | Diffraction angle |
| 2D | Two dimensional |
| 3D | Three dimensional |
| AFM | Atomic force microscopy |
| AM 1.5 | Air mass (solar energy) 1.5 |
| ATR | Attenuated total reflection |
| BDT | Benzo[1,2-*b*:4,5-*b*′]dithiophene |
| Biph | 4,4’-Biphenyl |
| BJH | Barrett, Joyner, Halenda |
| BET | Brunauer-Emmett-Teller |
| BnOH | benzyl alcohol |
| BSE | Back scattered electron |
| CCD | Charge-coupled device |
| CMC | Critical micelle concentration |
| COF | Covalent organic framework |
| CTF | Covalent triazine framework |
| $\delta$ | chemical shift |
| DBC | dibenzo[*g*,*p*]chrysene |
| DBCA | dibenzo[*g*,*p*]chrysene-2,7,10,15-tetraamine |
| DCM | Dichloromethane |
| DFT | Density functional theory |
| DMSO | Dimethylsulfoxide |
| DSC | Differential scanning calorimetry |
| EDX | Energy dispersive X-ray spectroscopy |
| EISA | Evaporation-induced self-assembly |
| EM | Electron microscopy |
| EQE | External quantum efficiency |
| EtOH | Ethanol |
| ETTA | 4,4′,4″,4‴-(Ethylene-1,1,2,2-tetrayl)tetraaniline |

| | |
|---|---|
| FET | Field-effect transistor |
| FTO | Fluorine doped tin oxide |
| FT-IR | Fourier-transform infrared spectroscopy |
| FWHM | Full width at half maximum |
| GID | Grazing-incident diffraction |
| GIWAXS | Grazing-incident Wide-angle X-ray scattering |
| HER | Hydrogen evolution reaction |
| HOMO | Highest occupied molecular orbital |
| HPLC | High-performance liquid chromatography |
| HRTEM | High resolution transmission electron microscopy |
| IPCE | Incident photon-to-current efficiency |
| IR | Infrared |
| ITO | Indium doped tin oxide |
| IUPAC | International Union of Pure and Applied Chemistry |
| LUMO | Lowest unoccupied molecular orbital |
| MAPB | 1-(4-Aminophenyl),3,5-diphenyl-benzene |
| MC | Monte Carlo methods |
| Mes | Mesitylene |
| MHz | Megahertz |
| MOF | Metal-organic framework |
| $MoO_x$ | Molybdenum oxide |
| N | Number of atoms |
| NA | Numerical aperture |
| NHE | Normal hydrogen electrode |
| NLDFT | Non-local density functional theory |
| nm | Nanometer |
| NMR | Nuclear magnetic resonance |
| OER | Oxygen evolution reaction |
| OFET | Organic field-effect transistor |
| OPV | Organic photovoltaics |
| $PC_{60}BM$ | [6,6]-Phenyl-C61-butyric acid methyl ester |
| $PC_{70}BM$ | [6,6]-Phenyl-C71-butyric acid methyl ester |
| PEC | Photoelectrochemical |
| PL | Photoluminescence |

| | |
|---|---|
| PXRD | Powder X-ray diffraction |
| $p^0$ | Saturation pressure |
| QSDFT | Quenched Solid density functional theory |
| R | Resolution |
| RT | Room temperature |
| SAED | Selected area electron diffraction |
| SAXS | Small angle X-ray scattering |
| SDA | Structure directing agent |
| $ScCO_2$ | Supercritical $CO_2$ |
| SE | Secondary electrons |
| SEM | Scanning electron microscopy |
| SNR | Signal-to-noise ratio |
| ssPL | Steady state photoluminescence |
| STEM | Scanning transmission electron microscopy |
| STH | Solar-to-hydrogen conversion efficiency |
| T | Temperature |
| TA | terephthalaldehyde |
| TAPA | Tris(4-aminophenyl)amine |
| TAPB | 1,3,5-Tris(4-aminophenyl)benzene |
| TCO | Transparent conducting oxide |
| TCSPC | Time-correlated single photon counting |
| TEM | Transmission electron microscopy |
| TEOA | Triethanolamine |
| TGA | Thermal gravimetric analysis |
| THF | Tetrahydrofuran |
| TT | Thieno[3,2-*b*]thiophene |
| µm | Micrometer |
| UV-Vis | Ultraviolet-visible |
| WAXS | Wide angle X-ray scattering |
| XRD | X-ray diffraction |
| Z | Atomic number |
| ZIF | Zeolitic imidazolate framework |

# 10. PUBLICATIONS AND PRESENTATIONS

## 10.1 PUBLICATIONS

### FIRST AUTHOR

1. *Switching on Crystallinity and Permanent Porosity in Fragile Covalent Organic Frameworks*

   **T. Sick**, S. Kandambeth, J. M. Rotter, N. N. Bach, M. Döblinger, A. Evans, J. Merz, O. A. von Mankowski, T. B. Marder, T. Clark, D. D. Medina, T. Bein

   Manuscript in preparation

2. *Stable and Photoactive Chrysene-Based Dual Pore Covalent Organic Frameworks – Closing the Gaps towards Planar and Conjugated Structures*

   **T. Sick**, N. Keller, N. N. Bach, A. Koszalkowski, J. M. Rotter, M. Döblinger, D. D. Medina, T. Bein

   Manuscript in preparation

3. *Oriented Films of Conjugated 2D Covalent Organic Frameworks as Photocathodes for Water Splitting*

   **T. Sick***,‡ A. G. Hufnagel,‡ J. Kampmann,‡ I. Kondofersky, M. Calik, J. M. Rotter, A. M. Evans, M. Döblinger, S. Herbert, K. Peters, D. Boehm, P. Knochel, D. D. Medina, D. Fattakhova-Rohlfing*, T. Bein*

   *J. Am. Chem. Soc.* **2017**, *138* (4), 1234–1239. (supplementary cover)

4. *From Highly Crystalline to Outer Surface-Functionalized Covalent Organic Frameworks – A Modulation Approach*

   M. Calik, ‡ **T. Sick**,‡ M. Dogru, M. Döblinger, S. Datz, H. Budde, A. Hartschuh, F. Auras, T. Bein*

   *J. Am. Chem. Soc.* **2016**, *138* (4), 1234–1239.

# CONTRIBUTIONS

5. *Molecular docking sites designed for the generation of highly crystalline covalent organic frameworks*

   L. Ascherl, T. Sick, J. T. Margraf, S. H. Lapidus, M. Calik, C. Hettstedt, K. Karaghiosoff, M. Döblinger, T. Clark, K. W. Chapman, F. Auras, T. Bein

   *Nat. Chem.* **2016**, *8*, 310-316.

6. *Photoactive and Conducting Covalent Organic Frameworks*

   D. D. Medina, T. Sick, T. Bein

   *Adv. Energy Mater.* **2017**, *7*, 1700387.

7. *Excited State Dynamics in Fully-Conjugated Covalent Organic Frameworks*

   A. C. Jakowetz, T. F. Hinrichsen, L. Ascherl, T. Sick, M. Calik, D. D. Medina, F. Auras, A. Rao, R. H. Friend, T Bein

   Manuscript in preparation

8. *Covalent organic framework films through Electrophoretic Deposition - a Top-down Approach.*

   J. M. Rotter, S. Weinberger, T. Sick, M. Shalom, T. Bein, D. D. Medina

   Manuscript in preparation

*These authors contributed equally

## 10.2 ORAL PRESENTATIONS

1. *From Highly Crystalline to Outer Surface-Functionalized Covalent Organic Frameworks - A Modulation Approach*

   Torben Sick, Mona Calik, Thomas Bein

   Materials Research Society (MRS) fall meeting 2016, Boston, United States of America.

2. *Preserving the Crystallinity and the Porosity of Solvent-Sensitive Covalent Organic Frameworks*

   Torben Sick, Sharath Kandambeth, Julian M. Rotter, Markus Döblinger, Dana D. Medina, T. Bein

   7th International FEZA Conference 2017, Sofia, Bulgaria

3. *Oriented Films of Conjugated 2D Covalent Organic Frameworks as Photocathodes for water splitting*

   Torben Sick, Alexander G. Hufnagel, Jonathan Kampmann, Dana D. Medina, Dina Fattakhova-Rohlfing, T. Bein

   30. Deutsche Zeolith-Tagung (DZT) 2018, Kiel, Germany.

## 10.3 POSTER PRESENTATIONS

1. *Property Enhancement of Covalent Organic Frameworks by a Modulated Synthesis*

   Torben Sick, Mona Calik, Mirjam Dogru, Laura Ascherl, Florian Auras, Thomas Bein

   Soltech Workshop, 2015, Kloster Banz, Germany.

2. *From Highly Crystalline to Outer Surface Functionalized Covalent Organic Frameworks – A Modulation Approach.*

   Torben Sick, Mona Calik, Mirjam Dogru, Markus Döblinger, Florian Auras, Thomas Bein

   CeNS Workshop 2015, Venice, Italy

3. *From Highly Crystalline to Outer Surface Functionalized Covalent Organic Frameworks – A Modulation Approach.*

   Torben Sick, Mona Calik, Mirjam Dogru, Markus Döblinger, Florian Auras, Thomas Bein

   1st European Conference on Metal Organic Frameworks and Porous Polymers (EuroMOF), 2015, Potsdam, Germany.

4. *From Highly Crystalline to Outer Surface Functionalized Covalent Organic Frameworks – A Modulation Approach.*

   Torben Sick, Mona Calik, Mirjam Dogru, Markus Döblinger, Florian Auras, Thomas Bein

   Soltech Workshop, 2016, Munich, Germany.

5. *Preserving the Crystallinity and the Porosity of Solvent-Sensitive Covalent Organic Frameworks*

   Torben Sick, Julian M. Rotter, Markus Döblinger, Dana D. Medina, Thomas Bein

   29. Deutsche Zeolith-Tagung (DZT) 2017, Frankfurt, Germany.

6. *Oriented Films of Conjugated 2D Covalent Organic Frameworks as Photocathodes for water splitting*

   Torben Sick, Alexander G. Hufnagel, Jonathan Kampmann, Dana D. Medina, Dina Fattakhova-Rohlfing, T. Bein

   Nanostructured functional Materials for sustainable Energy Provision, Munich, Germany

7. *Oriented Films of Conjugated 2D Covalent Organic Frameworks as Photocathodes for water splitting*

   Torben Sick, Alexander G. Hufnagel, Jonathan Kampmann, Dana D. Medina, Dina Fattakhova-Rohlfing, T. Bein

   Materials, Characterization and Catalysis Workshop, 2018, ETH Zurich, Switzerland

8. *Crystal Design and Processing Methods Aimed at Stable and Highly Porous Covalent Organic Frameworks*

   Torben Sick, Sharath Kandambeth, Julian M. Rotter, Laura Ascherl, Markus Döblinger, Dana D. Medina, Thomas Bein

   30. Deutsche Zeolith-Tagung (DZT) 2017, Kiel, Germany.